Physical properties of eclipsing binaries containing intermediate-mass pulsators or low-mass stars

Zachary Paul Stephen Jennings

Doctor of Philosophy

Department of Physics, Keele University

March 2024

Abstract

Precise stellar parameter measurements are crucial for improving our theoretical understanding of stellar structure. They help quantify model errors and uncertainties and provide vital constraints for interpreting observed phenomena, such as radius inflation in low-mass stars. To advance stellar theory, particularly for main-sequence intermediate-mass stars, we need to move beyond simplifications related to complex processes like mixing, convection, and magnetism.

Spectroscopically double-lined eclipsing binaries offer precise measurements of conventional properties like mass and radius using geometry-based methods, achieving model-independent precisions often better than 1%. Asteroseismology constrains stellar interiors, reducing model flexibility and enhancing theory-to-observation comparisons. Simultaneously, binarity narrows parameter space and resolves model ambiguities for asteroseismology. These synergies make double-lined eclipsing binary systems with pulsating components invaluable for advancing stellar theory, while also enabling investigations of tidal effects on pulsations.

This work presents the analysis of two doubled lined detached eclipsing binary systems, KIC 9851944 and KIC 4851217, each of which consists of a δ Scuti pulsator and another intermediate mass star. The masses and radii of the components in each EB are measured to precisions better than 1% on average. We report the detection of tidally perturbed pulsations in KIC 9851944 and tidally tilted pulsations, as well as a tertiary component in KIC 4851217. Pulsation mode identification would make these systems well-equipped for advancing intermediate-mass stellar theory with asteroseismology.

For low-mass stellar theory, observational constraints are limited due to the rarity of eclipsing systems featuring two spectroscopically detectable low-mass stars. Increasing instances of M dwarfs transiting brighter F/G dwarfs offer indirect measurements and calibration opportunities. By utilising TESS data and radial velocity measurements, we also improve the characterization of 12 such binaries in this work, in addition to two where we present the first measurements of the M dwarf's properties.

Acknowledgments

"*Nullius in verba*"
– as advocated by the Royal Society

I give thanks to John Taylor for arguing my case as well as being an excellent supervisor during my PhD. I thank the academic staff at Keele who were involved in giving me a chance, as well as those who inspired me as an undergraduate.

Thanks are in order for those who contributed to this work. Specifically, I thank Prof. Kresimir Pavlovski for contributing the atmospheric analysis of KIC 9851944 in Section 3.5, Dr. Timothy Van Reeth for contributing the asteroseismic analysis of KIC 9851944 in Section 3.8, as well as Dr. Barry Smalley for examining the Ca K lines in the disentangled components' spectra of KIC 9851944. I also thank Dr. John Taylor for analysing the light curves of KIC 9851944 and KIC 4851217, where these contributions were given in Sections 3.6 and 4.5, respectively; Dr. John Taylor also calculated the physical properties of these systems in Sections 3.7 and 4.6, for which I am grateful.

I thank Prof. Saul Rappaport for contributing an analysis of the SED of KIC 4851217 in Section 4.3.3. Prof. Saul Rappaport also helped me to develop a python code for modelling ETV signatures, which I then used in the analysis of KIC 4851217 in Section 4.3.2. This development benefitted from discussions with Prof. Tamas Borkovits who also contributed a joint photodynamical analysis of the the individual data sets for KIC 4851217 in Section 4.6.1. Prof. Gerald Handler performed a frequency analysis of KIC 4851217 and calculated reconstructions of phases and amplitudes of modes corresponding to tidally split multiplets, and this was outlined in Section 4.7.1. I am grateful for this contribution as well as discussions with Prof. Gerald Handler, Prof. Donald Kurtz, Prof. Jim Fuller and Prof. Saul Rappaport, which helped me interpret those modes in Section 4.7.2.

The remaining analysis sections presented in this thesis were carried out by myself. I thank my supervisor Dr. John Taylor for guidance and support in carrying out

and writing up these analyses. Prof. Saul Rappaport gave advice and comments on the entire KIC 4851217 chapter; for this I am grateful. Finally, those involved in obtaining or making available the observational data used in this work are due thanks. That is, Dr. John Taylor and Dr. Kelsey Clubb (Hamilton observations; Section 3.2.2), Dr. Jonas Debosscher and Dr. Timothy Van Reeth (HERMES observations; Section 4.2.3), Dr. Stuart Littlefair and Dr. Steven Bloemen (WHT observations; Section 4.2.2), as well as Dr. Pierre Maxted, Dr. John Taylor and Dr. Luigi Mancini (ground based light curves; Section 5.2.2).

We gratefully acknowledge financial support from the Science and Technology Facilities Council. This research has made use of the SIMBAD and CDS databases operated by the Centre de Données astronomiques de Strasbourg, France. This paper also made use of data from the *Kepler* and TESS missions obtained from the MAST data archive at the Space Telescope Science Institute (STScI). Funding for the *Kepler* and TESS missions is provided by the NASA Science Mission Directorate and NASA Explorer Program, respectively. STScI is operated by the Association of Universities for Research in Astronomy, Inc., under NASA contract NAS 5–26555. We are grateful to Songhu Wang and Nicolas Crouzet for providing us with their RV measurements for TYC 9535-351-1 via private communication.

I will not forget Elizabeth Todd who played a pivotal role in my progression. Finally, my eternal gratitude extends to my Mother for unwaveringly supporting my academic pursuits.

Zac Jennings
October 2023

Contents

List of Figures

List of Tables

1 Binary Stars and Asteroseismology

The aim of this chapter is to acquaint the reader with the scientific rationale behind the analysis of pulsating stars in eclipsing binary systems. To accomplish this, it is necessary to introduce the two fundamental topics: *binary stars* and *asteroseismology*. Notably, the study of binary stars extends to encompass considerations within hierarchical *multiple* systems. After establishing the key concepts necessary for study in these fields, a discussion of each field in the context of constraining our theoretical knowledge of stellar structure and evolution lays the groundwork for understanding the advantages of their integration.

1.1 Binary Stars

Multiple and binary systems make up the vast majority of all observed medium and high mass stellar objects in our Galaxy (Duchêne & Kraus, 2013). Such systems can be used to measure the properties of distant stars and this allows us to understand the galaxy beyond our solar neighbourhood. The distribution functions of the orbital parameters of binary stars feed directly into our understanding of binary formation, so they also contribute to the development of star formation theories (Duchêne & Kraus, 2013; Moe & Di Stefano, 2017; Murphy, 2018; Shahaf & Mazeh, 2019; Murphy et al., 2021). Many of the objects in the galaxy are the result of binary evolution (e.g., cataclysmic variable stars, black hole binaries, X-ray binaries, etc.) so an accurate understanding of binary evolution is necessary for a complete understanding of the galaxy (see Kopal, 1959; Morton, 1960; Paczyński, 1971; Zahn, 1977; Wellstein et al., 2001; Hurley et al., 2002; Paxton et al., 2015, for theories on binary evolution). In the context of this work, they are important because we can measure accurate stellar parameters from them. This section introduces the field of binary stars.

1.1.1 Roche Model and Morphology

1.1.1.1 Roche Model

The components in a binary system might not be spherically symmetric owing to tides and rotation. For well-*detached* binaries, the distortions may only consist of minor tidal bulges so can be approximated as small perturbations and described using Legendre polynomials (Hilditch, 2001); this approach is adopted to describe the angular dependence of stellar pulsations in Section 1.2.1.2. The approach is not adequate, however, for the case of strong tides and extreme distortions, i.e., close binaries (e.g., Bell & Malcolm, 1987) or those with evolved components. In general, a realistic model for the shapes of stars in binaries needs to provide a quantitative description of spheres as well as tidally distorted ellipsoids (Hilditch, 2001).

For a rigidly rotating star in hydrostatic equilibrium, surfaces of constant density, potential, and pressure coincide. Thus, the physical shape of a star follows the shape of an equipotential surface. This is the basis of the *Roche model* for approximating the shapes of stars. The Roche model assumes that the shapes of the components are determined by the *instantaneous* force field of two point masses surrounded by a massless envelope, which implies the assumption that deviations from hydrostatic equilibrium are damped on time-scales that are *negligible* compared to the orbital period (Prša, 2018).

The *Kopal* potential (Kopal, 1959) is the *dimensionless* effective potential due to a star in a binary system assuming a synchronous, aligned, and circular orbit. Wilson (1979) proposed a corresponding expression assuming, only, that the orbital and rotation axes are aligned, which follows,

$$\Phi = \frac{1}{\rho} + q\left(\frac{1}{\sqrt{\delta^2 + \rho^2 - 2\rho\lambda\delta}} - \frac{\rho\lambda}{\delta^2}\right) + \frac{1}{2}\mathbf{F}^2(1+q)\rho^2(1-\nu^2) \tag{1.1}$$

where δ is the instantaneous distance to the star in units of the separation of the components, $F = \Omega_{\rm rot}/\Omega_{\rm orb}$ is the synchronicity parameter defined as the ratio between the rotational and orbital angular velocities, q is the mass ratio of the components, and $\lambda = \sin\theta\cos\theta$ and $\nu = \cos\theta$ are direction cosines with θ the co-latitude of the location of interest with respect to the rotation axis of the subject star (Prša, 2018). The value of Φ can be calculated for any location around the two stars, allowing for surfaces of constant potential in a reference frame rotating with the orbit to be calculated (Hilditch, 2001).

1.1.1.2 Morphology of Binary Stars

Fig. 1.1 shows lines of constant potential calculated for a system with a mass ratio of $q = 5$. The red equipotentials from each star touch at the *inner Lagrangian point* L_1, and the saddle points at L_1 define the *Roche lobes*. The *Roche lobe radius*, the distance of L_1 from either point mass, depends on the mass ratio of the components and is larger for the more massive component (Boffin & Jones, 2019). The Roche lobe radii limit

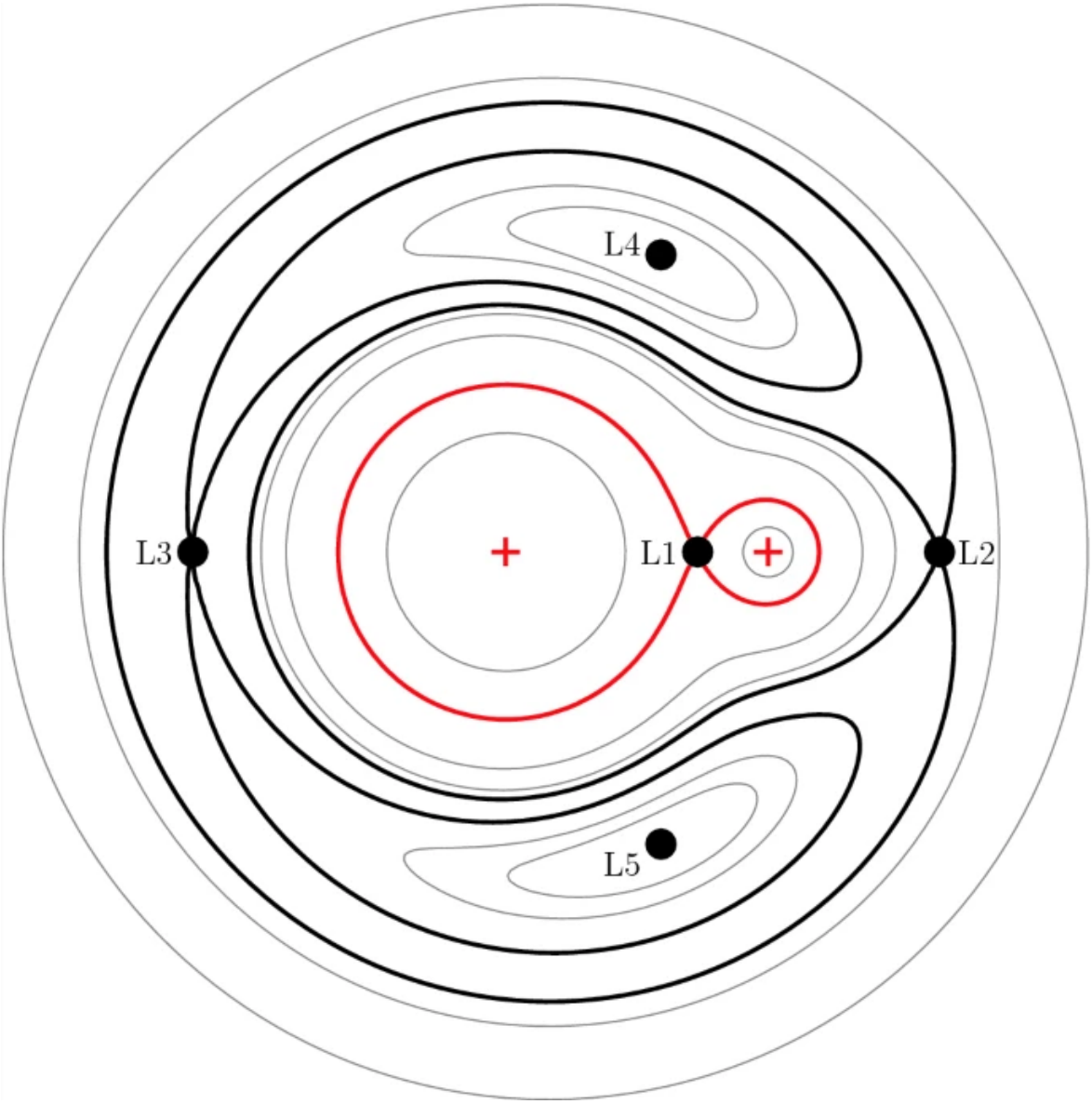

Figure 1.1: Lines of constant potential calculated for a system with a mass ratio of 5 from Boffin & Jones (2019). The five Lagrangian points are marked and the more massive component is on the left.

the possible sizes of the stars because stellar matter is only gravititationally bound to them if it is within their Roche lobe. This leads to a morphological classification of binary stars based on the sizes of the components compared to their Roche lobe radii.

Each component in a *detached* binary system is within its Roche lobe and their shapes correspond to circular equipotentials, i.e., the innermost grey equipotentials from the point masses in Fig. 1.1. The only way mass transfer occurs for these systems is through stellar wind (Boffin & Jones, 2019). These circular equipotentials become increasingly distorted as the stellar radius approaches the Roche lobe radius, and a *semi-detached* configuration occurs when one of the components fills its Roche lobe, e.g., at later evolutionary stages. Mass transfer may now proceed via the L_1 point with the shape of the overflowing, i.e., *donor*, star replicating the shape of its Roche lobe. When both stars fill their Roche lobes, the two stars are in physical contact via a narrow neck in the region of L_1 and are surrounded by a common envelope (Hilditch, 2001). These are *contact* binaries and take the shape of the equipotentials between the inner limiting potential (i.e., the red potential in Fig. 1.1), which contains L_1, and the outer limiting potential that contains the second Lagrangian point L_2.

The second, or *outer*, Lagrangian point L_2 is the location through which matter can escape from the gravitational field of the binary system most easily. The L_3 point is an additional escape route at a zone of higher potential (Hilditch, 2001). The potential maxima are located at L_4 and L_5.

1.1.2 Geometry and Orbital Dynamics

1.1.2.1 Relationships Between the Orbits

There are three orbits to consider for the components in a binary system. These are the two *barycentric orbits*, each describing the motion of either component about the centre of mass of the binary system, and the *relative orbit*. The latter describes the motion of the components *relative* to one another by considering the difference between the equations of motion implied by the gravitational acceleration experienced by either

body. A detailed overview of these orbits is given in Appendix A.

The relationships between these orbits is important; information that we obtain about the motion of the objects, i.e, radial velocities (RVs), correspond to how the objects behave in their barycentric orbits. On the other hand, eclipses depend on the geometry of the stars in their orbits *relative* to each other. Hence, the following relationships provide the necessary links between the different types of observational data (Hilditch, 2001).

First, consider that angular momentum is the cross product of the distance vector and linear momentum, so is perpendicular to the orbital plane. If angular momentum is conserved, it is fixed in this direction with respect to each of the orbits and the orbits are coplanar. Indeed, conservation of angular momentum is implied for binary orbits where no forces are acting on the system because the potential is central [1]. This further implies the periods and eccentricities must be equal (Prša, 2018),

$$P_1 = P_2 = P, \tag{1.2}$$

$$e_1 = e_2 = e, \tag{1.3}$$

where P and e are the period and eccentricity of the relative orbit, respectively. The subscripts 1 and 2 (and hereafter) denote the same values for the barycentric orbit of the primary and secondary star, respectively. Another consequence of the central potential is that $a_1 + a_2 = a$, where a is the semi-major axis of the orbit. These considerations, as well as further details for which we refer to Appendix A.1, lead to the following proportionalities,

$$a_1 : a_2 : a = M_2 : M_1 : (M_1 + M_2) = \dot{r_1} : \dot{r_2} : \dot{r}, \tag{1.4}$$

where M is stellar mass and $\dot{r}$ is the orbital speed.

[1] The potential is central because the only force acting is along the line connecting the stars. The force and distance vectors are parallel and the torque acting on the system $\boldsymbol{\tau} = \boldsymbol{r} \times \boldsymbol{F}$ is zero, i.e., no rotational acceleration or deceleration; angular momentum is conserved.

1.1.2.2 Orientation of the Orbit

The orientation of an orbit with respect to the plane of the sky is shown in Fig. 1.2 where the observer is defined to be along the z-axis and the x- and y- axes are in the plane of the sky, which is indicated by the dashed circle.

The inclination i is the angle measured from the sky plane to the orbital plane and assumes a value between 0 and $\pi/2$. The two points of intersection on the orbital path are the nodes and are where the apparent speed of the star is maximum; the motion is directed away from the observer at the *ascending* node, and toward the observer at the *descending* node. The argument of periastron ω is the angle measured from the ascending node to periastron and assumes a value between 0 and 2π; the value of ω for the secondary star's orbit is offset by π radians compared to that of the primary star's orbit. The longitude of the ascending node Ω is measured from a reference direction, e.g., north or the x-axis, to the ascending node counter clockwise, and defines the orientation of the orbit in space perpendicular to the observer (Prša, 2018; Hilditch, 2001).

The *ephemeris* of the system describes the periodicity of events, e.g., eclipses or periastron passage, relative to some reference time T_0. The period is then the period at $t = T_0$, i.e., P_0, and if this remains constant, the ephemeris is defined completely by these two parameters. The time of minimum flux is a suitable choice for T_0 for eclipsing systems because of efficient methods in determining its value (e.g., Kwee & van Woerden, 1956); the ephemeris is then written as,

$$\text{Min.I} = T_0 + P_0 E \tag{1.5}$$

where E is an integer counting the amount of successive orbital cycles since T_0; this is a linear ephemeris. A non-linear ephemeris arises if the observed period changes with time, i.e., when the times between consecutive eclipses, in this case, is not constant. Such *eclipse time variations* (ETVs) occur due to, e.g., *apsidal motion* or tidal effects (see section 1.1.3.4). Apsidal motion refers to the rotation of the line of apsides and arises due to gravitational torques in the system that are the result of, e.g., non-

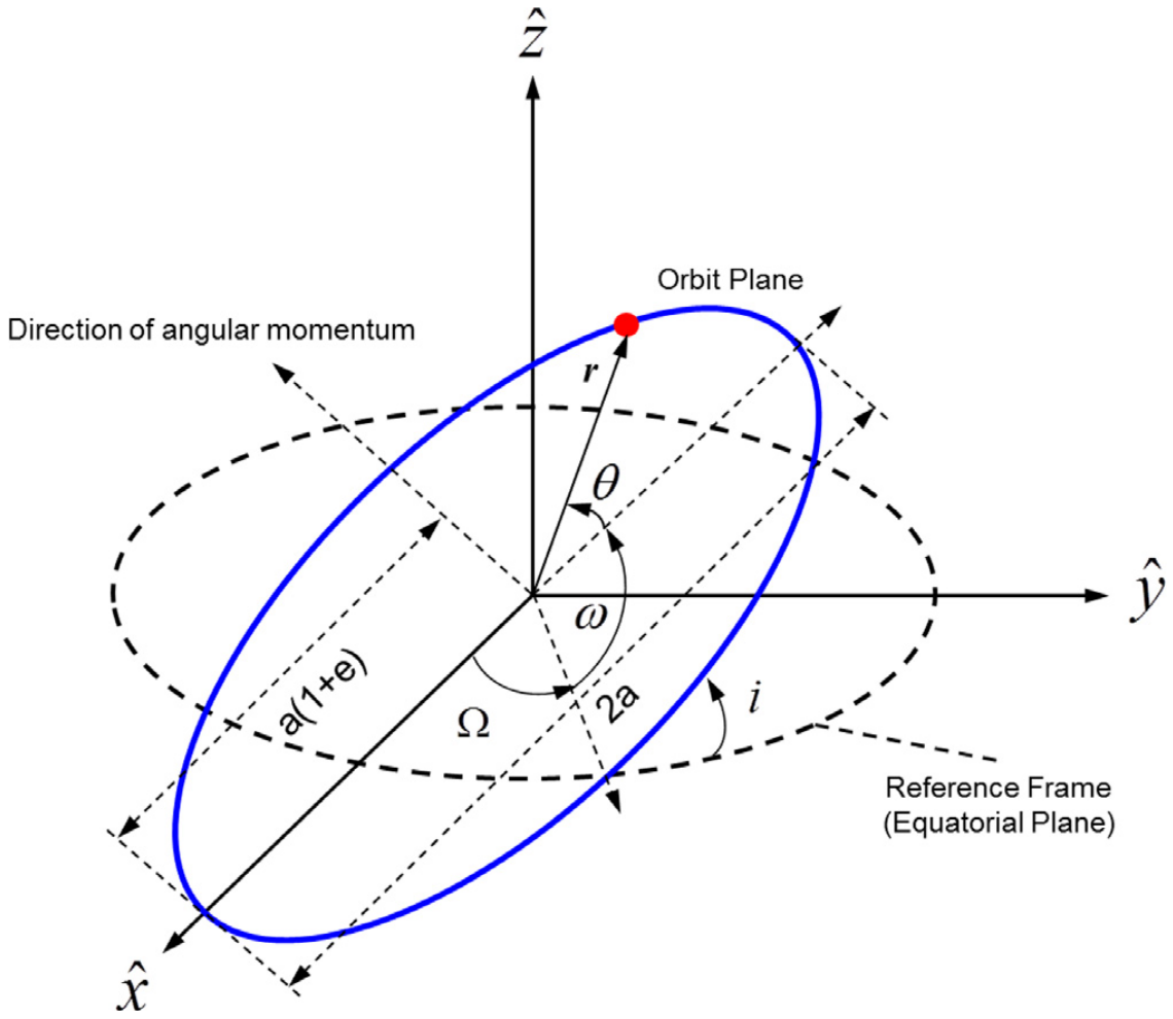

Figure 1.2: Orientation of the orbit from Shin et al. (2015). Note- the angle ν is indicated by θ in this figure.

spherical mass distributions in distorted stars[2]. ETVs imply a time-dependent value for ω so accurately accounting for such effects in Eq. 1.5 defines the orientation of the orbit in time.

This completes our parameters for describing the orbit: $P, T_0, a, e, i, \omega, \Omega$; these are the Campbell elements (Mendez et al., 2017; Halbwachs et al., 2023), where a and e describe the two-dimensional geometry of the ellipse and were introduced in the Section 1.1.2.1. The parameters P and T_0 specify in the time dimension, while i, ω, and Ω, extend the description to three-dimensions.

1.1.2.3 Kepler's Equation

The Hamiltonion describing the total energy of the orbit (Eq. A.3) can not be solved analytically for a star's position as a function of time $r(t)$. Thus it is solved for the position as a function of the *true anomaly* ν (see below) instead, leading to the *polar equation of orbit* (Eq. A.4) and the necessity of a link between $r(\nu)$ and $r(t)$.

Fig. 1.3 shows the *auxillary circle* of an ellipse. We start by exploiting the geometry of the configuration to define the following quantities: The *true anomaly* ν is the angle measured from periastron to the star's position P about the focal point of the ellipse, which is denoted by S in Fig. 1.3; the *eccentric anomaly* E is related to the true anomaly and is similar to the true anomaly except for a projection of the star's position onto the auxillary circle at Q and measured from the origin at O; a time dependence is explicitly introduced by the mean anomaly $\mathcal{M}$, which is defined as,

$$\mathcal{M} = 2\pi \frac{t - t_{\rm per}}{P} = \omega(t - t_{\rm per}), \tag{1.6}$$

where here, ω is the orbital frequency and $t_{\rm per}$ is the time of periastron passage (Moulton, 1895; Fulton et al., 2018). These three anomalies are used to solve the *Kepler*

[2]In Section 1.1.2.1, we assumed spherically symmetric stars so the potential depends only on the gravitational monopole moment, leading to a central potential with no torques acting in or on the system (see Appendix A.1). Non-uniform mass distributions, on the other hand, give rise to more complex gravitational fields that require higher order moments and are not purely radially directed.

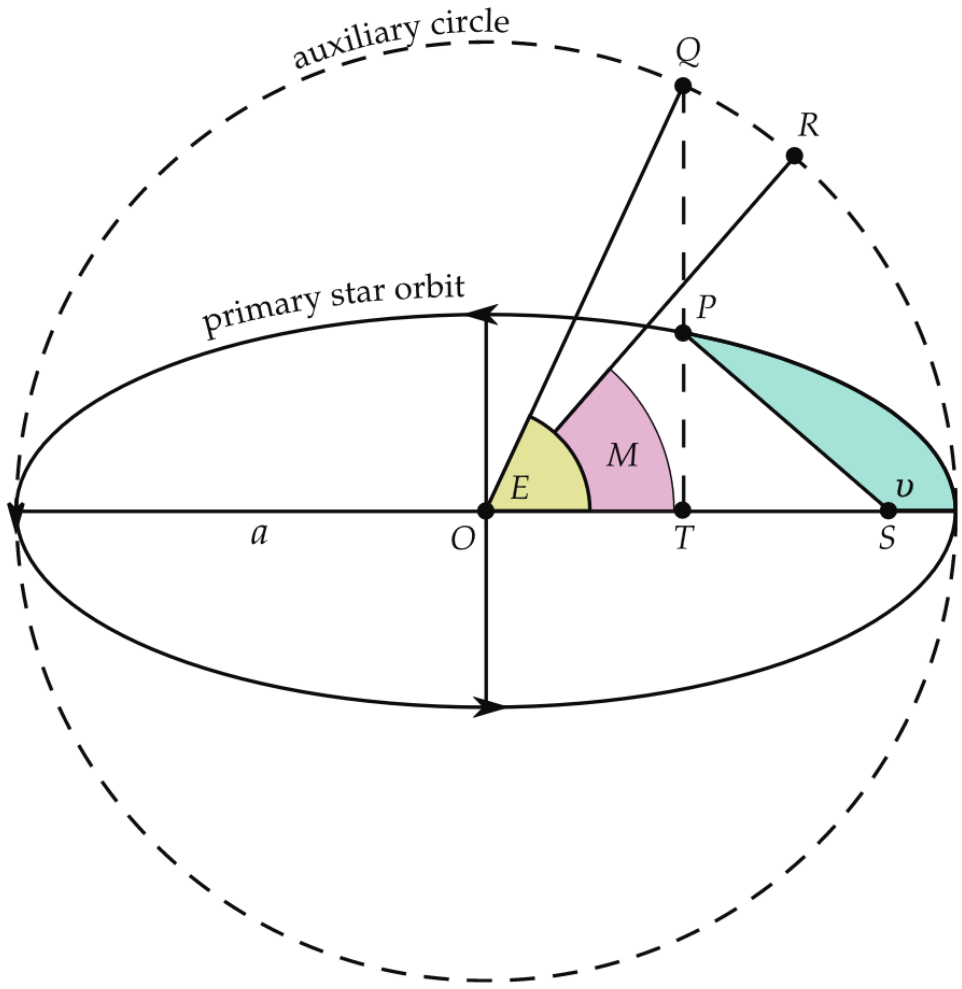

Figure 1.3: Auxillary circle from Prša (2018).

problem in Appendix A.3. The result is *Kepler's equation*,

$$E - e\sin E = \omega(t - t_{\rm per}) = \mathcal{M}, \tag{1.7}$$

which describes the complex time dependence of the of the stars position on an elliptical orbit, allowing to convert from $r(\nu)$ to $r(t)$ given the following relationship between E and ν (Smart & Green, 1977, see Appendix A.3),

$$\tan\frac{E}{2} = \sqrt{\frac{1-e}{1+e}}\tan\frac{\nu}{2}. \tag{1.8}$$

1.1.2.4 Radial Velocity

The radial velocity (RV) is the component of the velocity that we can measure through the Doppler effect, so here we are concerned with stellar motion along our line of site, i.e., the z-axis in Fig. 1.2. The z-component of the velocity is derived in Appendix A.4 as,

$$\dot{z} = \frac{a_1\omega\sin i}{1 - e\cos E}(\sqrt{1-e^2}\cos\omega\cos E - \sin\omega\sin E). \tag{1.9}$$

Using the trigonometric relations for $\sin E$ and $\cos E$ defined in Eq. A.24, the radial component of the velocity relative to the barycentre of the system can be written as,

$$V_r = \frac{2\pi a_1\sin i}{P\sqrt{1-e^2}}[e\cos\omega + \cos(\omega+\nu)]. \tag{1.10}$$

The terms outside the square brackets equate to the velocity semi-amplitude K. We further generalise by accounting for the motion of the barycentre along the line of site, the *systemic velocity* γ, by adding it to Eq. 1.10. This yields our model for the orbital motion of a star bound in Keplarian motion,

$$V_r = K[e\cos\omega + \cos(\omega+\nu)] + \gamma, \tag{1.11}$$

which is plotted as a function of orbital phase in Fig. 1.4 for varied values of e (top four panels) and ω (bottom four panels).

These *RV curves* depend on the orbital parameters via Eq. 1.11. For circular orbits, $e\cos\omega = 0$ so Eq. 1.11 is dominated by the variation in $\cos(\omega+\nu)$, where

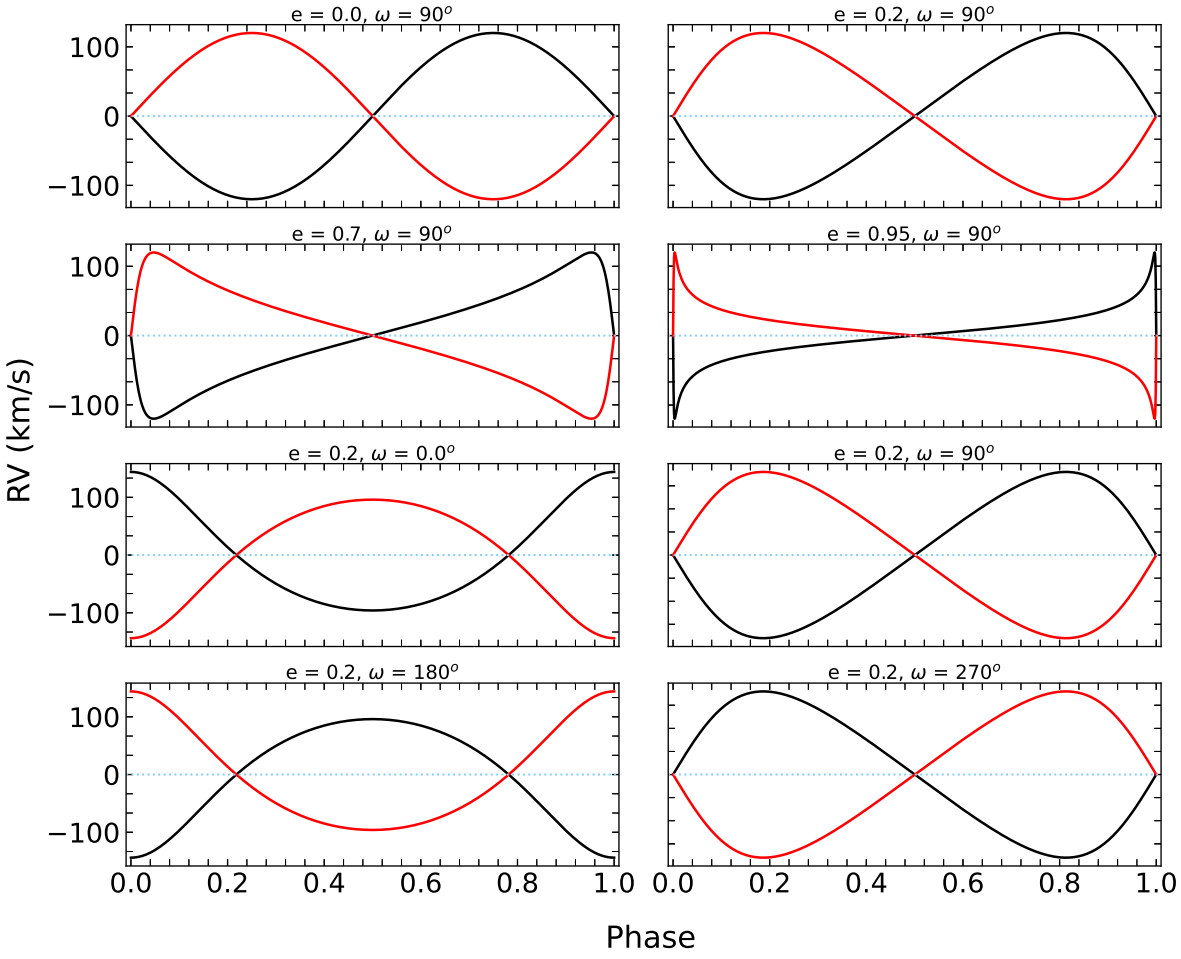

Figure 1.4: Top four panels: effect of varying e on RV curves with $\omega = 90°$ and $K = 120\,\mathrm{km\,s^{-1}}$. Bottom four panels: effect of varying ω on RV curves with $e = 0.2$ and $K = 120\,\mathrm{km\,s^{-1}}$.

$\omega = \pi/2 = constant$ for circular orbits and $\nu = E = \mathcal{M}$, so the RV curve is sinusoidal. However, in general, the time dependence of the true anomaly is complicated, as demonstrated in Section 1.1.2.3, and this is reflected in the RV curves of eccentric binaries (see Fig. 1.4). Furthermore, for $e > 0$, ω dictates what phases correspond to maxima and minima of the RV curve because ω dictates the location of the ascending and descending nodes relative to periastron passage, while the phase is calculated relative to the time of periastron passage in the dynamical analysis (i.e., the analysis of the components' barycentric motion).

1.1.2.5 Phase

The phase ϕ of the binary system specifies a particular position within the orbit, or the fraction of the current orbital cycle that has progressed, and assumes a value between 0 and 1. Phase is a linear function of the mean anomaly such that,

$$\mathcal{M} = 2\pi\phi, \tag{1.12}$$

so we can infer from Eq. 1.6 that,

$$\phi = \frac{t - t_{\rm per}}{P} \mod 1, \tag{1.13}$$

where we have taken the modulus to ensure $0 < \phi < 1$. Thus, for the dynamical analysis, the zero-phase corresponds to the time of periastron passage $t_{\rm per}$.

1.1.3 Multiple Systems

1.1.3.1 Spectroscopic Binaries

Measuring the RV curve for a binary system requires time-series RV measurements. RV measurements can be obtained for binary stars showing well resolved spectral lines because the wavelength location of spectral lines oscillates in correspondence to orbital motion via the Doppler effect; these are *spectroscopic binaries*. Double lined spectroscopic binaries (SB2s) are those where the motion of both components can be

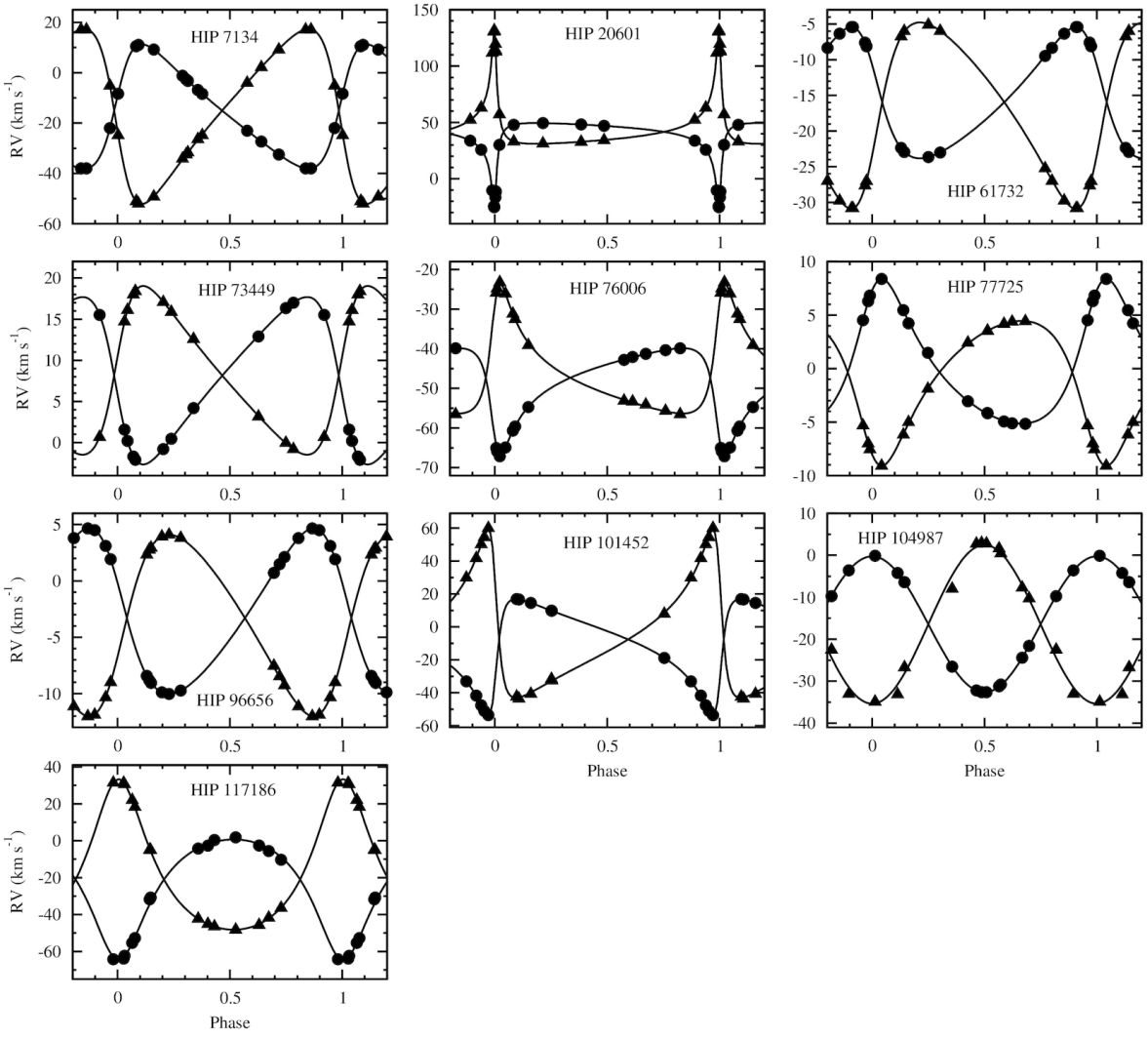

Figure 1.5: The spectroscopic orbits of 10 (labelled) SB2 binaries observed with the SOPHIE spectrograph at the Haute-Provence observatory; the circles refer to the primary component and the triangles to the secondary. Figure from the study by Halbwachs et al. (2020).

detected spectroscopically (e.g., Pickering, 1890; Halbwachs et al., 2020; Kounkel et al., 2021) and single lined spectroscopic binaries (SB1s) are those where only the brighter component is detected (e.g., Fernandez et al., 2009; Zhou et al., 2014).

For SB2s, the RVs for both components can be observed and then fitted via

Eq. 1.11 (with the help of Eq. 1.7) to obtain estimates for K_1, K_2, $t_{\rm per}$, P, e and ω (e.g., Halbwachs et al., 2020, see Fig. 1.5). Rearranging the expressions for $K_{1,2}$ (see Eq. 1.9 and Eq. 1.11) leads to expressions for the semi-major axes of the two barycentric orbits,

$$a_1 = \frac{P\sqrt{1-e^2}}{2\pi \sin i} K_1; \quad a_2 = \frac{P\sqrt{1-e^2}}{2\pi \sin i} K_2. \tag{1.14}$$

Using Eq. 1.4,

$$q = \frac{M_2}{M_1} = \frac{a_1}{a_2} = \frac{K_1}{K_2}, \tag{1.15}$$

so the mass ratio q can be measured directly for SB2s; q is important for morphological classification purposes as well as defining the shapes of stars since it appears in the Roche potential, i.e., Eq. 1.1. We can also write,

$$a = a_1 + a_2 = \frac{P\sqrt{1-e^2}}{2\pi \sin i}(K_1 + K_2), \tag{1.16}$$

so the separation of the components can be estimated if an independent measurement for i can be obtained.

Applying Kepler's third law to the relative orbit gives (see Appendix A.1 for the mass terms associated to each orbit),

$$\frac{4\pi^2 a^3}{P^2} = G(M_1 + M_2), \tag{1.17}$$

and using $a = a_1 + a_2$ with the relations in Eq. 1.15, we can express the masses of the components in terms of their velocity semi-amplitudes;

$$\begin{aligned} M_1 \sin^3 i &= \frac{P(1-e^2)^{3/2}}{2\pi G}(K_1 + K_2)^2 K_2, \\ M_2 \sin^3 i &= \frac{P(1-e^2)^{3/2}}{2\pi G}(K_1 + K_2)^2 K_1. \end{aligned} \tag{1.18}$$

As is the case for a, these are minimum estimations for the masses of the components because of the $\sin i$ dependence. For SB2s, absolute measurements for the masses can be obtained via Eq. 1.18 if i can be measured from, e.g., eclipses.

For SB1 systems, we can only measure the RV curve for the brighter component because the spectral lines of the other star are not present. The velocity semi-amplitude

of the fainter component is not accessible, but we can still measure $K_1, t_{\rm per}, P, \omega$ and e. From these quantities, we can derive the minimum estimation for the semi-major axis of the primary star's barycentric orbit using Eq. 1.14 as well as the *mass function*,

$$f(M) = \frac{P(1-e^2)^{3/2}}{2\pi G} K_1^3 = \frac{M_2^3 \sin^3 i}{(M_1 + M_2)^2}, \tag{1.19}$$

which is useful for SB1 systems because it can provide a minimum estimation for the mass of the secondary star.

1.1.3.2 Eclipsing Binaries

At superior and inferior conjunction, one star passes in front of the other and the two bodies are aligned with Earth. If the orbital parameters allow for it, one star will partially or totally block the light emitted from the other star. This is an eclipse. When the smaller body passes in front of the larger body, only a fraction of the light from the larger body is blocked, and this is described as a *transit* or *annular eclipse*. The opposite case, when a larger body completely shields the light from the smaller body, is described as an *occultation* or *total eclipse*. Depending on the inclination, it may be the case that the bodies only partially pass in front of one another; these are *partial eclipses*.

Time-series *photometric* measurements appropriately sampled over the orbital period allow us to observe the variation of the brightness of the system due to eclipses in a *light curve*. Fig. 1.6 shows four example binary star light curves measured by the WIRE satellite showing eclipses of different shapes for four different binary systems. The deeper eclipse is the *primary eclipse* and the shallower eclipse is the *secondary eclipse*. Therefore, the component that contributes most to the system flux is eclipsed during primary eclipse.

To determine whether one star will pass in front the other requires us to transform to the plane of the sky, contrarily to when we transformed to the line of sight to calculate RVs in Section 1.1.2.4. The plane of sky transformations for circular orbits from Prša

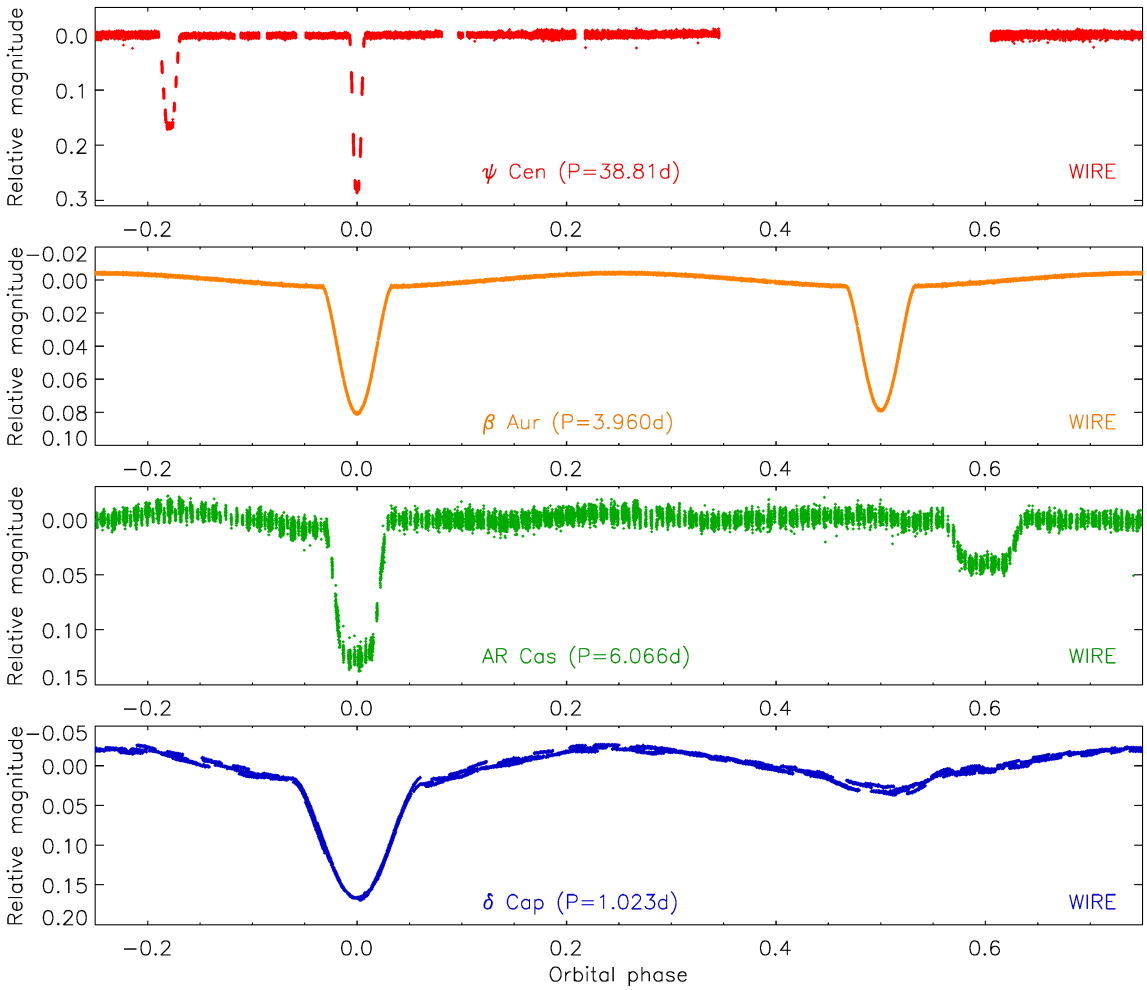

Figure 1.6: The light curves of four EBs measured by the WIRE satellite presented by Southworth (2021).

(2018) are,

$$\begin{aligned} x &= a[\cos\Omega\cos(\omega+\nu) - \sin\Omega\cos i\sin(\omega+\nu)], \\ y &= a[\sin\Omega\cos(\omega+\nu) + \cos\Omega\cos i\sin(\omega+\nu)], \end{aligned} \tag{1.20}$$

and the projected separation of the stars when one star is at the origin of the configuration is,

$$\Delta^2 = x^2 + y^2 = a^2[\cos^2(\omega+\nu) + \sin^2(\omega+\nu)\cos^2 i]. \tag{1.21}$$

The condition for eclipses is then,

$$\begin{aligned} &\text{no eclipse} &&: R_1 + R_2 < \Delta, \\ &\text{partial eclipse} &&: R_1 - R_2 < \Delta < R_1 + R_2, \\ &\text{total eclipse} &&: \Delta < R_1 - R_2. \end{aligned} \tag{1.22}$$

The *first contact point* T_1, with corresponding phase $\phi = \phi_1$, occurs when $\Delta = R_1 + R_2$. This is the instance when the eclipsing star begins to pass in front of the other star in the plane of the sky, and the reduction in the amount of light due to the eclipse is zero. The second contact point T_2 ($\phi = \phi_2$) occurs when $\Delta = R_1 - R_2$ and is the beginning of *totality*, i.e., a total eclipse. The end of totality occurs at T_3 ($\phi = \phi_3$) and the end of the eclipse occurs at $T_4(\phi = \phi_4)$. Partial eclipses do not have a second or third contact point so they contain less information than total eclipses.

Modelling the shapes of eclipses allows us to derive information about binary systems because the shapes of eclipses depend on the geometry of the components in their *relative* orbits as well as their sizes. The occurrence of an eclipse depends on Δ, which in turn depends on the phase and inclination i. For any such of these values that allows for an eclipse, the light lost during a *transit*, assuming stars are uniformly illuminated spheres, is proportional to the fraction of the larger star that is *blocked*, i.e., on the ratio of the stellar radii, $k = R_2/R_1 = r_2/r_1$, where we have assumed that star 1 (i.e., the primary star) is larger[3] and introduced the *fractional radii*,

$$r_1 = \frac{R_1}{a}, \quad r_2 = \frac{R_2}{a}. \tag{1.23}$$

[3]In some cases, the larger star is cooler due to, e.g., stellar evolution, in which case the light lost during the transit is proportional to the reciprocal of k assuming the convention that the primary (i.e., star 1) is always the hotter star, and this would also modify Eq. 1.24.

The fractional radii directly influence the occurrence, duration and shapes of eclipses, and are convenient quantities because of the degeneracy between absolute radius and separation; eclipses depend on the sizes of the stars as well as their separation (see Eq. 1.21 and Eq. 1.22). The fraction of light we receive during an occultation $f_{\rm occ}$ is the fraction of light emitted from the larger star. It follows that the fraction of light emitted from the other star is $1 - f_{\rm occ}$, which allows us to express the surface brightness ratio as,

$$J = \frac{k^2(1 - f_{\rm occ})}{f_{\rm occ}}. \tag{1.24}$$

Information on the orbital parameters is also contained in the timings of eclipses because the relative timing between primary and secondary eclipse depends on $e\cos\omega$, i.e., the tangential component of eccentricity. Additionally, the ratio of eclipse durations is tied to the radial component of eccentricity $e\sin\omega$ (Prša, 2018). These parameters, known as the Poincaré elements, complete our list of eclipse parameters for uniformly illuminated spheres: k, r_1, r_2, i, J, $e\cos\omega$, and $e\sin\omega$.

Complications in the derivation of the light lost during eclipses arise due to radiative effects, such as *limb darkening* (see Section 1.1.4). Because of this, calculations of the light lost during eclipses require substantial mathematical investigations to achieve analytical solutions (e.g., Kopal, 1959). The complications can also be mitigated via sophisticated numerical approaches, e.g., Prša et al. (2016), which allows for a full reconstruction of the Roche geometry of the components. Most modern techniques use numerical methods applied to discretised discs or Roche surfaces.

1.1.3.3 Eclipsing Spectroscopic Binaries

The occurrence of eclipses means we can account for the $\sin i$ dependence in the expressions for the masses and separation of the components (see Section 1.1.3.1). The absolute radii then follow from multiplication of the separation with estimations for the fractional radii from the eclipse model. Densities and surface gravities are then calculable. Given the parallax is known (from, e.g., *Gaia*; Gaia Collaboration 2021 or Hipparcos; Perryman et al. 1997), the effective temperature $T_{\rm eff}$ can be measured

directly (Smalley, 2005). To go further and derive other parameters usually relies on indirect methods, e.g., modelling each component's atmosphere.

The surface gravity of the unseen secondary component is the only fundamental parameter that can be derived directly for SB1 systems, as demonstrated by Southworth et al. (2007), using,

$$g_2 = \frac{2\pi}{P} \frac{\sqrt{1-e^2}}{r_2^2 \sin i}. \tag{1.25}$$

The density of the primary star can also be estimated using,

$$\rho_1 \approx \frac{3\pi}{GP^2 r_1^3}, \tag{1.26}$$

but this requires the assumption that $M_2 \ll M_1$. For SB1 systems, the rest of the physical properties follow from indirect methods which rely on the combination of the primary RV curve and eclipse model. One approach is to establish the properties of the primary component via isochrone fitting, leading to direct but model-dependent measurements of the properties of the unseen companion. Another is to assume that the system is rotationally synchronised. A third is to use empirical relations for solar-type stars to specify the properties of the primary component without using stellar theory (Enoch et al., 2010; Southworth, 2010; Hartman et al., 2015).

1.1.3.4 Hierarchichal Systems

The *Kepler* mission allowed us to discover that $\sim 20\%$ of binary systems show evidence of a tertiary component (Conroy et al., 2014; Prša, 2018). These are *hierarchical triple systems* within which a third star is gravitationally bound in orbit with the CM of the *inner* binary; we call this the *outer orbit*. The outer orbit introduces a light travel time effect (LTTE), or a *Roemer Delay* (Rappaport et al., 2013; Borkovits, 2022), causing ETVs, which were discussed in Section 1.2. ETVs are studied by calculating the residuals of the observed eclipse times against a linear ephemeris and displayed in an $\mathrm{O}-\mathrm{C}$ diagram (e.g., Rappaport et al., 2013, see Fig. 1.7).

To distinguish between ETVs caused by a third body and apsidal motion, one can compare the phase difference between the ETVs of the primary and secondary eclipses.

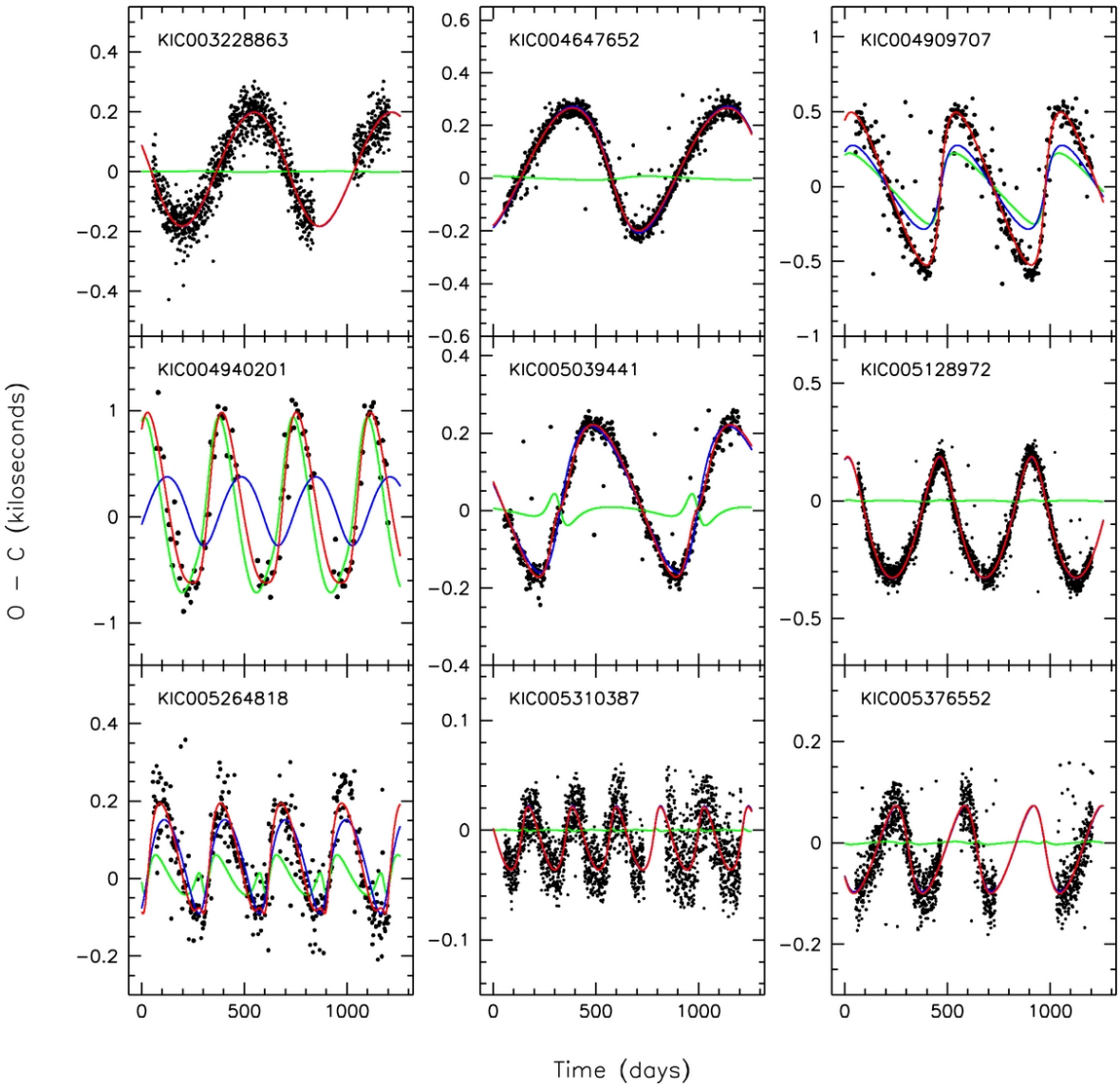

Figure 1.7: O - C data and model fits for nine systems by Rappaport et al. (2013). The red curves are the total of the ETV signature. Dark blue is the contribution to the model by the LTTE. The light green curves represent the contribution of the physical delay.

For ETVs due to an outer orbit, the primary and secondary signals are in phase, while for apsidal motion, the two signals are out of phase by π radians. Mass-transfer is another potential cause of the ETVs (Conroy et al., 2014); a considerable time-span of observations, longer than the outer orbital period, is required to discriminate between the periodic ETV due to a third component and the parabolic signals that are characteristic of mass-transfer.

The expression for the LTTE due to an EB in its outer orbit follows,

$$\mathcal{R}(t) = A_{\rm ltte}\Big[(1-e_3^2)^{1/2}\sin E_3\cos\omega_3 + (\cos E_3 - e_3)\sin\omega_3\Big], \tag{1.27}$$

where E_3, e_3, and ω_3, are the eccentric anomaly, eccentricity and argument of periastron, respectively, that correspond to the outer orbit and,

$$A_{\rm ltte} = \frac{G^{1/3}}{c(2\pi)^{2/3}}P_3^{2/3}\left[\frac{M_3\sin i_{\rm out}}{M_{\rm tot}^{2/3}}\right], \tag{1.28}$$

is the amplitude of the time delay, where P_3 and $i_{\rm out}$ are the period and inclination of the outer orbit, M_3 is the mass of the tertiary component, and $M_{\rm tot}$ is the total mass of the inner pair plus tertiary component (Rappaport et al., 2013). Note, the term in the square brackets is the cube root of the mass function for the outer orbit.

Similarly to the derivation of the mass function from the dynamical considerations of SB1 systems, Eq. 1.27 only considers one of the barycentric orbits; the outer orbit. The mass term for this barycentric orbit is $GM_3^3/(M_{\rm EB}+M_3)^2$ (see Appendix A.2) so from Kepler's third law we can express the semi-major axis of the outer orbit as,

$$a_{\rm out} = \left(\frac{GMP_3^2}{4\pi^2}\right)^{1/3} = \frac{G^{1/3}}{(2\pi)^{2/3}}P_3^{2/3}\left[\frac{M_3}{M_{\rm tot}^{2/3}}\right], \tag{1.29}$$

and therefore,

$$A_{\rm ltte} = a_{\rm out}\sin i_{\rm out}/c. \tag{1.30}$$

Plugging Eq. 1.30 into Eq. 1.27, multiplying by c (i.e., convert the time delay into a displacement), and accounting for the inclination, i.e.,

$$\frac{\mathcal{R}(t)c}{\sin i_{\rm out}} = a_{\rm out}\Big[(1-e_3^2)^{1/2}\sin E_3\cos\omega_3 + (\cos E_3 - e_3)\sin\omega_3\Big], \tag{1.31}$$

gives the z-component of the displacement of the CM of the inner binary. Thus, differentiating with respect to time retrieves Eq. 1.9, i.e., the z-component of the velocity (see Section 1.1.2.4). Since Eq. 1.31 is periodic with the outer orbit, this implies that the systemic velocity of the EB is not constant, i.e., $\gamma = \gamma(t)$.

Previously, we assumed a constant value for γ but in the presence of a third body it describes the barycentric motion of the EB's CM. The result is that the RV curve for each component of the inner EB is modelled as the superposition of its inner barycentric orbit and the outer barycentric orbit, i.e.,

$$V_r = K_{1,2}[e_{\rm in}\cos\omega_{\rm in} + \cos(\omega_{\rm in} + \nu_{\rm in})] + \gamma_{\rm in} + \gamma_{\rm out}, \tag{1.32}$$

where,

$$\gamma_{\rm in} = K_3[e_{\rm out}\cos\omega_{\rm out} + \cos(\omega_{\rm out} + \nu_{\rm out})], \tag{1.33}$$

and $\gamma_{\rm out}$ is the constant radial velocity of the entire triple system. Fig. 1.8 shows how the RV curve of an inner binary component is influenced by the outer orbit for different values of P_3 (row 1), P_1 (row 2), and e_3 (row 3). These models were evaluated over the full period of the outer orbit so they reflect the full amplitude of the centre of mass velocity variation over one outer orbital cycle.

Another third body effect is the *physical delay*, which describes *actual*[4] perturbations to the binary period, making it longer (Rappaport et al., 2013). If the outer orbit is eccentric or inclined, the magnitude of this perturbation changes through the orbit due to the changing tidal interaction. This leads to an additional contribution to the ETV curve which should be accounted for in the O-C formula if the effect is not negligible; the physical delay becomes significant for short outer orbital periods and long inner binary periods (Rappaport et al., 2013). Finally, we note that the gravitational interaction between the inner EB and the third star can result in apsidal motion of the inner pair's orbit. Therefore, accurate modelling of ETV curves may, in some cases, require the inclusion of multiple contributing effects (e.g., Fig. 1.7).

[4]The observed variations in period due to the LTTE are *apparent* because they only arise due to changes in the amount of time that it takes for the light to reach the telescope over the outer orbital period.

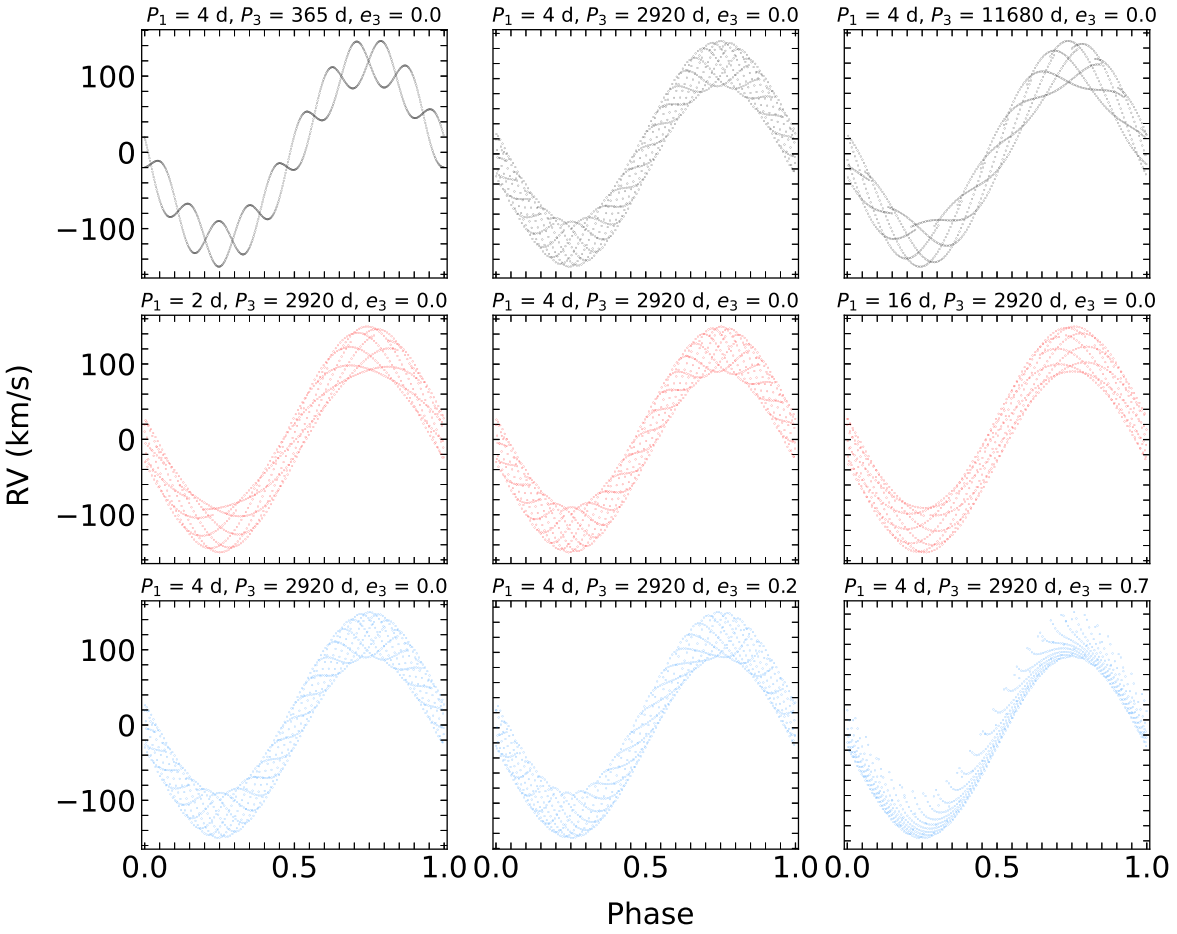

Figure 1.8: Model RV curves for the component of a binary system where the CM of the binary system is in Keplerian motion due to the influence of a third companion. RV curves are shown corresponding to different outer orbital periods (top row), inner orbital period (middle), and outer orbital eccentricities (bottom row). The RV curves were evaluated over the outer orbital period in all cases so capture the full amplitude of the variation in the systemic velocity over the outer orbital period.

The study of triple star systems gives new insights into the physics of EB's (Conroy et al., 2014). The orbital architecture and masses of the constituents can contribute to our understanding of processes that form multiple systems (Rappaport et al., 2013); the general interpretation for the formation of close binaries is that they become hardened over time through interactions with a third body (Conroy et al., 2014). It is noted that it is also possible for systems to have more than three components, and these higher-order systems have been observed.

1.1.4 Radiative Phenomena

An understanding of stellar radiation is essential for astrophysical research, in general, as well as for the following discussions on radiative effects associated with binary stars. Thus, a brief overview is provided in Appendix B. Such effects are why the light emitted over the surface of a star is not uniform and these are important considerations for predicting the shapes of eclipses. There is a temporal dependence on the visibility of individual surface elements so the flux distribution over the surface of the star has to be known in detail to make accurate predictions of the light lost during an eclipse.

1.1.4.1 Limb Darkening

The photosphere is the layer of the stellar atmosphere where photons scatter on average less than once, thus allowing them to escape; these are the photons that we measure. In the *Eddington approximation*, where the absorption coefficient κ_λ is independent of wavelength so that $\kappa_\lambda = \kappa$ (a so-called *grey atmosphere*), this occurs when the *optical depth* $\tau = 2/3$ (Gray, 2005).

The *geometrical depth* r that corresponds to $\tau = 2/3$ is different for different values of θ (see Fig. B.1), where $\cos\theta$ determines the projection of the path traversed l by a photon in order to emerge along our line of site relative to the radial direction. The result is that photons originate from shallower geometrical depths for larger values of θ. Thus, we see deeper into the star at its centre, where l is parallel to the surface

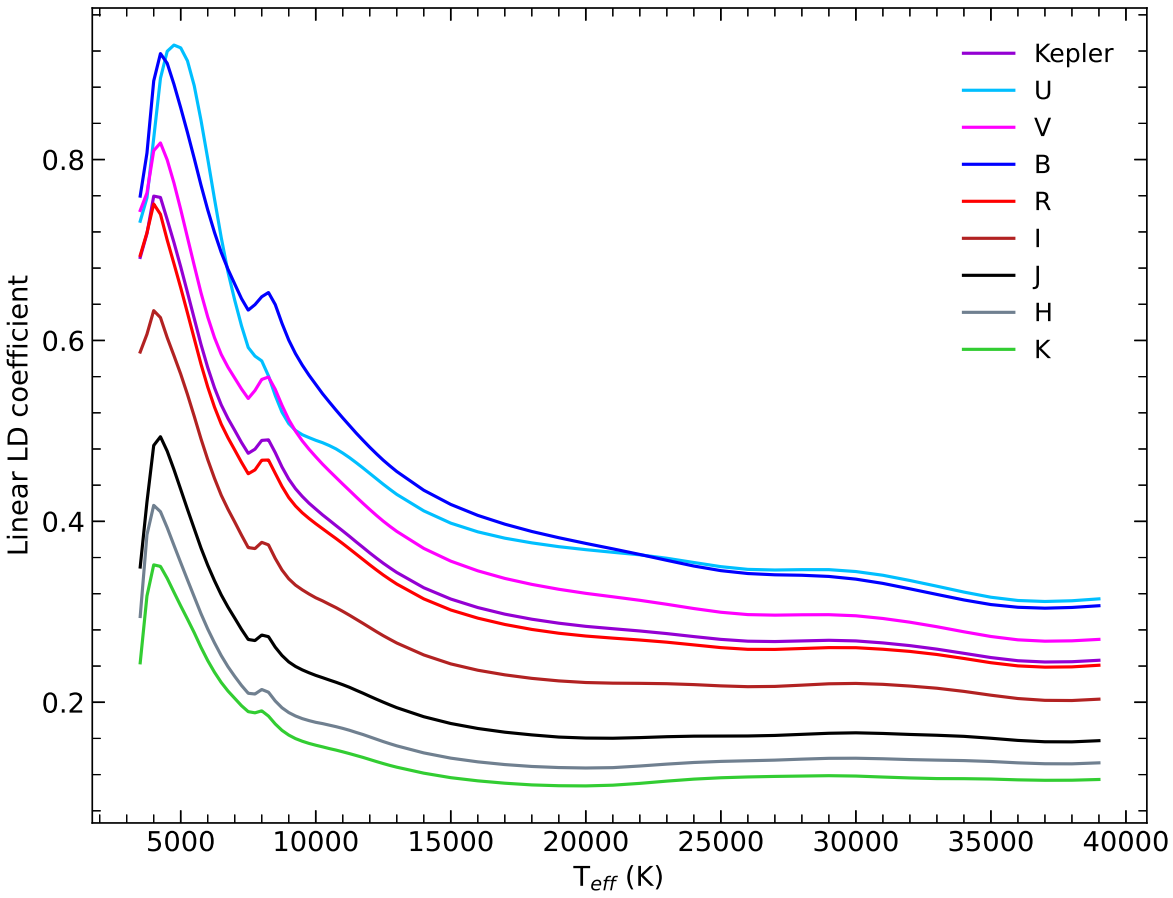

Figure 1.9: Variation of the linear LD coefficient with $T_{\rm eff}$ for values calculated by Claret & Bloemen (2011) for the *Kepler* band, as well as UVBRIJHK of the Johnson-Cousins photometric system.

normal ($\theta = 0$), than at the limb, where l is almost perpendicular to it ($\theta \sim \pi/2$). This leads to a phenomenon called *limb darkening* (LD).

The resulting flux distribution F_λ across the stellar surface due to LD affects the shapes of eclipses and depends on the strength of the effect. Introducing the variable $\mu = \cos\theta$, we may write,

$$F_\lambda = 2\pi \int_1^0 I_\lambda(\mu)\mu(-d\mu) = 2\pi I_{\lambda,\mathrm{norm}} \int_0^1 \mu\mathcal{L}(\mu)d\mu, \tag{1.34}$$

where $\mathcal{L}(\mu) = I_\lambda(\mu)/I_{\lambda,\mathrm{norm}}$ is the LD function (Prša, 2018). The flux is now described as the normal emergent intensity $I_{\lambda,\mathrm{norm}}$ scaled by $\int_0^1 \mu\mathcal{L}(\mu)d\mu$ over the stellar disc. Various models have been proposed for $\mathcal{L}(\mu)$ to account for its effect in modelling eclipses. Examples are the linear, quadratic, and power 2 laws. Theoretical predictions are available for the associated coefficients that determine the strength of LD in different photometric passbands, e.g., Claret & Bloemen (2011) and Claret (2017) for *Kepler* and TESS, respectively, but they can also be included as free parameters.

Since the specific intensity, and thus flux, is calculated by solving the *radiative transfer equation* (Eq. B.4), e.g., at the optical depth corresponding to the emergent photons (i.e, $\tau = 2/3$ in the Eddington approximation), the extent by which a star is affected by LD depends on the opacity because $\tau \propto \kappa_\lambda$; this is why theoretical LD coefficients are calculated in specified photometric passbands. The LD coefficients thus vary with T_{eff} and wavelength λ via the opacity dependence.

Fig. 1.9 shows how the linear LD coefficient increases with decreasing T_{eff} for values calculated by Claret & Bloemen (2011) for the *Kepler* band, as well as UVBRI-JHK of the Johnson-Cousins photometric system (see Section 2.1.1). Fig. 1.10 presents observations corresponding to 10 spectro-photometric passbands of the exoplanet transiting system HD 209458 from Knutson et al. (2007); the strength of LD increases at shorter wavelengths, i.e, bluer in the figure, as reflected by the shapes of the eclipses.

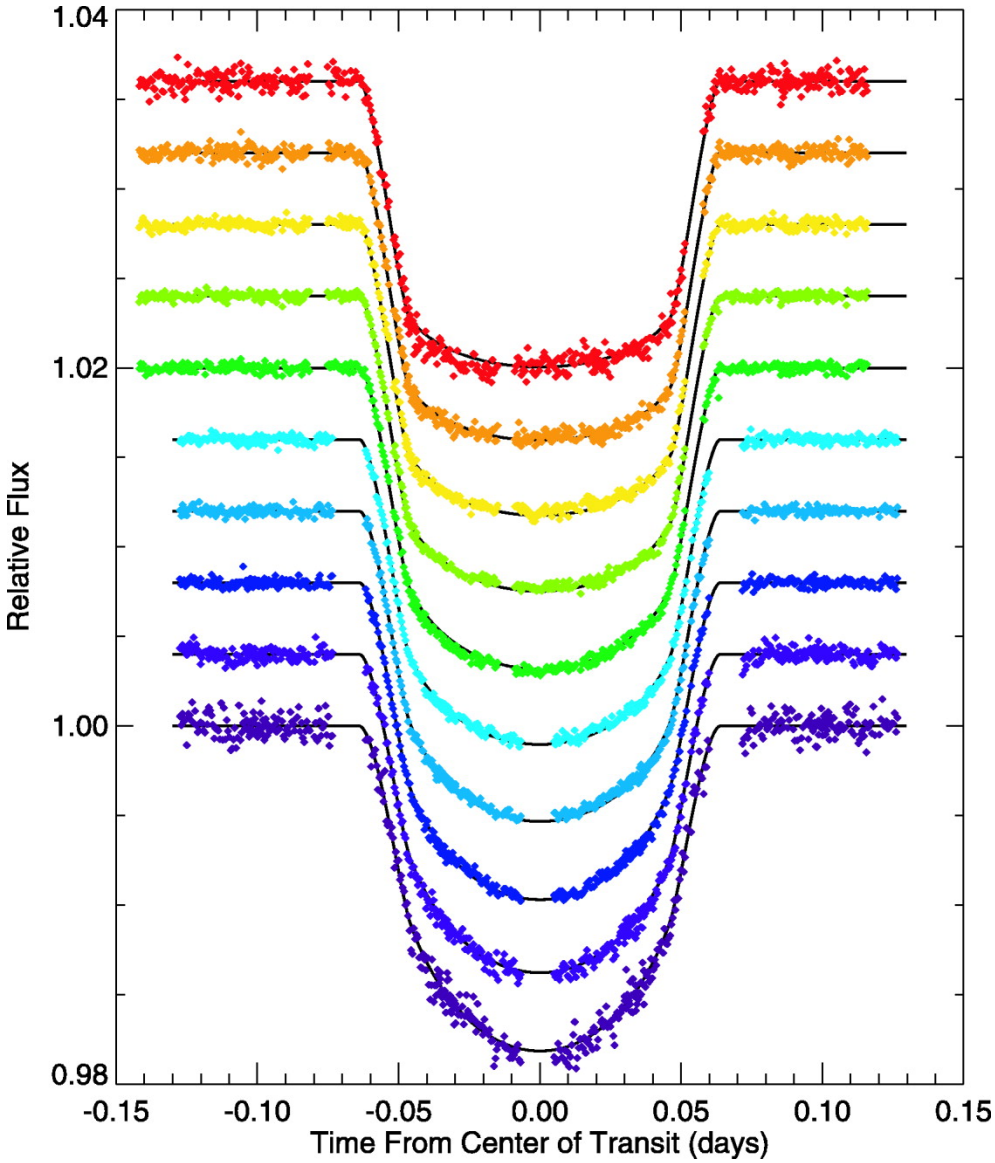

Figure 1.10: Observations corresponding to 10 spectro-photometric passbands of the exoplanet transiting system HD 209458 from Knutson et al. (2007). The passbands correspond to 10 subdivisions of HST STIS spectra equally spaced between 2090 – 10300 Å; the corresponding transits are vertically shifted to higher values for redder wavelengths.

1.1.4.2 Gravity Darkening

Tidal forces (due to binarity) and centrifugal forces (due to rotation) deform the shapes of stars from being spherical and this leads to a surface gravity distribution. Since stars are described to be in hydrostatic equilibrium (see Appendix C.3), the atmospheric pressure is relaxed in regions of lower surface gravity along with temperature. The resulting flux distribution is called *gravity darkening*. It was shown by von Zeipel (1924) that,

$$F_\lambda = -\frac{16T^3}{3\bar{\kappa}}\frac{dT}{d\Omega}g^\beta, \tag{1.35}$$

where $\bar{\kappa}$ is the *Rosseland mean opacity* (see Appendix C.6), ρ is the density of the gas, g is the local acceleration due to gravity, and β is the gravity darkening coefficient.

The value of β depends on the dominant energy transport mechanism. It was shown by von Zeipel (1924) that $\beta = 1$ for radiative envelopes ($T_{\rm eff} \gtrsim 8000$) while Kippenhahn (1977) presented a generalised formalism for the calculation, and Lucy (1967) computed an average value of $\beta = 0.32$ for purely convective envelopes ($T_{\rm eff} \lesssim 5000$). For stars where convective and radiative energy transport mechanisms play significant roles, accurate theoretical predictions were made by Claret (2000) and these were made based on the formalism of Claret (1999).

The left panel of Fig. 1.11 shows the gravity darkened surface brightness distribution of the host star to the transiting planet KELT 9b from a study by Ahlers et al. (2020). The star is brighter at the poles and cooler at the equator and this is reflected by the shape of the planet's transit shown in the right of the figure; there is clear asymmetry around the time of minimum light because at the time of first contact, the planet passes over the brighter regions of the star near the poles, and then passes over dimmer regions near the equator. The inadequacy of the transit model that does not account for gravity darkening (red line in the middle right panel of Fig. 1.11 with residuals in the upper right panel) is obvious. The blue line represents a model that directly fits for the gravity darkening exponents, yielding $\beta = 0.137 \pm 0.014$, and a much better fit to the data (initial guesses for β were taken from Espinosa Lara & Rieutord 2011).

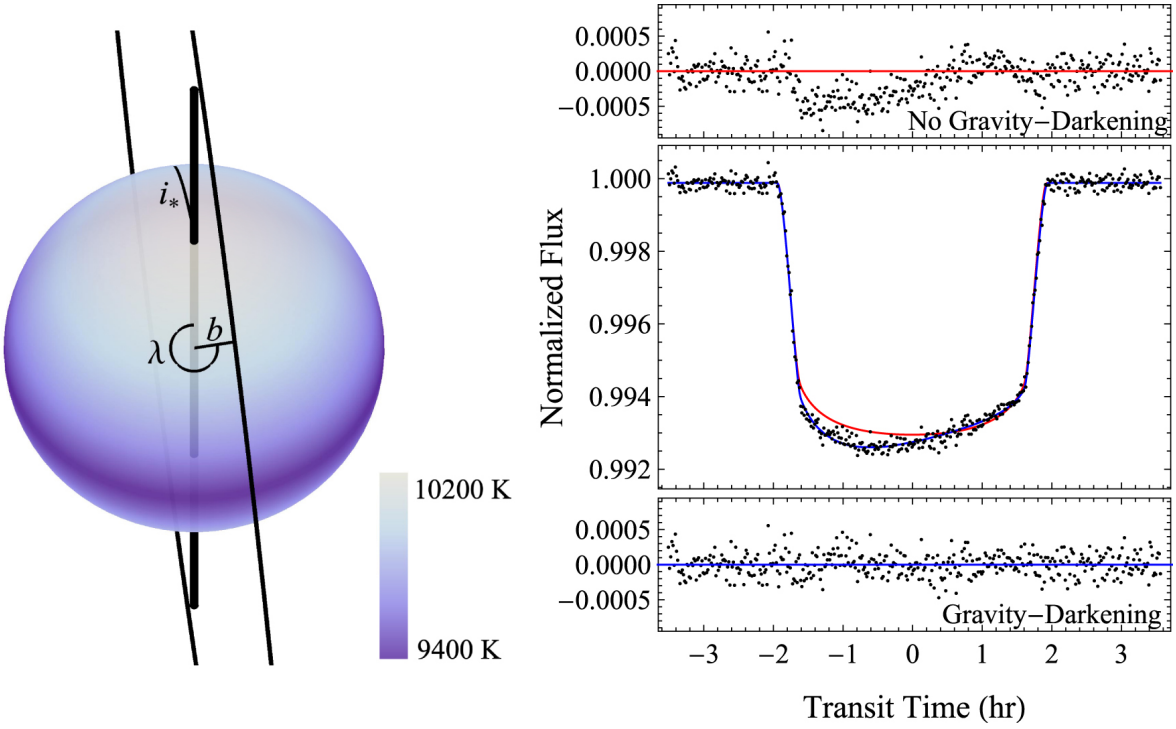

Figure 1.11: The surface brightness distribution over the surface of the rotating host of the transiting planet KELT 9b, along with the orientation of the planet's orbit with respect to the rotation axis of the host, is shown on the left. The right shows the shape of the resulting transit and a light curve fit to the data assuming no gravity darkening (red line) and accounting for gravity darkening (blue line). Figure taken from Ahlers et al. (2020).

1.1.4.3 Reflection Effect

A fraction of the flux radiated from one of the components in a binary system will be intersected by the other component and vice-versa, causing mutual surface irradiation. This becomes important when the radii of the components are more than $15\% - 20\%$ of the orbital separation (Prša, 2018). A part of the irradiating flux will be redistributed locally or globally causing heating or having a negligible effect, respectfully, while the other part is reradiated. The fraction of irradiated flux that is reradiated is determined by the bolometric albedo $\mathcal{A}$ of the irradiated star. Both reradiation and redistribution can contribute to the so-called *reflection effect*.

Wilson (1990) developed a rigorous treatment of the effect in binary stars and Prša (2018) provide a useful explanation, accounting for irradiation of a single surface element on the irradiated star due to all contributing surface elements on the radiating star. The reflection factors[5] $\mathcal{R}_{1,2}$ are used to recalculate the $T_{\rm eff}$s of surface elements accounting for both intrinsic and reflected energy as (Prša, 2018),

$$T_{\rm eff,new} = \mathcal{R}^{1/4} T_{\rm eff,old}. \tag{1.36}$$

If the fraction of irradiated flux that is absorbed is redistributed locally, as opposed to globally, we may expect an additional increase of the temperature in the intersecting region, as first worked out by Prša et al. (2016). Simplified treatments for the effects of reflection are discussed in e.g., Binnendijk (1960); Kopal (1966); Taylor (2006).

The reflection effect manifests in a light curve as a periodic signal in the *baseline* flux with maxima occurring at phases where the irradiated surface elements correspond to those aligned with the observer's field of view, e.g., phases of conjunction (see Fig. 1.12). In cases where reflection at both components is strong, the resulting signal is the superposition of the signals associated with each star, which are out of phase by π radians. The periods of the reflection effects associated with each component are equivalent to the orbital period.

[5]The reflection factors $\mathcal{R}_{1,2}$ are the ratio of the total emanating flux to that which is intrinsic to the star.

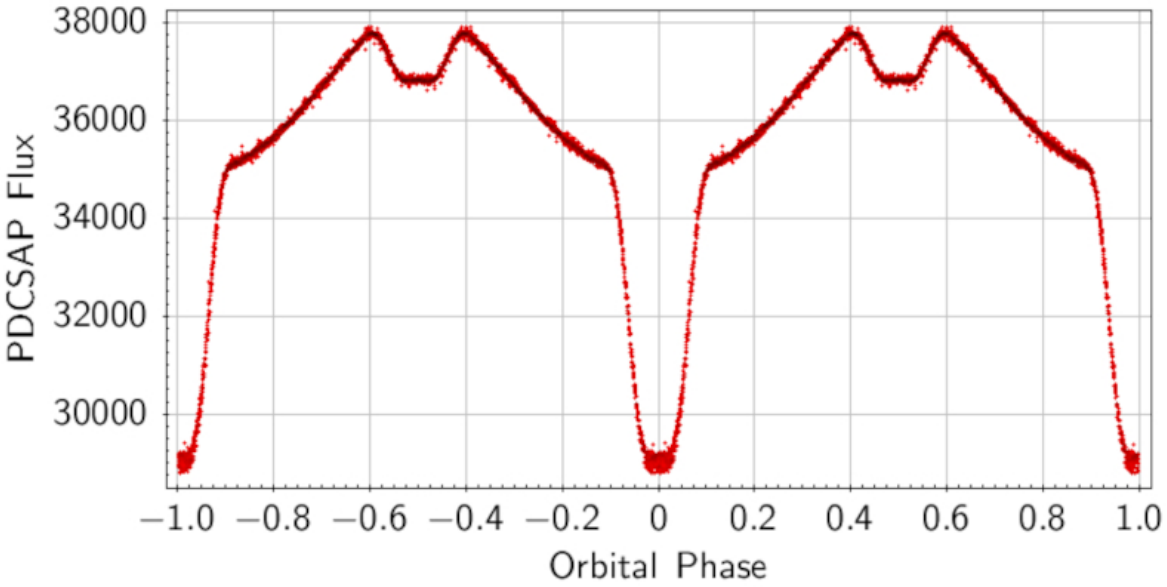

Figure 1.12: The PDCSAP flux light curve (see Section 2.1.3) of the post-common-envelope EB EPIC 216747137 from the study by Silvotti et al. (2020), observed by *Kepler* during its secondary $K2$ phase. This system demonstrates a strong reflection effect on the secondary component; the brightness of the system increases dramatically at secondary eclipse.

1.1.4.4 Ellipsoidal Effect

The *ellipsoidal effect* denotes to the fluctuation in the brightness of a binary system arising from the tidal distortion of the stars along the tidal axis. The resulting ellipsoidal shape becomes evident from our perspective at phases of quadrature (between eclipses); during eclipse, the tidal axis aligns with the line of site so the components appear to maintain spherical symmetry.

Thus, the specific intensity is integrated over a larger projected area ΔA during phases of quadrature and the system appears brighter. The associated variation in the baseline flux must have a period that is half the orbital period because there are two phases of quadrature in one orbital cycle. The amplitude must depend on the mass ratio and separation of the components since these quantities have a significant effect on the stellar shapes via Eq. 1.1, the Roche potential.

The fractional change in the brightness of one of the components (star 1) due to the ellipsoidal effect is given by Penoyre & Stone (2019) as,

$$\frac{\Delta_l}{l_1} \approx -\frac{12}{16}\frac{M_1}{M_2}\left(\frac{R_2}{a}\right)^3 \frac{3\sin^2 i\cos^2 \mathcal{M} - 1}{(1 - e\cos E)^3}. \tag{1.37}$$

The total effect in a light curve is then the superposition of the brightening of both components. The ellipsoidal effect is observed for the *Kepler* EBs KIC 9851944 and KIC 4851217 in Fig. 3.2 and Fig. 4.1, respectively.

1.1.4.5 Spots

Patches of reduced brightness – aka, star spots – are expected on the surfaces of stars with convective envelopes because they are associated with magnetism and the magnetic field is generated through the interaction between convection and rotation via shell dynamo action. Star spots introduce an additional brightness modulation that overlays the light curve. This modulation occurs periodically, determined by the star's rotation period, while the amplitude is dictated by the relative darkness of the spot in comparison to the photosphere. For a review of star spots, see Strassmeier (2009).

Describing star spots involves parameters such as their location (colatitude θ, longitude ϕ), radius $r_{\rm spot}$, and the temperature factor $\tau_{\rm sp}$ which characterises the temperature contrast between the spot and the nearby photosphere (Prša, 2018). The cumulative effect of multiple spots, rotating across various sections of the limb-darkened stellar disc, produces complex pseudo-periodic signals. These signals pose considerable challenges for precise integration into a light curve model, a challenge further compounded by their temporal evolution (Maxted, 2018). Consequently, it might be prudent to consider their exclusion, i.e., detrend spot signatures prior to modelling.

While star spots are relatively uncommon in intermediate mass stars (e.g., δ Scuti and γ Doradus stars) due to a significant reduction in the extent of the convection zone for $T_{\rm eff} \gtrsim 7000$ K, resulting in greater depth (see Fig. C.1), they feature prominently in the light curves of binary systems hosting low-mass stars.

1.1.4.6 Interstellar Extinction

Interstellar extinction is an effect that is extrinsic to both the stars and the binary system. It is associated with the wavelength-dependent attenuation of radiation by dust in the interstellar medium before reaching the observer. Since shorter wavelengths are affected more than longer wavelengths, interstellar extinction is also termed *reddening*.

Reddening is quantified by the colour excess which is defined as the difference between the observed colour index and that predicted by the star's spectral type,

$$E(B-V) = (B-V)_{\rm observed} - (B-V)_{\rm intrinsic}. \tag{1.38}$$

The slope with wavelength is given by the ratio of total visual to selective extinction,

$$R_V = \frac{A_V}{A_B - A_V} = \frac{A_V}{E(B-V)}, \tag{1.39}$$

within which, A_V and A_B are extinction coefficients in the B and V passbands, respectfully (Draine, 2003; Gontcharov, 2016; Prša, 2018).

The extinction due to molecules in our atmosphere is proportional to the reciprocal of the fourth power of wavelength, i.e., $A(\lambda) \propto \lambda^{-4}$, which results in $R_V \sim 1.2$;

for the interstellar medium, $R_V \approx 3.1$ (Schlafly & Finkbeiner, 2011). Thus, given a value for $E(B-V)$, one can derive the corresponding A_V. Dust maps, e.g., Lallement et al. (2018), offer a means to assess $E(B-V)$ based on an object's position and distance. Alternative approaches involve conversions from photometric systems (e.g., Kahraman Aliçavuş et al., 2017) or using the equivalent width of the Na D_2 interstellar line (Munari & Zwitter, 1997).

Reddening can result in data that does not accurately represent the intended target. For instance, it distorts spectral energy distributions and photometric indices, which in turn affects the determination of atmospheric parameters (Kahraman Aliçavuş et al., 2017). The observed dimming due to reddening can result in underestimated intrinsic luminosities of stars, consequently affecting distance estimations. Therefore, achieving precise astronomical analyses necessitates meticulous consideration of reddening effects.

1.1.5 Constraining Models

The combination of eclipses and RV curves allows for absolute measurements of the masses and radii of the components in binaries (see Section 1.1.3.3). These measurements are often obtained to a precision better than 1% (e.g., Clausen et al., 2008; Southworth, 2013, 2015). Since the methods employed to derive these measurements rely heavily on geometry and orbital mechanics (see Sections 1.1.2 and 1.1.3), they remain largely model-independent[6], These measurements serve as valuable calibration points for stellar evolution models (Lee et al., 2021).

For this reason, Double Lined EBs (DLEBs) are routinely used to critically assess stellar evolution theory (e.g., Pols et al., 1997; Pourbaix, 2000; Lastennet & Valls-Gabaud, 2002; de Mink et al., 2007; Stancliffe et al., 2015; del Burgo & Allende Prieto, 2018; Johnston et al., 2019b; Murphy et al., 2021). This is the most important of

[6]The properties of EBs can be derived using theoretical LD and gravity darkening coefficients, in which case the measurements are slightly model dependent

their applications in the context of this work. Before discussing it, we review stellar evolution and refer to Appendix C for an overview of stellar structure.

1.1.5.1 Stellar Evolution

The macro- and micro-physics (see Appendix C) govern structural changes leading to stellar evolution for which this section provides a brief overview; Fig. 1.13 shows the evolution of a 2 $M_\odot$ star calculated by MIST (MESA Isochrones and Stellar Tracks; Dotter, 2016) using the MESA (Modules for Expreriment in Stellar Astrophysics; Paxton et al., 2011, 2013, 2015) code. Uncertainties, particularly at later evolutionary phases, means that this is an on-going field of research, hence the continued efforts to measure the properties stars. Nevertheless, the following description is accurate to the level of detail intended.

Fully convective protostars condense out of collapsing interstellar clouds and contract until hydro-static equilibrium. This is the pre-main sequence (pre-MS), which is highlighted in blue in Fig. 1.13. Contraction proceeds as the star descends the *Hayashi track* and the internal temperature gradually increases, the convection zone begins to recede from the centre and then the star radiatively contracts along the *Henyey track*. The ignition of hydrogen burning into helium via the p-p chain ($0.08\,M_\odot \lesssim M \lesssim 1.15\,M_\odot$) or CNO cycle ($M \gtrsim 1.15\,M_\odot$) marks the beginning of the main-sequence (MS) phase, which is highlighted in black in Fig.1.13; brown dwarfs ($M < 0.08\,M_\odot$) do not attain such core temperatures.

The MS lasts $\sim 90\%$ of a stars lifetime, during which the mean molecular weight in its core increases (He > H). This implies a decrease in pressure (Eq. C.17) and consequently, the core contracts coupled with an increase in temperature[7]. This increases the nuclear energy generation rate, which in turn raises the pressure in the outer layers; this is why the radius increases over the MS phase in Fig. 1.13. The star continues to fuse H to He until it reaches the *terminal age main sequence* (TAMS) and H in its core

[7]By the Virial theorem, for a star in hydrostatic equilibrium, half of the released potential energy due to gravitational collapse is radiated away while the other half is transferred into thermal energy.

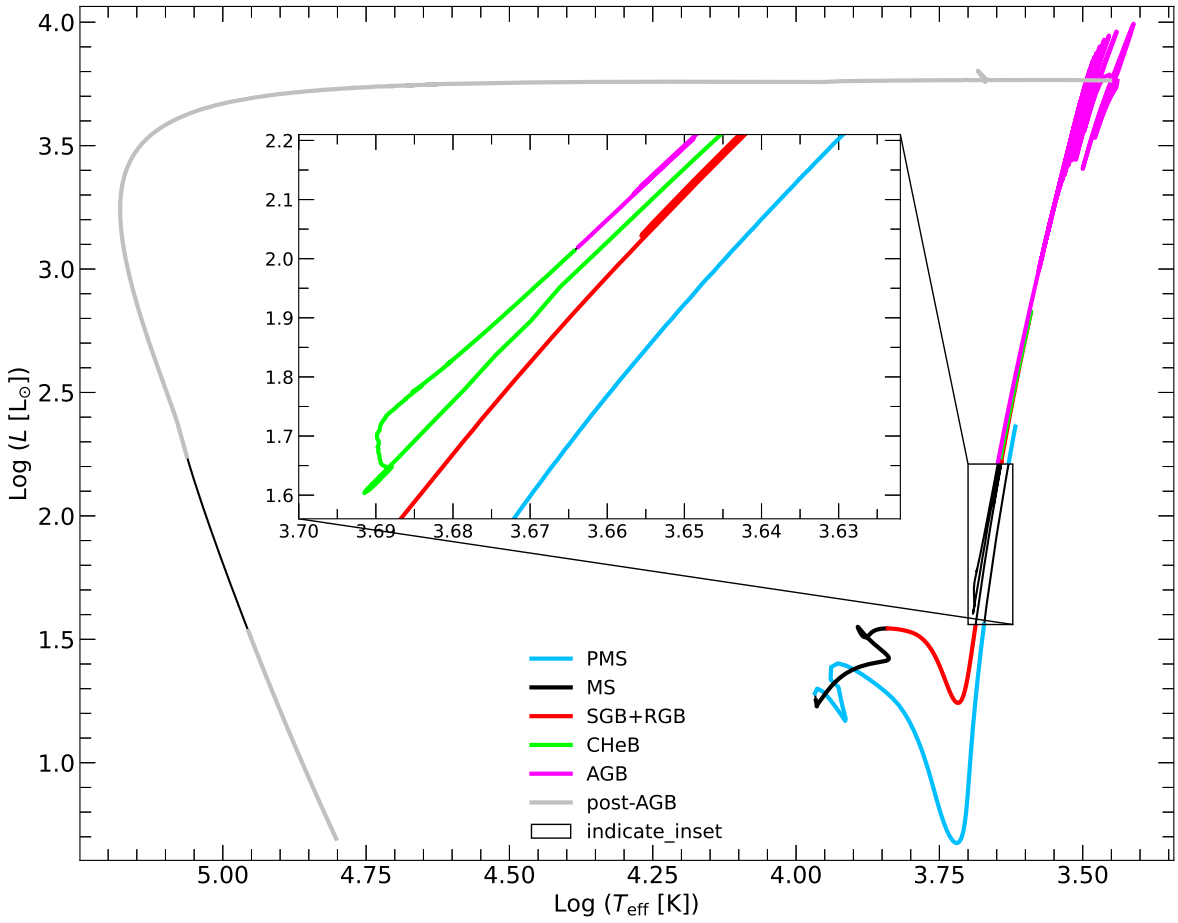

Figure 1.13: Evolution of a 2 $M_\odot$ star from the pre-MS to the post-AGB phase. The evolutionary track was calculated using the MESA code by MIST (Paxton et al., 2011, 2013, 2015; Dotter, 2016; Choi et al., 2016; Paxton et al., 2019) and the data was used here to generate this figure.

has been depleted. The result is an inert, isothermal core of He where no nuclear fusion takes place. However, hydrogen burning may proceed in a shell around the core. This places the star on the *sub-giant branch* (SGB), which is the beginning of the phase highlighted in red in Fig. 1.13.

Helium is deposited onto the core during this phase, increasing its mass, and causing it to collapse on a thermal time-scale when its mass reaches the Schönberg-Chandrasekhar limit. The accompanying rapid increase in temperature and shell burning causes the outer layers to expand considerably. Since the radiation can not escape quickly due to opacity, the luminosity ($L = 4\pi R^2 \sigma T^4$) remains constant and the temperature in the envelope drops in response to the expansion. These processes shift the star toward the 'dip' on the SGB (see Fig. 1.13), which is known as the *Hertzsprung gap* because few stars are observed making this rapid transition.

The *Hyashi forbidden zone*[8] prevents the envelope from cooling below $\sim 3000\,\mathrm{K}$, at which point the luminosity must increase with the expansion. The star climbs near vertically along the *red-giant branch* (RGB) to become a *red giant*. The RGB is highlighted in red together with the SGB and Hertzsprung gap in Fig. 1.13. The inset in Fig. 1.13 magnifies the region where the star ascends the RGB. The ascension can be seen to be near parallel with the Hayashi track on the pre-MS, as well as the descension onto the *horizontal branch*, or the *core helium burning* (CHeB) phase, which is highlighted in green.

For stars with masses of $2.3 \lesssim M \lesssim 9\,\mathrm{M}_\odot$, the transition onto the horizontal branch happens smoothly when the required temperatures to fuse helium via the triple-α reaction are attained during core collapse, effectively halting it. For stars with masses of $0.5 \leq M \leq 2.3\,\mathrm{M}_\odot$, the core continues to collapse until it becomes degenerate. Degeneracy pressure prevents further collapse and the conditions to ignite the triple-α reaction are attained from the continued deposition of helium from the surrounding shell. Due to the insensitivity of degeneracy pressure to temperature, the onset of

[8]The Hyashi forbidden zone arises because of the implied transparency of the envelope to radiation by the neutralisation of hydrogen at $\sim 3000\,\mathrm{K}$.

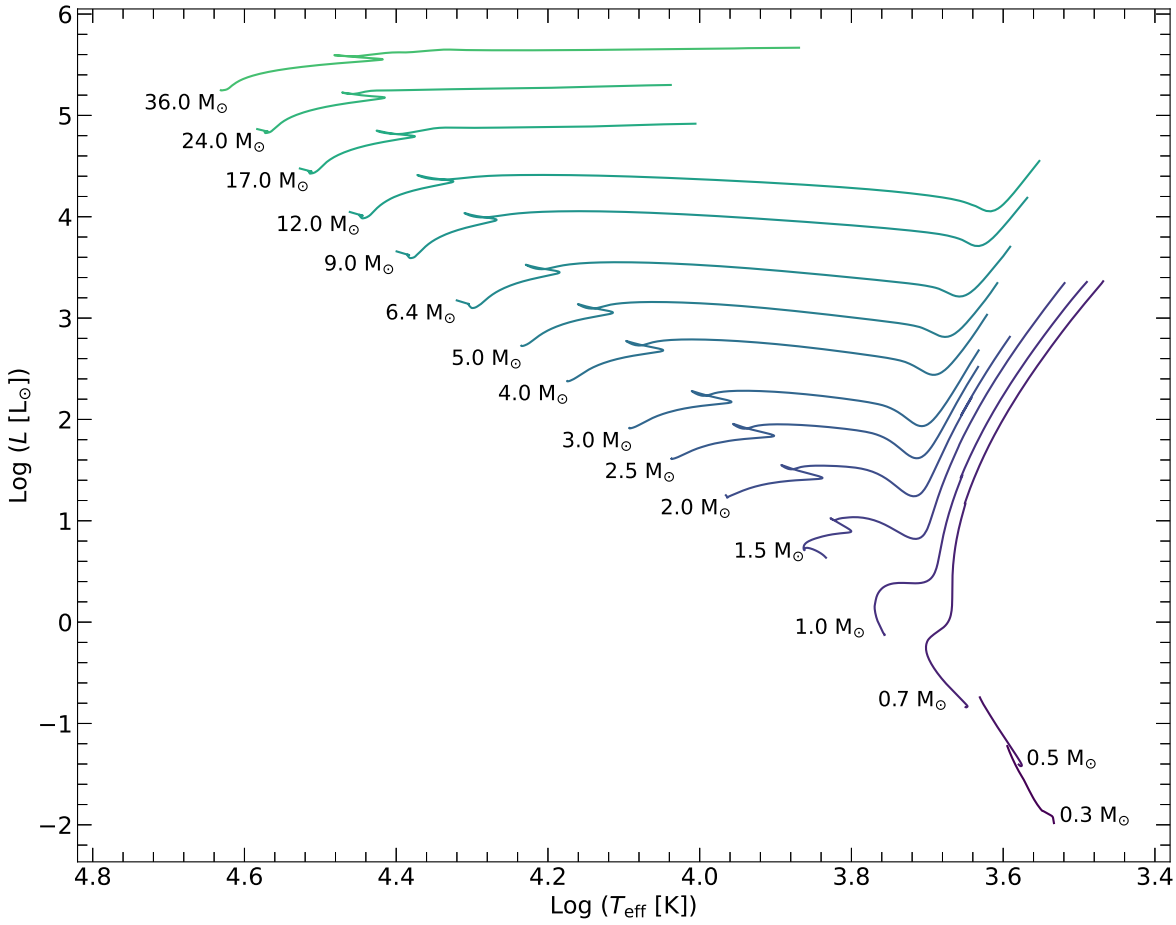

Figure 1.14: MIST evolution tracks starting from the ZAMS to the RGB phase calculated for masses between 0.3 $M_\odot$ and 36 $M_\odot$.

helium burning results in a *helium flash*, which is a runaway of thermal reactions that lifts the degeneracy so the ideal gas pressure sets back in. For both mass regimes, the ignition of helium causes the core to expand, cool, and reach an equilibrium. In response, the envelope contracts, increases in temperature, and the star settles on the horizontal branch, where hydrogen shell burning remains active.

Similar processes occur when horizontal branch stars exhaust the helium content in their cores. The stars burn helium in a shell surrounding the inert core, except with an additional hydrogen burning shell that surrounds the helium burning shell. The contraction of the core implies another extreme expansion, so the star ascends the *Asymptotic Giant Branch* (AGB), which is highlighted in purple in Fig. 1.13. The envelope of AGB stars is loosely bound at this stage. Hydrogen shell burning is eventually exhausted and the outer layers are expelled for AGB stars with $M \lesssim 9\,\mathrm{M}_\odot$, exposing the degenerate core as it traverses the post-AGB branch in Fig. 1.13. The result is a *white dwarf* star supported by electron degeneracy pressure.

Stars with $M \gtrsim 9\,\mathrm{M}_\odot$ undergo subsequent shell burning stages and reach central temperatures high enough to fuse heavier elements up to iron; no energy can be gained beyond iron. A degenerate iron core develops until electron degeneracy pressure is unable to support its weight, resulting in core collapse and a *supernovae* explosion. Neutron degeneracy pressure prevents further collapse when the core reaches nuclear densities if the mass of the core is below $\sim 3\,\mathrm{M}_\odot$; the result is a *neutron star*. For core masses exceeding this (uncertain) limit, core collapse continues, producing a *black hole*.

The evolution of a star depends on its mass, and to a lesser extent, on the initial chemical composition (Aerts et al., 2010). Fig. 1.14 presents 16 MIST evolution tracks calculated for masses between 0.3-36 $\mathrm{M}_\odot$ that cover the MS, SGB, Hertzsprung gap and RGB assuming solar metallicity. These calculations offer model predictions for the properties of stars but their accuracy depends on our understanding of the macro- and micro-physics that govern structural changes throughout the evolutionary stages. Observational constraints are necessary for testing the accuracy of such model predictions.

1.1.5.2 Observational Constraints from EBs

A *sophisticated stellar* model attempts to describe the *detailed* structure of a star and its evolution, and this requires higher degrees of complexity than is implied by the simplifications imposed on the standard stellar models described in Appendix C.3. Many theories have been published (e.g., Yonsei-Yale, Teramo, Dartmouth, PARSEC, MESA, Demarque et al., 2004; Pietrinferni et al., 2004; Dotter et al., 2008; Bressan et al., 2012; Nguyen et al., 2022; Paxton et al., 2019), but they still suffer from shortcomings due to relying on incomplete or over-simplified physics to account for complicated phenomena associated with, e.g., mixing; rotation; convection; magnetism; radiative opacities; degeneracies; nuclear reaction rates (del Burgo & Allende Prieto, 2018). Discriminating among the theories and improving them requires assessing their accuracy, and this necessitates measuring the properties of *real* stars[9].

High precision in the measurements is essential for their effectiveness as constraints, especially for mass, which requires precisions of $\sim 1-3\%$, because models are highly sensitive to this parameter (Torres et al., 2010). It is also preferable for measurement techniques to minimise their reliance on theory, particularly the models they aim to constrain, to ensure the constraints are reliable. Measurements satisfying this criterion can be made for the components of DLEBs (see Section 1.1.3.1).

Fig. 1.15 shows all objects from the Detached Eclipsing Binary CATalogue[10] (DEBCAT Southworth, 2015) plotted in the mass-radius plane. Main sequence evolutionary tracks calculated by MIST are also plotted showing the anticipated expansion as a star evolves off the zero-age MS (ZAMS) (see Section 1.1.5.1). Thus, the vertical location of the objects with respect to the ZAMS offers an age estimate assuming no mass-loss (Torres et al., 2010). The effect of mass-loss is apparent for higher masses ($M > 20\,\mathrm{M}_\odot$) in Fig. 1.15, as well as the fact that some objects in DEBCAT have evolved off the MS.

[9]The assessment of a theoretical description of *reality* requires that predictions made by the theory are compared to *reality*.

[10]DEBCAT is a catalogue of detached eclipsing binary systems with masses and radii measured to precisions of 2% and can be assessed at: https://www.astro.keele.ac.uk/jkt/debcat/.

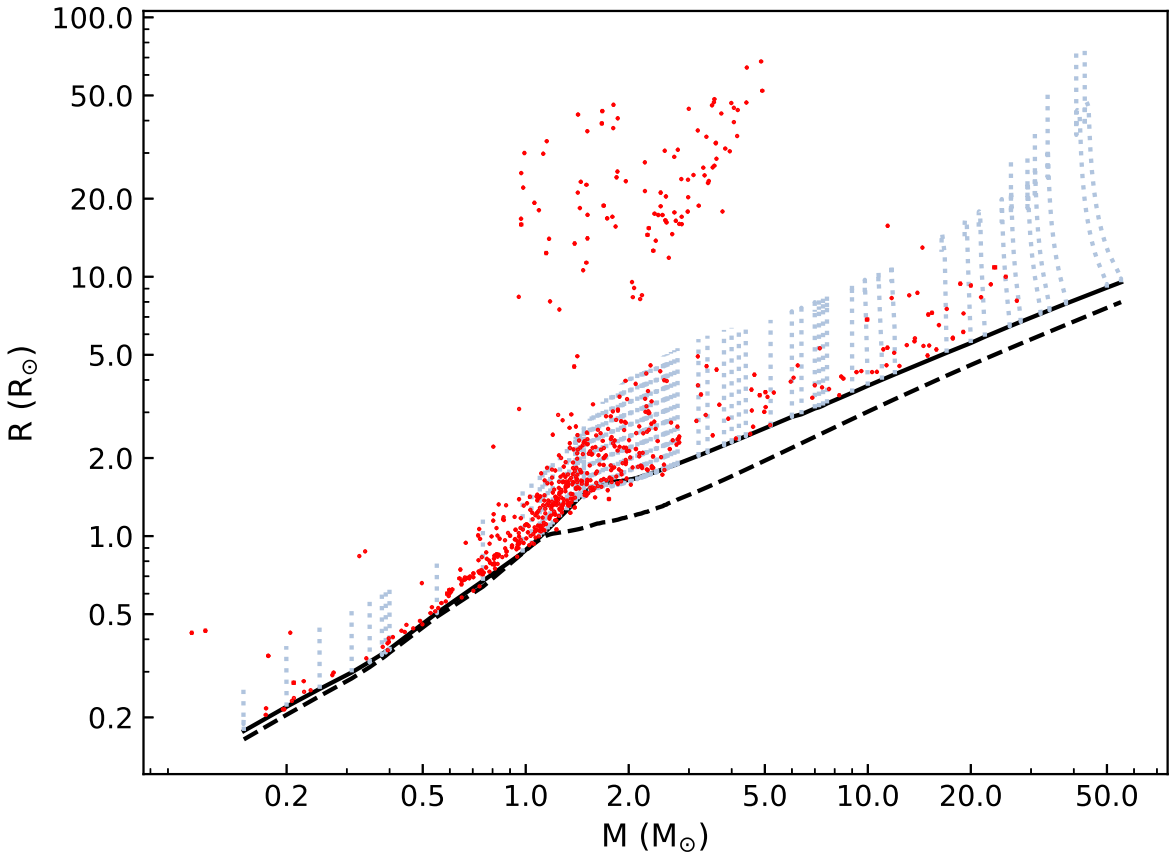

Figure 1.15: Radius plotted as a function of mass for stars taken from DEBCAT (red dots; Southworth, 2015). Also plotted are the theoretical ZAMS calculated from MIST evolutionary tracks for solar metallicity (black solid line) and [Fe/H]= −1.0 dex (black dashed line). The pale blue dotted lines show the evolution of the MIST tracks along the MS phase for solar metallicity.

A successful model will predict identical ages for both components in a binary system based on their measured masses and radii, while assuming a single chemical composition. This alignment stems from the concept of coevality, wherein the assumption is that the binary components share the same age and chemical composition. However, the sensitivity of the level of the ZAMS to chemical compositon (see Fig. 1.15) introduces an element of flexibility into the application coevality. To isolate the ZAMS and strengthen the test requires a precise measurement of the metallicity [M/H].

A more stringent test to the models follows with the addition of a measurement for the components' $T_{\rm eff}$, leading to the complete set of *conventional* observational constraints [$M, R, T_{\rm eff}$, [M/H]] (Torres et al., 2010). In this scenario, a strict assessment would use M and [M/H] as inputs and require accurate predictions for the components' radii and $T_{\rm eff}$ values (or luminosity) at a single age. The difficulty in meeting such demands increases with measurement precision.

While the best data can never *prove* a set of models right (Andersen, 1991; Torres et al., 2010), these tests allow for the most accurate theoretical descriptions of stellar structure and evolution to be identified, as well as exposing deficiencies that necessitate further development and calibration. The nature in which these deficiencies/uncertainties propagate into model predictions, and the stellar processes involved, depends on the mass regime and evolutionary stage. Here, we are interested in low- and intermediate-mass dwarfs so expand further on these details for such stars in the next two sections. However, our understanding is most incomplete at evolved stages (del Burgo & Allende Prieto, 2018).

1.1.5.3 Complications in Low-Mass Stars

Stellar theory is well understood for stars with masses of $1-5\,{\rm M}_{\odot}$ (Claret et al., 2021) compared to low-mass stars in the regime of $0.08-0.3\,{\rm M}_{\odot}$. Low-mass stars are challenging because of the complex and varied physics which occurs in their interiors, in particular, magnetic phenomena (Mullan & MacDonald, 2001); the magnetic field is stronger and more pervasive (Hawley et al., 2000). The lowest-mass stars are near the

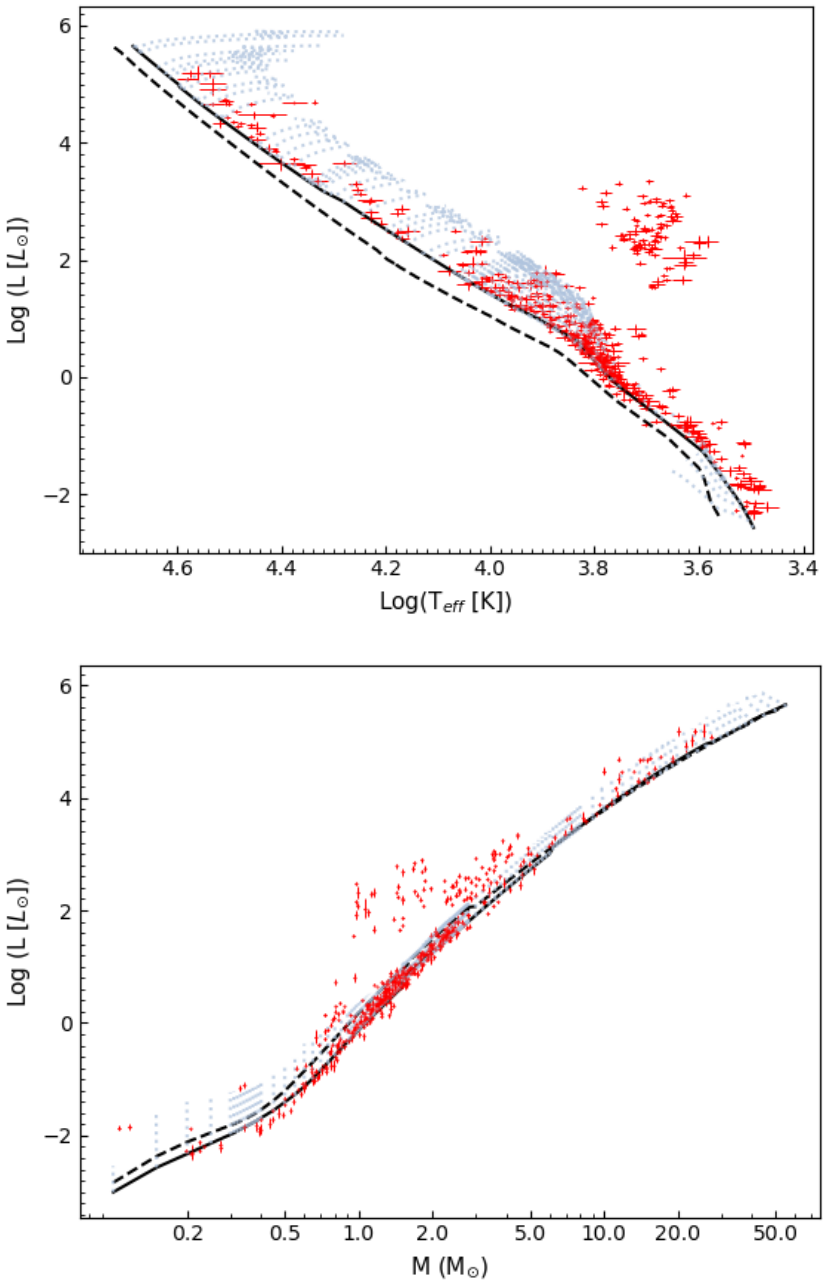

Figure 1.16: Same as Fig. 1.15 but in the Hertzsprung-Russell (top) and Mass-Luminosity planes (bottom).

hydrogen burning limit so the interior temperatures are cool enough (i.e., on the order of the electron *Fermi temperature*) for parts of the interior to behave as a partially degenerate gas (Chabrier & Baraffe, 1997, 2000; Beatty et al., 2007). Furthermore, the electron number density is such that the mean inter-ionic distance is on the order of the Fermi screening length, meaning the electron gas is polarised by the external field. Relatively lower temperatures would also allow for the recombination of molecular hydrogen and other molecules, such as TiO, meaning that the grey atmosphere approximation becomes least valid as the opacity spectrum becomes most complex.

The interior structure of fully convective low-mass stars is therefore complicated and different to that of partially radiative higher-mass stars. A lack of observational constraints on their properties (Swayne et al., 2021) makes it difficult to address inaccuracies in our understanding of their structure. For instance, the radii of low-mass stars are observed to be inflated by around $5-10\,\%$ compared to theoretical predictions (Hoxie, 1973; Lacy, 1977; López-Morales, 2007; Torres, 2013; Zhou, 2010). The discrepancy has also been observed to persist in stars with masses up to $1\,\mathrm{M}_{\odot}$ (e.g. Torres et al., 2021; Southworth, 2022). This suggests that the uncertainties surrounding these complex physical processes are significant, and must be addressed in stellar structure calculations for stars in this regime.

Since most of the objects with measured radii precise enough to usefully constrain theoretical models exist in EBs, it has been suggested that tidal interactions in EBs leads to faster rotation and increased magnetic activity, which decreases the efficiency of convective energy transport, causing the radius to expand (Mullan & MacDonald, 2001; López-Morales & Ribas, 2005; López-Morales, 2007). Surface activity detectable in some of their light curves (e.g. Torres et al., 2006; Morales et al., 2008) supports this hypothesis and, indeed, artificially low values for the mixing length parameter in the outer convective zone have been observed to reduce the discrepancy considerably (Torres et al., 2006; Chabrier et al., 2007). However, radius inflation has also been observed for isolated low-mass stars, which rotate slowly due to magnetic braking, so explanations should not be restricted to binary systems (Berger et al., 2006; Morrell & Naylor, 2019). Other possible causes such as metallicity and uncertainties in the input

physics have been discussed (e.g. Torres et al., 2010; Swayne et al., 2021). It should be noted that "radius inflation" is not observed for all M dwarfs (e.g., Bentley et al., 2009; Zhou et al., 2014) to within the measurement errors.

It is clear that more observational constraints are required in order to resolve the radius inflation problem and the associated uncertainties in descriptions of low-mass stellar interiors. As outlined in Section 1.1.3.1, it is possible to obtain these measurements to the required precision for DLEBs by modelling their light and RV curves (Andersen, 1991; Torres et al., 2010). However, known examples of DLEBs containing two low-mass stars are relatively rare due to the low binary fraction in low-mass stars (Duchêne & Kraus, 2013) and their intrinsic faintness.

A solution exists with the advent of wide-field searches for planetary transits which have led to the discovery of many eclipsing binaries with low-mass companions (EBLMs) (Beatty et al., 2007; Fernandez et al., 2009; Triaud et al., 2017; Collins et al., 2018; Zhou et al., 2015), where an M dwarf transits a much larger and brighter F or G dwarf. The faintness of the M dwarf secondary stars versus the F/G primary components means they are usually not detected in the spectra of the system, making EBLMs SB1 systems. However, these systems offer ways to obtain precise, but indirect, measurements of the masses and radii of M-dwarfs, as outlined in Section 1.1.3.3.

1.1.5.4 Complications Above 1.15 $M_\odot$

The nuclear energy generation is dominated by the CNO cycle for stars with masses above $\sim 1.15\,M_\odot$ so they have a convective core. The convective elements have mass, and thus inertia. The turbulence associated with convective regions means that the convective elements possess some velocity. Therefore, convective eddies approaching the boundary of the convective core will penetrate some distance into the convectively stable, radiative region, just outside the core. This phenomenon is termed *convective overshooting*. Convective overshooting mixes material from the radiative layers into the core, increasing the extent of the mixed region as well as the amount of nuclear fuel available on the MS. Overshooting has a significant effect on the evolution of a star;

the MS lifetime is extended, while the crossing of the sub-giant branch is accelerated.

Classical observations, particularly the use of DLEBs, have provided evidence for core overshooting (Andersen et al., 1990; Ribas et al., 2000; Claret, 2007), and some formulation of the effect is now included in most models for stars with convective cores (Torres et al., 2010). The discrepancy between dynamical masses derived from binaries and those predicted by evolutionary models, first presented by Ribas et al. (2000), was shown to significantly decrease by the inclusion of properly calibrated core-boundary mixing profiles in stars with convective cores by Higl & Weiss (2017) and Tkachenko et al. (2020). Developing the correct formulation for convective overshooting requires constraints on the profile of the implied mixing, its extent, and efficiency[11].

For intermediate-mass stars, with $T_{\rm eff}$ between around $7000-9000\,\mathrm{K}$, calibrating the extent of the convective region in the envelope may be difficult because these stars are in the transition region between fully convective and radiative envelopes. The mixing length parameter $\alpha_{\rm ml}$ is expected to change significantly over this temperature range. Another complication arises in stars with thin or fully absent convection zones because of the absence of magnetic braking; magnetic braking reduces stellar rotation. Fast rotation leads to bulging at the equator and modelling in two dimensions might be necessary. A further complication arises due to the implications fast rotation has on mixing and angular momentum transport (Aerts et al., 2018). Mixing influences the stratification of elements, modifies molecular gradients outside convective cores, and is further influenced by magnetism and pulsations.

The interior processes mentioned in this section are intricate and pose challenges in stellar modelling. However, continuing in the advancement of intermediate-mass stellar theory necessitates overcoming these challenges due to the already relatively accurate theoretical predictions. Given the complexity of these processes, calibrating their influence in stellar models is difficult and additional constraints on the stellar interior may be in order. Asteroseismology can deliver those constraints.

[11]The mass dependence of core overshooting (Claret & Torres, 2016, 2017, 2018, 2019) and the amount of core mixing in massive stars has been probed using DLEBs (Pavlovski et al., 2018; Tkachenko et al., 2020)

1.2 Asteroseismology

Asteroseismology offers ways to obtain less conventional constraints, such as the helium abundance Y or mixing length parameter $\alpha_{\rm ml}$, among other parameters, which are otherwise usually assumed or adjusted to improve compatibility with observations (Torres et al., 2010). This makes DLEBs compounded by asteroseismic constraints our most valuable data sources for testing stellar thoeries because the latter effectively eliminates any remaining elements of model flexibility which act to lessen the strength of such model comparison tests discussed in Section 1.1.5.2. We introduce asteroseismology in this chapter.

1.2.1 Stellar Pulsations

1.2.1.1 Describing The Oscillation Modes

Mechanisms that perturb a star's internal structure from its equilibrium state can result in oscillations of the stellar interior which manifest at the surface of the star as brightness, RV, and spectral line profile variations. There are several possible driving mechanisms which may act to disturb a star from its equilibrium state and each may give rise to many *modes* of oscillation, which are classified into two main groups depending on whether pressure (p modes) or gravity (g modes) is dominant in restoring the equilibrium (Kurtz, 2006; Aerts, 2021).

The oscillations are described in spherical coordinates, i.e., using the radial distance r from the centre, co-latitude θ, and longitude ϕ. Each component of the displacement of the oscillating elements of plasma ξ, i.e., the solutions to the equations of motion, are then (Kurtz, 2006),

$$\xi_r(r,\theta,\phi,t) = a(r)Y_l^m(\theta,\phi)\exp(-i2\pi\nu t), \tag{1.40}$$

$$\xi_\theta(r,\theta,\phi,t) = b(r)\frac{\partial Y_l^m(\theta,\phi)}{\partial\theta}\exp(-i2\pi\nu t), \tag{1.41}$$

$$\xi_\phi(r,\theta,\phi,t) = \frac{b(r)}{\sin(\theta)}\frac{\partial Y_l^m(\theta,\phi)}{\partial\phi}\exp(-i2\pi\nu t), \tag{1.42}$$

within which $a(r)$ and $b(r)$ are amplitudes and ν is the oscillation frequency. The $Y_l^m(\theta, \phi)$ terms are spherical harmonics given by,

$$Y_l^m = (-1)^m \sqrt{\frac{2l+1(l-m)!}{4\pi(l+m)!}} P_l^m(\cos\theta) \exp(im\phi), \tag{1.43}$$

where,

$$P_l^m(\cos\theta) = \frac{1}{2^l l!}(1-\cos^2\theta)^{m/2} \frac{\mathrm{d}^{l+m}}{\mathrm{d}\cos^{l+m}\theta}(\cos^2\theta - 1), \tag{1.44}$$

are Legendre polynomials. The spherical harmonics describe the angular dependencies of the pulsations and the normalization constant,

$$c_{l,m} = \sqrt{\frac{2l+1(l-m)!}{4\pi(l+m)!}}, \tag{1.45}$$

secures that the integral of $|Y_l^m|^2$ over the unit sphere equals unity (Aerts et al., 2010).

Stationary points on the surface of a pulsating star, i.e., surface nodes, are defined by the nulls of the associated Legendre polynomial for a mode (Handler, 2013), and the degree l specifies how many surface nodes there are; for $l \neq 0$, the mode is *nonradial*. The magnitude of the *azimuthal* order m specifies how many of the nonradial nodes are lines of longitude and therefore, the number of nodes that are lines of co-latitude is equal to $l - |m|$. The possible values of m range from $-l$ to $+l$, resulting in $2l + 1$ possible modes for each degree. The radial order n gives the number of nodes that are radial, i.e., concentric shells within the stellar interior. Each of n, l and m are quantum numbers describing a mode and take integer values.

For purely radial oscillations, $l = m = 0$, $P_l^m(\cos\theta) = 1$ (i.e., zero surface nodes), and the oscillatory motion is symmetric about the centre of the star. *Axisymmetric* modes have $l > 0$ and $m = 0$, while *sectoral* modes have $m = l$; anything in-between is referred to as a *tesseral* mode (Handler, 2013). Examples of nonradial modes at one instance of an oscillation cycle are shown in Fig. 1.17. Easy to visualise is the axisymmetric dipole mode (top left of Fig. 1.17) which has $n \geq 1$, $l = 1$, and $m = 0$. The surface node of constant co-latitude splits the northern and southern hemispheres which swell and contract in anti-phase; note that this node is accompanied by at least

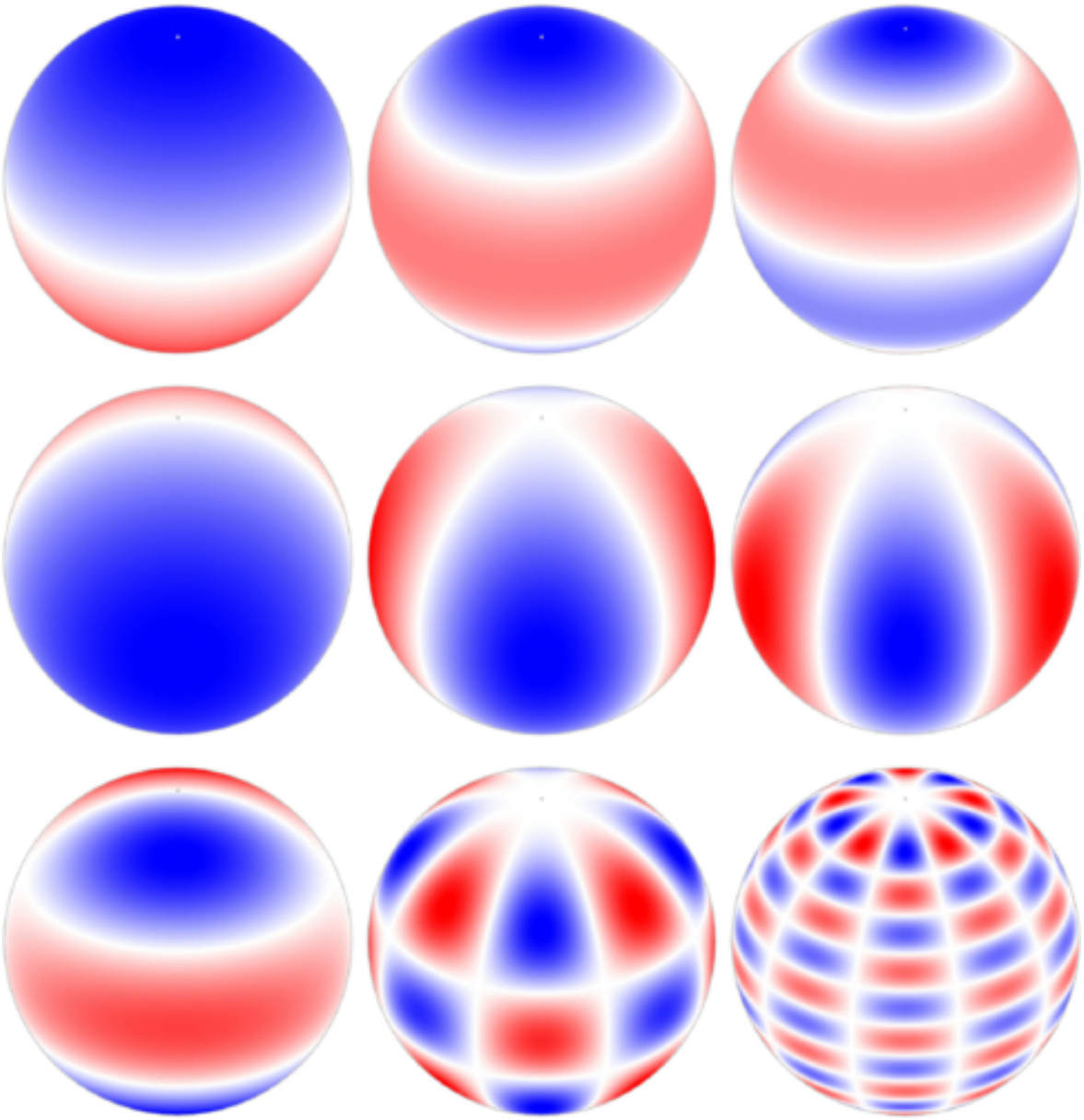

Figure 1.17: The angular dependence of the radial component of the displacement vector ϵ_r during one instance of an oscillation cycle for various nonradial modes seen at an angle of 60°. The white bands indicate the nodes of the oscillation mode where $\epsilon_r = 0$. The red represents contraction and the blue represents expansion. The first row shows axisymmetric modes with $m = 0$ and $l = 1, 2, 3$, from left to right; the second row shows sectoral modes with $m = l$ and $l = 1, 2, 3$; the third row are tessoral modes with $(l,|m|) = (3,1)$, $(6,4)$, $(15,5)$. From Aerts (2021).

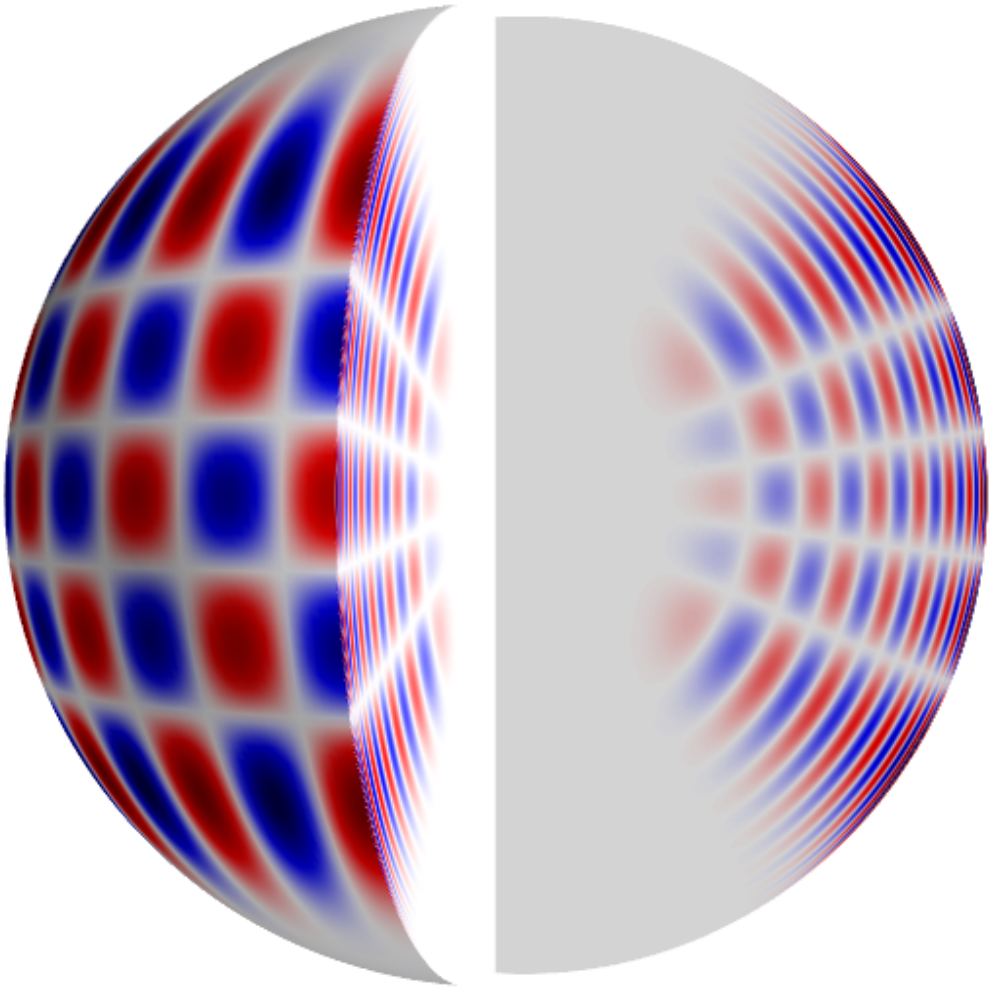

Figure 1.18: Same as Fig. 1.17 but for one solar p-mode with $n = 14$, $l = 20$, and $m = 16$; the behaviour in the interior is also shown here (Wikipedia contributors, 2023).

one radial node[12]. The resulting behaviour of the oscillating elements in the interior due to the presence of both surface and radial nodes is depicted in Fig. 1.18 for a p mode with $n = 14$, $l = 20$, and $m = 16$. The oscillating elements above or below a *radial* node are split into components moving in antiphase either side of the *nonradial* node.

Equations 1.40 and 1.43 combine to give a time dependence $\exp[-i(2\pi\nu t - m\phi)]$ for $m \neq 0$, meaning these are travelling waves (Kurtz, 2006; Aerts et al., 2010). By convention, $m > 0$ corresponds to waves travelling in the direction of rotation of the star (prograde modes) and vice versa for $m < 0$ (retrograde modes) (Kurtz, 2006; Aerts et al., 2010). Each of the $2l + 1$ modes within a multiplet with $|m| > 0$ have identical frequencies unless the degeneracy is lifted when the star rotates. This is because the frequencies of the prograde modes are decreased while the retrograde frequencies are increased in the *co-rotating* reference frame of the star due to the Coriolis force (Aerts et al., 2019; Aerts, 2021). The frequencies in the *observer's* reference frame are further Doppler shifted (Aerts et al., 2019) and for a uniformly rotating star are given by (Ledoux, 1951),

$$\nu_{nlm} = \nu_{nl0} + m(1 - C_{nl})\Omega/2\pi, \tag{1.46}$$

where ν_{nl0} is the central frequency of the multiplet, C_{nl} is the Ledoux constant and Ω is the angular velocity of the star.

1.2.1.2 Calculating the Oscillation Modes

To learn anything about the star from the oscillations requires we describe the resulting perturbations to stellar quantities in the form of equations. The uncertainties surrounding hydrodynamical processes, that are referred to in Appendix C.4, mean that similarly to convection, reaching a general solution using a complete hydrodynamical description of a star is impractical or impossible (Aerts, 2021). Instead, approximating

[12]We must have $n \geq 1$ for the dipole mode because otherwise, the dipole motion would require a movement of the centre of mass of the star with no external force (Handler, 2013).

stellar oscillations as small perturbations about some equilibrium structure suffices because their amplitudes are small compared to the scale of the star (Aerts et al., 2010; García & Ballot, 2019).

Uncertainties associated with 2D stellar structure models, especially in the presence of rotation, have led to stellar oscillation calculations usually relying on 1D equilibrium structures. This is justified for stars rotating up to 15% and 70% the critical rotation frequency for p and g modes, respectively (Aerts, 2021). Working in the *adiabatic approximation* to calculate oscillation frequencies (e.g., Aerts et al., 2018) was shown to be appropriate by Moravveji et al. (2015); Van Reeth et al. (2016); Ouazzani et al. (2017), with differences between adiabatic and non-adiabatic theoretical frequencies being less than the precision of the detected modes from a nominal *Kepler* light curve. If the model is also static, the equilibrium state takes that of a standard stellar model. Standard stellar models and the associated equations are described in Appendix C.3.

The oscillation equations are then derived by adding small perturbations to the equilibrium quantities, inserting them back into the standard stellar structure equations and then taking the difference between the equilibrium and perturbed versions of the expressions (Aerts et al., 2010; Aerts, 2021). The symmetry of the 1D structure permits the separation of the horizontal and radial variations, i.e., factoring out the spherical harmonics $Y_l^m(\theta, \phi)$ as a common factor. After linearising, the resulting linear, adiabatic stellar oscillation equations are presented in Appendix D. They constitute a system of ordinary differential equations, fourth order in the perturbations to the displacement of the gas ξ_r, pressure p', gravitational potential Φ' and acceleration $\mathrm{d}\Phi'/\,\mathrm{d}r$ (Aerts et al., 2010), where the apostrophe indicates that these are eigen-functions[13] describing the variation in the associated quantity (see below).

The key points for asteroseismology are as follows. The stellar oscillation equa-

[13]Since the solutions are non-trivial only for a discrete set of values of the oscillation frequency, the problem can be formulated as an eigen-value problem (García & Ballot, 2019). Consequently, the frequencies are often referred to as *eigen-frequencies* and the variation in the perturbed quantities are the *eigen-functions*.

tions have non-trivial solutions only for specific values of the oscillation frequency ν. These values form a discrete set of *eigen-frequencies* that correspond to the natural modes of oscillation for some stellar structure, and are determined by the coefficients in the oscillation equations (see Appendix D), i.e., the equilibrium quantities of the model: ρ, p, Γ_1 and g, where ρ, Γ_1 and g are the density, first adiabatic exponent, and unperturbed gravitational acceleration, respectively (Aerts et al., 2010). Therefore, the natural oscillation modes are determined by a star's equilibrium structure so it is possible to obtain them numerically for any given stellar model (García & Ballot, 2019); various codes have been developed for this task, (e.g., ADIPLS, LOSC, PULSE, POSC, GRACO, FILOU, GYRE; Christensen-Dalsgaard, 2008; Scuflaire et al., 2008; Brassard & Charpinet, 2008; Monteiro, 2008; Moya & Garrido, 2008; Suárez & Goupil, 2008; Townsend & Teitler, 2013). Conversely, the oscillation modes reveal information about the equilibrium structure. Indeed, seeking agreement between a set of observed and theoretical oscillation frequencies offers a way to constrain the free parameters of a stellar model (see Section 1.2.1.2).

1.2.1.3 Mode Trapping

The Cowling approximation ($n \gg 1$, $l \gg 1$) allows us to think, only, in terms of the displacement to stellar matter[14],

$$\frac{\mathrm{d}^2\xi_r}{\mathrm{d}r^2} = -K_s(r)\xi_r, \tag{1.47}$$

where,

$$K_s(r) = \frac{\omega^2}{c^2}\Big(\frac{N^2}{\omega^2} - 1\Big)\Big(\frac{S_l^2}{\omega^2} - 1\Big), \tag{1.48}$$

which is useful for gaining insights into *mode trapping* given that two important quantities appearing in the stellar oscillation equations (Eqs. D.1; D.3; D.5) remain. The first is the *characteristic acoustic frequency* S_l given by,

$$S_l^2 = \frac{l(l+1)c^2}{r^2} = k_h^2 c^2, \tag{1.49}$$

[14]Here, we ignore perturbations to the gravitational potential as well as derivatives of equilibrium quantities in the oscillation equations (Aerts, 2021).

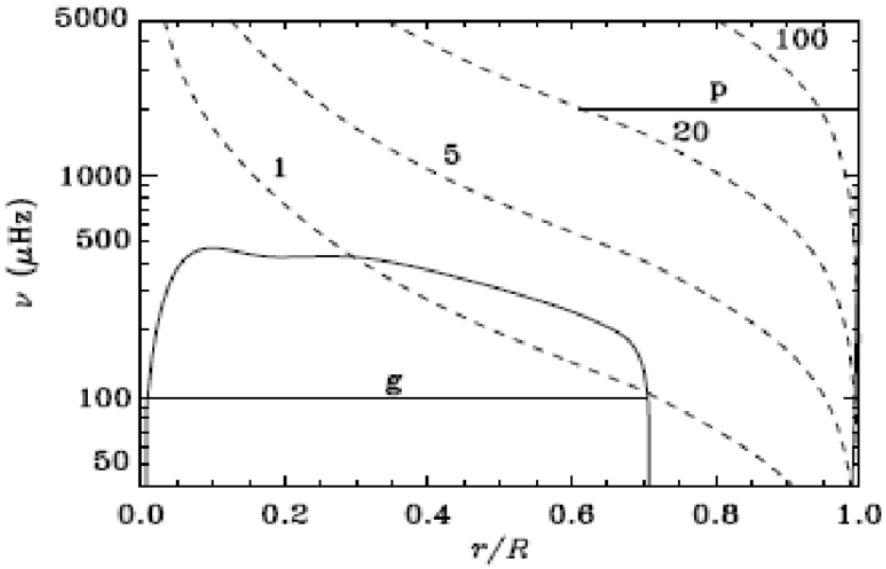

Figure 1.19: The characteristic acoustic frequency S_l (dashed lines for $l = 1$, 5, 20, and 100) and the Brunt-Väisälä frequency N (solid lines) against fractional radius in a standard solar model. The heavy horizontal lines indicate the trapping regions for a g mode with frequency $\nu = 100$ μHz and for a p mode with degree $l = 20$ and $\nu = 2000$ μHz. Figure taken from Ambastha (2010).

where k_h is the horizontal wave number (García & Ballot, 2019). The second is the *buoyancy*, or *Brunt-Väisälä frequency* given by,

$$N^2 = g\Big(\frac{1}{\Gamma_1 p}\frac{\mathrm{d}p}{\mathrm{d}r} - \frac{1}{p}\frac{\mathrm{d}\rho}{\mathrm{d}r}\Big). \tag{1.50}$$

Oscillations can only occur in regions of the stellar interior where $K_s > 0$; the modes are *trapped* in these regions and the boundaries of these trapping regions are defined by $K_s = 0$, referred to as *turning points*. Gravity modes exist in trapping regions where $|\omega| < N$ and $|\omega| < S_l$, while acoustic modes exist in trapping regions where $|\omega| > N$ and $|\omega| > S_l$. Fig. 1.19 shows S_l for modes with $l = 5$, 20, and 100, as well as N against fractional radius for a standard solar model (Ambastha, 2010). The figure shows how these two characteristic frequencies trap p modes in the surface layers and g modes near the core regions given the above conditions. Hence, p modes are sensitive to the outer layers of the star and g modes carry information about the near-core regions.

Two propagation cavities can arise for a single mode if the corresponding frequency satisfies both trapping conditions, e.g., the intermediate mode in Fig. 1.20. This mode exists near the core with g-mode character and near the surface as a p mode. These *mixed modes* occur because S_l decreases as a star evolves, while N increases.

The condition for convective instability is $N < 0$ (Aerts et al., 2010) so g modes can not propagate in convective regions, and hence the rapid approach of N to zero as it approaches the convective core in Fig. 1.20. The sharp spike prior to this due to chemical gradients of CNO processed material and is discussed in Section 1.2.2.4. These features are absent in Fig. 1.19 because it represents a solar-mass model.

1.2.1.4 Asymptotic Representations

Tassoul (1980) presented second-order approximate solutions[15] to the oscillation equations by means of the asymptotic technique devised by Olver (1956). These asymptotic

[15]The asymptotic analysis using the full fourth order set of equations for SPB and γ Doradus stars, as in Smeyers & Moya (2007), predicts the same patterns as the second order asymptotic analysis (Aerts, 2021).

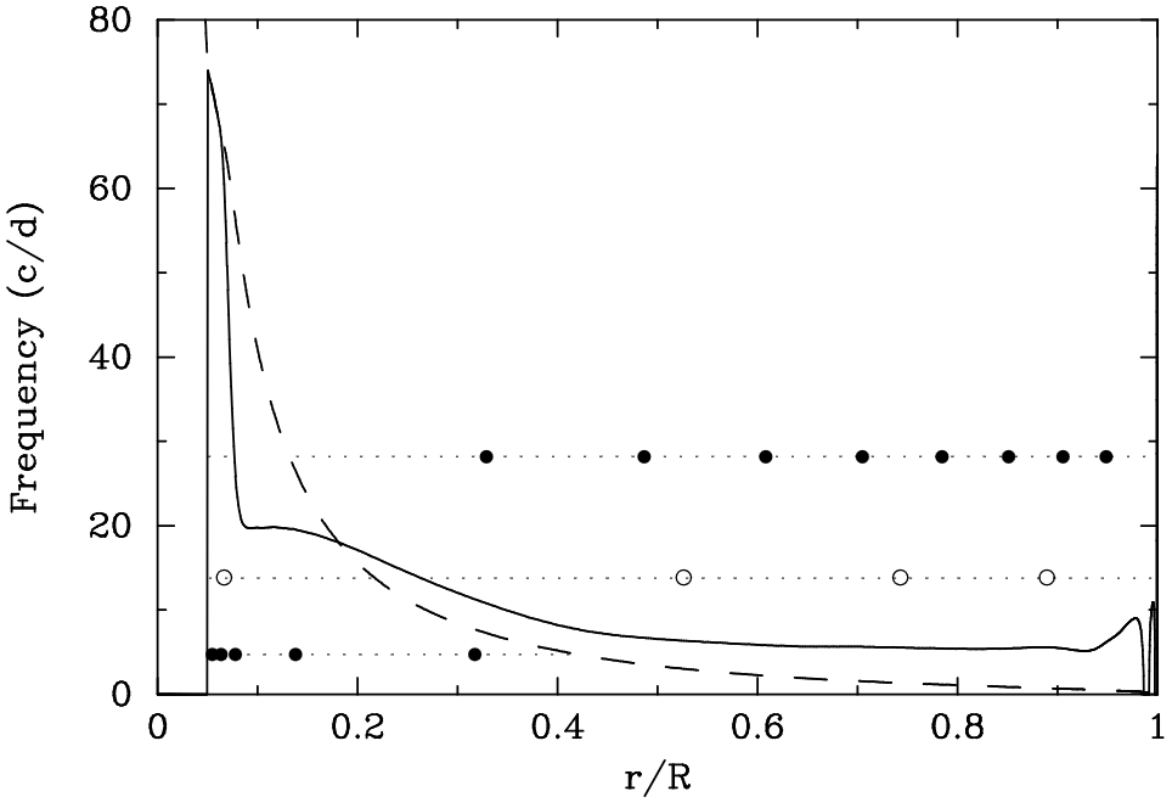

Figure 1.20: The characteristic acoustic frequency S_l (dashed line) and Brunt-Väisälä frequency N against fractional radius for an evolved $2\,\mathrm{M}_\odot$ stellar model, taken from Handler (2013). The lowest frequency oscillation corresponds to a g_5 mode, the highest frequency is a p_8 mode, while the intermediate frequency is a mixed mode. For this evolved case, N and S_l trap the mixed modes in two regions near the core and surface.

representations of the mode frequencies are valid for $n \gg l$ and show that for p modes,

$$\nu_{nl} = \Big(n + \frac{l}{2} + \frac{1}{4} + \alpha\Big)\Delta\nu, \tag{1.51}$$

where $\Delta\nu$ is the *large frequency separation* and the inverse of the sound travel time across a stellar diameter (Chaplin & Miglio, 2013) given by,

$$\Delta\nu = \Big[2\int_0^R \frac{\mathrm{d}r}{c(r)}\Big]^{-1}, \tag{1.52}$$

and α is a constant of order unity (Aerts et al., 2010). Eq. 1.51 predicts that p modes of the same degree l, but consecutive radial order n, are equally spaced by $\Delta\nu$ (e.g., Fig. 1.21)[16]. We would also expect the frequency of a mode ν_{nl} to be approximately equal to the frequency of a mode $\nu_{n-1,l+2}$. Fig. 1.21 shows that this is not the case with a smaller, but clear, separation between the $\nu_{n-1,l=2}$ and $\nu_{n,l=0}$ oscillation modes. This is the *small frequency separation* $\delta\nu$ and is explained by expanding further in the asymptotics to yield (Chaplin & Miglio, 2013),

$$\delta\nu_{nl} = \nu_{nl} - \nu_{n-1,l+2} \simeq -(4l+6)\frac{\Delta\nu}{4\pi^2\nu_{nl}}\int_0^R \frac{\mathrm{d}c}{\mathrm{d}r}\frac{\mathrm{d}r}{r}. \tag{1.53}$$

The large separation is related to the evolutionary stage of the star because the sound travel time increases as the radius expands. The small separation depends on the sound speed gradient in the deep stellar interior, and the sound speed gradient is sensitive to the hydrogen and helium composition profiles (Aerts, 2021); those profiles are directly influenced by nuclear fusion so $\delta\nu$ can be used as an age diagnostic (Kurtz, 2006). Plotting $\delta\nu$ against $\Delta\nu$ allows for an unambiguous determination of the stellar mass and evolutionary state (Handler, 2013).

The corresponding prediction for g modes is,

$$P_{nl} = \frac{\Pi_0}{\sqrt{l(l+1)}}(|n| + \alpha_{l,g}), \tag{1.54}$$

[16]The Gaussian-like modulation of the observed powers with frequency in Fig. 1.21 is a property of solar-like oscillators, such as 16 Cyg A, where excitation of the modes is due to turbulence in the outer convective envelope. Such stars are not the topic of interest here, but the figure gives a good representation of $\Delta\nu$.

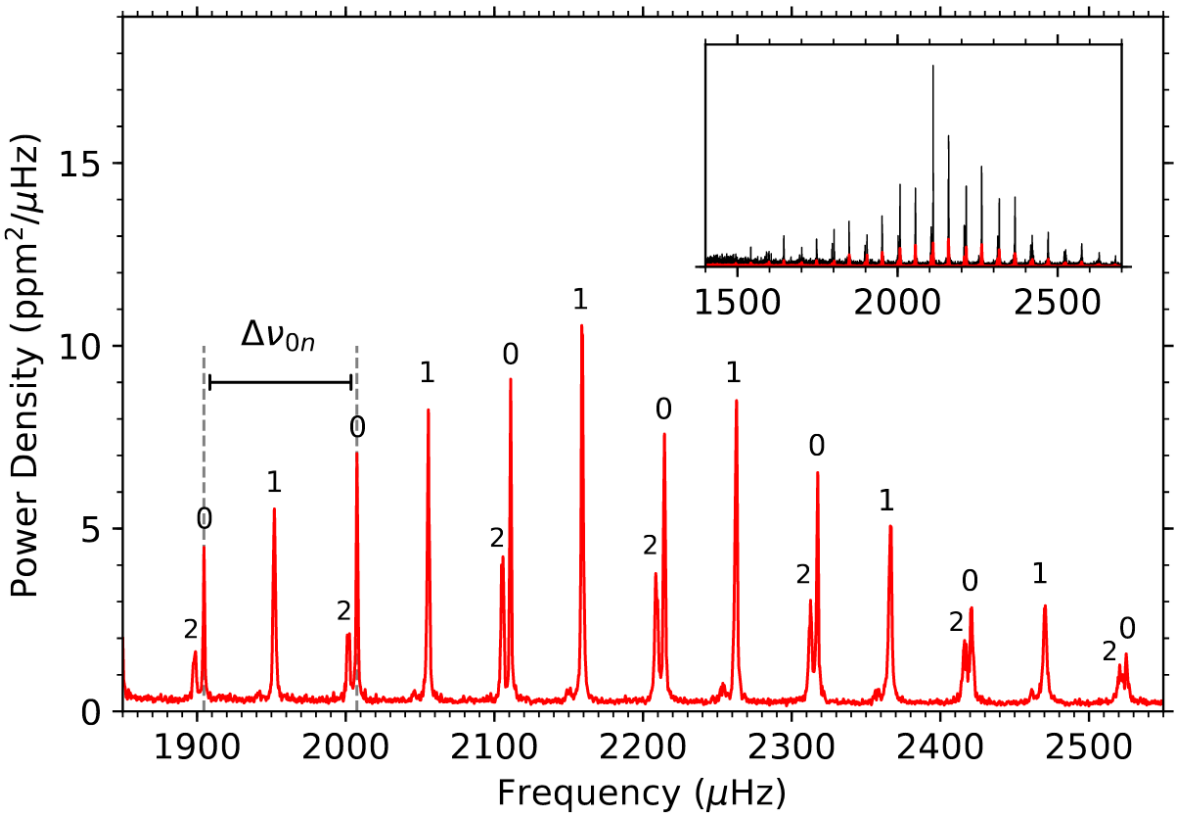

Figure 1.21: An enlargement (red) of the pulsation spectrum (see Section 1.2.2.1) of 16 Cyg A calculated from data acquired by the *Kepler* Satellite. The p modes are labelled with by their degree l and the large frequency separation $\Delta\nu$ is indicated using the $l = 0$ radial modes. Figure is adapted from Chaplin & Miglio (2013) and taken from Aerts (2021).

where,

$$\Pi_0 = 2\pi^2 \Big(\int_{r_1}^{r_2} \frac{N}{r} \, \mathrm{d}r \Big)^{-1}, \tag{1.55}$$

within which, r_1 and r_2 are the inner and outer boundaries of the trapping region ($K_s = 0$) and $\alpha_{l,g}$ is a phase term depending on whether the star has a radiative or convective core (Aerts, 2021). The prediction here is that the periods of oscillation modes of consecutive radial order are equally spaced by the buoyancy travel time Π_0 normalised by $\sqrt{l(l+1)}$ (e.g., Fig. 1.22).

Departures from this uniformly predicted spacing of periods offer an excellent diagnostic for near-core rotation, chemical gradients, and mixing. Further details follow in the next section and in Section 1.2.2.4.

1.2.1.5 Accounting for Rotation

How rotation is treated depends on the spin parameter $S = 2\Omega/\omega$. If $S \ll 1$, the Coriolis force can be treated as a small perturbation in the oscillation equations. These can be first order perturbations if the centrifugal force ($\sim \Omega^2$) can be ignored but second order perturbations may be necessary to account for non-negligible deformations (e.g., Suárez et al., 2005, for the δ Scuti star HD 187642, aka Altair). The condition $S \ll 1$ is satisfied for slowly rotating stars, i.e, stars with extensive convective envelopes, or for high values of the oscillation frequency $\nu = \omega/2\pi$, i.e., p modes.

Making rotation a function of geometrical depth r, i.e., $\Omega = \Omega(r)$, the basic idea behind the perturbative approach to rotation requires an expansion of the discussion in 1.2.1.1 with the introduction of a rotational kernel. The rotational kernal weights the contributions of the different layers within the non-rigidly rotating star in the overall determination of the rotational splittings (Aerts et al., 2019). The maximum of the rotational kernal profile therefore corresponds to the region within the star that the splittings are most sensitive; indeed, this occurs near the core for g modes (Aerts, 2021).

The modes are said to be *gravito-inertial* (Aerts, 2021) when the spin parameter is larger than unity, i.e., g modes where the oscillation frequency is comparable

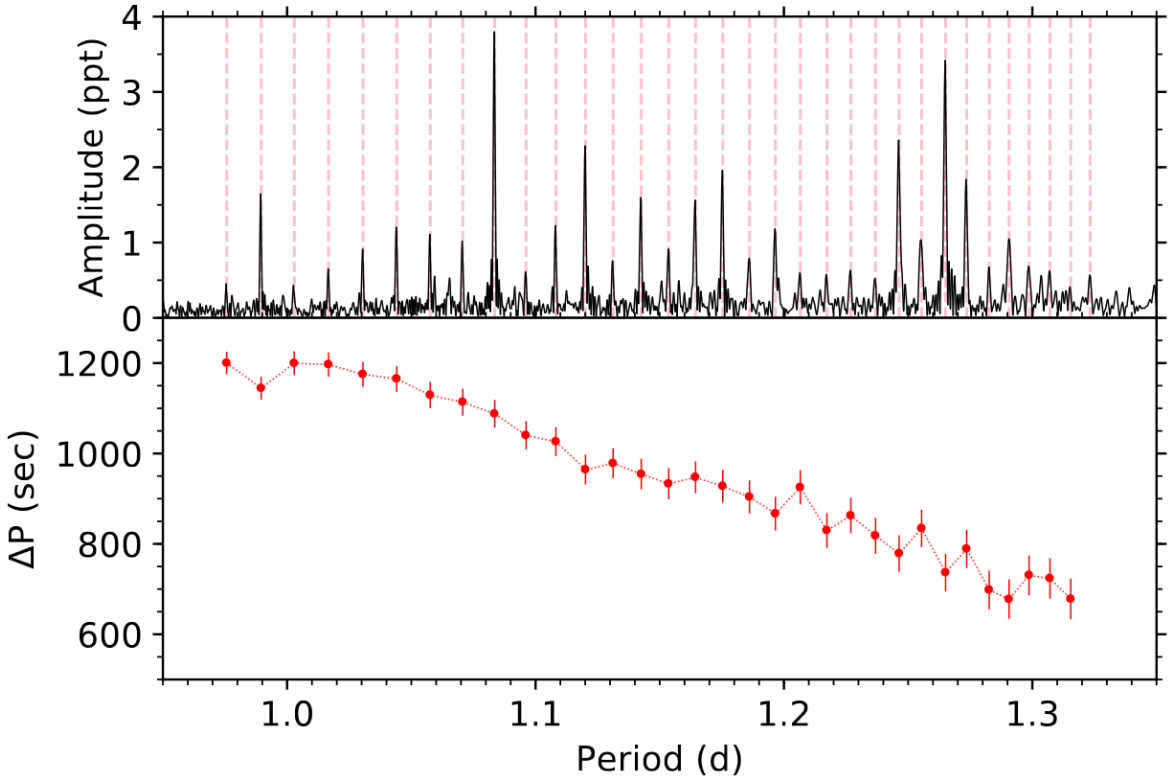

Figure 1.22: Top Panel: The pulsation spectrum (black) in terms of oscillation period for the γ Doradus star KIC 11721304 calculated from data acquired by *Kepler*. The red vertical dashed lines indicate the mode periods with dominant amplitude. Bottom panel: period spacing pattern derived from the dipole sectoral prograde modes. Figure is taken from Aerts (2021) and based on data from Van Reeth et al. (2015a).

to the rotation frequency. The Traditional Approximation to Rotation (TAR) (Lee & Saio, 1987a,b, 1989) has been used in order to account for the Coriolis force in this circumstance (e.g., Bouabid et al., 2013; Van Reeth et al., 2016, 2018). The resulting asymptotic period spacing of g modes within the TAR framework is equal to the buoyancy travel time Π_0 normalised by the eigen-value of the Laplace tidal equation λ_{lms} for a g-mode with quantum numbers l, m, and spin parameter S (Aerts et al., 2019),

$$\Delta\Pi_{l,m} = \frac{\Pi_0}{\sqrt{\lambda_{l,m,S}}}. \tag{1.56}$$

If S tends to zero, normalisation by $\sqrt{l(l+1)}$ is recovered.

This introduces a slope in the period-spacings of gravito-intertial modes with a negative gradient for prograde modes, e.g., Fig. 1.22, and a positive gradient for retrograde modes. The TAR allows for the period spacing patterns to be modelled when they show such trends which yields an estimation for the rotation frequency near the core. It is also possible to supplement this measurement with the identification of l and m (e.g., Van Reeth et al., 2016, in a study of 68 γ Doradus stars).

1.2.1.6 Driving the Oscillations

Whether any of the natural modes corresponding to an equilibrium model are excited depends on specific conditions/mechanisms being present to overcome the implied damping to oscillations due to stars being in hydrostatic equilibrium (Handler, 2013)[17]. The assessment of a *driving mechanism's* success in exciting a mode requires computation of its growth rate (Aerts, 2021), which in turn relies on the calculation of the imaginary part of the mode's frequency ω_i. Using the example from Aerts et al. (2010) regarding a particular class of driving mechanisms (see below), then,

$$\omega_i = \frac{1}{2\omega^2} \frac{\int_V \frac{\delta\rho^*}{\rho} \delta(\Gamma_3 - 1)\delta(\rho\epsilon - \nabla\cdot\mathbf{F})\,\mathrm{d}V}{\int_V \rho|\,\mathrm{d}\mathbf{r}|^2\,\mathrm{d}V}, \tag{1.57}$$

[17]Like any musical instrument, you have to do something for the instrument to make a sound.

where "*" denotes the complex conjugate, V is stellar volume, Γ_3 is the third adiabatic exponent, and perturbations to the density $\delta\rho$ and heating $\delta(\rho\epsilon - \nabla \cdot \mathbf{F})$ are given for a Lagrangian reference frame. Here, instability arises when $\omega_i > 0$ so $\delta\rho^*$ and $\delta(\rho\epsilon - \nabla \cdot \mathbf{F})$ have the same sign (Aerts et al., 2010). Therefore, when $\delta\rho^*$ is positive and the system contracts, $\delta(\rho\epsilon - \nabla \cdot \mathbf{F})$ is also positive and heating occurs. This is analogous to a thermodynamic heat engine, which converts thermal energy into mechanical energy, hence giving rise to the *heat engine* class of excitation mechanisms.

The *heat engine* mechanism is responsible for most of the self driven oscillations across the HR diagram; in particular, it is responsible for exciting the oscillations in δ Scuti and γ Doradus stars. The driving of the oscillations via the heat engine mechanism is evidently linked to perturbations in the local flux, i.e., Eq. C.5, via changes in $\mathrm{d}q/\,\mathrm{d}t$, so is a non-adiabatic process. Nevertheless, when the *quasi-adiabatic approximation* is valid (see below), ω_i is calculated using the adiabatic eigen-functions (see Section 1.2.1.2).

In the quasi-adiabatic approximation, assuming L is constant, considering radial oscillations and neglecting convection, the *work integral* (numerator of Eq. 1.57) can be expressed as,

$$W \simeq -L \int_M \frac{\delta\rho}{\rho}(\Gamma_3 - 1)\frac{\mathrm{d}}{\mathrm{d}m}\Big(\frac{\delta L}{L}\Big)\,\mathrm{d}m. \tag{1.58}$$

The work integral expresses the energy gained by a mode over one pulsation period (Cox, 1967, 1974; Aerts et al., 2010). Thus, we have a net gain when W is positive and this requires the gradient in the luminosity perturbation $\frac{\mathrm{d}}{\mathrm{d}m}\Big(\frac{\delta L}{L}\Big)$ to be negative toward the surface during compression, i.e, when $\delta\rho/\rho$ is positive everywhere. In this case, $W > 0$ implies the energy gained by the mode overcomes the energy lost due to damping. A positive gradient would act as a release valve for energy to escape above the layer of interest, contributing to the damping (Cox, 1974); this is often termed radiative damping.

Since $\frac{\mathrm{d}}{\mathrm{d}m}\Big(\frac{\delta L}{L}\Big)$ is usually positive toward the surface, most stars do not show variability (Cox, 1974). However, *precisely* located ionisation zones can lead to a negative gradient, facilitating excitation via the $\kappa - mechanism$. This is because

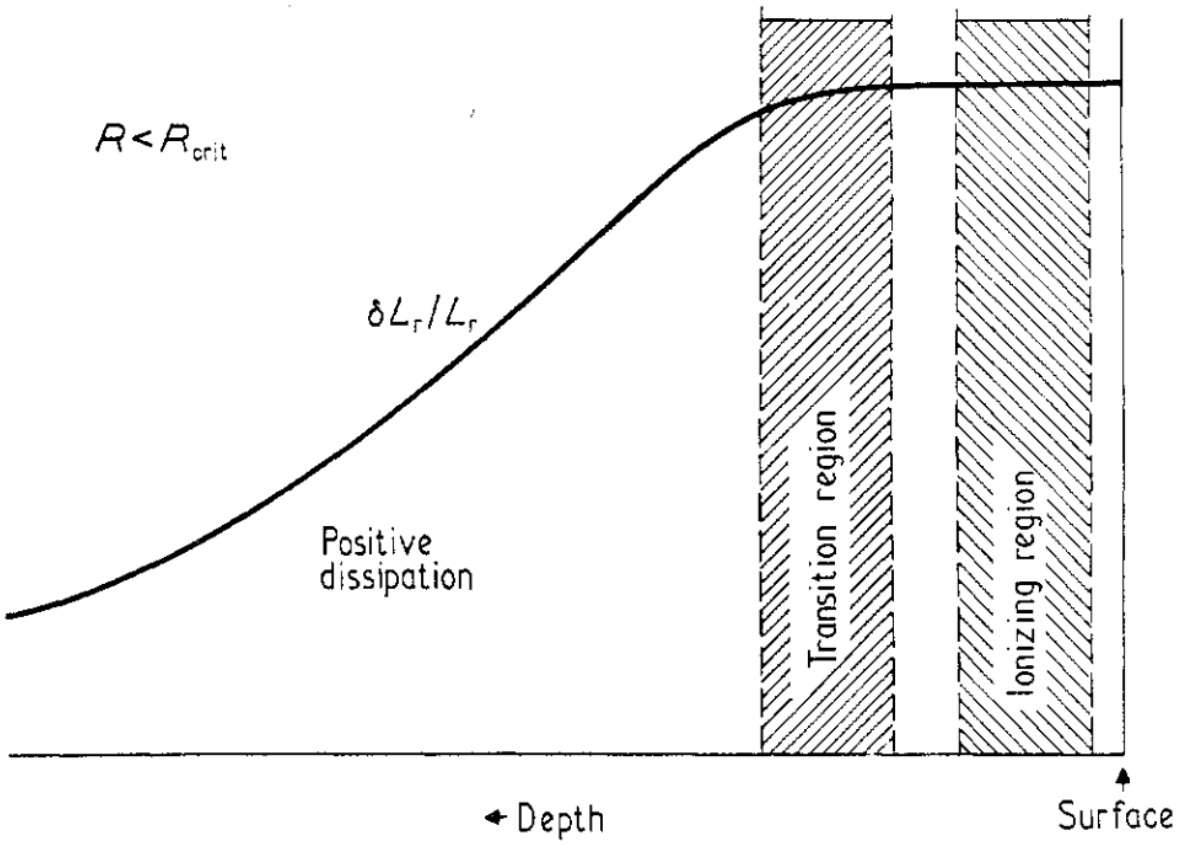

Figure 1.23: $\delta L/L$ against geometrical depth within the star at the instance of minimum stellar radius during a compression. Here, the He+ ionisation zone is located at $R > R_{crit}$. From (Cox, 1974).

the strong increase in opacity associated with ionisation zones acts to decrease the radiative flux (see Eq. C.6). The *precise* location of an ionisation zone required to excite a pulsation mode depends on where the transition occurs between the quasi- and non-adiabatic regions; Eq. 1.58 is a quasi-adiabatic expression.

In a quasi-adiabatic region, the flow of energy over a pulsation period is small compared to the overall energy content of the surrounding layers (Aerts et al., 2010), i.e., deeper layers within the star. In contrast, relatively little energy is stored in the surrounding layers at the surface (Cox, 1974), so the surface layers are non-adiabatic. Since L is effectively *frozen* at the surface due to negligible nuclear energy generation, the

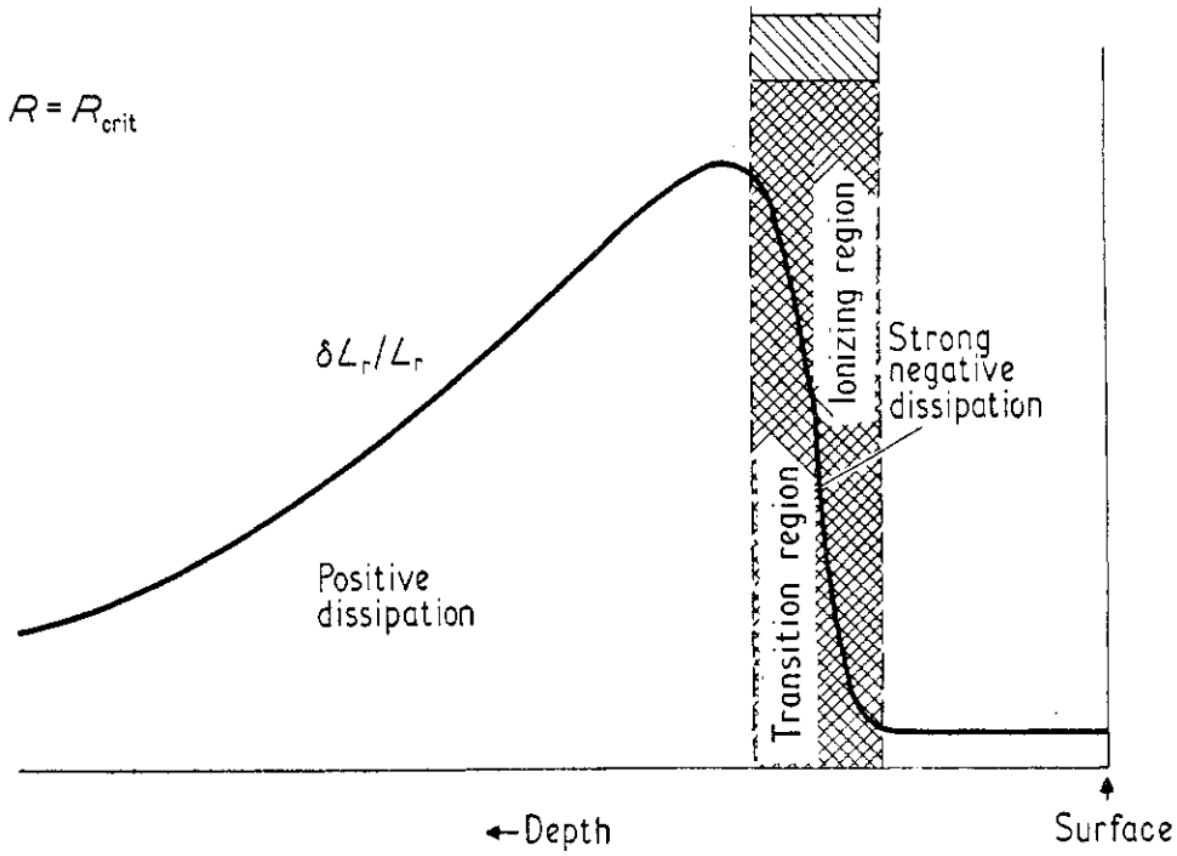

Figure 1.24: Same as Fig. 1.23 except the He+ ionisation zone is located at the critical radius $R = R_{crit}$. From (Cox, 1974).

ionisation zone must be located in the quasi-adiabtic region for it to have any influence on $\frac{\mathrm{d}}{\mathrm{d}m}\left(\frac{\delta L}{L}\right)$ at all (see Fig. 1.23). However, excitation will only occur if the ionisation zone coincides *precisely* with the transition between quasi- and non-adiabatic at R_{crit} because the immediate transition into non-adiabaticity prevents radiative damping by the tendency for $\frac{\mathrm{d}}{\mathrm{d}m}\left(\frac{\delta L}{L}\right)$ to revert back to positive values, i.e., after already being reduced in the lower portion of the ionisation zone; Fig. 1.24 illustrates this elegently.

It is noted that a decrease in Γ_3 can result in a negative perturbation to the luminosity, and excitation, leading to the $\gamma - mechanism$ (Aerts et al., 2010). Furthermore, when the convective time-scale is long compared to the pulsation period, the

convective flux blocking mechanism can contribute to the excitation of modes (Dupret et al., 2004; Handler, 2013); this is important for γ Doradus stars (see Section 1.2.3.2).

1.2.1.7 Instability Domains

Quantifying the arguments in Section 1.2.1.6 allows for domains of instability to be derived for different modes in the HR diagram. If the ratio of thermal energy content surrounding a given layer within a star to the energy radiated by it over a pulsation period Π is given by,

$$\Psi = \frac{< c_v T > \Delta m}{\Pi L}, \tag{1.59}$$

where Δm is the mass of the surrounding layers and $< c_{\rm v} T >$ is a suitable average, then the transition between quasi-adiabatic and non-adiabatic occurs where $\Psi = 1$ (Cox, 1974). This shows that higher frequency modes have transition regions near the surface where the surrounding energy content is small. Thus, given that the ionisation zones are located in shallower layers for earlier type stars, it is no surprise that the range of unstable modes in δ Scuti stars are predicted, and observed, to move to higher frequencies in those with higher $T_{\rm eff}$ (Pamyatnykh, 2000; Dupret et al., 2005; Balona & Dziembowski, 2011; Xiong et al., 2016).

The arguments developed by Cox (1967, 1974), which form the basis of this discussion, refer specifically to Cephieds, but the general principles can be applied wherever convection can be ignored (Aerts et al., 2010); hence the above. However, accounting for the interaction between convection and pulsations is necessary, e.g., for reproducing the red edge of the classical instability strip due to the associated damping effects, such as thermodynamic coupling between convection and oscillations (Xiong et al., 2016).

1.2.2 Probing Stellar Structures

With the theoretical framework established, asteroseismology finds practical applications in observational astronomy. It is essential to first measure the pulsation fre-

quencies before attempting to identify them and draw inferences about the internal structures of stars.

1.2.2.1 Frequency Analysis

Pulsations manifest in time-series observations as brightness, radial velocity, and line profile variations (Handler, 2013). Taking the Fourier transform of these signals allows for the individual frequencies to be decomposed and visualised in a *pulsation amplitude spectrum*. Fig. 1.25 shows the photometric time-series observations of seven *Kepler* slowly pulsating B-type (SPB) stars with their pulsation amplitude spectrum overplotted. Many frequencies combine to yield the overall variable signals in the brightness of the systems, i.e., many oscillation modes are present. The frequencies of the oscillation modes can be extracted by fitting sinusoids via, e.g., least squares minimisation. A technique often employed is to optimise the most dominant frequency, remove it from the signal, and repeat the process on the residuals until a threshold minimum signal to noise (S/N) is reached. This technique is called *pre-whitening*.

The time-base of the observations limits the maximum period of a mode that can be reliably determined and frequencies separated by less than the inverse of the time base (i.e, the Rayleigh frequency) can not be resolved. The highest frequency that can be measured is half the sampling frequency (i.e., the *Nyquist frequency*) (Handler, 2013). Another limitation is that the surfaces of stars can not usually be resolved. The result is *geometric cancellation* which refers to the reduction of the amplitudes of nonradial modes with high spherical degree due to the implied averaging of disc integrated measurements. It can be assumed that modes with $l > 4$ are completely cancelled out (Handler, 2013).

Some of the observed frequencies do not possess asteroseismic significance. For instance, the subtraction of an imperfect eclipse model would result in unwanted artifacts in the Fourier spectrum at harmonics of the orbital frequency, not to be mistaken for tidally induced frequencies. Nonlinear interactions between two or more parent frequencies can lead to *combination frequencies* (Sekaran et al., 2020), but these can

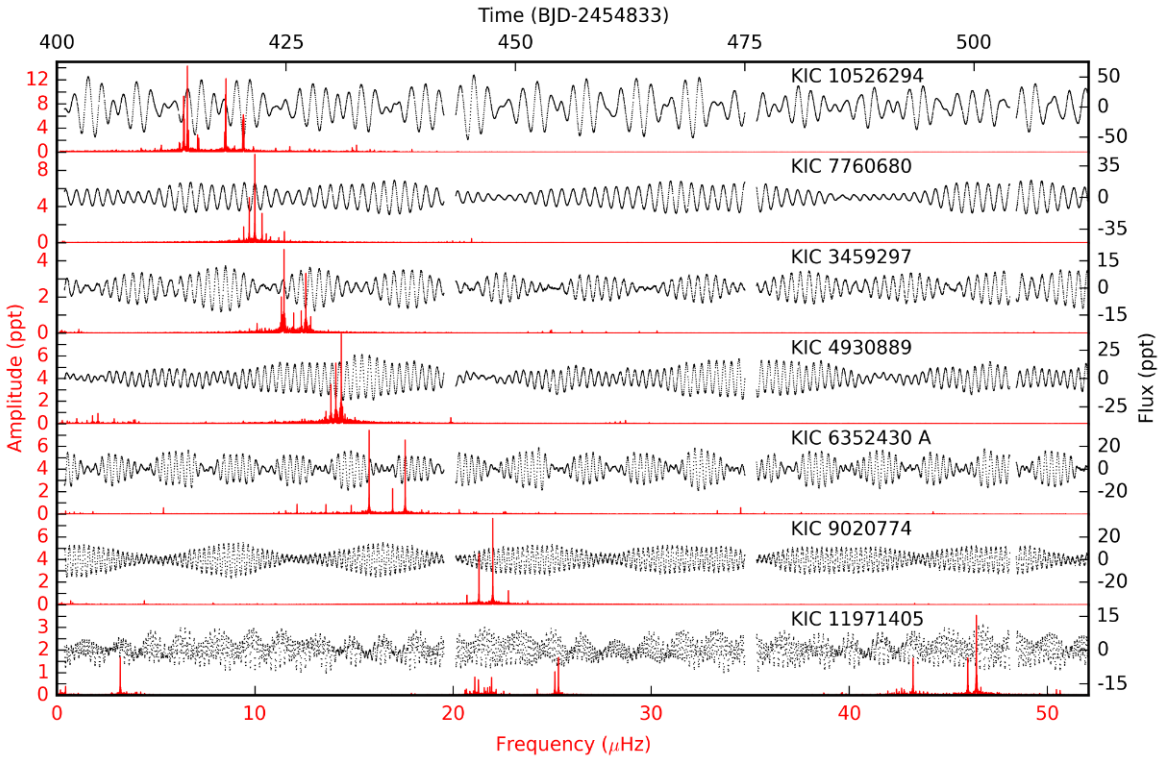

Figure 1.25: 110 d excerpt of the 1500 d long cadence *Kepler* observations (black dots) of seven SPB stars with their KIC identifier shown. Overplotted in red is the amplitude spectrum calculated by taking the Fourier transform of the photometric time-series (more details regarding *Kepler* in Section 2.1.3). The frequency of maximum amplitude increases with the rotation frequency of the star from the top panel to the bottom panel. Figure from Aerts (2021) based on data from Pápics et al. (2017).

also arise without a physical interpretation resulting from the mathematical analysis of frequencies in terms of harmonic functions; to differentiate requires analysing their phase behaviour (Degroote et al., 2009).

1.2.2.2 Scaling Relations

Solar-like oscillations follow simple scaling relations (Ulrich, 1986; Aerts, 2021) based on the large frequency separation $\Delta\nu$ (Eq. 1.52) and the frequency of maximum power $\nu_{\max}$. These observables are readily available once the frequency spectrum has been measured, without having to identify the modes. The scaling based on $\Delta\nu$ follows,

$$\frac{\Delta\nu}{\Delta\nu_{\odot}} = \Big(\frac{M}{\mathrm{M}_{\odot}}\Big)^{1/2}\Big(\frac{R}{\mathrm{R}_{\odot}}\Big)^{-3/2}, \tag{1.60}$$

and for $\nu_{\max}$,

$$\frac{\nu_{\max}}{\nu_{\max,\odot}} = \Big(\frac{M}{\mathrm{M}_{\odot}}\Big)\Big(\frac{R}{\mathrm{R}_{\odot}}\Big)^{-2}\Big(\frac{T_{\mathrm{eff}}}{T_{\mathrm{eff},\odot}}\Big)^{-1/2}. \tag{1.61}$$

This procedure assumes the same physics as the sun (Lampens, 2021) so does not allow for discernment among different theories. However, assuming that solar-like stars do indeed share similar physics as the sun, then a measurement of T_{eff}, $\Delta\nu$ and $\nu_{\max}$ means seismic masses and radii are readily available for use in various fields of astrophysics (Aerts, 2021). Model dependent seismic ages follow using M and R as described in Section 1.1.5.2.

1.2.2.3 Mode Identification

A crucial step in asteroseismology is the successful identification of the oscillation modes (Guo et al., 2019), i.e., determining the radial order n, degree l, and azumithal order m for the observed modes.

Échelle diagrams are often used to identify l and n by plotting the frequencies as a function of their modulus with respect to $\Delta\nu$; modes of the same l line up along quasi-vertical ridges (e.g., Chaplin & Miglio, 2013). For δ Scuti stars, these ridges

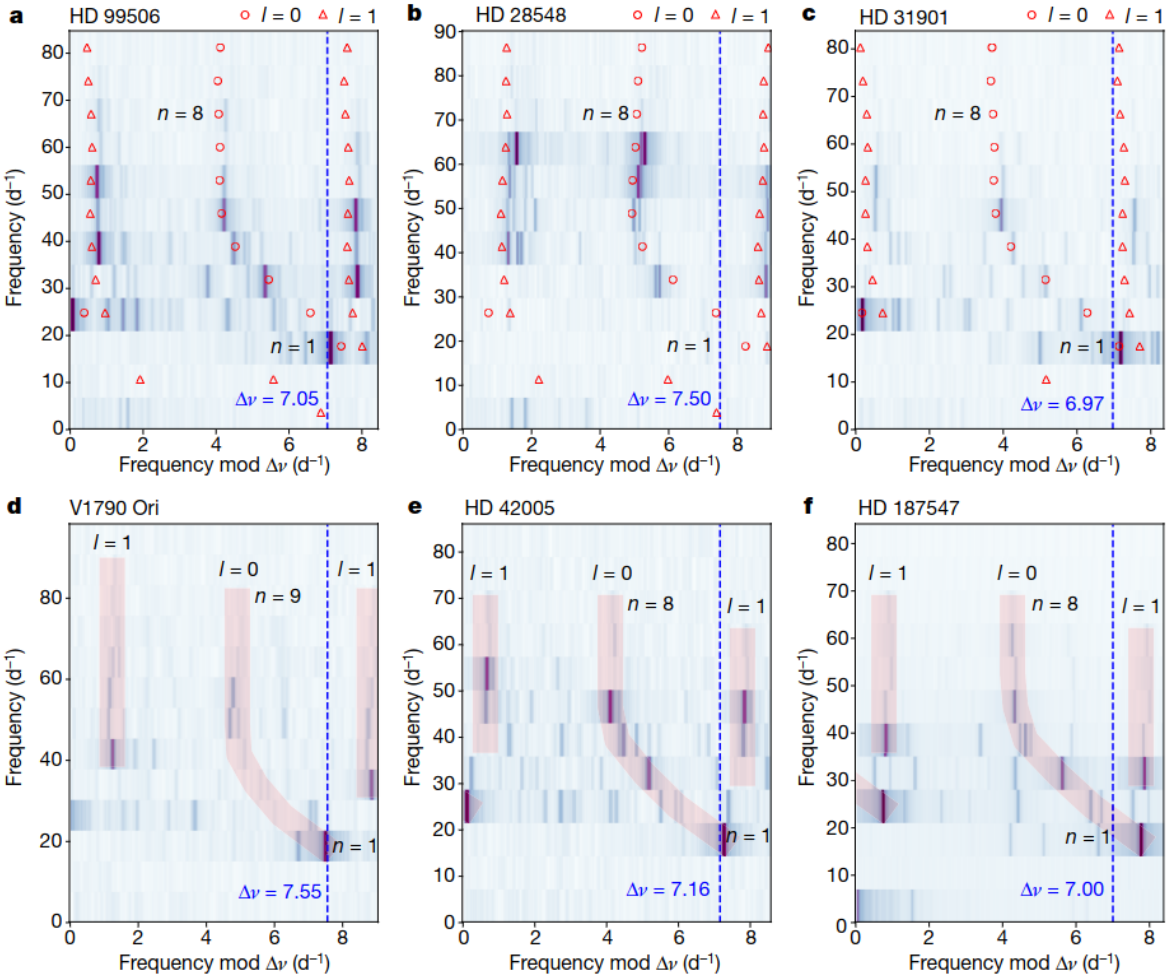

Figure 1.26: Mode identification using échelle diagrams for six δ Scuti stars with their names labelled. The greyscale shows the observed échelle amplitude spectrum. Red symbols (rows a-c) are values calculated from models which which allow mode identification in other stars, e.g., rows d-f. From Bedding et al. (2020).

display curvature owing to departures of their low-order modes from the asymptotic regime (e.g., Fig. 1.26; Bedding et al., 2020).

Detection of a complete rotationally split multiplet immediately reveals l and m. Also, recall from Section 1.2.1.5 that the sign of the gradient in a period-spacing diagram reveals the sign of m and that both l and m can be derived simultaneously

with the near-core rotation using the TAR framework (Van Reeth et al., 2016).

Photometric mode identification entails analysing the amplitude differences and phase behaviour of modes in different photometric filters since these relationships depend on l. This method requires multi-colour observations and only l can be identified.

Spectral line profiles are rotationally broadened which allows the stellar surface to be reconstructed by *Doppler imaging*. Pulsations add additional components of velocity (Doppler shift) and this leads to *line profile variations*. The shape of the distorted line profile depends on the resulting velocity field of the contributing modes. Spectroscopic mode identification fits theoretically calculated 3D velocity fields to the observed line profles to identify l and m (Handler, 2013). Spectroscopic data is less sensitive to geometric cancellation effects so modes of higher degree can be identified than with photometric data.

1.2.2.4 Modelling Period Spacings

Structural glitches in the deep interior, also termed *buoyancy glitches*, lead to sharp features in the Brunt-Väisälä frequency. Using the ideal gas equation (Eq. C.17), the Brunt-Väisälä frequency can be expressed as,

$$N^2 = \frac{g^2\rho}{p}(\nabla_{\rm ad} - \nabla + \nabla_\mu), \tag{1.62}$$

which depends on the molecular gradient ∇_μ (Aerts et al., 2010). The buoyancy travel time Π_0 depends on the detailed shape of N (Moravveji et al., 2015) so high order g modes are affected by ∇_μ (see Eq. 1.54). This results in substructures in the period-spacing patterns; an example is given in Fig. 1.22, which also shows the effect of rotation.

Miglio et al. (2008) expanded on the analysis of Tassoul (1980), finding that molecular gradients manifest in the period-spacing patterns as recurring quasiperiodic deviations. The amplitude of the deviations was found to be linked to the steepness of the chemical gradient, while the periodicity is related to its location (Van Reeth et al., 2016). Bouabid et al. (2013) confirms that the inclusion of mixing acts to partially

reduce the gradient so this decreases the amplitude of the deviations (Van Reeth et al., 2016). Modelling these trends offers a less exacting way to obtain constraints on such processes compared to a full blown modelling of every individual frequency.

This was exploited by Moravveji et al. (2015) to determine that the inclusion of extra diffusive mixing above the overshoot region is essential to explain the structure in the observed period spacing pattern of KIC 10526294, as well as deducing the most appropriate overshoot profile $D_{\rm ov}$; an exponentially decaying prescription was found to be more appropriate than a step-function. Modelling the period-spacing patterns of g modes has also led to an increasing number of stars that have both the surface and near-core rotation rates measured (Aerts et al., 2017, 2019; Salmon et al., 2017) (see Section 1.2.1.5), revealing angular momentum history (Guo et al., 2019).

Following the first detection of period-spacing patterns in CoRoT photometry by Degroote et al. (2010), many studies involving the detection and modelling of period-spacings have been published (e.g., Kurtz et al., 2014; Saio et al., 2015; Sekaran et al., 2020; Bedding et al., 2015; Van Reeth et al., 2015a; Ouazzani et al., 2017; Pápics et al., 2017; Mombarg et al., 2019; Li et al., 2019, 2020a). Modelling the observed period-spacing patterns with theoretical models (e.g., Schmid & Aerts, 2016; Sekaran et al., 2020) provides stronger constraints on stellar structure compared to fitting for Π_0 (Ouazzani et al., 2019; Mombarg et al., 2020; Sekaran et al., 2020).

1.2.2.5 Modelling Frequencies

In Section 1.2.1.2, it was discussed how seeking agreement between observed and theoretical oscillation frequencies constrains the free parameters of a stellar model. Considering every oscillation frequency in the seismic modelling is a more exacting diagnostic than modelling the period spacing patterns because the frequencies are not considered independent. Instead, they constitute a single parameter Y (Aerts et al., 2018). Since each frequency has a different propagation cavity, accurately predicting every frequency simultaneously requires accurate understanding of the entire star, particularly if the star oscillates in a broad range of frequencies.

This makes modelling the oscillation frequencies a powerful diagnostic for constraining our interpretation of processes occurring throughout the full interior by including the free parameters that describe these processes in the modelling. For example, since convection contributes to the damping, excitation and trapping of modes (see Section 1.2.1.3; Bowman et al., 2016; Aerts, 2021), modelling the full set of frequencies could yield constraints on $\alpha_{\rm ml}$ (e.g., Viani et al., 2018), which is expected to vary significantly over the δ Scuti mass range. This is in addition to the constraints obtainable from modelling the period spacing patterns of g modes, e.g., on overshoot profiles and the associated mixing above the overshoot region (Kippenhahn et al., 2013; Aerts et al., 2018). The latter is affected by rotational, magnetic and pulsational effects which may influence mixing in radiative regions well above the convective core. Accounting for such effects is an improvement on simplifications where mixing is assumed only to occur in convective regions (see Appendix C.5), and such improvements have revealed information about angular momentum transport in radiative regions (Moravveji et al., 2015; Triana et al., 2015; Aerts et al., 2018).

The heightened sensitivity of the individual oscillation frequencies to conditions where they are trapped makes them ideal for discriminating among different choices of input physics in different regions of the star. If the modes are stable to the Schwarzchild criterion but not the Ledoux criterion (see Appendix C.4), a transition between the adiabatic and radiative temperature gradient might be appropriate; this leads to *semi-convection* and might be expected at the transitions between convective and radiative regions (Aerts et al., 2010, 2018; Aerts, 2021). Opacity and chemical mixtures are components of the micro-physics that were shown by Moravveji et al. (2015); Aerts et al. (2018) to have a significant effect on the oscillation frequencies for both pressure and gravity modes. Additionally, microscopic diffusion consists of gravitational settling, concentration diffusion, thermal diffusion and radiative levitation (Aerts et al., 2018), and influences the pulsations zones through their influence on convection zones. Such microscopic processes probably do not have a discernible impact in the HR diagram.

To assess such input physics of a stellar model, one can repeat the pulsation modelling for varied theories and compare the results. Uncertainty in the input physics

obviously leads to uncertainty in the theoretically predicted frequencies. Limitations associated with using 1D equilibrium structures, the absence of magnetic and centrifugal forces as well as higher order terms in the perturbations being neglected, adds to this uncertainty. Thus, retaining higher orders in the perturbations in the oscillation equations, or the accurate integration of 2D structure models is desirable. Indeed, 2D structure models are currently the frontier of asteroseismology and progress is advancing (Guo et al., 2016). In any case, there is uncertainty on both sides of the modelling which introduces *heteroskedasticity*. Another complication arises because the free parameters might be strongly correlated. The Mahalanobis distance (Aerts, 2021) is a more sophisticated merit function compared to using the χ^2 and better accounts for these complications (Aerts, 2021). However, constraints from binarity are particularly effective in breaking degeneracies among parameters of the seismic models...

1.2.3 Classes of Pulsating Stars

Different seismic diagnostics exploit different types of oscillation modes (p modes, g modes, high-order asymptotic modes, etc...) and different modes have different probing capabilities. The presence of different oscillation modes depends on the type of star and its position in the HR diagram. Thus, the capabilities of seismic tools depend on the class of pulsator and its evolutionary status (Steindl et al., 2021). It works in the favour of asteroseismology that pulsations occur across the entire HR-diagram and at all evolutionary stages because this allows for all the available tools to be exploited.

Fig. 1.27 shows the different regions of instability in the HR diagram that correspond to different classes of pulsator and Table 1.1 gives an overview of the classes of pulsator shown in Fig. 1.27. Here, we are concerned with the δ Scuti and γ Doradus classes of pulsators. From Fig. 1.27, there is a clear overlap in their domains of instability, so we also discuss δ Scuti/γ Doradus hybrids.

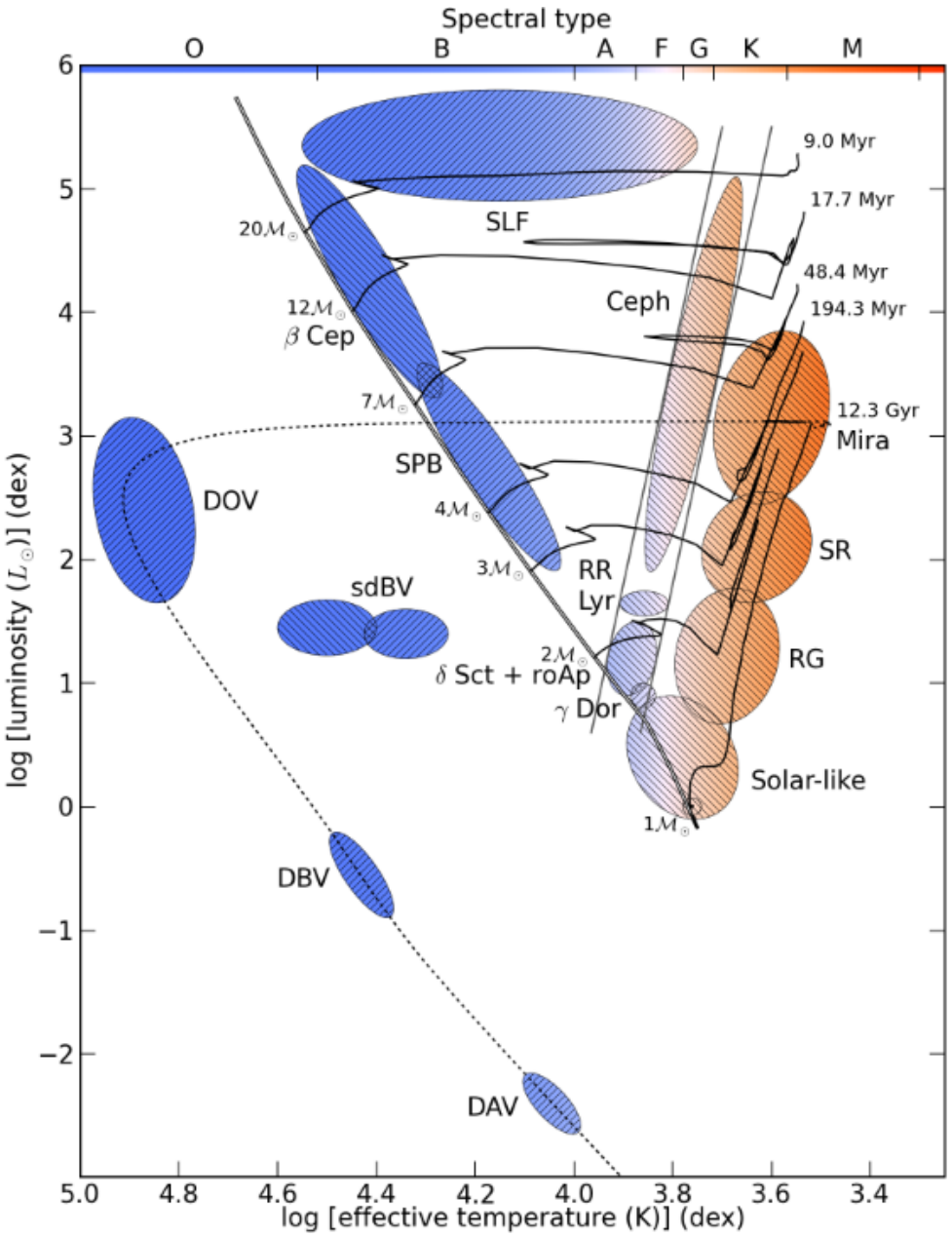

Figure 1.27: Pulsation HR-diagram from Aerts (2021).

Table 1.1: Basic overview of the classes of pulsator from Handler (2013).

Name Approx.	Periods	Discovery/Definition
Mira variables	100 – 1000 d	Fabricius (1596)
Semiregular (SR) variables	20 – 2000 d	Herschel (1782)
δ Cephei stars	1 – 100 d	1784, Pigott, Goodricke (1786)
RR Lyrae stars	0.3 – 3 d	Fleming (1899)
δ Scuti stars	0.3 – 6 h	Campbell & Wright (1900)
β Cephei stars	2 – 7 h	Frost (1902)
ZZ Ceti stars (DAV)	2 – 20 min	1964 Landolt (1968)
GW Virginis stars (DOV)	5 – 25 min	McGraw et al. (1979)
Rapidly oscillating Ap (roAp) stars	5 – 25 min	1978, Kurtz (1982)
V777 Herculis stars (DBV)	5 – 20 min	Winget et al. (1982)
Slowly Pulsating B (SPB) stars	0.5 – 3 d	Waelkens & Rufener (1985)
Solar-like oscillators	3 – 15 min	Kjeldsen et al. (1995)
V361 Hydrae stars (sdBVr)	2 – 10 min	1994, Kilkenny et al. (1997)
γ Doradus stars	0.3 – 1.5 d	1995 Kaye et al. (1999)
Solar-like giant oscillators	1 – 18 hr	Frandsen et al. (2002)
V1093 Herculis stars (sdBVs)	1 – 2 hr	Green et al. (2003)

1.2.3.1 δ Scuti

The δ Scuti class of pulsator was identified early because δ Scuti stars are relatively numerous and luminous (Breger, 1979; Rodríguez et al., 2000; Guo et al., 2019). Their relatively short pulsation periods, ranging from 15 min to 8 h (Uytterhoeven et al., 2011; Aerts et al., 2010), has resulted in the currently known number of δ Scuti pulsators being higher than other classes because the detection of a full period of oscillation does not require long stretches of continuous observation (Kahraman Aliçavuş et al., 2017; Liakos & Niarchos, 2017; Lampens, 2021; Kahraman Aliçavuş et al., 2022). The position of the δ Scuti class is indicated in Fig. 1.27 at the intersection of the lower part of the classical Cepheid instability strip and the main-sequence (Breger, 2000; Dupret et al., 2005; Liakos & Niarchos, 2017; Miszuda et al., 2021). Spectral types range from A0 – F5 and they are typically in the the main-sequence of evolution (Miszuda et al., 2021, 2022), however, there are known cases of δ Scuti stars evolving through

the Hertzsprung gap and in the pre-MS phase (e.g. Rodríguez et al., 2000; Dupret et al., 2005; Aerts et al., 2010; Liakos & Niarchos, 2017; Murphy, 2018; Murphy et al., 2019). The masses of δ Scuti stars range from about $1.5-2.5\,M_{\odot}$ (Yang et al., 2021; Hong et al., 2022), which places them in the transition region between lower mass stars with thick outer convection zones and massive stars with thin outer convection zones (Bowman, 2017; Bowman & Kurtz, 2018; Yang et al., 2021).

Their pulsations are generally low-order, nonradial pressure modes excited via the κ-mechanism. As explained in Section 1.2.1.6, the κ-mechanism is responsible for driving the oscillations when a significant perturbation in the radiative flux results from a strong increase in the opacity. For δ Scuti stars, the partial ionisation zone of He II is responsible for the increased opacity and driving most of the oscillation modes (Pamyatnykh, 1999; Breger, 2000; Antoci et al., 2014; Murphy et al., 2020). However, higher-order, nonradial pulsations have also been observed in δ Scuti stars, e.g., τ Peg (Kennelly et al., 1998), and the κ-mechanism may not be sufficient in explaining the excitation of these modes; such modes may be explained by excitation due to the turbulent pressure in the hydrogen convective zone (Antoci et al., 2014; Grassitelli et al., 2015). The current understanding of the excitation mechanisms acting in δ Scuti stars has resulted in theoretical predictions for the range of unstable modes, calculated from models with current opacities, that agree with observations (Pamyatnykh, 2003; Dupret et al., 2005; Casas et al., 2009; Zwintz et al., 2014; Kahraman Aliçavuş et al., 2022). However, constant stars, i.e., not pulsating, do exist in the δ Scuti instability strip. Many of such stars are Am stars showing peculiar element abundances. The radiative levitation and diffusive settling believed to cause these peculiarities may deplete He from the δ Scuti driving region and damp the modes (Guo, 2021); other explanations are associated with binarity,

Although the understanding of the pulsations in δ Scuti stars is generally good, performing asteroseismology using δ Scuti stars (i.e., using the pulsations to infer global and interior properties) is less advanced and the main reason for this is the difficulties associated with identifying the modes (Breger, 2000; Bowman & Kurtz, 2018; Murphy et al., 2021; Guzik, 2021); mode identification is a preliminary step for seismic mod-

elling. Mode identification relies heavily on recognising patterns (Guo et al., 2019), which is challenging for δ Scuti stars because the frequency spectra are rich and messy (Goupil et al., 2005; Handler, 2009b; Yang et al., 2021). Fast rotation leads to overlapping of rotationally split multiplets and the low order p modes do not follow the regular asymptotic frequency spacings. A recent breakthrough is the discovery that *some* δ Scuti stars *do* pulsate in regular patterns that form ridges in an échelle diagram (e.g., Bedding et al., 2020, see Fig. 1.26); this allows mode identification similar to the case of solar-like oscillations (see Fig. 1.26) but is only possible for some δ Scuti stars close to the ZAMS (Zero-Age Main-Sequence), including the pre-MS (Murphy et al., 2021). Pairs of low-order radial modes can have period ratios that allow those modes to be identified (Petersen & Christensen-Dalsgaard, 1996; Murphy et al., 2021) but the method can only be used if each corresponding mode is driven to observable amplitudes; this is not always the case in δ Scuti stars.

Having identified some of the oscillation modes in δ Scuti stars, further difficulty in their modelling arises due to their relatively fast rotation, which generally requires two-dimensional equilibrium structure models to account for the distortion (Guo et al., 2016); the calculation of 2D models in the presence of rotation comes with major uncertainty (Aerts, 2021). Examples of 2D modelling of δ Scuti stars are, e.g, Deupree (2011); Deupree et al. (2012). Alternatively, sticking with 1D models, the rotation can be treated by perturbations to second order, e.g., Suárez et al. (2005). As stated above, the modes are low order p modes, meaning they are not in the asymptotic regime; nevertheless, Suárez et al. (2014) showed that an *average* large frequency separation $\Delta\nu$ can be determined and used to derive the mean density (Guzik, 2021). Further characterisations of single δ Scuti stars are presented in e.g., Casas et al. (2009); Zwintz et al. (2014); Chen et al. (2016). See Guzik (2021) for a review of discoveries with δ Scuti variable stars from the *Kepler* era.

1.2.3.2 γ Doradus

The γ Doradus stars were identified as a class of pulsator in the late 20th century (Breger & Beichbuchner, 1996; Kaye et al., 1999; Guo et al., 2016). They share a similar domain in the HR diagram as the δ Scuti stars (see Fig. 1.27), but with a narrower mass regime of $1.4-2.0$ $M_{\odot}$, near the red edge of the classical instability strip. They show low frequency light variations (Kaye et al., 1999; Yang et al., 2021) due to high-order g modes with pulsation periods between $0.3-3$ days (Guo et al., 2016), which are believed to be excited by the interaction between convection and pulsations (Guzik et al., 2000; Dupret et al., 2005; Grigahcène et al., 2010; Hong et al., 2022); i.e., the convective flux blocking mechanism at the base of the convective envelope (see section 1.2.1.6).

The g modes of γ Doradus stars are in the gravito-inertial regime ($S \gtrsim 1$), so are subject to both buoyancy and Coriolis forces (Guzik, 2021). This is due to the fast rotation of intermediate mass stars, in general, and the relatively low frequencies of the g modes. Therefore, they should be treated in the TAR framework, which necessitates that rotation is included as a free parameter in the modelling of their frequencies. Since g modes predominantly trace the radiative regions near the convective core, near-core rotation rates can be derived for γ Doradus stars (Zhang et al., 2020). Indeed, γ Doradus stars are also suited for constraining parameters such as $D_{\rm ov}$ and $D_{\rm ext}$ (see Section 1.2.2.5).

Individual frequencies in γ Doradus stars are not generally exploited because of the difficulty in modelling the interaction between convection and oscillations (Guo et al., 2019). Therefore, seismic modelling is carried out using the period-spacings in the merit function instead (Saio et al., 2015; Schmid & Aerts, 2016); γ Doradus stars are amenable to revealing period-spacing patterns due to their *high-order* g modes being in the asymptotic regime (Guo et al., 2019). The diagnostics associated with modelling the non-uniform period-spacing patterns (see Section 1.2.2.4) has revealed information regarding the inner chemical composition, chemical composition gradients, diffusive mixing, evolutionary status (e.g. Miglio et al., 2008; Moravveji et al., 2015;

Sekaran et al., 2021; Yang et al., 2021), core rotation rates (e.g., Bouabid et al., 2013; Bedding et al., 2015; Saio et al., 2015; Van Reeth et al., 2016; Ouazzani et al., 2017) and coupling between g modes and inertial modes (e.g., Ouazzani et al., 2020; Saio et al., 2021) for many γ Doradus stars. Thus, the γ Doradus class of pulsators have proven to be of considerable seismic value.

1.2.3.3 Hybrids

Stars exhibiting oscillation modes characteristic of two different classes of pulsator are called hybrids (Handler & Shobbrook, 2002) and the overlap of the δ Scuti and γ Doradus instability strips supports the existence of hybrids among these classes (Breger & Beichbuchner, 1996; Handler & Shobbrook, 2002; Yang et al., 2021). Several δ Scuti/γ Doradus hybrids had been detected from the ground (e.g., Handler & Shobbrook, 2002; Handler, 2009a) but it wasn't until space missions such as CoRoT (Baglin et al., 2008) and *Kepler* that it was realised hybrid behaviour might be common (Grigahcène et al., 2010). This is because the unprecedented precision and continuous monitoring of these space missions has allowed for the detection of low-amplitude and low-frequency oscillations that were otherwise undetected. Furthermore, the overlapping region in early calculations of the δ Scuti and γ Doradus instability domains by Dupret et al. (2005) did not span a very broad range in $T_{\rm eff}$, so hybrids were expected to be rare.

Later calculations by Xiong et al. (2016) predicted a much broader overlapping region which conforms better with the findings from studies utilising data from space. For example, most of the *Kepler* objects in the study by Grigahcène et al. (2010) show hybrid nature from their rich pulsation spectra; Uytterhoeven et al. (2011) used a sample of 750 *Kepler* A-F stars and found that 63% are either δ Scuti or γ Doradus and 35% are hybrids; a similar study on a larger sample by Bradley et al. (2015) also suggests hybrids are very common and Balona et al. (2015) showed that low-frequencies are present in most δ Scuti stars observed by *Kepler*. These studies suggest that hybrid behaviour is normal in these stars and that, potentially, all δ Scuti stars exhibit low-frequency pulsations (Balona, 2010; Guo et al., 2019).

This is important because hybrids have great potential for asteroseismology (Schmid & Aerts, 2016). The p modes probe the stellar envelope while the g modes carry information about the near core regions (Yang et al., 2021; Grigahcène et al., 2010; Kurtz et al., 2014; Saio et al., 2015). Specifically, diagnostics applicable to δ Scuti stars can be combined with diagnostics applicable to γ Doradus stars. The presence of both types of oscillations also means different driving mechanisms that operate in different regions can be studied or reviewed simultaneously (Hong et al., 2022). Xiong et al. (2016) show that both the κ-mechanism and the coupling between convection and oscillations both play a major role in the excitation of δ Scuti stars and γ Doradus stars, with the former mainly for warmer δ Scuti stars and the latter for cooler δ Scuti and γ Doradus stars. This leads to the conclusion that there is no substantial difference between the excitation mechanisms among these stars. Then the slight offset of the γ Doradus instability strip compared to the δ Scuti instability strip in the study by Xiong et al. (2016) only arises due to p modes being of higher frequency, and higher frequencies are more likely in stars with higher $T_{\rm eff}$ as discussed in Section 1.2.1.6).

Hybrid δ Scuti/γ Doradus stars are the key to improving our knowledge regarding mode excitation mechanisms in intermediate mass stars and we need a statistically large sample to make the advancement (Guo et al., 2016). This would aid a better understanding of the effects of convection, rotation, tidal interactions, and nonlinearity on pulsations.

1.3 Pulsators in Eclipsing Binary Systems

Since the majority of stars belong to a binary or multiple system (Lampens, 2021), we must think of a pulsating star in a binary as the "normal" situation. It is well known that binarity and, in particular, g mode asteroseismology complement each other and there are a number case studies exploiting this (e.g., Maceroni et al., 2009, 2013; Welsh et al., 2011; Chapellier & Mathias, 2013; Debosscher et al., 2013; Hambleton et al., 2013; Keen et al., 2015; Schmid et al., 2015; Schmid & Aerts, 2016; Matson et al., 2016; Zhang et al., 2020; Guo & Li, 2019; Guo et al., 2017a,b, 2019; Sekaran et al., 2020, 2021). DLEBs with a pulsating component are especially useful but challenging objects to study.

1.3.1 Complementary Methods

Seismic masses and radii can be derived for ensembles of solar-like oscillators because the scaling relations do not require modes to be identified. For solar-like oscillators existing in DLEBs, the independent and reliable measurements of the masses and radii derived using conventional methods provide a way of determining the accuracy and reliability of those derived from scaling relations, and thus their usefulness. Themeßl et al. (2018) measured dynamical and seismic properties of pulsating red-giants; they confirmed that the scalings are accurate when accounting for an empirically derived value for the large frequency separation.

Sekaran et al. (2021) measured the fundamental parameters of the components in the pulsating EB KIC 9850387 using conventional methods, as well as measuring Π_0 and $\Delta P_{\rm n,l}$ of the $l = 1$ and $l = 2$ period-spacing patterns. The authors carried out evolutionary modelling based on the fundamental properties, as well as a purely seismic modelling of the period spacings. They find that binarity yields stronger constraints on the *conventional* properties, e.g., $M, R, T_{\rm eff}, \log(g)$, while the modelling of g mode period spacings yields stronger constraints on the *internal* properties, e.g., the convective core mass $M_{\rm cc}$, overshooting parameter $f_{\rm ov}$, and mixing in the envelope $D_{\rm mix}$.

These findings demonstrate how the two data sets complement each other; each data set provides stronger constraints for different types of stellar parameters.

DLEBs have been used to obtain constraints on overshooting in intermediate- and high-mass stars (see Section 1.1.5.4). Since the net effect of overshooting is to increase the convective core mass so the star appears brighter, it is degenerate with stellar mass and classical constraints from binary systems are unable to distinguish between different overshoot profiles (Sekaran et al., 2021). The presence of g modes in these systems extends the analysis capabilities, enabling for the discrimination between different overshoot prescriptions, such as step overshooting (also termed convective penetration) and diffusive exponential overshooting. (e.g., Moravveji et al., 2015, as outlined in Section 1.2.2.4 and Section 1.2.2.5).

Guo et al. (2017b) and Guo & Li (2019) found that the short-period EBs KIC 9592855 and KIC 7385478 both contain a γ Doradus pulsator that is tidally synchronised at the surface as well as the near-core region. Guo et al. (2019) determined that KIC 4142768 has a slowly-rotating core and a sub-psuedo-synchronous slow-rotating surface. Such measurements allow for the calibration of the time-scales for synchronisation at the surface compared to the core, and thus the time-scales associated with angular momentum transport, which further aids in the discrimination among angular momentum transport theories. Van Reeth et al. (2018) finds that differential rotation is stronger in binary stars. They hypothesise that angular momentum transport between the stars rotation and the orbit of the binary is facilitated by coupling between the tides and g modes, and this induces differential rotation. This study of pulsations in binary stars provides evidence that g modes participate in angular momentum transport.

1.3.1.1 Constraining Models

Assuming the complete set of conventional constraints derived from EBs, i.e., $M, R, T_{\rm eff}$, [Fe/H] (see Section 1.1.5.2), a successful model needs to simultaneously predict the radii and $T_{\rm eff}$s of the components for their measured masses, whilst also satisfying the imposition of coevality (single age and metallicity). If one of the components in the binary

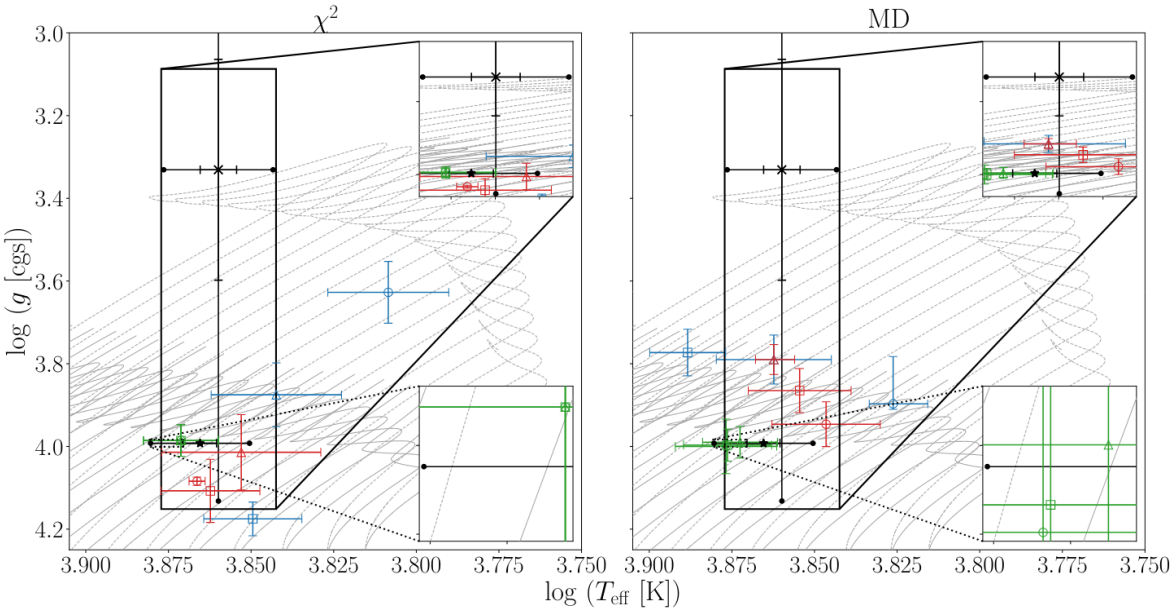

Figure 1.28: The resulting positions of the best fitting models from modelling the $l = 1$ and $l = 2$ period-spacings of KIC 9850387 in a Kiel diagram from the study by Sekaran et al. (2021). The main plots show the full grid, and the insets show the resulting grids after imposing spectroscopic constraints (solid box) and dynamical constraints (dotted box). Results obtained from imposing $\Delta P_{l=1}$ and $\Delta P_{l=2}$ separately are shown by blue and red symbols, respectively, and green symbols when they were imposed together. Results from the full grid, spectroscopic grid, and dynamical grid are are indicated by circles, triangles and squares. *Left panel*: results of using a χ^2_{red} merit function and *right panel*: results of using an MD merit function. Grey curves are MESA evolutionary tracks with input parameters described in Sekaran et al. (2021). The error bars on the asteroseismic solutions are based on 68% HPD intervals of the Monte Carlo parameter distributions. Figure from Sekaran et al. (2021).

is pulsating, it is possible to simultaneously model the pulsations; the model, coupled to a pulsation code, must additionally predict the observed frequencies or period spacing patterns to within the observational error. The binary measurements isolate the location of the objects in the HR diagram and this leads to an exacting constraint on the seismic component of the modelling. Conversely, the seismic constraints eliminate any remaining elements of model flexibility (e.g., non-conventional parameters) which act to lessen the strength of model comparison tests (see Section 1.1.5.2).

Fig. 1.28 shows the size of the parameter space of the resulting evolutionary model grids after imposing spectroscopic constraints and binary constraints compared to the full grid used in the purely seismic analysis by Sekaran et al. (2021). The resulting grid based on binary constraints is significantly smaller, even compared to the grid resulting from spectroscopic constraints. Indeed, binary constraints are more effective than those that can be obtained for single stars, even when considering the luminosity which can be derived for single stars (Sekaran et al., 2020) from asterometric data provided by *Gaia* (Gaia Collaboration et al., 2016; Gaia Collaboration, 2018, 2021). With binary constraints, the conventional properties are effectively eliminated from the investigation, allowing for the intricate details of the model to be tuned more accurately using the pulsation signatures.

The accuracy of a model required to successfully predict seismic observables when binary constraints are imposed was demonstrated in the analysis of KIC 10080943 by Schmid et al. (2015). This system was non-eclipsing so the complete set of binary constraints were not available; only the imposition of coevality and the observed mass-ratio could be used to constrain the seismic modelling. That said, the authors were still not able to simultaneously predict the p modes and g mode period-spacings as well as satisfying those constraints (Lampens, 2021).

Isolating the location of the objects in the HR diagram dramatically reduces the parameter space in the seismic modelling, but since degeneracies exist among the free parameters of the models (e.g., Valle et al., 2017), one might still expect an undesired number of solutions. However, this is not the case because the binary constraints also act to alleviate these degeneracies and the use of seismic diagnostics to constrain stellar

theory is significantly improved, as shown by Johnston et al. (2019a).

1.3.1.2 Mode Identification

Since we can resolve the surfaces of pulsating stars in EBs during the eclipses, we can identify the spherical wave numbers l and m of the nonradial modes by exploiting the screening effect (using the spatial filtration or the dynamic eclipse mapping method Gamarova et al., 2003, 2005; Bíró & Nuspl, 2011; Lampens, 2021), allowing for a comparison between observed and predicted pulsation modes.

Fuller et al. (2020) modelled the stellar response to the static tide, obtaining *tidally influenced* oscillation frequencies as well as perturbed eigenfunctions. The perturbed eigenfunctions are found to be trapped at the pole, equator, or some intermediate lattitude (Guo, 2021). The associated amplitude and phase modulation of the modes can be modelled and used as a mode identification method (e.g., Section 4.7).

1.3.2 The effect of Tides on Pulsations

Binarity implies several phenomena that interact with pulsations, which offer the opportunity to further our understanding of pulsations by investigating the influence of these effects on their behaviour. Such effects concern mass transfer, which modifies the structure in the envelope, and tides. Tidal effects can be classified into two categories. The non-wavelike equilibrium tide causes a global, static deformation whereas the wave-like dynamical tide causes a harmonic tidal forcing with an associated angular frequency (Polfliet & Smeyers, 1990; Remus et al., 2012). The former *influences* self driven pulsations while the latter *excites* pulsations (see Guo, 2021, for a review of tides and mass transfer on pulsations in close binaries). We do not discuss mass transfer given that here we are interested in *detached* configurations.

1.3.2.1 The Equilibrium Tide and Pulsations

The *static* tide is associated with close binaries with circularised and synchronised orbits. The associated deformation to the shape of the star may also imply deformation of the pulsation cavity, changing the equilibrium properties that the pulsations are derived from and modifying their eigen-functions (Polfliet & Smeyers, 1990). These are *tidally perturbed pulsations* (TPPs) and were predicted theoretically by Reyniers & Smeyers (2003a,b, sumarised in Balona 2018). Theory predicts equidistant splittings of the modes spaced by the orbital frequency in the observed Forurier spectrum. The multiplet structures observed for the pre-MS δ Scuti RS Cha can be interpreted as TPPs (Steindl et al., 2021), similar to the conclusion for some of the p modes exibited by U Gru (Bowman et al., 2019). The first tidally perturbed g modes were discovered by Jerzykiewicz et al. (2020) for the SPB star π^5 Orionis, followed by Van Reeth et al. (2022) for V456 Cyg, after which Van Reeth et al. (2023) present a sample of close EBs exibiting tidally perturbed g modes. This raises the question of how significant is the effect of the equilibrium tide in the near-core regions (Lampens, 2021).

The *tidal trapping* of modes (Springer & Shaviv, 2013) later led to the interpretation of *tidally tilted pulsations* (TTPs; Fuller et al., 2020), where the pulsation axis is aligned with the tidal axis (Handler et al., 2022). As is the case for TPPs, tidal tilting results in multiplet structures so TPPs and TTPs can each be considered sub-classes of tidally split modes. The first TTPs were discovered in the ellipsoidal variable HD 74423 by Handler et al. (2020), followed by Kurtz et al. (2020) and then Rappaport et al. (2021) in CO Camelopardalis and TIC 63328020, respectively. To discriminate among TPPs and TTPs requires detailed investigations of the pulsation amplitude and phase dependences with orbital phase.

The effect of the equilibrium tide is observed in the relationships between orbital and pulsation properties for binaries containing δ Scuti stars. Soydugan et al. (2006) observed a connection between the orbital period and dominant pulsation period for these systems. Zhang et al. (2013) made the first theoretical justification for this connection, where they find that the relation is a function of pulsation constant, filling

factor of the pulsating component, and mass ratio of the system. Liakos & Niarchos (2017) propose a threshold for a binary systems orbital period of 13 d beyond which binarity does not affect pulsations. Kahraman Aliçavuş et al. (2017) almost doubled this threshold by considering eclipsing systems only (Liakos, 2020).

1.3.2.2 The Dynamical Tide and Pulsations

Tidally excited oscillations (TEOs) occur when the forcing frequency associated with the *dynamical* tide of an eccentric binary comes close to an eigen-frequency of a natural oscillation mode (Aerts et al., 2010); the dynamical tide acts as the driving mechanism. This causes the excitation of gravity modes that are multiples of the orbital frequency (e.g., Welsh et al., 2011; Hambleton et al., 2013; Fuller, 2017; Guo et al., 2019) (pressure mode frequencies are too high to be excited by the dynamical tide). They can be observed in heartbeat (HB) systems containing A- F- and OB-type stars because their radiative envelopes facilitate the propagation of gravity waves (Guo, 2021).

Asymptotic approximations of gravity waves were used to study tidally excited waves by Zahn (1975, 1977) and Goldreich & Nicholson (1989), then extended to include the effects of rotation by Mathis (2009). Numerical calculations include the effects of non-adiabaticity and rotation (e.g., Savonije et al., 1995; Papaloizou & Savonije, 1997; Savonije & Papaloizou, 1997), while the detailed calculations of Witte & Savonije (1998, 1999) studied the binary evolution and intricate effects such as resonant locking in massive stars (Guo, 2021).

TEOs are a direct manifestation of the dynamical tide. Hence, they provide the opportunity to develop our understanding of tidal processes, e.g., tidal heating and synchronisation, from the energy that is deposited by TEOs and their contribution to angular momentum transfer (Guo, 2021).

2 Methods

Having introduced the topics of EBs and asteroseismology, as well as their intersection, it is evident that these fields' advancement hinges on the crucial link to the stars provided by *photometric* and *spectroscopic* data. These foundational datasets enable a diverse range of analytical methods; we begin with the application of photometry and then spectroscopy.

2.1 Photometry

2.1.1 Photometric Measurement

The most accessible data acquisition method in astronomy is undoubtedly photometry (Prša, 2018). Photometry converts brightness into a physical quantity. That physical quantity may be the flux, or the magnitude (see below). Early instruments used to perform photometry were e.g., *photographic plates*, and the first *electronic* photometric device was the photoelectric multiplier. Now, photometry is usually carried out using a charge-coupled-device (CCD), which is an array of photosensitive pixels recording the photons striking each pixel (Prša, 2018).

The stellar flux is diluted with the square of the distance compared to the surface value (Eq. B.7) because of the solid angle dependence, and *reddened* (see Section 1.1.4.6); *atmospheric* scattering and extinction introduce additional effects for observations taken from the ground. Considerations intrinsic to making a photometric measurement are, e.g., instrumental efficiency of the optical assembly, quantum efficiency, and the *passband* filter. Thus, the *measured flux* is,

$$F_\lambda^{\text{instrumental}} = \mathcal{P}(\lambda) R^{\text{ext}}(\lambda) R^{\text{optics}}(\lambda) R^{\text{ccd}}(\lambda) F_\lambda^{\text{bol}}, \tag{2.1}$$

where $\mathcal{P}(\lambda)$ is the passband filter transmission function, F_{bol} is the *bolometric* flux, which is the flux integrated over the entire spectral energy distribution (SED), and the remaining R coefficients account for the optical layout and extinction (Prša, 2018).

It is impossible to observe the entire SED (LeBlanc, 2010) and measurements must be taken within a given wavelength range defined by $\mathcal{P}(\lambda)$, which dominates the spectral range of the measurement response of the photometer. The instrumental flux then needs to be transformed into a *standard photometric system* (see Bessell, 2005, for an overview of determining the transformation equation), which is defined by a list of standard magnitudes and colours measured in specific passbands for a set of stars that are well distributed around the sky (Bessell, 2005). These may be broad-band ($\Delta\lambda < 1000$Å), intermediate-band (70Å$< \Delta\lambda < 1000$Å), narrow-band ($\Delta\lambda < 70$Å)

photometric systems, or those which access infrared (IR) wavelengths (Bessell, 2005). A series of broad-band systems are shown in Fig. 2.1.

For historical reasons, the fluxes are usually expressed in terms of *magnitude* (Bessell, 2005). The magnitude measures the logarithmic value of the flux, which conforms with the sensitivity of the human eye but takes the form of an inverse scale. The modern definition of magnitude is,

$$m - m_0 = -2.5 \log \left(\frac{F}{F_0} \right), \tag{2.2}$$

where m_0 is the magnitude zero-point that corresponds to the flux F_0[1] (Prša, 2018). The propagation of flux error to magnitude error is not symmetric. The errors can be calculated following Prša (2018) as,

$$\sigma_m^{\pm} = -2.5 \log \left(1 \pm \frac{\sigma_F}{F} \right), \tag{2.3}$$

where $\sigma_{F,m}$ are the standard deviation of the measurements. It is customary to either use σ^+ or take an average between the two (Prša, 2018).

A colour index is defined by the difference between the magnitudes measured in two photometric bands. From these quantities, we introduce the observational HR diagram – the Colour-Magnitude diagram – where colour represents the $T_{\rm eff}$. In order to make adequate comparison between theory and observation, much effort goes into converting passband magnitudes and colours into those which corresponds to the bolometric flux and $T_{\rm eff}$, respectively (Bessell, 2005).

2.1.2 Photometry from Space

Photometric space campaigns such as *Kepler* (Koch et al., 2010; Borucki et al., 2010), K2 (Howell et al., 2014), TESS (Ricker et al., 2015), CoRoT (Baglin et al., 2006; Auvergne et al., 2009) and BRITE (Weiss et al., 2014), have delivered a large amount of

[1]The UVBRI systems magnitude zeropoints were set by defining Vega to have colours of zero. Its resulting magnitude is 0.03 in all passbands (Bessell, 2005).

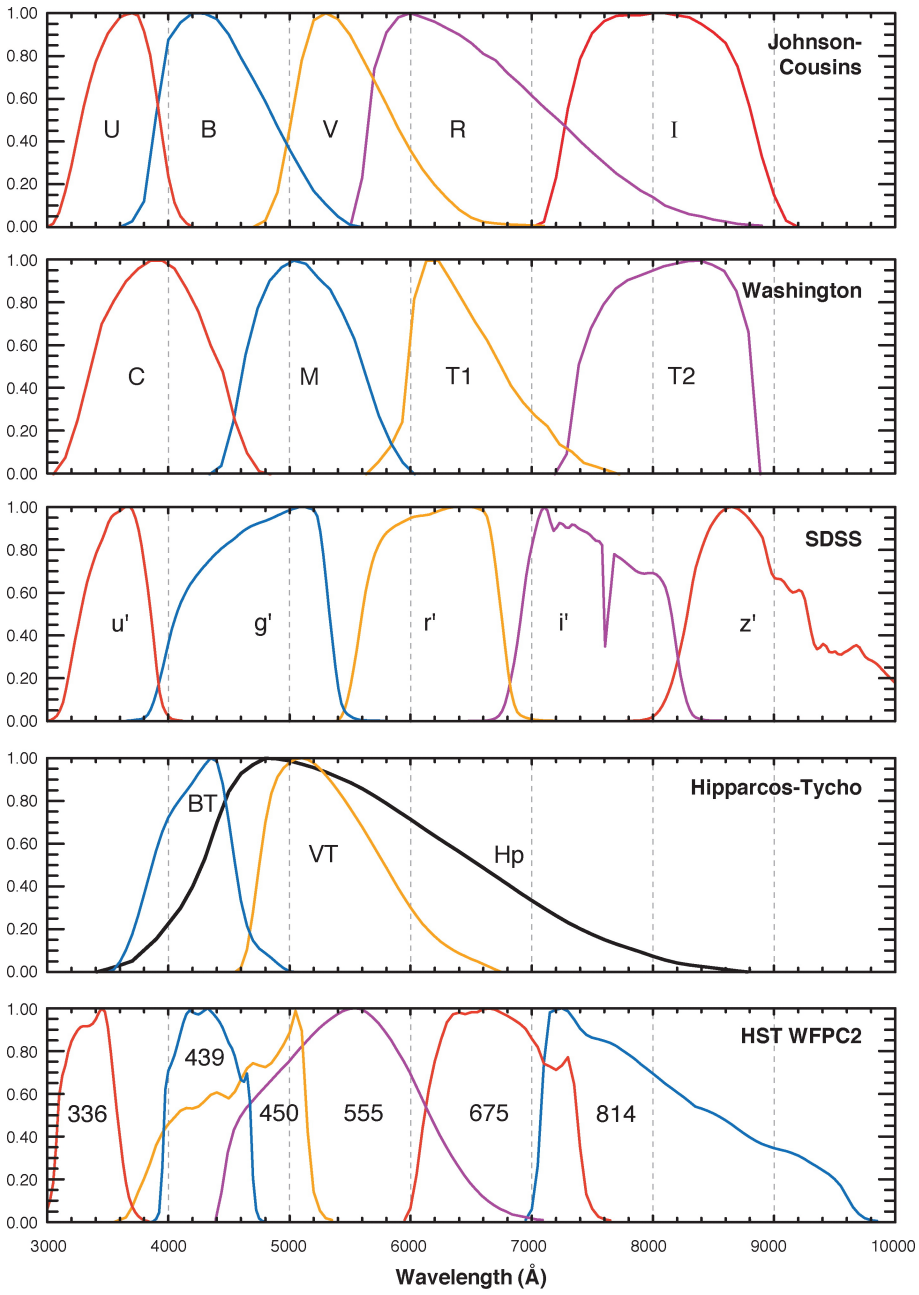

Figure 2.1: The series of the Johnson-Cousins (Johnson, 1965; Cousins, 1976), Washington (Canterna, 1976), SDSS (Abazajian et al., 2003, 2004), Hipparcos-Tycho (Perryman et al., 1997), HST (Holtzman et al., 1995) photometric systems. Also shown are the central wavelengths of the passbands in nm. Figure from Bessell (2005).

photometric data with precisions on the order of tenths of a mmag (see Southworth, 2021, for a review). The unprecedented precision has allowed for the detection of extremely low-amplitude pulsation frequencies (Murphy et al., 2013; Bowman & Kurtz, 2018) while long sequences of continuous observations (Lehmann et al., 2013) means that longer period pulsations can be studied. Such observations are not subject to aliasing issues and photometric stability problems associated with ground based observations (Breger, 2000; Liakos, 2020; Grigahcène et al., 2010).

Such issues mainly affect the γ Doradus frequency range. Therefore, it is no surprise that space missions led to the discovery that hybrid behaviour is common (see Section 1.2.3.3), in contrast to the view based on observations from the ground. The full interior-probing potential of g mode period-spacing patterns, discussed in Section 1.2.2.4, was unlocked due to the advent of the high-precision, high duty cycle, space-based photometric data, allowing us to further our understanding of near core phenomena (Saio et al., 2015; Lovekin & Guzik, 2017; Sekaran et al., 2020).

The number of known EBs has benefitted significantly because of photometric campaigns from space. There are 2878 EBs detected by *Kepler* and presented in the *Kepler* Eclipsing Binary Catalogue (KEBC) by Kirk et al. (2016); Deleuil et al. (2018) catalogued 2269 EBs detected by CoRoT; 4484 EBs observed by TESS have been catalogued (Prša et al., 2022). These large samples have the potential to reveal many EB candidates suitable for use in refining stellar theories, as well as those that show pulsation signatures (see, Grigahcène et al., 2010; Murphy, 2018; Gaulme & Guzik, 2019; Guzik, 2021; Shi et al., 2022). At least 2000 δ Scuti stars have been detected in the main *Kepler* field of view alone (Balona & Dziembowski, 2011; Balona, 2014a; Bowman et al., 2016).

The studies presented later in this work use data obtained by *Kepler* and TESS. Further details are provided for these missions in the next two subsections. Further information about the other space missions that have been mentioned can be found in the corresponding references.

2.1.3 *Kepler*

2.1.3.1 Mission Overview

The *Kepler* space telescope was launched in March 2009 with the primary aim of detecting Earth-like extrasolar planets in the habitable zones around solar-like stars by continuously monitoring the brightness of ~ 150000 MS stars; solar-like stars were preferred to maximise the results. Distinguishing between dwarfs and giants led to measurements for $T_{\rm eff}$ and $\log(g)$ being compiled in the Kepler Input Catalogue (KIC)[2], which was used to rank and select stars (Batalha et al., 2010). As a by-product of *Kepler*'s primary objective, the mission has also provided a huge amount of high-quality data on stars and stellar systems (Hong et al., 2022; Kahraman Aliçavuş et al., 2022).

The telescope on board was a 1 m class Schmidt telescope with a 0.95 m aperture and a 115.6 deg^2 field-of-view (FOV) pointed in the direction of the constellations Cygnus and Lyra for the entirety of the mission. The decision to choose the constellation Cygnus and Lyra was partly motivated by the 55° sun avoidance angle of the telescope, which meant that the star field was limited to $> 55°$ above the ecliptic plane; the Cygnus region appeared to be the richest choice (Koch et al., 2010).

The spacecraft maintained a continuous pointing on the single region of sky by occupying an Earth-trailing heliocentric orbit of 372.5 days. There is a multitude of advantages associated with pointing to a single region of the sky, e.g., selecting the richest available star field, optimising spacecraft design, simplifying operations, etc, (see, Koch et al., 2010); additional advantages associated with the orbit are an enhanced stability regarding the pointing attitude and the avoidance of high radiation dosages related to earth orbits. The most important advantage in the context of this work is maximising the duty cycle, allowing for continuous asteroseismic measurements to be made over long periods of time (see Gilliland et al., 2010a, for details regarding the *Kepler* asteroseismology program).

[2]The KIC can be accessed at: `https://archive.stsci.edu/kepler/kepler_fov/search.php`.

To keep the solar arrays pointed toward the sun during its Earth-trailing heliocentric orbit, the spacecraft was rotated by 90° every three months (one quarter). Thus, the data are split into quarters defined by successive rotations. Most of the same stars remain visible during each quarterly rotation due to the four-way symmetrical pattern covered on the sky by the photometer on board, which was an array of 42 CCDs arranged in 21 modules, each with 2200x1024 pixels.

The data were collected via two modes of observation; long cadence (29.5 min sampling rate) provides the primary data for planet detection, and short cadence (58.5 s sampling rate) allows for improved timings of planetary transits and facilitates asteroseismology[3] (Koch et al., 2010; Gilliland et al., 2010a). The photometric precision of these observations was sufficient to detect a 6.5 h transit from an Earth-sized planet passing in front of a 12th-magnitude G2 star at the $4\,\sigma$ level (Borucki et al., 2010; Koch et al., 2010). This was achieved by ensuring that the combined differential photometric precision (CDPP) remained below ≤ 20 ppm (an Earth-Sun transit produces a signal of 84 ppm).

The CDPP calculation considers shot noise, stellar variability and measurement noise added in quadrature. Considering that the Sun's variability during solar maximum on the timescale of a transit is typically 10 ppm (Koch et al., 2010), the shot noise and measurement noise were budgeted at 14 and 10 ppm, respectively. The shot noise demand was met by the 0.95 m aperture for a solar-like star with a visual magnitude (V) of 12, and the demand in measurement precision required a pointing stability of better than 0.003 arcsec / 15 min and a thermal stability of the CCD better than 0.15 K d^{-1}.

The shot noise budget is met when 5 billion photoelectrons are obtained in 6.5 h. During a single 6.02 s integration, this corresponds to 1.4 million electrons. Considering *Kepler*'s tightest pixel response functions (PRFs) concentrate 60% of the energy into a single pixel, stars with a brightness exceeding $Kp \sim 11.5$ will saturate the detector

[3]Asteroseismology with Kepler is conducted by the Kepler Asteroseismic Science Consortium (KASC): `https://phys.au.dk/~hans/KASC/`.

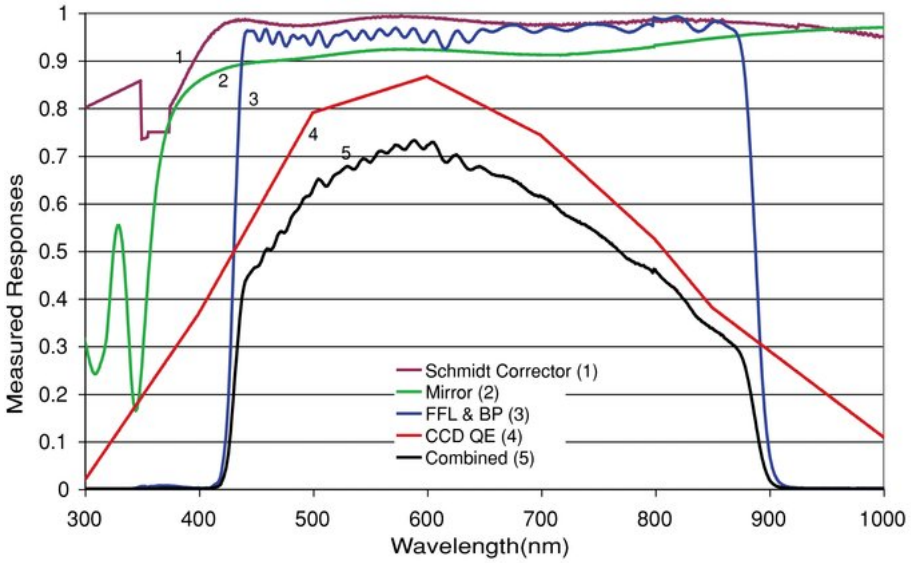

Figure 2.2: The *Kepler* passband. Figure from Koch et al. (2010).

depending on the FOV. However, the photometric aperture size could be adjusted for saturated stars in order to preserve the photometric precision. Stars fainter than $Kp \sim 15$ are also useful because shot noise dominates over instrumental noise. The dynamic range in magnitude for *Kepler* was from at least $Kp = 7-17$ (Gilliland et al., 2010b; Koch et al., 2010).

The passband response was $> 5\%$ between $423-897$ nm, defining its spectral range, which was chosen to maximise the signal-to-noise (S/N) for solar-like stars. The blue cutoff (< 423 nm) avoids UV and the Ca II H and K lines. Also, 60% of the Sun's irradiance variation occurs below 400 nm, yet photons below 400 nm only account for 12% of the Sun's flux (Krivova et al., 2006). The red cutoff avoids fringing due to internal reflection of light in the CCDs. Note, the overall measurement response within the passband is determined by a combination of the optics, the quantum efficiency (QE) of the CCDs, as well as the BP filters (Koch et al., 2010) (see Fig. 2.2). The maximum of the spectral response is at ~ 575 nm (Van Cleve & Caldwell, 2016).

The original *Kepler* mission lasted until May 2013 when it lost two of its reaction

wheels. In May 2014, NASA authorized the spacecraft's repurposing to observe the ecliptic plane as part of the K2 mission.

2.1.3.2 Kepler Data

After receiving and calibrating the raw pixel values, the data pass through the *Kepler* photometric analysis module. The photometric analysis module of the *Kepler* Science Operations Centre (KSOC) data processing pipeline is responsible for generating the flux time series and centroid time series for each of the target stars observed (Jenkins, 2017). Secondary photometric analysis functions are also performed by the Pre-search Data Conditioning (PDC) module before going through the transit planet search module and finally data validation

Prior to computation of the fluxes by the photometric analysis module, argabrightening events are mitigated, cosmic rays are removed, and a background estimate is subtracted from the pixels in the target apertures (Witteborn et al., 2011; Jenkins, 2017). To optimise the photometric figure of merit, a subset of pixels is collected for each target based on factors such as the estimated S/N at each pixel, the CDPP of light curves produced by candidate apertures based on these pixels, as well as other heuristics (Jenkins, 2017). The photometric flux at each cadence is then calculated from the optimal apertures by summing the constituent pixels (Jenkins, 2017). This is simple aperture photometry and gives rise to the Simple Aperture Photometric (SAP) fluxes. See Jenkins (2017), chapter 6, for more details on the architecture and algorithms of the photometric analysis component of the KSOC data processing pipeline that are used to generate the SAP fluxes.

Secondary functions of the photometric analysis module compute metrics to monitor instrument performance and support systematic error correction in the PDC module, giving rise to the PDCSAP fluxes. The PDCSAP fluxes are corrected for light curve signatures that correlate with error sources from the telescope and spacecraft (e.g., pointing drift, focus changes, and thermal transients), data anomalies such as the Sudden Pixel Sensitivity Dropouts (SPSDs), residual outliers and data gaps (such

as during intra-quarter downlinks), as well as excess flux in the target apertures due to background sources (Jenkins, 2017). The systematic artifacts are characterised by quantifying the most common of such features to hundreds of strategically-selected quiet targets on each detector channel. Then for each channel and quarter, the characterisations are stored as 16 best fit vectors called Cotrending Basis Vectors (CBVs), representing the most common trends found over each channel ranked by relative amplitude that they contribute to the overall systematic trend (Dotson, 2012). The CBVs are then subtracted from the SAP time-series. This correction is unique to each target and can be tuned (see Jenkins, 2017, chapter 8, for an in-depth overview of the PDC architecture and algorithms used to generate PDCSAP light curves).

The detrending and correction procedures in the PDC module were designed with the objective in mind to hunt planets. Thus, the additional processing *could* introduce unwanted artifacts (e.g., Balona et al., 2011; Balona & Dziembowski, 2011) and biases for other science cases. In particular, the processes could affect pulsation signatures. On the other hand, users need to be aware that SAP light curves can be contaminated by astrophysics from neighbouring sources, as well as motion and focus systematics (Dotson, 2012). However, asteroseismology of δ Scuti and γ Doradus pulsators based on the SAP fluxes have been hugely successful because signals associated with frequencies $\gtrsim 1\,\mathrm{d}^{-1}$ are mostly unaffected by the majority of instrumental aritifacts (Balona & Dziembowski, 2011; Balona et al., 2011; Dotson, 2012).

Both the SAP and PDCSAP flux measurements are available at the Mikulski Archive for Space Telescopes (MAST)[4].

2.1.4 TESS

2.1.4.1 Mission Overview

The *Kepler* mission revolutionised exoplanetary science by revealing that planets with masses between that of Earths and Neptunes are abundant with a wide range of posi-

[4] `https://mast.stsci.edu/portal/Mashup/Clients/Mast/Portal.html`

tions and configurations (Ricker et al., 2015). However, given that most of the *Kepler* stars are too faint for detailed follow-up observations, the next logical step would be to search the *nearest* and *brightest* stars for transiting planets. This was the objective of the Transiting Exoplanet Survey Satellite (TESS) mission.

TESS's primary mission goal is to identify numerous transiting planets smaller than Neptune orbiting stars bright enough to facilitate subsequent spectroscopic follow up observations for a comprehensive understanding of these planets' characteristics. This objective led to the implementation of an all-sky survey because the brightest stars are generally evenly distributed across the celestial sphere. Consequently, the collected data were grouped into sectors based on their positions in the sky.

Stars with spectral types earlier than F5 exhibit rapid rotation, leading to broader spectral lines. This broadening effect imposes limitations on the precision with which RVs can be determined, so these stars are not ideal for spectroscopic follow up observations. Contrarily, stars with spectral types later than M5 are both rare and optically faint. Therefore, TESS focuses its observations on MS dwarfs with spectral types between F5 – M5. TESS pre-selected 2×10^5 such stars, based on transit detectability, to observe with a cadence of 2 min. A sampling of 2 min satisfies the requirements for transit observations as well as enabling asteroseismology[5] (Ricker et al., 2015). The limiting magnitude of the selected stars in the Cousins I band (I_c) is $I_c \leq 10$ –13, depending on spectral type. TESS also observes with a 30 min cadence using the entire, four camera field of view ($24^\circ \times 96^\circ$), and stores the data as full frame image (FFI) files to facilitate additional science.

A passband range of 600 – 1000 nm was chosen due to the following considerations. First, a wide spectral range reduces shot noise, but if the range is too wide, this presents challenges in constructing a wide-field and well-focused optical system. Also, sensitivity at redder wavelengths is desired in order to detect small planets; small planets are more easily detected around small stars, which are cool and red (Ricker et al., 2015). The

[5]Asteroseismology with TESS is conducted by the TESS Asteroseismic Science Consortium (TASC): `https://tasoc.dk/info/tasc.php`.

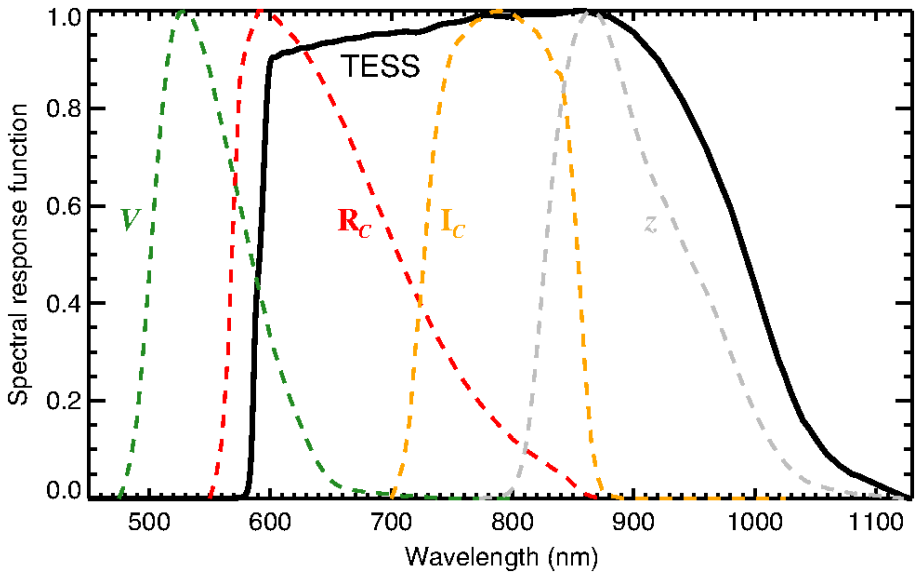

Figure 2.3: The TESS passband. Figure from Ricker et al. (2015).

TESS passband is centred on the traditional Cousins I band at 786.5 nm, but wider, as shown in Fig. 2.3.

The aperture of the space telescope is 10 cm, chosen as of the predicted requirements for detecting hundreds of super-Earths. This is smaller than the 0.95 m aperture of the Kepler telescope. The advantage of a smaller aperture is that it provides a larger field of view. Similar photometric performance to *Kepler* was expected by TESS, with an expected bright limit of $I_c \approx 4$.

The TESS orbit is high and elliptical with a period of 13.7 d around Earth. The high Earth orbit provides a more stable platform for precise photometry than a low Earth orbit (Ricker et al., 2015) and the approximate perigee at a distance of 17 times the radius of Earth means the spacecraft would be close enough to Earth, for at least a portion of the orbit, to facilitate data transfer (Ricker et al., 2015). At perigee, the science operations are interrupted for ≤ 16 h for data downlink.

2.1.4.2 TESS Data

The TESS science pipeline was developed by the Science Processing Operations Centre (SPOC) at NASA Ames Research Centre based on the KSOC pipeline (Jenkins et al., 2016a). Thus, like the *Kepler* pipeline, TESS provides calibrated pixels, simple and systematic error-corrected aperture photometry, and centroid locations for all 200,000 of its targets observed over the 2 yr prime mission, along with uncertainties. Since SPOC is based on KSOC, the architecture and algorithms are similar; the photometric analysis module provides the SAP fluxes and the PDC module corrects for systematics to yield the PDCSAP fluxes, where both measurements are, again, available via MAST. A detailed discussion of the SPOC architecture and algorithms is provided by Jenkins et al. (2016a). Similar arguments can be made as in Section 2.1.3.2 about the benefits and drawbacks of using the PDCSAP or SAP fluxes.

A significant difference between TESS and *Kepler* is that the TESS FFIs are collected using a 30 min cadence compared to *Kepler*'s monthly FFIs. This is important because it makes the FFIs amenable to a broader scope of scientific cases, e.g., time-series analyses of eclipsing binary stars (Ricker et al., 2015).

2.1.5 Light-Curve Modelling

Given a time series of photometric measurements collected, e.g., by NASA as described in the previous section, of an EB, we can construct a light curve and, hopefully, observe some eclipses. Modelling the light lost during eclipses becomes analytically feasible when assuming uniformly illuminated spheres, as demonstrated in Section 1.1.3.2. The shapes of the eclipses depend solely on the geometrical parameters of the stars in their relative orbit and the ratio of their surface brightnesses. However, when radiative effects like limb darkening, reflection, and asphericity come into play, the calculations require a different approach. Such calculations involve summing up light contributions from discretised surface elements across the stellar discs, allowing for more realistic representations of stars in the presence of such complexities. The contribution of each

surface element to the total system light depends on its visibility and the extent to which it is influenced by radiative effects. Before employing numerical codes to perform these calculations, light curve analyses usually involve preliminary procedures.

2.1.5.1 Preliminary light curve analysis

The light curve should be studied carefully to identify systematic trends and outlying data points, and then corrected for them. Such *detrending* might still be necessary for both the SAP and PDCSAP *Kepler*/TESS light curves; the former are already processed by the primary functions of the photometric analysis modules and the latter by further secondary functions. Fig. 2.1.5.1 (left) shows a SAP light curve for the *Kepler* EB KIC 4851217, where there is an overlaid systematic trend and outlying data points.

Difficulty describing the systematic trend in Fig. 2.1.5.1 mathematically arises because of the ellipsoidal brightening at phases of quadrature. In the absence of such effects, one can simply mask the eclipses and model the baseline flux. In Fig. 2.1.5.1, a second-order polynomial was fitted to fluxes that correspond to positions of quadrature, i.e., the maximum of the ellipsoidal brightening, to estimate the systematic trend. Subtracting the difference between this model and the median flux of the light curve yields a model for the *local median* level of out-of-eclipse flux. This is then divided out, removing the systematic trend. Outlying data points (purple crosses in Fig. 2.1.5.1) were located by subtracting a smoothed version of the light curve and rejecting positions with residuals larger than an appropriate threshold determined by visual inspection. The right panels in Fig. 2.1.5.1 shows the result after detrending (top) as well as phase folding (bottom). Other modulating signals, e.g., starspots, also introduce difficulties in obtaining a *cleaned* light curve. Starspots can be fitted with combinations of sinusoids and divided out prior to light-curve modelling (e.g., Chapter 5, Section 5.2).

After such preliminary steps, the light curves are ready for modelling using dedicated codes.

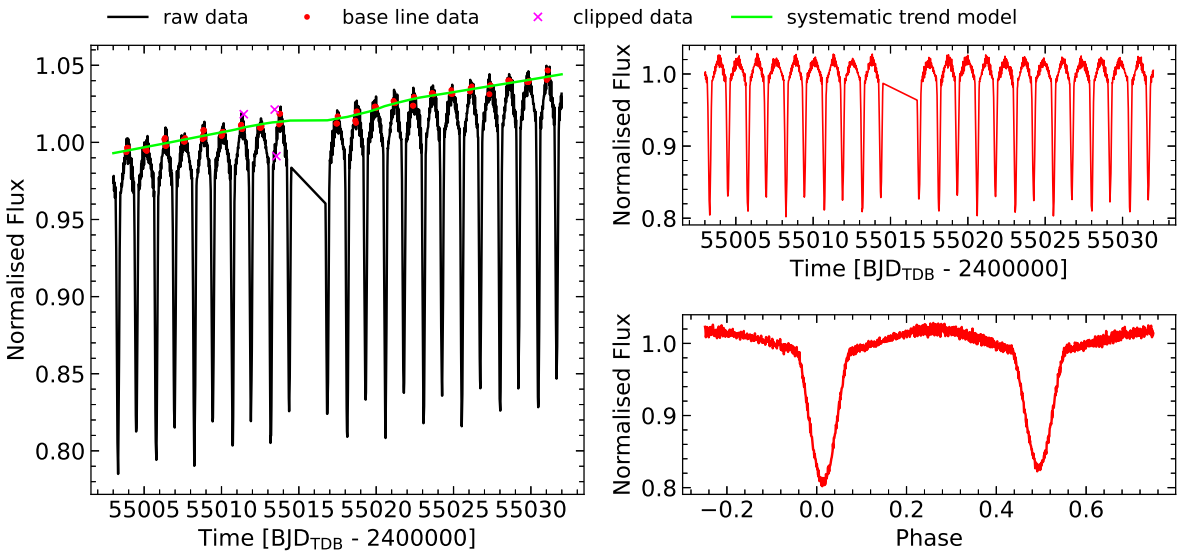

Figure 2.4: Left; raw SAP light curve of the *Kepler* EB KIC 9851944 from quarter-2 with clipped data and data used to estimate the systematic trend model indicated. Right; detrended light curve as a function of time (top) and phase (bottom).

2.1.5.2 jktebop

The JKTEBOP code (Southworth et al., 2004a) is based on the EBOP code (Etzel, 1975). The EBOP code uses the NDE biaxial ellipsoidal model (Nelson & Davis, 1972) to approximate stellar shapes with modifications as described in Popper & Etzel (1981). A further modification incorporated in JKTEBOP is the use of the Levenberg-Marquardt minimisation (LM) algorithm to optmise the eclipse parameters (Southworth et al., 2007). The NDE model is simple and efficient, involving relatively few calculations compared to, e.g., the WD code which employs the full Roche prescription of equipotential surfaces (Wilson & Devinney, 1971). Using this model, JKTEBOP discretises the stellar discs into concentric rings from which contributions are summed up using simple numerical integration.

The biaxial ellipsoid approximation to stellar shapes is only satisfactory up to values for the oblateness of ~ 0.04 (Popper & Etzel, 1981; Taylor, 2006). Thus, JKTEBOP is appropriate for EBs that are well detached so the shapes are close to spherical;

systems with fractional radii of up to $r \sim 0.25$ are limiting cases of applicability (North & Zahn, 2004).

The adjustable parameters of the JKTEBOP code are those which are most closely related to the shape of the light curves. These are: r_1, r_2, k, J, third light contamination L_3, i, q, and the Poincairé elements $e \sin \omega$ and $e \cos \omega$ (see Section 1.1.3.2) as well as P and T_0. A scale factor associated with the out-of-eclipse light of the system as well as a parameter describing the phase of T_0 relative to phase zero are also included. Reflection coefficients can also be included in the fit, which is dealt with in a simple bolometric manner based on Binnendijk (1960) and calculated from the geometry of the system. The approximation breaks down for largely non-uniform temperature distributions over the surfaces of the components or when the $T_{\rm eff}$s of the components differ significantly.

Significant extentions to JKTEBOP were presented in Southworth et al. (2007) and Southworth (2008), allowing spectroscopic light ratios and times of minimum light to be input as observational data, and the implementation of non-linear limb-darkening laws including the quadratic, square root, logarithmic, cubic, and power-2 laws; the associated limb darkening coefficients may be included or fixed in the fitting procedure. Southworth (2013) introduced simultaneous fitting of the light curve and RVs of both stars in JKTEBOP.

Estimations for the uncertainties are produced by the LM algorithm calculated from the solution covariance matrix, but are unreliable in the presence of parameter correlations (Southworth, 2008). Correlations arise, e.g., between the ratio of the radii and light ratio when eclipses are partial (Southworth et al., 2005a). The method of Monte Carlo has been implemented within JKTEBOP to evaluate random errors and correlations of the parameters derived from a JKTEBOP light curve fit (Southworth et al., 2004b). In this method, a best fit to the actual data is used to generate a synthetic light curve with the same sampling, and added Gaussian noise of the same magnitude, as the observations. Fitting for the synthetic light curve in the same way as the observations many times, but perturbing the initial parameters so the result is a distribution of best fitting parameters, allows for detailed exploration of the parameter space and parameter correlations (Southworth, 2008), similar to the results of the

Markov Chain Monte Carlo techniques.

The Monte Carlo algorithm does not properly account for correlated 'red' noise (Southworth, 2008). Systematic errors can be assessed using the residual-permutation algorithm that is also implemented in JKTEBOP. This algorithm shifts the residuals of the best fitting light curve solution to the next data point on each iteration, with those at the end of the data set being wrapped around to the start (Southworth, 2008). A fit is repeated after each shift, resulting in a distribution of fitted parameter values, from which uncertainties can be assessed after a full cycle of iterations and the residuals are back where they started.

2.1.5.3 Wilson Devinney code

For binary systems where the oblateness or fractional radii of the components exceeds the limitations of the JKTEBOP code, a full discretisation of the Roche equipotential surfaces describing the shapes of the components is required. An example of a light curve code which utilises the Roche model is the Wilsen-Devinney (WD) code (Wilson & Devinney, 1971; Wilson, 1979), where points are defined on the surface of the star, distributed approximately uniformly in spherical coordinates, and the model is fitted to observations using differential corrections.

Fitted parameters include P, T_0, e, ω, i, q, the rotational velocities of the stars $v_{\rm rot,1}$ and $v_{\rm rot,2}$, the gravitational potentials ϕ_1 and ϕ_2, $T_{\rm eff,1}$, $T_{\rm eff,2}$, the light contributions l_1 and l_2, gravity brightening coefficients β_1 and β_2 and reflection coefficients $\mathcal{R}_1$ and $\mathcal{R}_2$. The effective wavelength of the observations λ is supplied as a control parameter. Reflection coefficients are calculated by considering the irradiation of each individual discretised surface element due to every surface element on the other star, and are very computationally expensive calculations. The WD code allows for linear, logarithmic, and square root laws to account for LD.

The disadvantage of using the WD code is that it is computationally expensive so is much slower than JKTEBOP. The advantage of using the WD code is that it allows for a very realistic approximation of the shapes of the components in a binary system,

regardless of morphology. The WD code is described in Wilson & Devinney (1971) and Wilson (1979, 1990, 2008).

An alternative to the WD is the PHOEBE code which portrays a similar level of sophistication and realism in approximating the components of binary systems (Prša et al., 2016), and indeed the original PHOEBE code was based on WD. The PHOEBE2 code is not.

2.2 Spectroscopy

Photometric observations measure the flux integrated over some wavelength interval across the SED of the star whereas spectroscopic observations measure the flux as a function of wavelength. This allows the study of both spectral lines and the continuum of the SED depending on the resolving power of the spectrograph, which is defined as,

$$R = \frac{\lambda}{\Delta\lambda}, \tag{2.4}$$

where $\Delta\lambda$ is the wavelength interval over which the spectrum is measured and λ is the wavelength location in the spectrum, i.e., $\lambda_{\rm min} + n\Delta\lambda$, where n is an integer between unity and the number of wavelength intervals defining the length of the spectrum. Thus, the measured spectrum is a discretisation of the continuous spectrum and the resolving power changes across it. The measured intensity at λ corresponds to the flux integrated across $\Delta\lambda$, so $\Delta\lambda$ behaves like a fine photometric band. In fact, the lowest resolution spectra have values for $\Delta\lambda$ of around $10-50\,$Å, which is comparable to some narrow-band photometric systems (Bessell, 2005).

Such low resolution spectra offer the opportunity to measure the stellar continuum because most of the detail (e.g., spectral lines) is averaged out over $\Delta\lambda$. Conversely, detailed studies of the stellar atmosphere requires high resolution observations ($\Delta\lambda \sim 0.01\,$Å) in order to capture the detailed shapes of line profiles (see Section 2.2.6).

2.2.1 Spectrographs

The basic astronomical spectrograph consists of an entrance slit at the focus of the telescope to control how much light enters the spectrograph, a collimator that intercepts the divergent telescope beam, a dispersing element to split the light, and a camera that focuses the dispersed light onto a detector.

The dispersing element may be, e.g., a prism or plane diffraction grating. In astrophysics, reflection gratings are used where the grating consists of a large number of parallel grooves which are smooth, of the same shape and equally spaced. Light

reflected by the grating is the sum of all contributions of diffracted wavelets from all portions of the grating, with their corresponding phase shifts, directed in an arbitrary direction (Gray, 2005).

As with the classical example of the diffraction of monochromatic light through two slits, i.e., the Young double slit experiment, the resulting interference pattern consists of maxima and minima. Interference maxima are recognised by their order n, which increases with diffraction angle away from the central, zeroth order ($n = 0$) maximum. Illuminating a reflection grating with polychromatic light results in a collection of interference maxima for each order, comprising the nth order spectrum; the zeroth order spectrum is undispersed, or white light (Gray, 2005). The number of orders increases with the number of grooves in the grating and the dispersion of wavelengths increases for higher orders. The dispersion also increases for smaller spacing between the grooves. Increasing the dispersion means increasing the resolution, and therefore, since typical grating spectra work in low orders, they require a small spacing between grooves (e.g., $300-1200$ lines/mm) to reach the appropriate resolution (Gray, 2005).

On the other hand, cross dispersed échelle spectrographs work in high orders ($n > 80$) to attain high resolutions, but only use around, e.g., 79 lines/mm. A cross dispersing grating or prism is used to separate and stack the orders, requiring a two-dimensional detector to record them (Gray, 2005). The combination of working with a large groove spacing and high orders allows a large wavelength range to be observed at high resolution. Each order contains a cut of the entire spectrum which overlap with increasing extent for bluer wavelengths because dispersion is also higher for smaller wavelengths.

2.2.2 Reduction

Raw spectrographic observations are 2D. For spectral analysis, these observations are first extracted into 1D by summing up the flux measurements along the spectral axis at each pixel in the dispersion axis. The dispersion axis must be calibrated from pixel units to wavelength units. This is done by assigning the known wavelength values of a

selection of familiar lines in the spectrum to the corresponding pixels. A polynomial fit of wavelength against pixel number determines the wavelength solution. Normalisation usually involves fitting a series of polynomials to a selection of regions free of lines to estimate the continuum. Alternatively, spectra can be compared to theoretically calculated *synthetic spectra*. In Section 2.2.2.2, the normalisation of échelle orders is considered but the method can be adapted to normalise grating spectra. Each of the stages which are outlined in the following sections regarding the processing of the 1D extracted spectra and determination of RVs have been implemented in a code written by myself (SPECORB; see Section 2.2.4).

2.2.2.1 Cosmic Ray Correction

Cosmic rays are high energy ions and electrons originating mostly from outside the solar system (Lee, 2001) and partly from the outer region of the heliosphere (i.e., solar cosmic rays). Cosmic rays manifest in the extracted spectrum as a spike in flux. The rate and density of cosmic ray events depends on the location of the observatory, altitude, and shielding; at mid-point altitudes and at sea-level, a 2 h exposure results in 1 event/mm^2 on the detector (Gray, 2005).

Cosmic ray spikes need to be located and removed for spectral analysis. Motivated by the process from Blanco-Cuaresma et al. (2014a), we resample the spectra onto a homogeneous grid with a step size which is small enough to respect the original sampling at all wavelengths. The spectra are then smoothed using a median filter with an appropriate kernal sufficient to remove the cosmic rays without smoothing out spectral features, and then they are resampled back onto the original grid. Pixel locations where the difference between the smoothed and original fluxes is larger than σ times the observed flux, where σ is a value determined via trial and error (typically between 0.01 and 0.05), are flagged. The corresponding fluxes can then estimated by interpolating between the flagged pixel locations.

2.2.2.2 Blaze Correction of Échelle Orders

A systematic defect of échelle spectra arises due to the non-uniformity in the sensitivity of the detecting chips which results in more flux being detected in their centres. This issue manifests within échelle orders as a curve in the continuum baseline and is mathematically described by the so-called blaze function, which should be divided out prior to spectral analysis. A theoretical model can be calculated, which depends on the grating parameters, and divided out. However, the observed blaze function may contain departures from the theoretical prediction, leaving residual variations in the resulting blaze corrected continuum (Xu et al., 2019). Another approach is to divide by the blaze of a flat field calibration source, e.g., a lamp. Difficulties in this approach arise due to the black body signature of the calibration source being superimposed on the blaze function. To avoid such difficulties, the blaze function can be modelled empirically. However, blaze correction via polynomial fitting requires those of high orders to follow the slope of the blaze (Xu et al., 2019), and poses the risk of spurious modelling of the continuum in the presence of strong spectral lines.

We employ the method of Xu et al. (2019). An alpha shape (Edelsbrunner et al., 1983), which is a polygon enclosing the data set, is calculated to capture the general shape of the blaze function. This entails tracing the shape of the spectrum with a circle of radius α (see figure 1 of Xu et al., 2019). Local polynomial regression (Cleveland, 1979) is then used to fit a model to the upper boundary of the *alpha shape* and used as a preliminary estimation for the blaze function. Local polynomial regression is more suited to modelling complex data than ordinary polynomial regression owing to its ability to adapt to local characteristics compared to fitting a single model (Xu et al., 2019); at each pixel, a polynomial model is calculated by weighted least squares, giving more weight to points closer to the subject pixel. The spectrum is then divided by this preliminary model, resulting in a first estimation for the normalised spectrum.

No consideration has yet been made in order to ensure that the blaze estimation did not *dip* into spectral lines. To address this, the first estimation for the normalised spectrum is split into windows separated at points where the upper boundary of the

alpha shape calculated in the previous step intersected the original spectrum. The point of normalising by the preliminary estimation of the blaze function is so that the fluxes within these windows can be split into local quantiles q relative to the same continuum level (i.e., ~ 1). Flux values that lie within the $1 - q$ upper quantile are selected and the polynomial regression is iterated using these fluxes only. These points generally do not lie in absorption lines (Xu et al., 2019) because of the way in which the windows localising the quantiles were defined. However, it may be necessary to manually mask lines which are known to require special attention, e.g., the Balmer lines.

It is recommended to use,

$$\alpha = \frac{\max(\lambda) - \min(\lambda)}{6}, \tag{2.5}$$

when performing this operation using the python implementation AFS by Xu et al. (2019). Good results are then typically observed for $q = 0.95$, such that 5% of the fluxes within each window are used in the final regression, and $m = 0.25$, where m determines the smoothness of the polynomial fit to the points in the upper quantiles. For high S/N, one may trust that all fluxes at the height of the spectrum belong to the continuum, and as such choose $q = 0.99$. Though usually, the true continuum will be slightly lower than the upper 1-percentile that is usually dominated by noise.

The method outlined here demonstrates the basic considerations for normalising spectra, in general, so can be adapted and applied to normalise grating spectra.

2.2.2.3 Edge Correction

Since the blaze function approaches zero at the edges, small errors in the estimation of the blaze function there are magnified upon division (Xu et al., 2019). A further difficulty arises when the edge of an order splits an absorption line. However, échelle orders overlap (see Section 2.2.1) and a weighted average of the overlapping fluxes yields a better estimation in those regions.

Employing the method of Xu et al. (2019), we apply the weights such that fluxes

further away from the edge within their own order are favoured, i.e.,

$$y_{\text{corrected}} = w_l y_{1,l} + (1 - w_l) y_{2,l}, \qquad l = 0, ..., n-1, \tag{2.6}$$

where $y_{1,l}$ and $y_{2,l}$ are a pair of fluxes corresponding to pixel l from the overlapping sections of the *left* and *right* order respectively, n is the total amount of pixels in the overlapping region and $w_l = 1 - l/(n-1)$. When $l = 0$, y_2 is the flux at very left edge of the right order and y_1 is the flux that is furthest from the right edge in the left order; w_l is maximum in this circumstance and y_1 is favoured.

Note, the orders have to be re-sampled onto a new axes with a globally shared wavelength increment before the edge correction procedure is carried out. Failing to do so introduces shifts in the pixel locations of corresponding fluxes relative to each other in the overlapping region, i.e., $l_1 \neq l_2$ and $n_1 \neq n_2$

2.2.2.4 Merging Échelle Orders

The result of the edge correction procedure is that neighbouring orders share a common edge. Fluxes can, therefore, be merged directly without resulting in discontinuities.

Fig. 2.5 shows the result of the boundary correction applied to three spectral orders between 5900 – 6200 Å, each normalised as described in Section 2.2.2.2. The orders in Fig. 2.5 are from spectral observations of the *Kepler* EB KIC 9851944. The overlapping regions can be deduced because orders plotted in red possess a degree of transparency. The inset magnifies the point of departure between two orders at the position indicated by the grey vertical dashed line. No discontinuities are observed meaning that the fluxes can be resampled onto a homogeneous wavelength scale covering the full spectral range after truncating the spectra in the centre of the overlapping regions to ensure no fraction of fluxes are duplicated.

Note that the spectra in Fig. 2.5 are broadened due to the rotation of the components in KIC 9851944, and the S/N is relatively low. The reader is encouraged to see Fig. 2.6, which shows the result of the normalisation procedure described here, but applied to the standard star HD 10606.

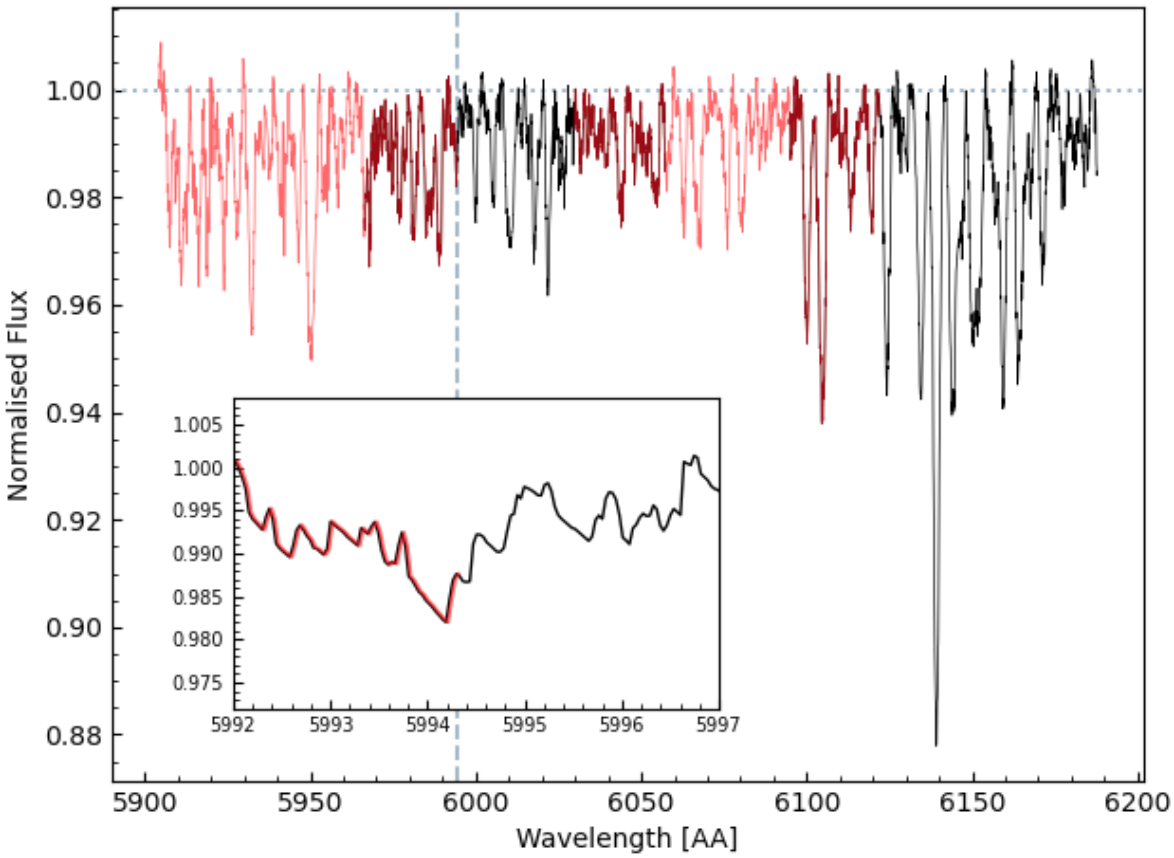

Figure 2.5: The normalised and boundary-corrected spectral orders between 590 – 620 nm. The dotted horizontal line indicates unity for reference. The inset shows a close-up of the departure of two overlapping orders at the position indicated by the vertical dashed line. Spectral orders plotted in red are transparent such that overlapping regions are a darker shade of red.

We employ the python implementation SPECTRES (Carnall, 2017) for the re-sampling of spectral fluxes, which uses a weighted method to assign the correct fraction of fluxes into the appropriate bins.

2.2.3 Radial Velocity Analysis

2.2.3.1 Radial Velocity Extraction

Expanding on Section 1.1.2.4, the RV is the component of a star's velocity that we can measure because the locations of spectral lines are sensitive to RV via the Doppler effect,

$$\frac{\lambda - \lambda_0}{\lambda_0} = \frac{\Delta\lambda}{\lambda_0} = \sqrt{\frac{1 + (V/c)}{1 - (V/c)}} - 1, \tag{2.7}$$

where λ is the observed wavelength of light emitted from a source, λ_0 is the wavelength of the corresponding light in a reference frame that is stationary relative to the source, V represents the velocity difference between the observer's reference frame and the source's frame along the line of sight, and c is the speed of light.

There are different methods for measuring RVs from the Doppler shifts of spectral lines, such as, fitting Gaussian profiles to individual spectral lines (e.g., Southworth & Clausen, 2007), using *least squares deconvolution* (LSD) and fitting for the resulting, average line profile (e.g., Tkachenko et al., 2013; Sekaran et al., 2020) and spectral disentangling (see Section 2.2.5). The primary approach that we employ involves cross correlating the observed spectrum of the binary against stationary template spectra. The cross correlation technique can be executed in one dimension, as outlined in Tonry & Davis (1979), or the cross correlation function (CCF) can vary in two dimensions, as in Zucker & Mazeh (1994). The latter, TODCOR, is the method utilised in this work, though the former is useful for checking for consistency. In any case, accurate RV extraction requires that the spectral observations are corrected for the observers motion about the solar barycentre. We calculate the magnitude of the correction using Astropy's RADIAL-VELOCITY-CORRECTION package (Astropy Collaboration et al.,

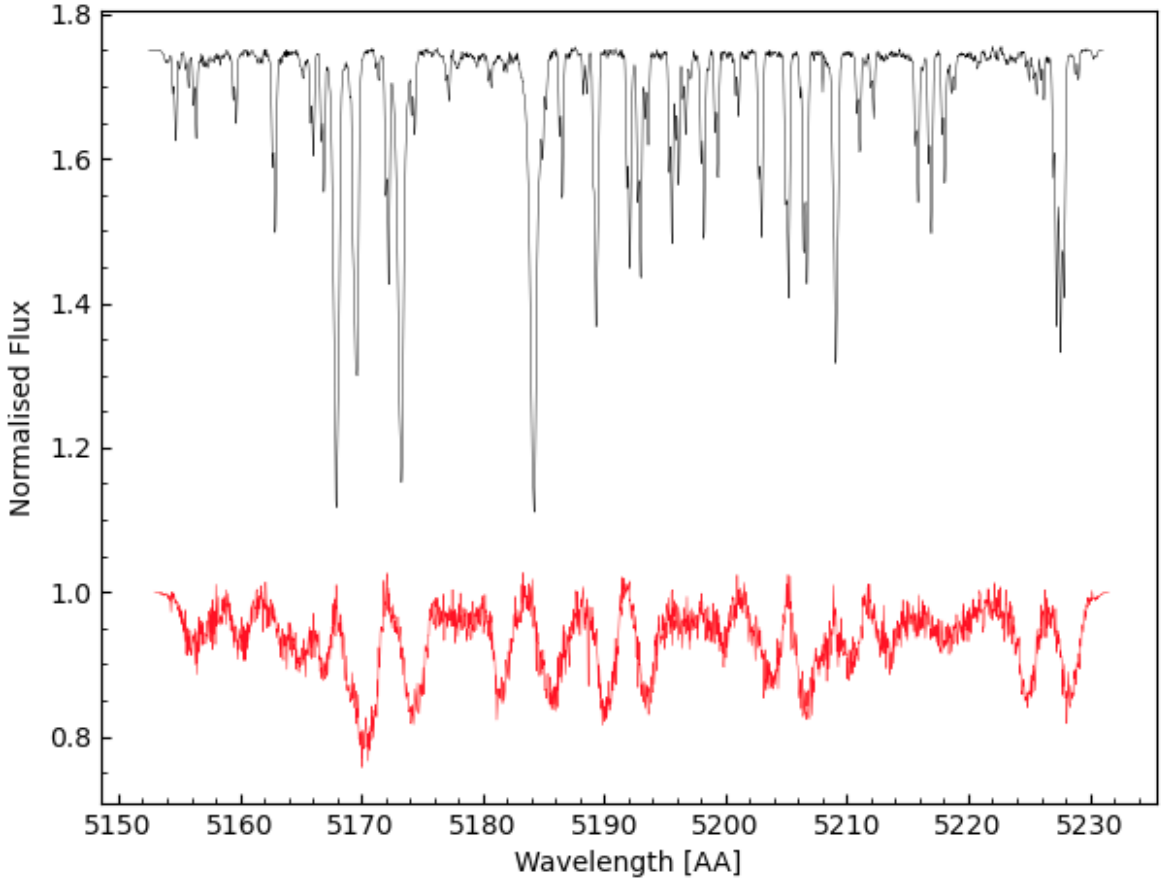

Figure 2.6: Normalised and apodised spectral order 50 of KIC 9851944 (red) and HD 101606 (black and offset by +0.75). Note that the lower S/N for KIC 9851944 meant that a smaller q value was necessary. For HD 101606, we can trust that most of the flux at the height of the spectrum will be continuum rather than noise.

2013, 2018), which is consistent with the IDL implementation of Wright & Eastman (2014) to the level of $10\,\mathrm{mm\,s^{-1}}$.

The cross correlation algorithms act in the Fourier domain so apodising the spectra removes any ringing in the Fourier transform by smoothing the ends of the spectra (target and template) to zero (Kurtz & Mink, 1998). Apodisation is achieved by multiplying a spectrum by an appropriate window function. We employ a cosine taper function, which is equivalent to the Hann window (Blackman & Tukey, 1958) when the

fraction of the window inside the cosine tapered region is set to unity, and equivalent to a rectangle window when the fraction is set to zero. We prefer to set the fraction to 0.1 in agreement with Kurtz & Mink (1998), who begin their taper 5% from the ends of the spectrum. Fig. 2.6 shows order 50 from a Hamilton échelle observation of KIC 9851944 and the standard star HD 10606 after being normalised and apodised.

The template spectrum may be synthetic or that of a standard star. Barycentric corrections should be applied to the template in the latter case, as well as correcting for its RV. The observed and template spectra are then re-sampled onto a common wavelength scale linear in log space, such that a velocity difference between the target and templates corresponds to a uniform linear shift in the peak of the CCF (Tonry & Davis, 1979). The template is broadened to match the observed broadening of the targets spectral lines due to the rotational velocity of the components' along our line of sight $v \sin i$. A preliminary estimate for $v \sin i$ can be obtained by cross correlating the template against the target after broadening the template according to a range of $v \sin i$ values. Broadening a spectrum to a specified value of $v \sin i$ involves convolving it with the corresponding rotational kernal. This can be achieved using Pyastronomy's ROT-BROAD package (Czesla et al., 2019), which implements rotational broadening as described in Gray (2005). Observations used in the determination of $v \sin i$ should be taken at phases away from conjunction so that the peaks of the CCFs are well resolved. The heights of the resulting grid of CCF peaks can then be interpolated to determine an estimation for $v \sin i$.

The benefit of the TODCOR algorithm is that it uses two templates, one for each component. Thus, the above procedures can be tailored for each template in accordance to the properties of each component in the binary system. This enhances the correlation at the point in the CCF that corresponds to the true RV for both components simultaneously. Performing cross correlation in one dimension either requires preparing a template that conforms to a suitable average of the properties of the components, or favouring one of them. In the former case, this leads to weaker peaks in the CCF, and in the latter case, the corresponding peak is enhanced for one of the components but reduced for the other.

The construction of the TODCOR CCF, which we denote R, requires the calculation of the one dimensional CCFs, $C_1(s_1)$ and $C_2(s_2)$, between the target and each of the templates, along with that between the two templates themselves, $C_{12}(s_2 - s_1)$, where $s_{1,2}$ denote the shift at each iteration of the calculation. Either Eq. 2.8 or Eq. 2.9 is then used to compute R depending on whether the light ratio α is known.

$$R = \sqrt{\frac{C_1^2(s_1) - 2C_1(s_1)C_2(s_2)C_{12}(s_2 - s_1) + C_2^2}{1 - C_{12}^2(s_2 - s_1)}}, \tag{2.8}$$

$$R(\alpha') = \frac{C_1(s_1) + \alpha' C_2(s_2)}{\sqrt{1 + 2\alpha' C_{12}(s_2 - s_1) + \alpha'^2}}, \tag{2.9}$$

where $\alpha' = (\sigma_2/\sigma_1)\alpha$, within which σ_{g_1} and σ_{g_2} are the root mean square (RMS) of the primary and secondary templates respectively. The sensitivity of the alogorithm to the light ratio means that TODCOR can be used to obtain a spectroscopic light ratio.

An example TODCOR CCF is shown in Fig. 2.7. This example was taken from an analysis of KIC 9851944, which consists of similar components and hence, there are two peaks of similar heights. The tallest peak is indicated by the black triangle in Fig. 2.7. The coordinates of the tallest peak correspond to the best estimates for the Doppler shifts of each component in the binary. The peak is then isolated and the RVs corresponding to its maximum determined at the sub-pixel level by, e.g., fitting a two dimensional polynomial to it, as demonstrated in Fig. 2.8.

2.2.3.2 RV Errors

Errors in the RVs can be determined as in Tonry & Davis (1979). It is assumed that the one-dimensional CCF is the sum of a perfect correlation function and a remainder function. The remainder function distorts the position of the peak in the perfect correlation function due to anti-symmetric parts within it, i.e., noise. Then the error is regarded as the difference between the position of the perfect correlation function and the observed one, which is derived by Tonry & Davis (1979) as,

$$\epsilon = \frac{1}{4}\frac{N}{2B}\frac{1}{1+r}, \tag{2.10}$$

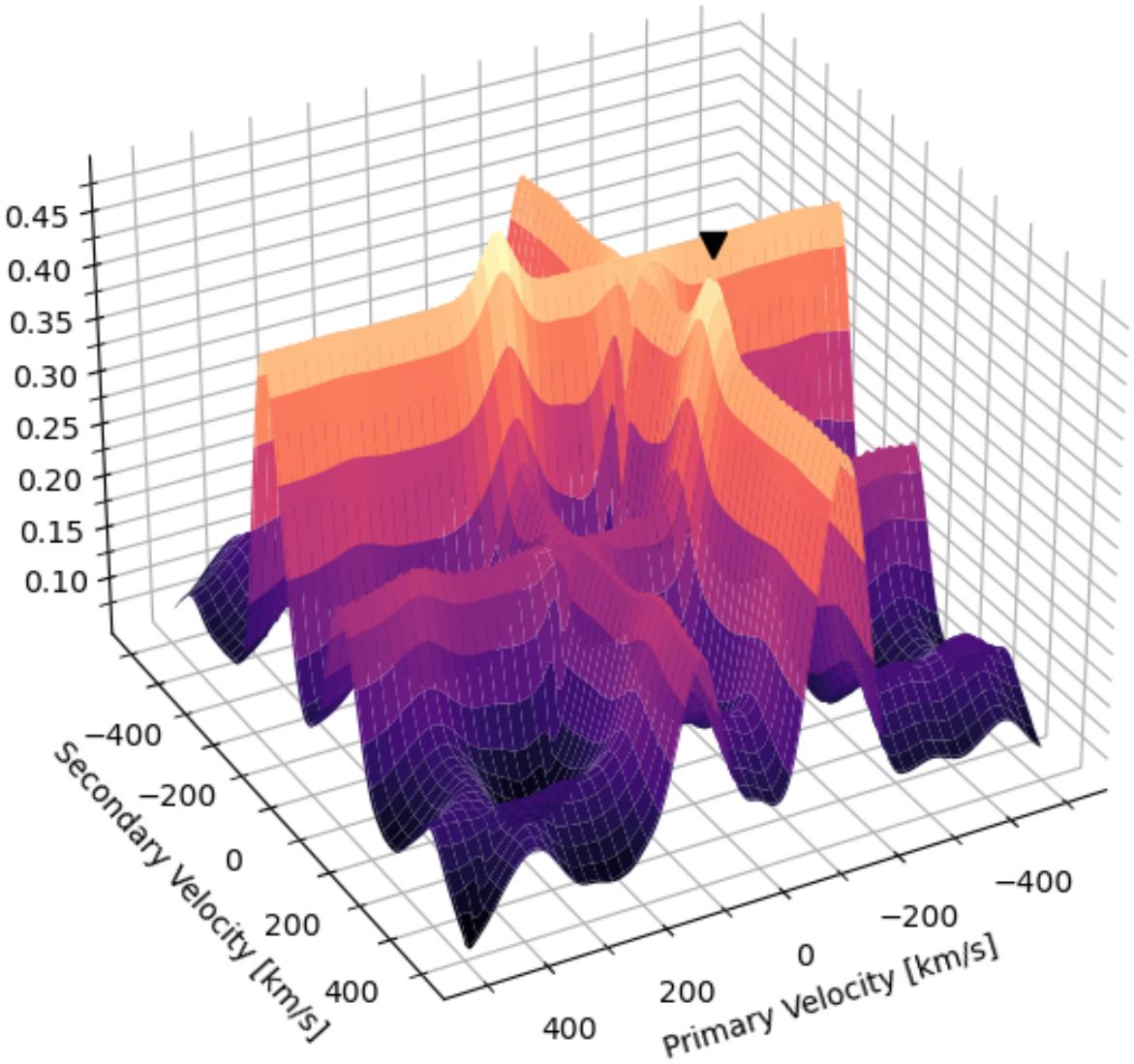

Figure 2.7: Example TODCOR CCF which was obtained in the process of extracting RVs from spectral observations of the *Kepler* EB KIC 4851217 (see Chapter 4).

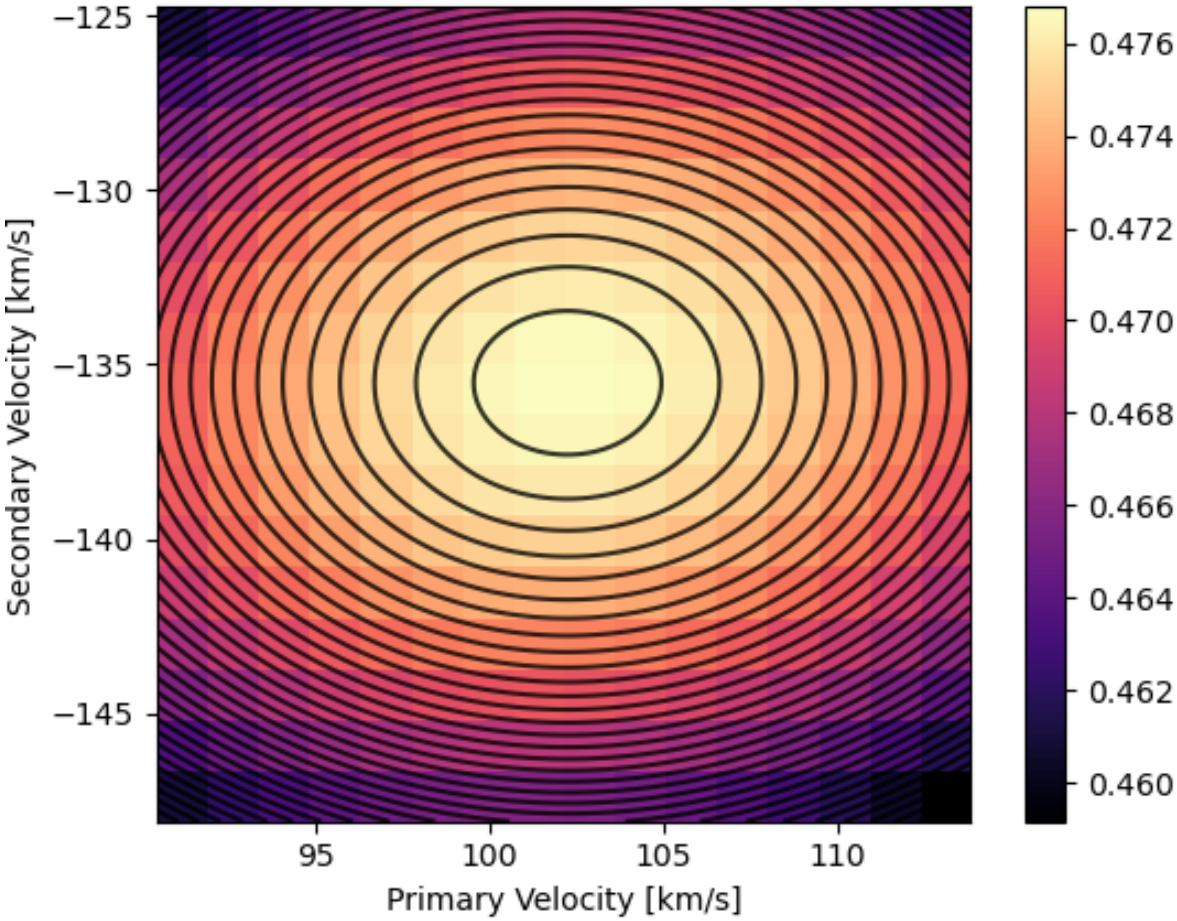

Figure 2.8: A fit indicated by the black contours to the tallest peak of the CCF in Fig. 2.7. The black marker in Fig. 2.7 indicates which peak was the highest and corresponds to the peak being fitted above.

where B is the highest wave-number where the Fourier transform of the true CCF has appreciable amplitude, N is the length of the input spectra, and r is the ratio of the height of the peak of the true CCF to the RMS height of the remainder function. The coefficient $\frac{1}{4}\frac{N}{2B}$ is adjusted in practice such that the predicted error fits external errors (Tonry & Davis, 1979). Kurtz & Mink (1998) find a value of $\frac{3w}{8}$ is appropriate for sinusoidal noise, where w is the full width at half maximum of the correlation peak, which provides a suitable first estimation.

This description for the calculation of the errors was developed for RVs extracted using 1D cross correlation. However, this method can be applied to the TODCOR analysis by considering each axis in the TODCOR CCF individually and carrying out the calculation whilst fixing the other axis to its maximum value (Zucker & Mazeh, 1994). An investigation into the resulting error estimations using this process shows that, in general, the smaller the difference in the extracted velocities, i.e., the closer the two peaks in the 1D CCFs, the larger the resulting error. This suggests that the anti-symmetric part of the remainder function corresponding to the peak of either component is dominated by the peak of the other component.

Alternatively, errors can be estimated via Monte Carlo simulations, i.e., introducing synthetic noise (e.g., Poisson noise based on the S/N of the data) into the observed spectra, and re-running the cross-correlation and RV measurement process multiple times on these synthetic spectra. This results in a distribution of RV measurements from which the standard deviation can be calculated. In any case, final estimations for the errors are scaled to yield a reduced chi-square χ^2_ν of unity when fitting a model RV curve to the measured RVs; these methods to serve to deliver the relative sizes of the uncertainties corresponding to a time-series of observations.

2.2.3.3 RV Corrections

Systematic errors in RVs measured using the cross correlation technique as large $3\,\mathrm{km\,s^{-1}}$ can arise due to the effects of line blending between the spectral lines of both components (Latham et al., 1996), and the problem is exacerbated by rotation

which broadens spectral line profiles. For double-lined spectra, the main correlation peak for one component is disturbed by the side lobe pattern of the other. A more severe disturbance occurs when the two main peaks interfere near phases of conjunction, and this leads to an underestimated RV measurement. In general, however, the resulting systematic error in the derived RV is expected to show a complex dependence on the relative Doppler shifts of the two stars[6] (Latham et al., 1996).

This makes it difficult to attain the required accuracy in the component velocity semi-amplitudes, and therefore their masses, to critically assess stellar evolution models (Andersen, 1991). For traditional spectrographic measurements, it is possible to identify and use lines that are not blended with those of the other star (Popper, 1967; Andersen, 1975b; Popper, 1980; Andersen, 1991; Latham et al., 1996). However, the averaging properties inherent to cross correlation techniques preclude detailed line-by-line evaluation of blending effects (Latham et al., 1996). The net line blending effect is expected to be smaller for larger spectral windows and numbers of lines; the net line blending errors in SB2 spectra have been shown to be smaller than $0.1\,\mathrm{km\,s^{-1}}$ over the 1500 Å spectral range covered by the CORAVEL instruments (Latham et al., 1996). However, for smaller spectral windows, e.g., the 45 Å window of the Centre for Astrophysics (CfA) Digital Speedometers, significant blending effects should be expected (Latham et al., 1996), and they can not be ruled out over the 400 Å window between 4400 –4800 Å typically used in the current work for the analysis of A – F stars.

The effect can be investigated by synthesising the observed spectroscopic orbit by adding synthetic spectra, weighted appropriately according to the relative light contributions of each component, after applying Doppler shifts according to the RVs derived from a preliminary fit to the observations (e.g., Latham et al., 1996; Torres & Ribas, 2002; Southworth & Clausen, 2007). The set of synthetic SB2 spectra are then subject to the same velocity extraction process used to obtain the original RVs. The difference between the recovered values and the synthetic RVs gives an indication

[6]For single star spectra, the single main peak and the accompanying side-lobe pattern oscillates together in correspondence to the orbital motion and are not expected to interfere with one another. Therefore, the uncertainty is accurately accounted for by the errors calculated as in Section 2.2.3.2.

of the magnitude and direction of the effect, and implies a correction that should be applied to improve the accuracy of original RVs.

The line blending problem is shown to be largely eliminated when using TODCOR (e.g., Latham et al., 1996; Torres et al., 2000) instead of the one-dimensional cross correlation technique, but it should not be assumed a priori that the implied errors are negligible (Southworth & Clausen, 2007). The magnitude of the effect depends sensitively on the characteristics of the system and subtle details such as filtering and the amount of end masking (Torres et al., 1997). Torres et al. (2000) applied the corrections, derived as outlined above, to the RV observations of EI Cephei. The authors find an increase of $\sim 0.25\%$ in the calculated velocity semi-amplitudes compared to before applying the corrections, and this translates to a $\sim 0.75\%$ increase in mass, which is about twice the size of the derived uncertainty. Torres et al. (1997) find the magnitude of the line blending effect to be as high as $2-3\%$ of the velocity semi-amplitudes of the components of HS Hya, translating to $6-9\%$ errors in mass. Torres & Ribas (2002) find that their derived corrections imply a 5% error in the masses of the components of YY Geminorum.

2.2.3.4 Modelling the Orbit

The extracted RVs are modelled using Eq. 1.11, which was derived in Section 1.1.2.4. The first step is to calculate the mean anomaly $\mathcal{M}$ (Eq. 1.6) in order to calculate the eccentric anomaly E through Kepler's equation (Eq. 1.7), which is related to the true anomaly ν using Eq. 1.8. We employ the python implementation KPE of Zechmeister (2018) to solve Kepler's equation. With the true anomalies corresponding to each phase of the observation calculated, the equation describing the orbital motion (Eq. 1.11) can be fitted to the RVs.

The problem involves finding the best estimates of the parameters, K, γ, ω, e, P and $T_{\rm per}$ by minimising the sum of the squared residuals between the observed RVs

and those predicted by a model with those parameters, i.e., we minimise,

$$\sum_i \{V_i - (\gamma + K[e\cos(\omega) + \cos(\omega + \nu_i)])\}^2, \tag{2.11}$$

where V_i is the observed RV at time t_i, and ν_i is the corresponding true anomaly. For linear least squares problems, the solution can be obtained analytically via (Hastie, 2009),

$$\beta = (X^T X)^{-1} \cdot X^T Y, \tag{2.12}$$

where β is a vector containing the model parameter estimates, X^T is the transpose of the design matrix X, and Y is a vector containing the observations. The covariance matrix is then calculated as,

$$C(\beta) = \sigma^2 (X^T X)^{-1}, \tag{2.13}$$

where σ is the variance of the residuals between the model and observations.

However, since our objective function, Eq. 2.11, is nonlinear in ω and ν, iterative optimisation methods are required such as, e.g., the Levenberg-Marquardt (LM) algorithm[7]. The LM algorithm can be thought of as a combination of the Steepest descent and Gauss-Newton methods (Lourakis, 2005), which iteratively update parameter estimates based on the Jacobian matrix[8]. Such algorithms require starting values before the routine can begin. An appropriate guess for K can be obtained by dividing the sum of the absolute values of the maximum and minimum of the RV measurements by a factor of two. Subtracting this value from the maximum value then yields an estimation for the systemic velocity γ. Input guesses for P and $T_{\rm per}$ (used in the calculation of ν), eccentricity e and argument of periastron ω are usually available from photometry but should be reliably determined without constraint.

For nonlinear problems, the covariance matrix is estimated based on the properties of the optimisation algorithm. The covariance matrix is an $N \times N$ matrix where N

[7]SciPy's python package CURVE-FIT allows for minimisation via the LM algorithm (Virtanen et al., 2020).

[8]The Jacobian matrix contains the partial derivatives of the objective function.

is the number of optimised parameters. The diagonal elements contain the variances of each of the parameters and the off-diagonals contain the covariances between them. The errors on the parameters are estimated as the square root of the variances. Correlations among the parameters are estimated by dividing the covariances between the parameters of interest by the product of the square root of the of their individual variances, i.e., $C_{ij}/\sqrt{C_{ii}C_{jj}}$. For circular orbits, $T_{\rm per}$ and ω are 100% correlated, although in this situation it is appropriate to fix these parameters at $T_{\rm per} = T_0$ and $\omega = \pi/2$, respectfully.

A measure for the goodness-of-fit is obtained by weighting the residuals of the fit by the square of the uncertainties for each of the $i^{\rm th}$ measurements and summing them, i.e, the chi square statistic. More commonly used in the context of model evaluations is the *reduced* chi square, $\chi^2_\nu = \chi^2/\nu$, where ν is the degree of freedom. A χ^2_ν greater than unity indicates that the errors are underestimated while a value smaller than unity indicates they are overestimated. To yield a χ^2_ν of unity requires the error bars to be scaled by $\sqrt{\chi^2_\nu}$, derived from setting $\chi^2_\nu = 1$.

Alternatively to least squares methods, Markov Chain Monte Carlo (MCMC) samplers are often used as a method of Bayesian inference [9]. Mathematically, Bayes' theorem states,

$$P(\theta|D) = \frac{P(D|\theta) \cdot P(\theta)}{P(D)}, \tag{2.14}$$

where $P(\theta|D)$ is the posterior probability distribution of the model parameters θ given the observed data set D, $P(D|\theta)$ is the probability of observing the data given specific values of the model parameters (also called the likelihood function), $P(\theta)$ is the prior probability distribution and $P(D)$ is the marginal likelihood, which ensures the posterior is properly normalised. The MCMC algorithm is used to draw samples from $P(\theta|D)$ based on the product of $P(D|\theta)$ and $P(\theta)$ and some acceptance criterion, forming a Markov-chain, which explores the parameter space until convergence at the target distribution. Statistical inferences can then be made for the parameters of

[9]The package EMCEE (Foreman-Mackey et al., 2013) is an MIT licensed pure-Python implementation of the Goodman & Weare (2010) affine invariant MCMC ensemble sampler.

interest, i.e., $\theta = [K, e, \omega, \gamma, P, T_{\rm per}]$, by marginalising over other parameters, i.e., summing/integrating them out of the joint distribution $P(\theta|D)$.

Assuming Gaussian errors, the likelihood function follows,

$$P(D|\theta) = \prod_{i=1}^{N} \frac{1}{\sqrt{2\pi\sigma_i^2}} \exp\Big(- \frac{(V_i - M_i)^2}{2\sigma_i^2}\Big), \tag{2.15}$$

where σ_i is the uncertainty associated with the observation V_i; for the case of modelling the RV curve, V_i is the measured RV and,

$$M_i = K\Big[e\cos(\omega) + \cos(\omega + \nu_i)\Big] + \gamma, \tag{2.16}$$

i.e., Eq 1.11. Optimising Eq. 2.15 by, e.g., least squares, yields an independent estimate of the parameters θ and is usually used as the starting point for the Markov-chain. The prior distribution $P(\theta)$ encodes any prior knowledge about the parameters θ, such as constraints or physically acceptable ranges (Foreman-Mackey et al., 2013). This gives the MCMC fitter flexibility and is a key advantage.

2.2.4 specorb

Most studies of binary stars involve analysing a time series of numerous spectroscopic observations, and these might be échelle spectra consisting of up to $\sim$ 100 orders. I wrote the python code SPECORB, where its name was derived from its primary purpose of extracting SPECtroscopic ORBits, which constitutes a workshop for executing the tasks outlined in the previous sections of this chapter on multiple spectra automatically. The functionalities wrapped into the code allow for a quick transition from raw extracted 1D spectra to an orbital fit to RVs, regardless of whether treating échelle orders individually or merging them.

This transition involves various sub-components of the code, for which we give details here in the correct order they should be executed. Each component relies on functions contained in the master functions file (SPECORB_FUNCTIONS) and the external functions file. The external functions file contains open source codes which

were downloaded from other authors and modified (in some cases) for integration with SPECORB (e.g., AFS, KPE, SPECTRES, ROTBROAD; Xu et al., 2019; Zechmeister, 2018; Carnall, 2017; Czesla et al., 2019). Each component takes a list of inputs; common to each is the requirement to provide the folder containing the input data, i.e., the spectra, and the name of the intended output file to store, e.g., processed spectra or results.

spec-prep implements the method of Xu et al. (2019) to normalise grating spectra, or *deblaze* and merge échelle spectra as outlined in Sections 2.2.2.2; 2.2.2.3; 2.2.2.4. Preliminary steps involve cosmic ray correction, as outlined in Section 2.2.2.1, and correcting for the observer's motion about the solar barycentre, as outlined in Section 2.2.3.1. Formatting and scale of time stamps must be given as input to ensure times are properly corrected to $\mathrm{BJD_{TDB}}$. This task will return merged and corrected échelle orders or return them as individual orders. Also returned is a data file, which contains necessary data for the operations by the RV task (see below).

vsini implements the procedures outlined in Section 2.2.3.1 for estimating $v \sin i$ for each of the components.

RV implements the *primary function* of the code, to extract RVs as described in Section 2.2.3.1, so an example configuration file for this component of the code is given at the end of this section. The RV task can handle multiple échelle orders and treat them individually for every time stamp, or it will assume one spectrum per time stamp; the option must be given as input so the code knows what statistics to perform on the results. If the observations are already on a logarithmic scale, this must be given as input. Templates are provided as input and can be optionally broadended to input values of $v \sin i$. Other necessary procedures which are performed by the RV task were outlined in Section 2.2.3.1. RVs can be extracted using either the 1D cross correlation technique or using my implementation of the TODCOR algorithm. Errors are

calculated as in Section 2.2.3.2. A preliminary orbital fit is calculated to the extracted RVs and saved in the output folder along with extracted RVs.

SSB2 creates a synthetic SB2 model, as outlined in Section 2.2.3.3, based on the output files of the RV task.

velcor calculates velocity corrections by executing the RV task on the synthetic SB2 model spectra. The corresponding corrections to the original RVs are then readily calculable by the code and saved as output.

keporb performs a least-squares fit to the extracted RVs allowing flexibility in the fitted parameters. Parameters can be fit jointly for both components in the binary system, or the RVs of each component can be fitted independently. The task includes the option to fit for the centre of mass acceleration of the binary, as well as fixing to a circular orbit. Other functionalities include scaling the errors to yield a χ^2_ν of unity and supplying boundary constraints. The implementation relies heavily on SCIPY (Virtanen et al., 2020).

The scripts for each of these components of SPECORB rely on the functions built into the master functions file (SPECORB_FUNCTIONS) and the external functions file, and therefore these modules are imported in each of the scripts. This design gives generality to SPECORB. Instead of using the scripts corresponding to each of the ready-made components outlined above, it is possible to make other scripts on the fly by importing the master file as, e.g., "SPF", and performing any of the desired operations, e.g., "SPF.ccf" to calculate the raw cross correlation function between two signals. However, note that the required input and output files of the ready-made components to SPECORB are all aligned so each step can be performed without requiring intermediate organisation of input data. This retains automatic flow throughout the full procedures. The way the code handles output files further depends on whether orders are treated individually or there is one RV per observation. The full code relies heavily on NUMPY (Harris et al., 2020).

```
Radial Velocitiy Input File:       Notes
============================       ========================

target folder:    merged_spectra   # Folder containing spectra (see note below)
target name:      merged_spec      # prefix of spectra names   (same for all)
time stamp file:  data_files/times # file containing time stamps
method:           todcor           # either todcor or onecore
orders:           1,               # 1 order means spectra are merged or grating
period:           2.163901775      # input guesses for initial fit
t_zero:           56308.3040718    # ...
e:                0.012            # ...
w:                90.0             # ...
light ratio:      None             # This is fixed or calculated by todcor
out folder:       RV_files         # folder to store output folders/files
observations:     33               # number of observations to perform operations
scale:            lambda           # wavelength scale of axis (lambda or exp)

template1
----------
template1 folder:    synthetics                           # Folder containing templates
template1 name:      Hamilton_v0_T6964_g3.873_m0.0.dat  # name of template
vsini1:              46.33                                # broadening to apply (km/s)
LD1:                 0.6                                  # LD to apply to to template
rad1:                None                                 # RV of template


template2
-----------
template2 folder:    synthetics                  # same as above for second template
template2 name:      Hamilton_v0_T6840_g3.761_m0.0.dat  # required if using todcor
vsini2:              57.15
LD2:                 0.6
rad2:                None

show plot:           False

Notes
=================

-target folder  - This is the path to the location of the
                  spectra that will be used for the velocity
                  extraction. Spectra should be saved in ASCII
                  format column wise; col1 = wavelegnth, col2 = flux

-target name    - This is the name of the observations. You
                  must ensure that your spectra are named with the
                  corresonding formation when merged or saved individually:

       merged     | "<name>_<No._obs>.dat"   (where No._obs = No. of observation).

       individual | "<name>_<No.obs>_<No.order>.dat" (where No._order = No. of order).

       Examples   |  spectrum_1.dat  spectrum_1_56.dat
```

2.2.5 Spectral Disentangling

Spectral disentangling is an extension of the spectral separation technique which is used to *separate* a composite binary star spectrum into its constituent primary and

secondary components. The observed flux y_i at the location λ_i is the sum of the component fluxes plus some observational noise (Ilijić, 2003),

$$y_i = \rho\sigma + \sum_{k=1}^{n_*} l_k \hat{x}_k((1-\beta_k)\lambda_i, \{x_{k\alpha}\}), \tag{2.17}$$

where l_k is the fractional contribution of component k to the continuum, ρ is a random number drawn from a unit variance normal distribution, σ is the uncertainty in the flux measurement, the function $\hat{x}_k((1-\beta_k)\lambda_i, \{x_{k\alpha}\})$ represents the spectrum of component k and estimates its amplitude at λ_i according to a set of M_k parameters $x_{k\alpha}$, $\alpha = 1, ..., M_k$, and within the function, β_k is the radial velocity of component k due to the orbital motion of the system in units of the speed of light. The integer n_* is *2* for the purposes of this discussion regarding SB2 binary stars.

Then for J observations we have a set of equations of the form Eq. 2.17, each linear in the sum of the two sets of parameters M_1 & M_2. The system of equations can be solved for $x_{k\alpha}$ at every i_{th} pixel, $i = 1, ..., N$, where N is the total number of pixels, thus reconstructing the component spectra. When modelling real data, rather than an exact solution, we minimise the sum of the square residuals between the observed and calculated model, which in this case, neglecting the noise, follows (Ilijić, 2003):

$$r^2 = \sum_{j=1}^{J}\sum_{i=1}^{N}\left(y_{ij} - \sum_{k=1}^{n_*} l_k \hat{x}_k((1-\beta_{kj})\lambda_{ji}, \{x_{k\alpha}\})\right)^2, \tag{2.18}$$

Hence, Eq. 2.18 comprises a system of $J \times N$ coupled linear equations in $2 \times N$ unknowns, i.e., the two component fluxes at every i_{th} pixel (Hadrava, 2009; Simon & Sturm, 1994).

The spectral separation technique assumes that the RV values are known. However, is is possible to allow the β_{kj} values to be free parameters and optimised throughout the procedure. This is spectral disentangling and can be performed in the wavelength domain as in Simon & Sturm (1994) or the Fourier domain as first proposed by Hadrava (1995). The advantage of using the Discrete Fourier Transform (DFT) is that the system can be uncoupled into $\frac{1}{2}N + 1$ systems, each with two unknowns (Hadrava, 2009; Ilijic et al., 2004). In order to retain stability in the procedure, it is preferred to optimise the orbital parameters instead of the individual RVs such that the resulting

β_{kj} values are calculated using the standard equations of orbital motion (see Section 1.1.2.4).

2.2.6 Atmospheric Analysis

Studying the stellar atmosphere entails modelling stellar spectra, which requires an understanding of what shapes the continuum and how spectral lines are formed, as well as their behaviour in response to different stellar conditions. Line profiles contain information about atmospheric conditions because they depend on the atmospheric temperature and pressure, as well as the abundances of chemical species, which further depend on mass and age as well as other physics governing the structure of stars (Gray, 2005). Since the atmosphere provides the boundary conditions for stellar models, a complete understanding is essential for the accuracy of stellar evolution theory.

2.2.6.1 The Stellar Continuum and Spectral Lines

The stellar continuum is shaped by the continuous absorption coefficient κ_ν which is dominated by absorption from bound-free transitions of neutral hydrogen in B- A- and F-type stars, giving rise to certain features. The Balmer jump signifies a drop in opacity when wavelengths exceed 3646 Å because the energy of such photons is not sufficient to ionise hydrogen from the $n = 2$ level (see Fig 2.9), and this transition no longer contributes to κ_ν (see Fig. 2.10). Free-free transitions and stimulated emission also influence continuous opacity. In cooler stars, the absorption from neutral hydrogen diminishes and absorption from negative hydrogen (and potentially molecular absorption and Rayleigh scattering) increases (Gray, 2005).

Spectral line shapes and strengths depend on various factors, including atomic absorption coefficients α_ν associated to bound-bound transitions of a chemical species. Line broadening mechanisms, e.g., natural, pressure, and thermal broadening affect line profiles via their contributions in shaping α_ν. *Microturbulence* and *macroturbulence* account for the motions of turbulent cells that are smaller and larger, respectively, than

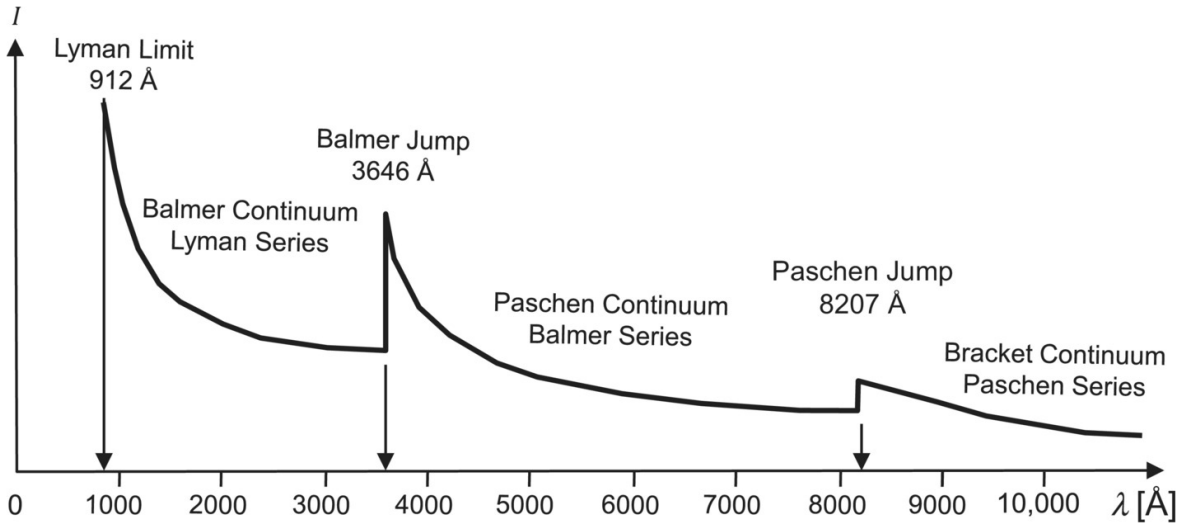

Figure 2.9: The variation of the intensity of the stellar continuum as a function of wavelength. Indicated are the limits associated with the Bracket (ionization from $n = 4$), Paschen (ionisation from $n = 3$), Balmer (ionisation from $n = 2$) and Lyman (ionisation from $n = 1$) continua. From Trypsteen & Walker (2017).

a unit optical depth (Gray, 2005). Microturbulence acts to increase the thermal broadening component of α_ν and in this way, enters the radiative transfer equation. Like rotation, macroturbulence does not influence α_ν or specific intensity calculations. The overall line profile is the convolution of the intrinsic profile with those of macroturbulence and rotation. Rotation dominates for values exceeding $\approx 13\,\mathrm{km\,s^{-1}}$ (Landstreet et al., 2009) so macroturbulence probably isn't detectable in δ Scuti stars.

Calculation of the overall line absorption coefficient l_ν entails further accounting for the abundances of individual species as well as their excitation and ionisation states. Considering the addition of l_ν to κ_ν, the emergent flux can then be mapped as a function of wavelength across a spectral line, thus permitting the calculation of theoretical spectral lines. Weak lines' strength is proportional to abundance until saturation, after which pressure broadening dominates (see Fig. 2.11). Strong lines increase in strength approximately as the square root of abundance beyond saturation. Pressure plays a role in pressure-related broadening mechanisms for strong lines. In general,

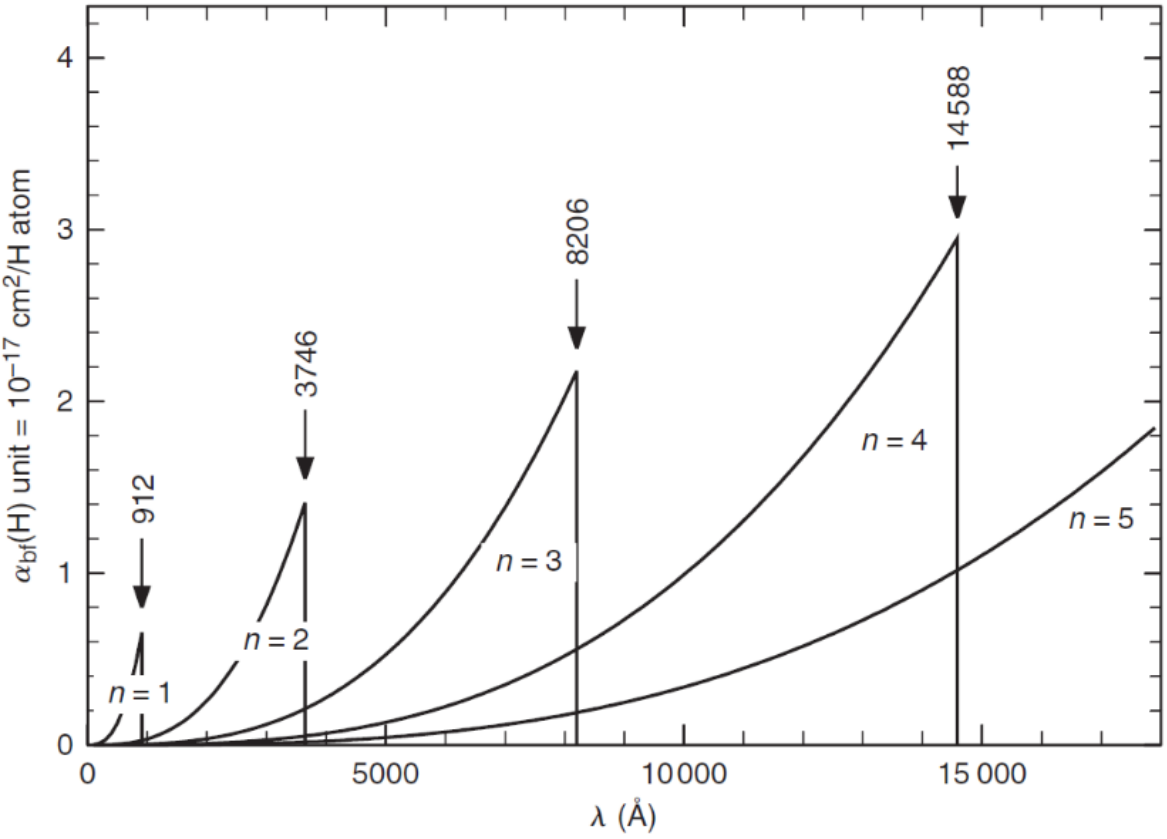

Figure 2.10: Individual absorption coefficients associated with each of the transitions which contribute to the continuum flux in Fig. 2.9. From Gray (2005).

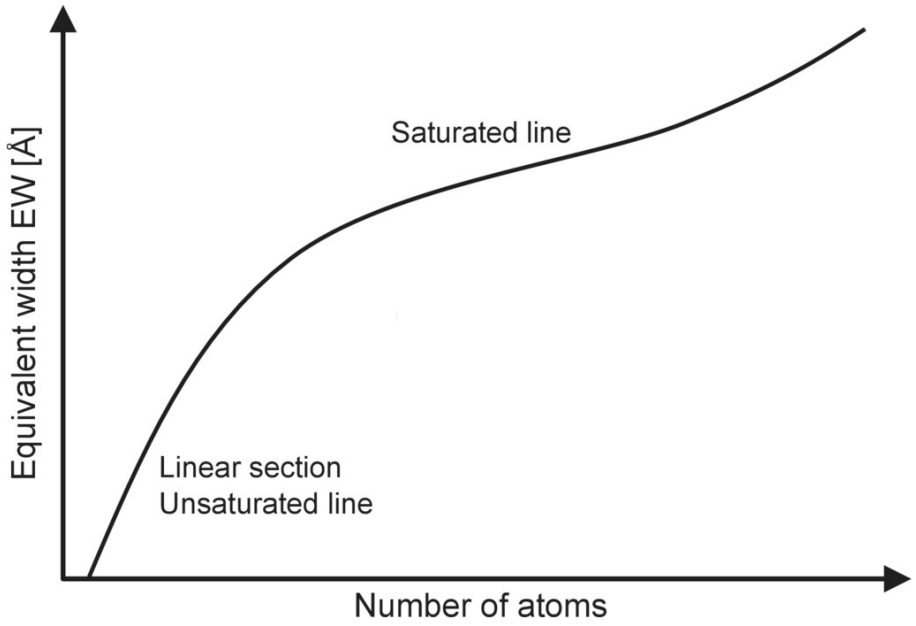

Figure 2.11: A representation of the a curve of growth. From Trypsteen & Walker (2017).

decreasing surface gravity reduces pressure and continuous opacity, leading to increased line strength. Pressure's effect on line strength is generally weaker than temperature's influence.

Temperature significantly influences line strength through excitation and ionisation processes. Elevated temperatures can increase line strength by enhancing excitation, but they may also induce ionisation, reducing line strength. Temperature's net effect depends on its impact on continuous to line opacity ratios and excitation potentials. The Balmer series exhibits relatively high excitation potential, allowing the strength of Balmer lines to increase beyond temperatures at which most other chemical species become multiply ionised, up to around 9000 K. Since most other chemical species are multiply ionised at these temperatures, their lines tend to appear in the blue and ultraviolet. This makes the spectral region between $4400-4800$ Å suitable for measuring RVs from δ Scuti star spectra ($6500 < T_{\rm eff} < 9500$ K).

2.2.6.2 Atmospheric parameters

The dependencies of the stellar spectrum on the atmospheric conditions, e.g., excitation and ionisation; broadening mechanisms; abundances of chemical elements, are parameterised by $T_{\rm eff}$, [M/H], $v \sin i$, surface gravity $\log(g)$, microturbulence $v_{\rm mic}$ and macroturbulence $v_{\rm mac}$. These parameters can be derived for a star by seeking agreement between a theoretically computed spectrum and an observed one. Deriving the parameters in this way is called a synthetic spectral fit (SSF).

The atmospheric structure needs to be known (i.e, temperature profile $T(\tau)$ and pressure profile $P(\tau)$) or computed, in order to synthesise the spectrum. For an overview of calculating the atmospheric structure of a star, see, e.g., LeBlanc (2010, chapter 4). Libraries of pre-calculated atmospheric structures exist (e.g., MARCS GES, ATLAS9; Gustafsson et al., 2008; Kurucz, 2005; Kirby, 2011; Mészáros et al., 2012). Given a model of the atmospheric structure, computation of a theoretical spectrum requires solving the radiative transfer equation as a function of wavelength in the photosphere. This requires the atomic data for spectral lines so l_ν can be evaluated. The product of the statistical weight g and the oscillator strength f (i.e., the *weighted oscillator strength*, usually the logarithm) is sufficient for line opacity calculations as opacity is proportional to this value (LeBlanc, 2010). Other atomic data concerns the energy levels including degeneracies among them, ionisation energies as well as photoionisation cross sections from the various atomic levels. There are various radiative transfer codes available for the computation of the spectrum (e.g., SPECTRUM, TURBOSPECTRUM, SME, MOOG; Gray & Corbally, 1994; Alvarez & Plez, 1998; Plez, 2012; Valenti & Piskunov, 1996; Piskunov & Valenti, 2017; Sneden et al., 2012).

An alternative method to determine the parameters is the *equivalent width* (EW) method (Takeda et al., 2002), which involves measuring the equivalent widths of individual iron absorption lines and relating these measurements to the free parameters of the atmosphere by imposing; 1, the average iron abundance is equal to the average ionised iron abundance; 2, no trends are found when the abundances are plot against line excitation potential as well as against equivalent width (Blanco-Cuaresma et al.,

2014a). Values for $v_{\rm mac}$ and $v \sin i$ are not determined using this method because this technique is based on the intrinsic line strength derived from the radiative transfer equation which these two broadening mechanisms do not enter.

The ISPEC (Blanco-Cuaresma et al., 2014a) python framework allows users to make use of the libraries of available atmospheric models to carry out the SSF and EW techniques using a choice of radiative transfer codes. On the other hand, CHROMASTARPY (Short et al., 2018) is a tool written in python that allows both atmospheric modelling and spectral synthesis.

2.2.6.3 ispec zj wrapper

The ISPEC ZJ wrapper combines the functionalities of ISPEC allowing for easy use as well as automating the steps involved in modelling atmospheres and measuring abundances. The wrapper allows flexibility in the selection of model atmosphere, fixed and fitted parameters, selected line regions, among other functionalities for which we refer to the notes in the example input file which is given at the end of this section.

The initial resolution of the observation to be analysed needs to be supplied as input, this is then degraded by ISPEC to the resolution of the line list. Either the SSF or the EW method can be selected and used for atmospheric parameter determination. The fast abundance method determines abundances by fitting for all lines of a species contained in the line regions selected for analysis simultaneously, while the slow method does this line by line. The line list contains the atomic data and a multitude of choices are included in ISPEC (see the example input file). This is similarly the case for the choice of atmospheric model. If an atmospheric model is specified, the ISPEC ZJ wrapper carries out the analysis for that model only, but users can specify to use every atmospheric model and statistics on the results will be printed as output.

The free parameters to fit for in the atmospheric modelling are easily specified in the ISPEC ZJ wrapper input file (see below) and initial estimates are either specified or there is the option to estimate them from a pre-computed grid included in ISPEC. One may opt to calculate $v_{\rm mic}$, $v_{\rm mac}$ and α-enhancement using empirical relations.

```
iSpec input file
------------------
Configuration                          NOTES
=====================================  ======================================================
Input                                  - For methods, type 'ssf' or 'ew'
------                                 - For abundances, type 'fast', 'slow' or 'None'
spectrum file:      MGIII_pri.dat      - For line list, choose an option from below.
method:             ssf                - For atmospheres, choose option from below
initial resolution: 85000              - For estimates, type 'grid' or 'specified':
abundances:         fast                        > if grid - initial guesses estimate from grid.
line list:          GESv6_atom_hfs_iso.420_920nm   > if specified - initial guesses are specified in
atmosphere:         all                           free parameters section next to 'fixed' or 'free'
estimates:          specified
lines:              all                - For free parameters, type 'free' to fit them
empirical vmac:     False                or 'fixed' to fix them (Initial guesses and fixed
empirical vmic:     False                values are specified on the same line).
enhance alpha:      False
output path:        MGIII/primary_MH/  - Line lists:                      _
                                         > GESv6_atom_hfs_iso.420_920nm |
                                         > SPECTRUM.300_1100nm          |
                                         > VALD.300_1100nm              | DO NOT ERASE THESE!
Free parameters                                                         | YOU NEED TO COPY THESE
---------------                        - Atmospheres:                   | OPTIONS EXACTLY AS
Teff:               fixed  7834          > MARCS.GES                    | WRITTEN HERE...
logg:               fixed  3.982         > ATLAS9.Castelli              |
MH:                 free   0.00          > ATLAS9.APOGEE                |
vmic:               fixed  3.011         > ATLAS9.Kurucz                |
vmac:               fixed  0             > ATLAS9.Kirby                 |
vsini:              fixed  43.6          > all                         _|
Resolution:         fixed  85000
vrad:               fixed  0.0         - lines specifies which spectral regions will be included
LD:                 fixed  0.6           in the fit; choose either:
alpha:              free   0.04             - metal       all in line list of pre selected lines.
                                             - hydrogen    all hydrogen lines
                                             - MgII4481A   MgII A line at 4481 angstroms
                                             - all         every line in the spectral range
                                          Note- custom line regions can and have been added.

                                          - For empirical vmac, vmic and enhance alpha,
                                            use True or False.
```

3 Physical properties of the eclipsing binary KIC 9851944 and analysis of its tidally-perturbed p- and g-mode pulsations

The work outlined in this chapter has been published in the Monthy Notices of the Royal Astronomical Society (MNRAS) main journal (Jennings et al., 2023b).

3.1 Introduction

KIC 9851944 is an EB showing δ Scuti/γ Doradus hybrid pulsation signatures. Therefore, the object is an ideal candidate for testing our understanding of stellar structure and evolution given the large amount of constraints that can be obtained due to the advantages associated with hybrid behaviour as well as binarity. KIC 9851944 is included in the *Kepler* Eclipsing Binary Catalogue (KEBC; Prša et al. 2011; Kirk et al. 2016), as well as a study by Matson et al. (2017) who presented RVs for 41 *Kepler* EBs. Gies et al. (2012, 2015) studied the eclipse times for KIC 9851944 and found no evidence of apsidal motion or a third body; the object was also included in a catalogue of precise eclipse times of 1279 *Kepler* EBs by Conroy et al. (2014).

Guo et al. (2016) combined the analysis of *Kepler* photometry with medium-resolution spectra ($R = \lambda/\Delta\lambda \sim 6000$) to determine the atmospheric and physical properties of KIC 9851944; we list these results in Table 3.10. Evolutionary modelling based on these properties shows the post-MS secondary to be more evolved than the MS primary. The authors concluded that both components show δ Scuti type pulsations, which they interpreted as p modes and p and g mixed modes, and attempted to identify the modes by comparison with theoretically computed frequencies; the range of theoretically predicted unstable modes agreed roughly with observations but the authors conclude that mode identification is still difficult in δ Scuti stars, even with

constrained mass, radius and $T_{\rm eff}$.

This work aims to be complementary to the work by Guo et al. (2016) on KIC 9851944; we additionally include observations by TESS in our photometric analysis and combine this with the analysis of high-resolution ($R = 60000$) spectroscopic observations. Section 3.2 outlines the photometric and spectroscopic observations. We determine the orbital ephemeris based on the photometric observations in Section 3.3. In Section 3.4, we analyse RVs derived from the spectroscopic observations and in Section 3.5, we present the spectroscopic analysis. The analysis of the photometric light curves is given in Section 3.6 and in Section 3.7 we present the physical properties of the system. An investigation of the pulsations is given in Section 3.8. The discussion and conclusion are given in Sections 3.9 and 3.10, respectively.

3.2 Observations

3.2.1 Photometry

KIC 9851944 was observed by *Kepler* in six quarters (0, 12, 13, 14, 16, 17) in short cadence mode between May 2009 and May 2013. The object was also observed by TESS in sectors 14, 15, 41, 54, 55 and 56 between July 2019 and September 2022. Details regarding the *Kepler* and TESS missions are given in Sections 2.1.3 and 2.1.4, respectively.

The light curves from the *Kepler* quarters and TESS sectors mentioned above were downloaded from the Mikulski Archive for Space Telescopes (MAST) and are used in Section 3.3 to determine the ephemeris of the system, as well as Section 3.6 to obtain the final model of the light curve. Both SAP and PDCSAP measurements are available; the SAP and PDCSAP fluxes were similar, which we verified by inspecting the SAP fluxes with the PDCSAP fluxes over-plotted after dividing them by their median flux values to put them on the same scale. Thus, we used the SAP measurements to avoid possible biases due to the additional processing applied to the PDCSAP data. A

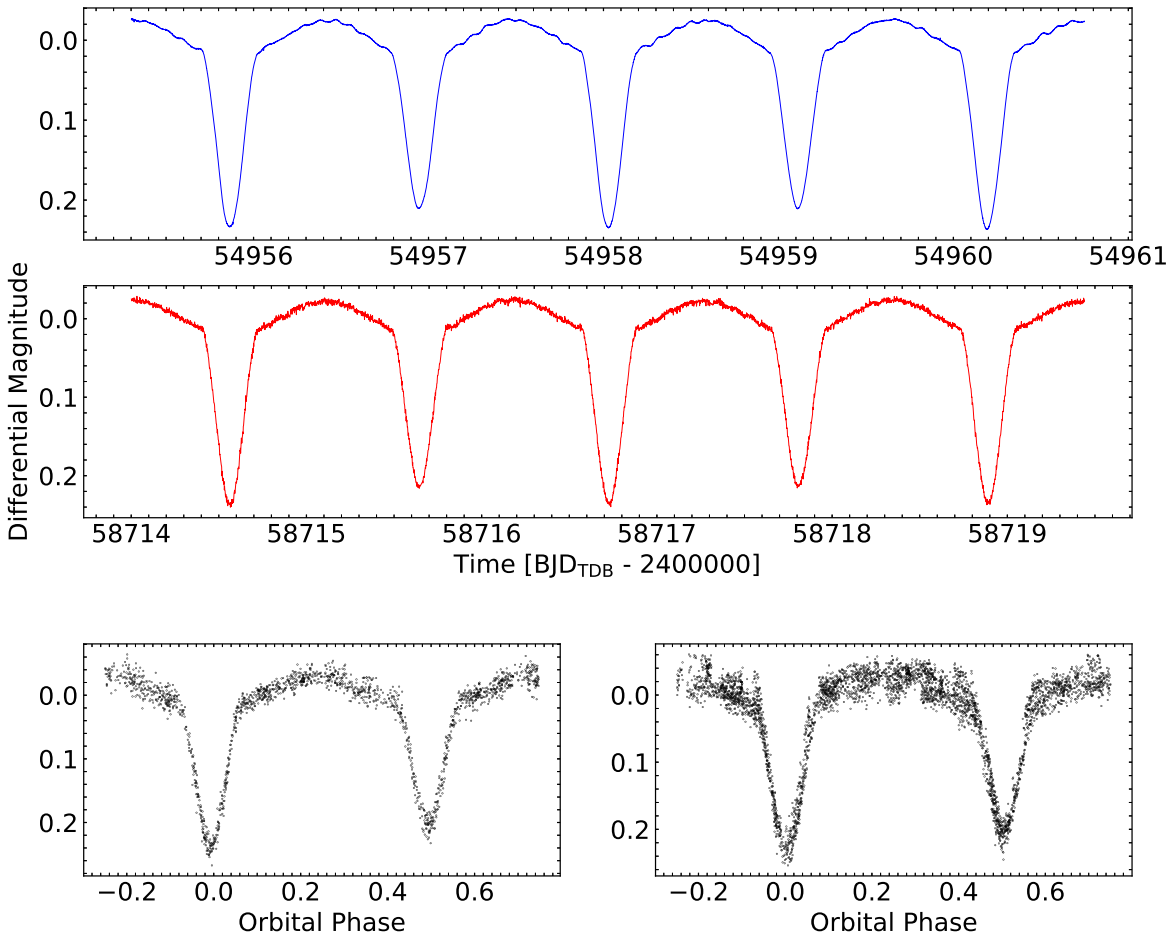

Figure 3.1: Parts of the *Kepler* Quarter 0 (top panel) and TESS Sector 15 (middle panel) processed light curves. Also shown in the bottom panels are the phase-folded light curves observed by WASP between May 2007 and July 2007 (left), and between June 2008 and July 2008 (right).

second-order polynomial was fitted to fluxes that correspond to positions of quadrature, i.e., the maximum of the ellipsoidal brightening, to estimate systematic trends present in the light curves. Subtracting the difference between this polynomial and the median flux of the light curve yields a model for the local median level of out-of-eclipse flux. This model was then divided out to remove systematic trends. The residual value of a smoothed version of the light curve subtracted from the observed light curve was calculated and observed fluxes that deviated by more than 1% were rejected. Fluxes were converted to magnitudes and errors were propagated following Prša (2018). The short cadence *Kepler* light curve from Quarter 0 and the two-minute cadence TESS light curve from Sector 15, after performing these operations, are shown in the top and middle panels of Fig. 3.1, respectively.

KIC 9851944 was also observed by the Wide Angle Search for Planets (WASP) telescope (Butters et al., 2010) between May 2007 and July 2010. WASP consisted of two robotic observatories, one in the Nothern Hemisphere at Observatorio del Roque de los Muchachos on La Palma and the other at the South African Astronomical Observatory (SAAO), each with eight 20 mm telescopes on a single mount. Observations of KIC 9851944 collected by WASP between May 2007 and July 2007 as well as between June 2008 and July 2008 are shown in the bottom panels of Fig. 3.1 phase folded about the orbital period determined in Section 3.3. The data collected by WASP for KIC 9851944 were only used to constrain the times of primary minima when performing preliminary fits to the *Kepler* and TESS light curves in Section 3.3, to determine the orbital ephemeris.

3.2.2 Spectroscopy

The following spectroscopic observations were obtained by Dr. John Taylor (2012) and Dr. Kelsey Clubb (2012 and 2013).

A set of 33 spectroscopic observations were obtained for the target using the Hamilton échelle spectrograph (Vogt, 1987) on the Shane 3 m telescope at Lick Observatory during two observing runs, one in July 2012 and the other in June 2013. The

data were obtained using CCD chip no. 4, giving a wavelength coverage of 340 – 900 nm over 89 échelle orders at a resolving power of $R \approx 60000$.

The data were reduced using the standard pipeline for the spectrograph (e.g. Fischer et al., 2014). Flat-fields were obtained with a quartz lamp and divided from the spectra. The wavelength calibration was obtained from exposures of a thorium-argon emission lamp taken roughly every hour during the night.

Details for the normalisation of the one-dimensional extracted spectra are given in Sections 3.4 and 3.5 because each of those components of the analysis used different approaches.

Table 3.1 gives the epochs of each of the 33 spectrosopic observations as well as the signal-to-noise ratio (S/N), estimated as the square root of the counts close to the peak of the best-exposed échelle order. Also given are the corresponding RVs of each component that are derived in Section 3.4.

3.3 Orbital ephemeris

A first model of the *Kepler* and TESS light curves was obtained using the JKTEBOP code (Southworth, 2013) (see Section 2.1.5.2). We fitted for the period P, epoch T_0, surface brightness ratio J, sum of the fractional radii $r_{\rm A} + r_{\rm B}$, ratio of the radii $k = \frac{r_{\rm B}}{r_{\rm A}}$, inclination i, the Poincaré elements $e\cos\omega$ and $e\sin\omega$, and a light scale factor. We define star A to be the star eclipsed at the primary (deeper) minimum and star B to be its companion.

We also fitted for the linear coefficients u of the quadratic limb darkening (LD) law while quadratic terms were taken from Claret & Bloemen (2011) and Claret (2017) for the *Kepler* and TESS bands, respectively; we used the estimated atmospheric parameters reported in the KIC to choose the appropriate values for the quadratic coefficients. We performed fits to the WASP light curve but the lower quality of these data compared to the *Kepler* and TESS light curves means that including these results in the calculation of the overall preliminary eclipse model would lead to less

Table 3.1: RVs and S/N corresponding to the spectroscopic observations taken at times given in the BJD column. An asterisk next to the BJD value means that observation was not used to derive the orbital parameters in Section 3.4.

BJD	RV Star A	RV Star B	S/N
2456133.71296	-122.47 ± 1.33	103.45 ± 1.14	59
2456133.72724	-119.89 ± 1.37	101.95 ± 1.08	59
2456133.74151	-118.46 ± 1.26	99.54 ± 1.03	57
2456133.75578	-114.54 ± 1.21	96.79 ± 0.93	57
2456133.80101	-104.26 ± 1.28	87.87 ± 1.13	60
2456133.83920	-94.81 ± 1.26	79.68 ± 1.25	58
2456133.87945	-84.36 ± 1.02	71.67 ± 1.67	59
2456133.90977	-77.35 ± 1.31	63.03 ± 1.97	58
2456133.94924	-64.66 ± 1.51	51.37 ± 2.85	60
2456133.98702*	-41.04 ± 5.71	34.50 ± 5.52	57
2456134.70808	117.69 ± 1.01	-121.35 ± 1.39	57
2456134.72235	116.88 ± 0.88	-120.01 ± 1.68	59
2456134.73662	116.27 ± 0.92	-119.12 ± 1.65	58
2456134.75090	114.89 ± 0.81	-118.39 ± 1.66	55
2456134.78975	109.50 ± 0.96	-113.29 ± 1.81	53
2456134.82917	104.240 ± 1.02	-107.26 ± 1.72	50
2456134.86653	97.71 ± 0.94	-99.91 ± 1.60	56
2456134.91057	86.88 ± 0.84	-91.01 ± 1.74	53
2456134.94964	77.43 ± 1.15	-82.09 ± 1.50	54
2456134.98739	65.92 ± 1.34	-72.46 ± 1.18	52
2456469.93848	115.04 ± 1.08	-115.25 ± 1.17	31
2456469.97977	115.86 ± 0.98	-120.41 ± 1.65	55
2456470.72325*	-41.06 ± 2.92	29.87 ± 5.18	41
2456470.79028	-69.87 ± 1.09	56.92 ± 2.79	35
2456470.84339	-84.53 ± 0.94	69.97 ± 1.69	57
2456470.90594	-101.34 ± 1.04	83.79 ± 1.11	56
2456470.96852	-116.02 ± 1.22	95.28 ± 1.17	57
2456470.99830	-121.03 ± 1.23	99.82 ± 1.12	54
2456471.71677*			43
2456471.77503*	19.52 ± 2.84	-29.63 ± 2.40	30
2456471.87251	58.97 ± 1.67	-68.30 ± 1.74	50
2456471.90957	69.15 ± 1.34	-79.35 ± 1.53	54
2456471.93874	79.31 ± 1.00	-85.78 ± 1.15	54

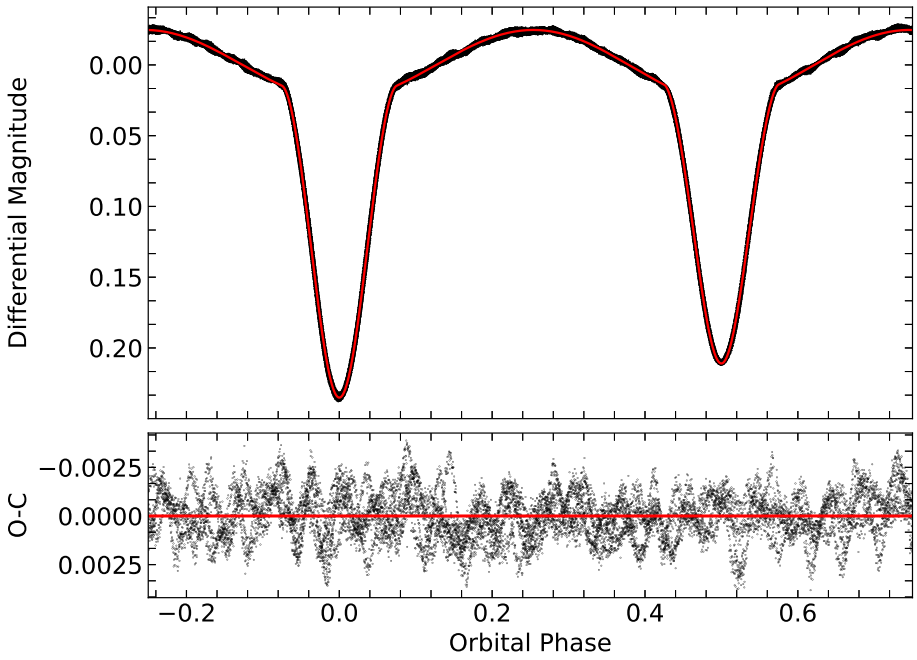

Figure 3.2: JKTEBOP model fit to the phase folded *Kepler* light curve from quarter 0.

well determined parameters. Thus, we simply include the epochs of primary minimum estimated from the WASP light curves as additional observational constraints on T_0 in the preliminary fits to the *Kepler* and TESS light curves.

The adopted values for the light curve parameters from this preliminary analysis were taken as the weighted averages of the results from the fits to the individual *Kepler* quarters and TESS sectors, where the reciprocal of the squared errors from the covriance matrix were used as weights. These values are given in Table 3.2, and Fig. 3.2 shows the fit to the *Kepler* Quarter 0 light curve; high-frequency variability due to pulsations of the δ Scuti type is clearly visible at all orbital phases in the residuals shown in the lower panel, with amplitudes of around ± 0.2 mmag.

The value for $r_{\rm A} + r_{\rm B}$ in Table 3.2 suggests that the components of KIC 9851944 are deformed beyond the limits of applicability of the biaxial ellipsoidal approximation (Popper & Etzel, 1981) due to their close proximity and thus strong mutual deformations; the ellipsoidal variation (~ 0.04 mag) observed in Fig. 3.1 and Fig. 3.2 is an-

Table 3.2: Prelimimary light curve results from JKTEBOP fits to the *Kepler* and TESS light curves. We do not present the error bars of the parameters in Table 3.2 for two reasons. First, the uncertainties from the covariance matrix of a light curve fit are notoriously underestimated and the results from these preliminary fits are not reliable (see below) so we did not attempt to derive better uncertainties. Second, excluding the error bar from the result makes it clear that these are not our final values for the light curve parameters.

Paramter	Value
J	0.7956
$r_A + r_A$	0.5091
k	1.591
$i(^\circ)$	74.294
$e\cos\omega$	-0.000120
$e\sin\omega$	-0.012329
u_A	0.684
u_B	0.310

other indication of this. Furthermore, plotting the results from individual quarters and sectors against each other reveals strong degeneracies between the fitted parameters, specifically $r_\mathrm{A} + r_\mathrm{B}$, k, i, J and the LD coefficients. This is highlighted by the results giving a wide range of ratios of the light contributions of the two stars. Therefore, we present a detailed analysis of the *Kepler* and TESS light curves using a more sophisticated modelling code, as well as constraints on the light ratio $\ell_\mathrm{B}/\ell_\mathrm{A}$ from our spectral analysis, to reliably determine the light curve solution in Section 3.6.

Among the reliably constrained parameters from this preliminary analysis are the period and epochs of primary minimum from individual quarters and sectors. Therefore, the analysis is useful for establishing the orbital ephemeris. A linear ephemeris was fit to the resulting values of T_0 against orbital cycle using the reciprocal of the squared errors from the covariance matrix as weights; these errors were rescaled during the fitting procedure to yield a reduced chi-squared value of $\chi^2_\nu = 1$. Fig. 3.3 shows the residuals of the fit and the red line represents the linear ephemeris.

There seems to be a trend in the O-C diagram compared with the linear ephemeris,

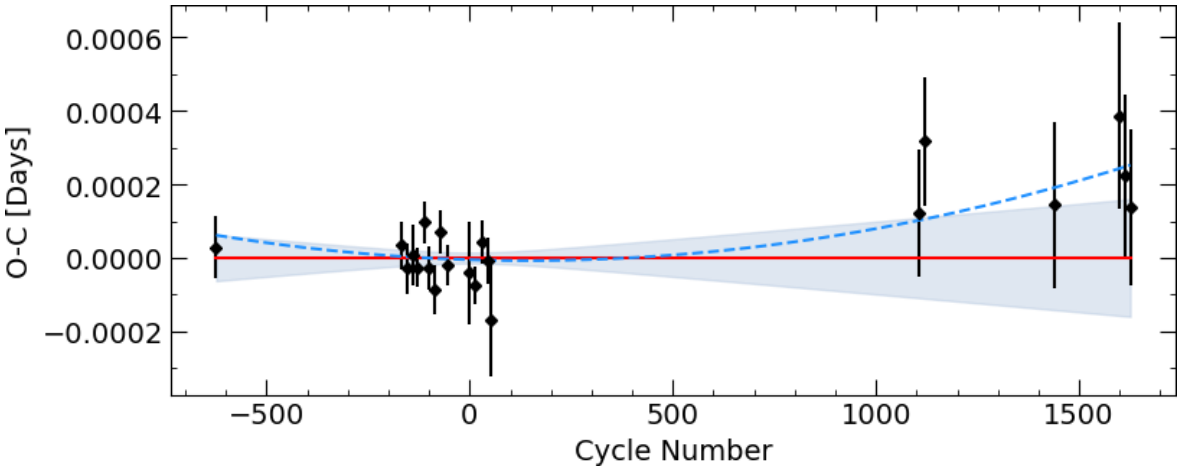

Figure 3.3: O-C plot from the linear fit (red line) to the times of primary minimum (black dots), where the grey shaded region represents $1\,\sigma$ uncertainty associated with the corresponding calculated values.. The blue dashed line represents an attempt to additionally fit for a quadratic term.

with data points corresponding to TESS observations (>1000 cycles) all appearing above the red line. Thus, we also attempted to fit for a quadratic ephemeris, which is represented by the blue dashed line in Fig. 3.3. However, the corresponding quadratic term was a similar size to its errorbar. We therefore decided to stick with the linear ephemeris which was measured to be:

$$\text{Min I}\,(\text{BJD}_{\text{TDB}}) = 2456308.304072(14) + 2.163901775(98)\,\text{E}.$$

3.4 Radial velocity analysis

The spectral range between $4400-4800\,\text{Å}$ is a suitable region to carry out the RV extraction procedure for A- and F-type stars because there are many well-resolved spectral lines (see Section 2.2.6.1) and the region does not contain any wide Balmer lines. Thirteen échelle orders within this range were cosmic ray corrected, deblazed and merged as outlined in Chapter 2.2.

Preliminary estimations for the projected rotational velocity, $v \sin i$, of the components of KIC 9851944 were obtained by cross correlating the observed spectra with a template broadened to a range of $v \sin i$ values between 0 and $150\,\mathrm{km\,s^{-1}}$ in steps of $10\,\mathrm{km\,s^{-1}}$. Observations taken less than 0.125 orbital phases from the eclipses were excluded to minimise issues arising due to lines from each component blending or being eclipsed. Interpolating the peak heights of the correlation functions and taking the maximum yields $v \sin i_{\mathrm{A}} = 46.3 \pm 0.4\,\mathrm{km\,s^{-1}}$ and $v \sin i_B = 57.2 \pm 0.5\,\mathrm{km\,s^{-1}}$ for the primary and secondary component, respectively. These values for $v \sin i$ were then used and applied to synthesise primary and secondary templates using the ISPEC code (Blanco-Cuaresma et al., 2014b). In the first iteration, the T_{eff} and $\log(g)$ values were taken from the Kepler Input Catalogue (KIC). For the final iteration of the RV extraction, the atmospheric parameters of the templates corresponded to those derived from our atmospheric analysis of the disentangled spectra (see Section 3.5.1.)

Our own implementation of the TODCOR two-dimensional algorithm was used to extract the RVs (see Section 2.2.3.1). Systematic errors arise when using the cross-correlation technique to extract RVs because neighbouring peaks and side-lobes in the doubled-peaked CCF disturb each other, and this is related to blending between the spectral lines of the two components (Andersen, 1975a; Latham et al., 1996). We obtained corrections and added them to our measured RVs as outlined in Section 2.2.3.3.

This procedure was iterated multiple times using templates with different atmospheric parameters; the top panel of Fig. 3.4 shows the resulting orbital fit to the corrected velocities that were derived in our final iteration, where we used templates with atmospheric parameters corresponding to those derived in Section 3.5.1, and the results are presented in Table 3.3. The middle panel of Fig. 3.4 shows the residuals of the fit and the lower panel, split into two for the primary and secondary, gives the corrections that were applied to the extracted RVs. RVs with corrections larger than $2.5\,\mathrm{km\,s^{-1}}$ were excluded and are not shown because these RVs correspond to phases of conjunction, where line blending effects are most severe, and negligible information is contained on the velocity semiamplitudes. The fit was constrained to a circular or-

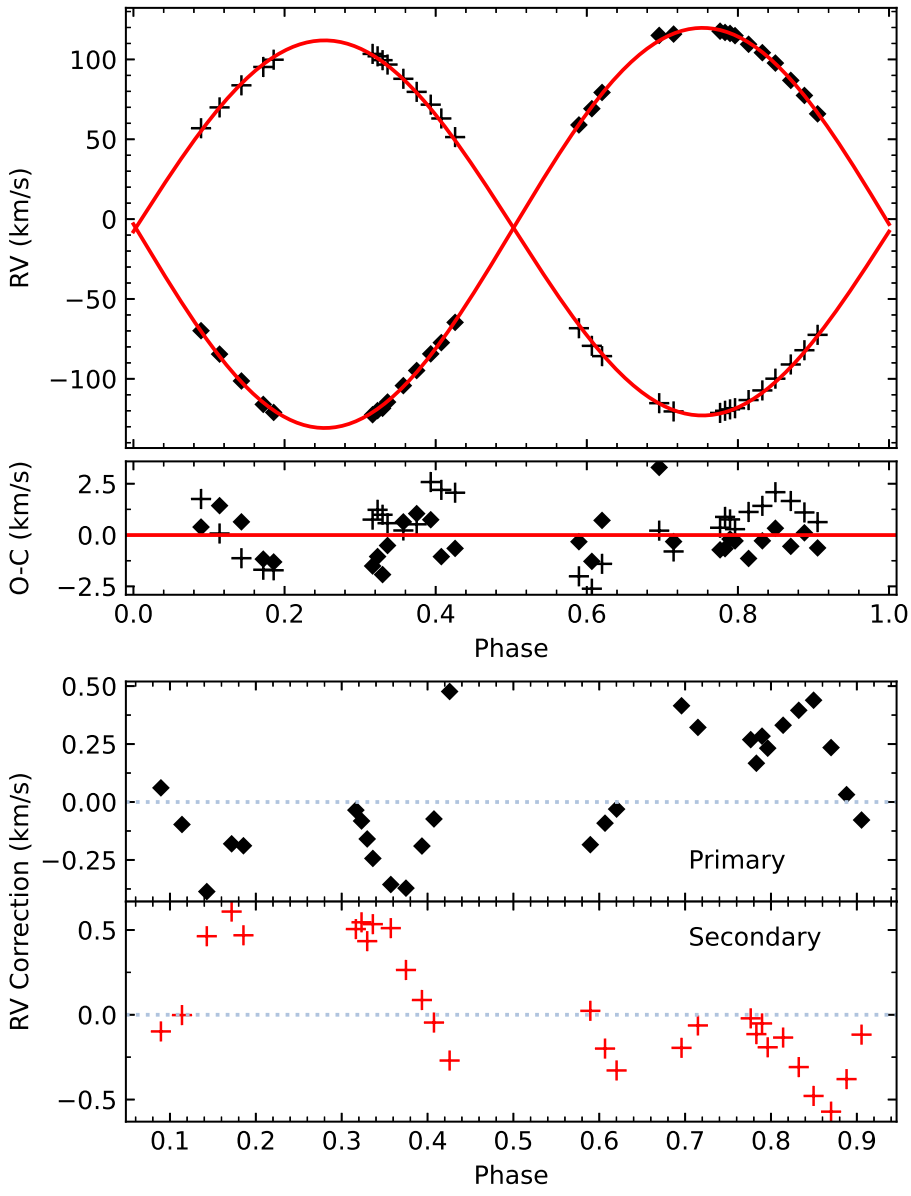

Figure 3.4: Top: orbital fit to the corrected RVs using the merged approach. Bottom: velocity corrections for the corresponding RVs.

Table 3.3: Orbital parameters derived for KIC 9851944.

Parameter	Value
$K_{\rm A}$ (km/s)	125.282 ± 0.269
$K_{\rm B}$ (km/s)	117.453 ± 0.328
γ (km/s)	-5.52 ± 0.16
$\ell_{\rm B}/\ell_{\rm A}$	1.222 ± 0.136

bit because attempts to fit for eccentricity yielded values consistent with zero and the study by Guo et al. (2016) suggests that this system has circularised. The uncertainties on the RV measurements were rescaled by a constant factor during the fitting procedure to yield a χ^2_r of unity. The root mean square (RMS) of the residuals of the fit compared to the RVs for the primary and the secondary are 1.1 $\mathrm{km\,s^{-1}}$and 1.4 $\mathrm{km\,s^{-1}}$, respectively.

The differences between our final results for $K_{\rm A}$ and $K_{\rm B}$ presented in Table 3.3 and those derived from the initial run (both after applying corrections), which used templates with atmospheric parameters corresponding to those from the KIC, was $\sim$ 0.1%. The corresponding difference in $\ell_{\rm B}/\ell_{\rm A}$ was $\sim$ 9%. This shows that the TODCOR light ratio is more sensitive to the atmospheric parameters of the templates than the derived RVs. We added these differences in quadrature, to the uncertainties derived from the covariance matrix of the fit for the orbital parameters, and to the standard error in the mean value of $\ell_{\rm B}/\ell_{\rm A}$ derived from different observations, in our calculation of the parameter error bars in Table 3.3.

Applying the corrections resulted in an increase in the velocity semiamplitudes $K_{\rm A}$ and $K_{\rm B}$ by 0.2% and 0.3%, respectively. This is a small increase, suggesting that TODCOR is less sensitive to blending effects than the one-dimensional cross correlation technique. However, the 0.2% and 0.3% increase in the velocity semiamplitudes translates to a 0.6% and 0.9% increase in the derived masses, which is significant considering that we aim to achieve precisions smaller than these values. This suggests that the corrections are necessary. Furthermore, the corrections are clearly systematic, and de-

pend on the relative Doppler shifts of the components, as shown in the bottom panels of Fig. 3.4.

3.5 Spectral analysis

The following atmospheric analysis was performed by Prof. Kresimir Pavlovski in collaboration with myself, and is included in this thesis because it is an important part the analysis for this object.

3.5.1 Atmospheric parameters

The method of spectral disentangling (SPD) makes it possible to separate the spectra of individual components from a time-series of binary or multiple star spectra (Simon & Sturm, 1994), as outlined in Section 2.2.5. The disentangled spectra are still in the common continuum of the binary system, but can be renormalised if the light ratio between the components is known from other sources, e.g., from the analysis of light curves (Hensberge et al., 2000; Pavlovski & Hensberge, 2005, 2010). Alternatively, the disentangled spectra can be fitted with synthetic spectra to determine the light ratio between the components, and this can be useful for partially-eclipsing systems where there is a degeneracy between the radius ratio and light ratio in the system (Tamajo et al., 2011; Tkachenko, 2015; Pavlovski et al., 2023). In well-determined cases, the precision of the light ratio can approach 1% (Pavlovski et al., 2022).

Since we planned to apply the method of SPD to extract the individual spectra of the components, normalisation of the observed spectra was of critical importance. We used a different approach than that in Section 3.4, where we extracted RVs. Here, we used the dedicated code described in Kolbas et al. (2015). First, the blaze function of échelle orders was fitted with a high-order polynomial function. Then, the normalised échelle orders were merged. When overlapping regions of successive échelle orders are sufficiently long, the very ends were cut off because of their low S/N. Échelle orders

Table 3.4: Determination of the atmospheric parameters from disentangled spectra for the components of KIC 9851944. The surface gravity for each component was fixed to the values determined from light curve and RVs solution as listed in Table 3.7.

Parameter	Hβ	Hα	Metals
Wavelength range (Å)	4750–4890	6500–6600	5120–5220
Primary			
$T_{\rm eff}$[K]	6980±55	6940±70	7205±90
$\log g$ [cgs]	3.873	3.873	3.873
$v \sin i$ [$\mathrm{km\,s^{-1}}$]	56.2	56.22	56.5±1.9
LDF	0.432±0.005	0.434±0.007	0.4390.009
Secondary			
$T_{\rm eff}$[K]	6875±45	6770±65	6990±80
$\log g$ [cgs]	3.761	3.761	3.761
$v \sin i$ [$\mathrm{km\,s^{-1}}$]	67.2	67.2	67.2±1.5
LDF	0.568±0.004	0.566±0.006	0.561±0.009

containing broad Balmer lines, in which it is not possible to define the blaze function with enough precision, were treated in a special way. For these échelle orders, the blaze function was interpolated from adjacent orders. This produces more reliable normalisation in spectral regions with broad Balmer lines than the usual pipeline procedures. For recent applications of this approach, please see Pavlovski et al. (2018, 2023); Lester et al. (2019, 2022); Wang et al. (2020, 2023).

SPD was performed in the Fourier domain with the prescription by Hadrava (1995). The FDBinary code, developed in Ilijic et al. (2004), was applied to the time-series of normalised échelle spectra of KIC 9851944. FDBinary uses the fast Fourier transform approach (see Section 2.2.5) which allows flexibility in selection of spectral segments for SPD whilst still keeping the original spectral resolution. The orbital parameters, specifically $K_{\rm A}$ and $K_{\rm B}$, were fixed to the solution reported in Table 3.3, thus SPD was used in pure separation mode (Pavlovski & Hensberge, 2010). At this point, the reconstructed individual spectra of the components were still in the common continuum of the binary system. A portion of separated spectra for both components in the spectral range 4900 – 5290 Å is shown in Fig. 3.5.

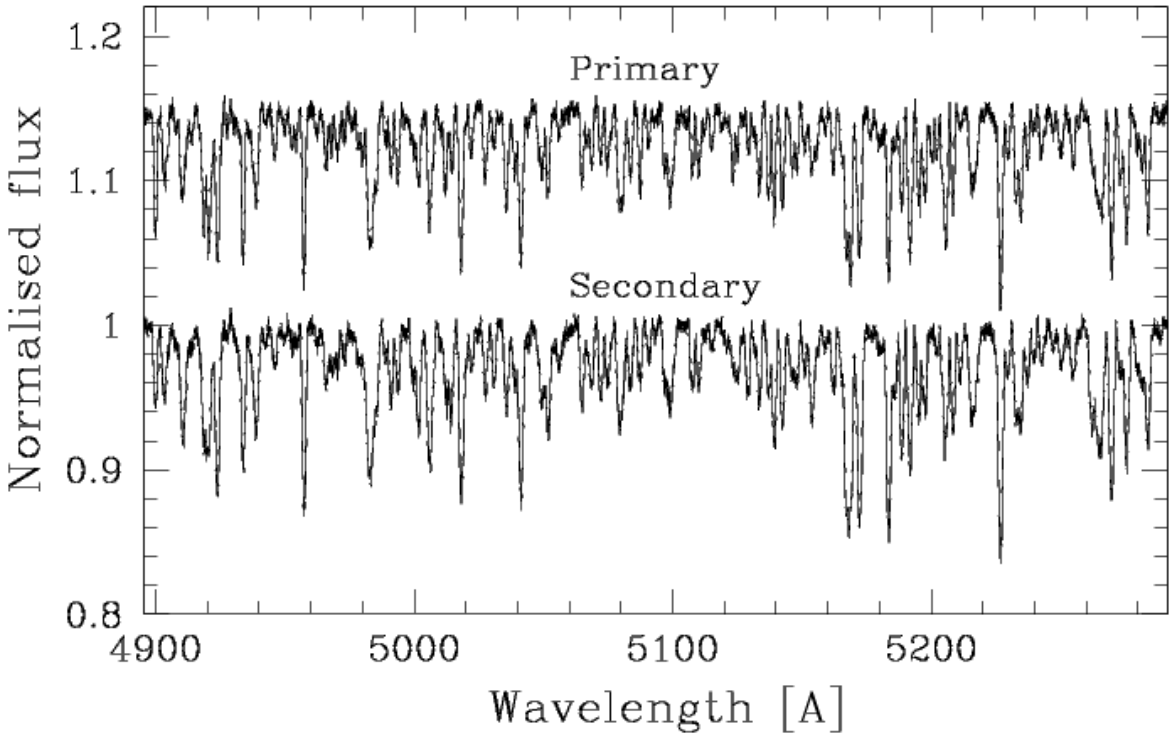

Figure 3.5: Portion of disentangled spectra in the spectral range 4900–5290 Å. The similarity between the spectra of both components is obvious.

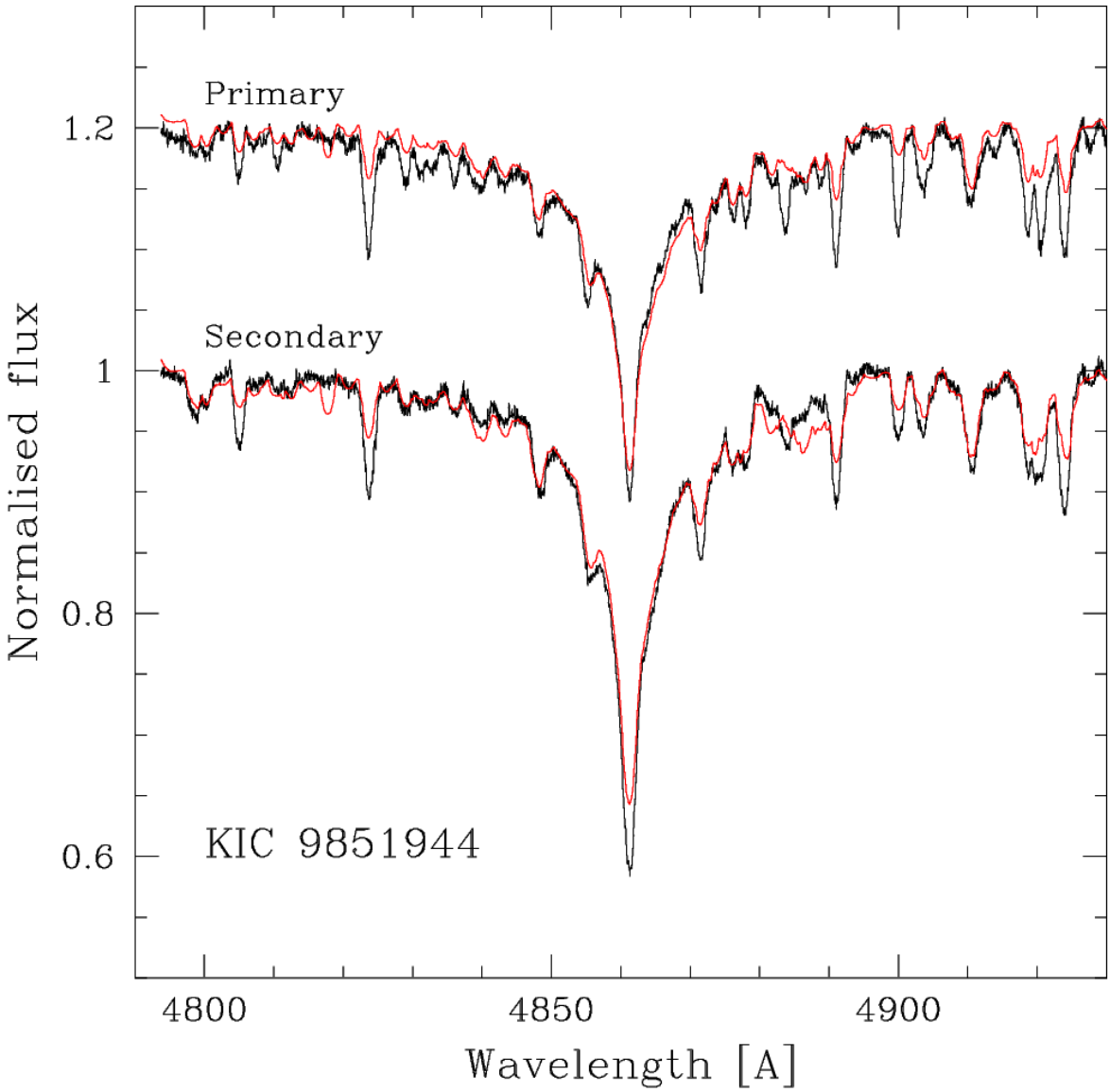

Figure 3.6: Optimal fitting of the wings for Hβ lines in disentangled spectra of binary system KIC 9851944. The spectral lines of metals were masked during the fitting, so were not included in calculations of the merit function. The disentangled spectra are shown in black, and the optimal fits in red.

Overall, a slight difference in line depth between the two components is seen. The more massive component has deeper lines and slightly faster rotation. The Balmer lines are broadened by Stark broadening, and generally are not sensitive to the rotational broadening. Thus, we first optimised portions of the disentangled spectra free of the Balmer lines, primarily to discern the $v \sin i$ values. We then performed optimal fitting of disentangled spectra centred on the Hβ and Hα lines, with fixed $v \sin i$.

It is well-known that the hydrogen Balmer lines are excellent diagnostic tools for the determination of the $T_{\rm eff}$s for stars with $T_{\rm eff} < 8000$ K because the degeneracy with the surface gravity vanishes (Gray, 2005). Moreover, we can use $\log(g)$ determined for the components since this quantity is determined with high precision from the analysis of DLEBs. In the case of KIC 9851944, the $\log(g)$ values are determined with uncertainties of about 0.01 dex, for both components. Therefore, preference is given to the determination of the $T_{\rm eff}$ for the components in KIC 9851944 from line profile fitting of Balmer lines, with fixed surface gravity. This is advantageous over the calculation of the $T_{\rm eff}$ from metal lines because their strength depends on the metallicity of the stellar atmosphere.

Without any appreciable changes in the light ratio in the course of the orbital cycle, i.e. no spectra were observed in eclipse, ambiguity exists in the reconstruction of the components' spectra and only separation of the spectra still in the common continuum of the binary system is possible. The components' spectra are correctly reconstructed but with scaling factors, i.e. the shapes of the spectral lines are correct, but not their strength. In such a case, the light ratio can be determined from fitting the separated spectra with synthetic (theoretical) spectra, in the course of determination of the atmospheric parameters. The optimal fitting was performed in constrained mode, as defined in Tamajo et al. (2011), with the condition that the sum of the light dilution factors is equal to unity. The STARFIT code (Kolbas et al., 2015) uses a genetic algorithm to search for the best fit within a grid of synthetic spectra pre-calculated using the UCLSYN code (Smalley et al., 2001). The uncertainties were calculated using the MCMC approach described in Pavlovski et al. (2018). This task was straightforward due to the fixed surface gravities and $v \sin i$ values: only the light ratio and $T_{\rm eff}$s were

optimised.

The results of the optimal fitting for all three spectral segments are given in Table 3.4. We adopt the weighted average of the results from Hα and Hβ for $T_{\rm eff}$, which is 6964 ± 43 K and 6840 ± 37 K for the primary and secondary, respectively; these values are used to obtain the light curve solution in Section 3.6 and are presented formally in Section 3.7. Our $T_{\rm eff}$ values indicate that the KIC $T_{\rm eff}$ (6204 K) for this object is underestimated, consistent with prior studies (e.g., Molenda-Żakowicz et al., 2011; Lehmann et al., 2011; Tkachenko et al., 2013; Niemczura et al., 2015) reporting similar underestimations for stars with $T_{\rm eff} \sim 7000$ K.

With the $T_{\rm eff}$ determined from the Balmer lines, the depths of the metal lines cannot be matched – the metal lines for both components are slightly deeper than the synthetic spectra for given parameters. This could be explained with the metallicity effect, which affects metal lines more than broad Hβ and Hα lines for which Stark broadening dominates. The effects of metallicity explain the somewhat higher $T_{\rm eff}$ (by about 200 K) found from the metal lines. From a grid of calculated synthetic spectra for given atmospheric parameters derived from Balmer lines, we found that the metallicity for both components is [M/H] ~ 0.15 dex. Since the components of KIC 9851944 are at the cool end of where Am stars are found, this motivated us to disentangle the spectra between 3853 – 4067 Å and compare the Ca K lines to synthetic spectra; the comparison was carried out by Dr. Barry Smalley whose findings did not suggest Am peculiarity although the Ca K line for the primary appears slightly weakened. Due to the relatively high $v \sin i$ for both components, and thus severe line blending, we did not attempt to determine individual elemental abundances.

The light ratio from the optimal fitting of the wings of Hβ and Hγ lines, spectral segments containing only metal lines, and the Mg I triplet at around 5180 Å, are 1.315 ± 0.018, 1.304 ± 0.025 and 1.278 ± 0.033 (Table 3.4). All three values for the light ratio are consistent within their 1σ uncertainties, with the light ratio determined from the wings of the Hβ line being the most precise of the three.

Guo et al. (2016) determined atmospheric parameters from tomographically reconstructed spectra of the components. Their spectra cover the wavelength range

3930 – 4610 Å at a medium spectral resolution of $R = 6000$. The analysis by Guo et al. (2016) was similar to ours, but with an important difference that they fitted complete separated spectra, whilst we concentrate on the wings of Balmer lines. Our results for the Balmer lines corroborate their findings to within 1σ. We also find good agreement for the $v \sin i$ values, which are also within 1σ for both components. Guo et al. (2016) obtained a mean light ratio of $\ell_{\rm B}/\ell_{\rm A} 1.34 \pm 0.03$ from spectra centred at 4275 Å – this is slightly larger than but still consistent with our own results.

3.5.2 Direct fitting for the light ratio

We were initially unable to constrain the light ratio of the system from the photometric analysis alone (see Section 3.3), so estimated it using several independent methods. The first method was the TODCOR light ratio reported in Table 3.3, the second was the optimal fitting of the disentangled spectra (ODS), and a third method is developed here.

We minimise the sum of the squared residuals between synthetic composite spectra and the observed spectra, where the synthetic composite spectra are built by adding Doppler-shifted synthetic spectra weighted by light fractions according to some value of $\ell_{\rm B}/\ell_{\rm A}$, and with atmospheric parameters from the ODS analysis. We search in a grid of $\ell_{\rm B}/\ell_{\rm A}$ values between 0.8 and 2 with ten uniformly spaced samples; these bounds were determined after an initial trial run with bounds of 0.5 to 3. The minimum of a polynomial fit to the sum of the square residuals against trial values for $\ell_{\rm B}/\ell_{\rm A}$ then yields a best estimate for its value. The only free parameters of the minimisation for each trial $\ell_{\rm B}/\ell_{\rm A}$ were the coefficients of a sixth-order polynomial that was used to normalise the observed spectra against the synthetic spectrum. The applied Doppler shifts were fixed according to the corresponding RV values derived in Section 3.4. The minimisation was carried out using the Nelder-Mead method as implemented in the Scipy python package MINIMIZE (Virtanen et al., 2020).

We repeated the process for all spectral orders showing sufficient well-resolved lines in regions unaffected by tellurics from Earth's atmosphere. To save computing

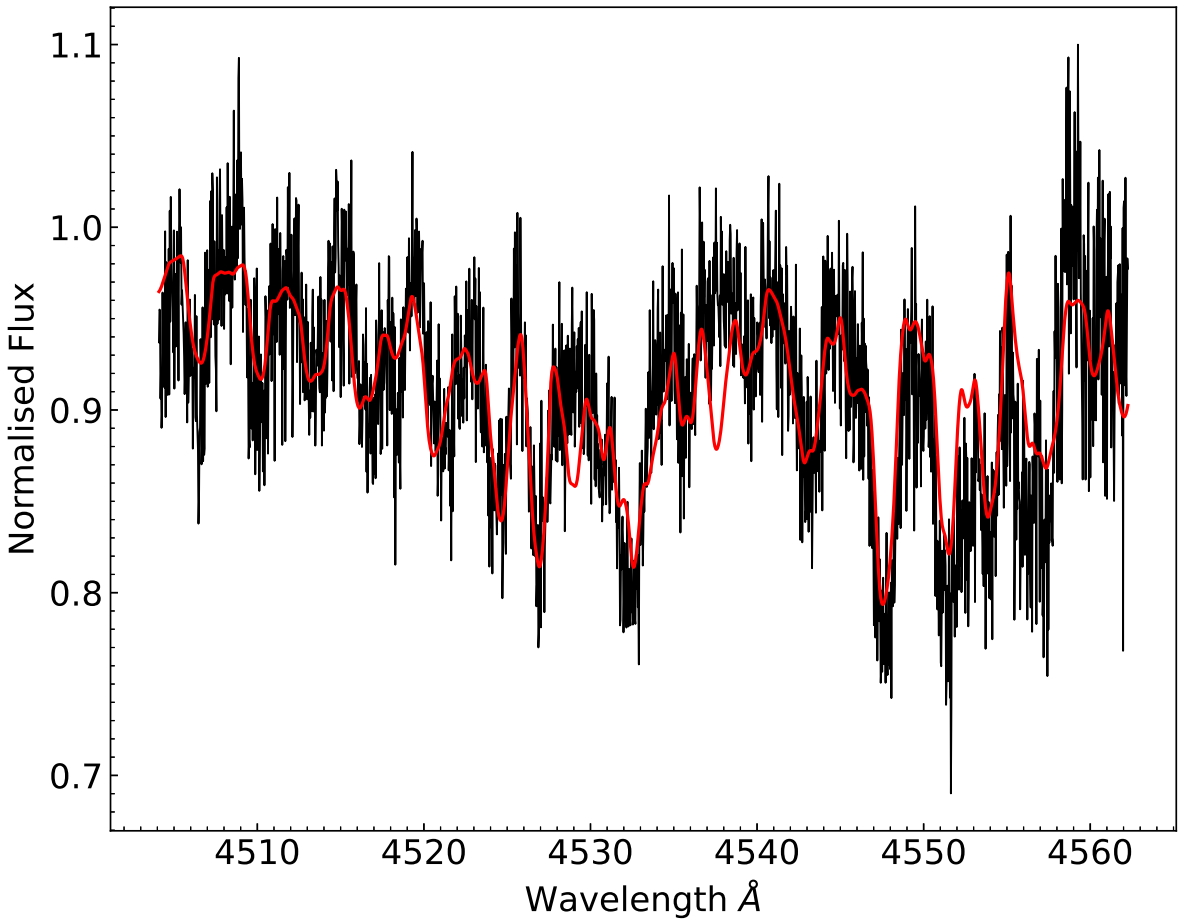

Figure 3.7: Spectral fit to order 66 using the grid search method with optimal normalisation.

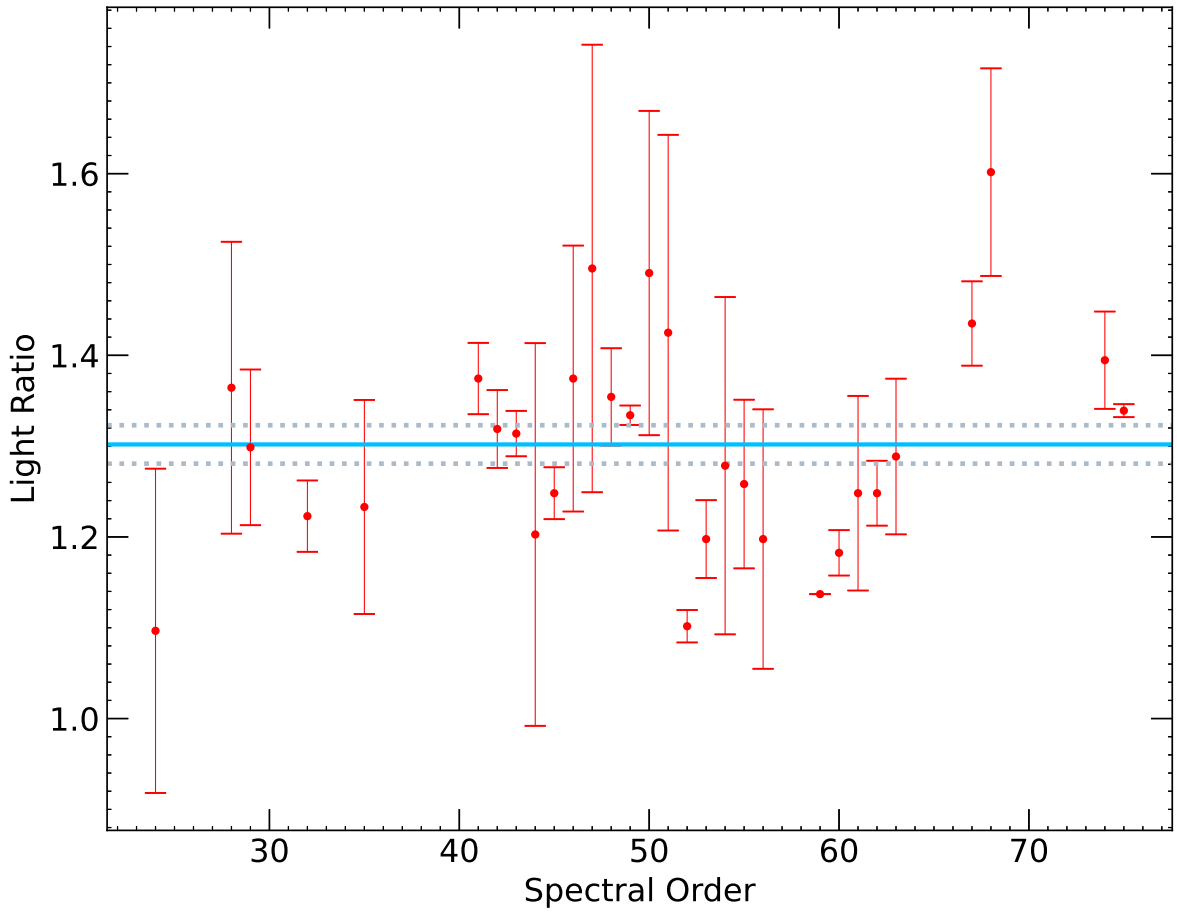

Figure 3.8: Resulting ℓ_B/ℓ_A values from the grid search method averaged over the orders.

Table 3.5: Light ratios measured and adopted for KIC 9851944.

Source	Light Ratio ℓ_B/ℓ_A
TODCOR	1.222 ± 0.136
ODS	1.300 ± 0.015
Direct Fit	1.302 ± 0.021
Adopted	1.300 ± 0.036

time, only the two observations closest to positions of quadrature were used. This approach resulted in 30 spectral orders showing adequate fits with well defined minima in the sum of the square residuals. Fig. 3.7 shows the result of this method applied to order 66, which demonstrates the effectiveness of optimising the normalisation of the observed spectra in the fitting routine for an order where line blending is significant. The resulting values for ℓ_B/ℓ_A after applying this method to the selected orders are shown in Fig. 3.8, where each result is the average of the result from each of the two observations used.

Thus, after taking the average of the results in Fig. 3.8, which corresponds to the blue line, we have three independent estimations for the light ratio of the system, i.e., TODCOR, ODS, and direct fitting for the light ratio. These estimations are given in Table 3.5, where we take the average and its standard deviation from the ODS method. For the rest of this study, we adopt $\ell_B/\ell_A = 1.300$ as the weighted mean of those values, with an errorbar of ± 0.036 which is their standard deviation. This value is used to ascertain the correct light curve solution is obtained in the next Section.

3.6 Analysis of the light curve

The following analysis of the light curve, which uses the WD *code, was performed by Dr. John Taylor, and is included in this thesis because it is an important component of the analysis for KIC 9851944.*

The components of KIC 9841944 are close to each other and thus have a significant tidal deformation. We therefore sought to model the light curve using a code that is based on Roche geometry. We selected the Wilson-Devinney (WD) code (Wilson & Devinney, 1971; Wilson, 1979) for this, and used the 2004 version of the code driven using the JKTWD wrapper (Southworth et al., 2011). The user guide which accompanies the WD code (Wilson & Van Hamme, 2004) includes a description of all input and output quantities discussed below.

The WD code is computationally expensive and is not suited to the analysis of the full 500 000 short-cadence datapoints in one step. We therefore used the orbital ephemeris determined in Section 3.3 to convert the datapoints to orbital phase, and then binned them into a much smaller number of points. We chose a bin size of 0.001 orbital phases during the eclipses and 0.005 outside the eclipses, resulting in a total of 456 phase-binned datapoints suitable for analysis with the WD code.

Through a process of trying a large number of different fits with a range of fixed and fitted parameters, we arrived at a good solution to the light curve. We adopt this as the default solution, plot it in Fig. 3.9, and give the fitted parameters in Table 3.6. It was obtained in Mode = 0 with the following fitted parameters: the light contributions of the two stars; their potentials; their gravity darkening coefficients; the linear coefficients of the logarithmic LD law; and the orbital inclination. We fixed the mass ratio at the spectroscopic value, the orbital eccentricity to zero, the albedos to 1.1, the logarithmic coefficients of LD to values from Van Hamme (1993), third light to zero, and the rotation rates to synchronous. We adopted the maximum numerical precision values of `N1` = `N2` = 60 and `N1L` = `N2L` = 60, the simple treatment of reflection, and the Cousins R-band as a proxy for the *Kepler* passband. This solution gives a light ratio in excellent agreement with the spectroscopic values in Table 3.5. The fractional radii in Table 3.6 are volume-equivalent values calculated by the LC component of the WD code.

The main confounding factors in fitting the light curve were the albedo and gravity darkening. Albedo values around 1.0 give a good fit to the data, but there is a wide local minimum of χ^2 at albedos in the region of 0.0 that gives a worse fit

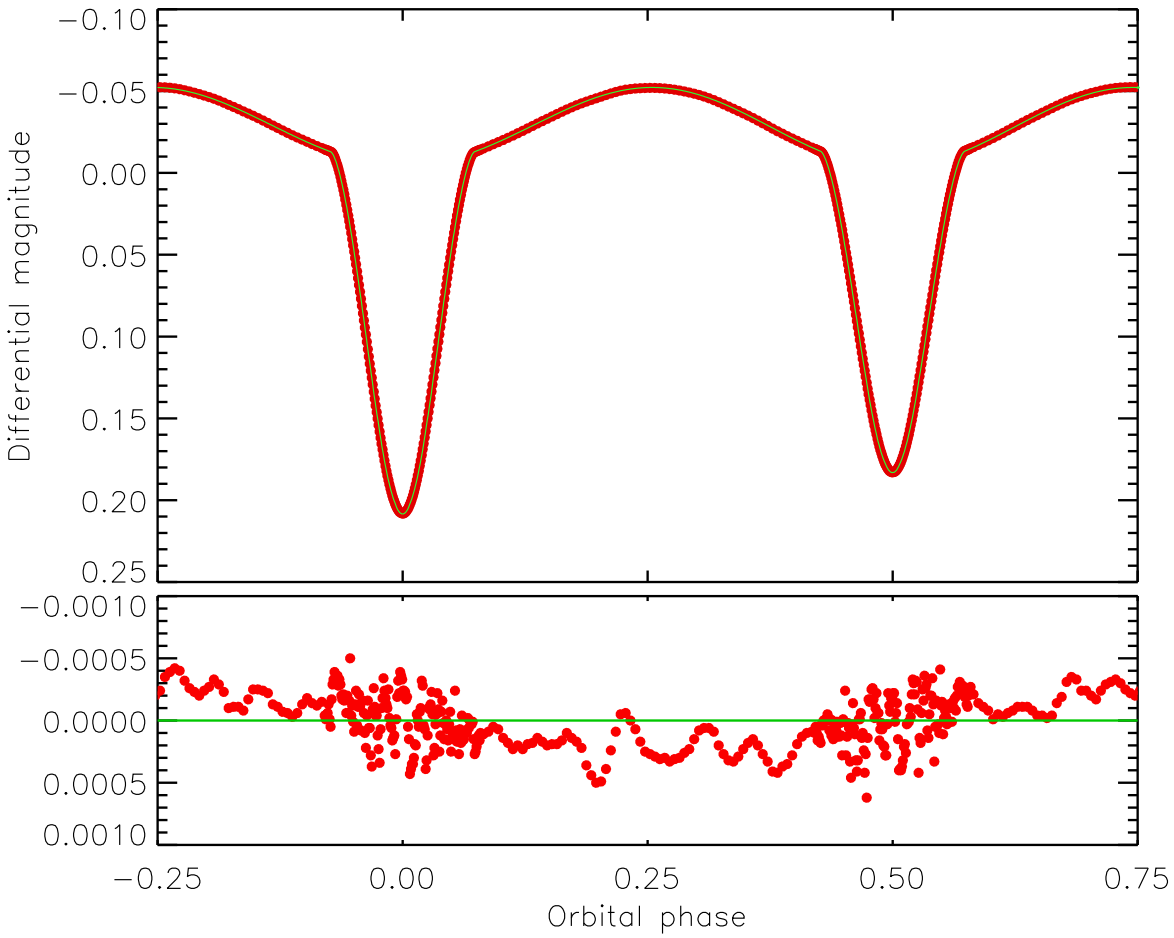

Figure 3.9: The best-fitting WD model (green line) to the *Kepler* phase-binned light curve of KIC 9851944 (red filled circles). The residuals of the fit are plotted in the lower panel using a greatly enlarged y-axis to bring out the detail.

but is frequently found by the steepest-descent minimisation method implemented in the WD code. After extensive experimentation, we found that fixing the albedos to values slightly above 1.0 yielded the best fits and did not risk descending into the local minimum at lower abedo values. Fitting for gravity darkening turned out to be a crucial step in obtaining a good model, and the best-fitting values were somewhat varied but generally around 0.8 for the primary star and 1.1 for the secondary star. We interpret this as a systematic issue caused by residual pulsations in the light curve and account for it in the uncertainties.

For the determination of the uncertainties of the fitted parameters we ran a wide range of solutions with a large number of different possible approaches to modelling the light curve (see Southworth 2020). We calculated the errorbar for each parameter by adding in quadrature the contribution from every model choice, which in turn was taken to be the amount that parameter changed by versus the default solution. The following different approaches were explored.

1. We varied the amount of binning prior to the WD solution, finding that it had a negligible effect on the fitted parameters.

2. We changed the numerical precision to `N1` = `N2` = `N1L` = `N2L` = 50. This modified the fractional radii by a maximum of 0.5%.

3. We tried the detailed reflection effect and found almost identical results.

4. Attempts to fit for mass ratio returned a value very close to the spectroscopic one and almost no change in the other parameters.

5. Fitting for the rotation rates of the stars yielded values close to and consistent with synchronous rotation and little change in the other parameters.

6. Fitting for albedo gave a poorer fit but again very little change in the other parameters.

7. Allowing for third light gave very similar parameters and a very small amount of third light consistent with zero.

8. Fitting for one of the temperatures of the stars instead of the two light contributions directly (namely Mode = 2) changed the fractional radii by 0.2%.

9. Fixing the limb darkening coefficients to theoretical values changed the fractional radii by 0.5%.

10. Using the square-root instead of logarithmic limb darkening law had a negligible effect.

The best-fitting parameters were highly robust against all these experiments. The only significantly discrepant fit (neglecting our original exploratory ones) was when we used the Cousins I-band instead of the R-band. However, we are able to reject this fit as it is not consistent with the spectroscopic light ratio. The calculated uncertainties are given in Table 3.6.

Fig. 3.9 shows that the best fit is extremely good, with an r.m.s. of 0.20 mmag, but that there are systematics remaining in the residuals. We attribute these to the WD numerical integration for points during the eclipses, and residual pulsations for points outside eclipse. Our approach of phase-binning the data gives a light curve practially without Poisson noise, so makes any imperfections in the fit easily noticable. We note that the systematics in the residuals of the fits we found to the data are too small to show up in plots of unbinned data, so may well be present in previous work on this object.

3.7 Physical properties

The physical properties of the KIC 9851944 system reported in this section were calculated by Dr. John Taylor.

We determined the physical properties of KIC 9851944 from the spectroscopic and photometric results obtained above. For this, we used the JKTABSDIM code (Southworth et al., 2005b), modified to use the IAU system of nominal solar values (Prša

Table 3.6: Summary of the parameters for the WD2004 solutions of the light curves of the system. Detailed descriptions of the control parameters can be found in the WD code user guide (Wilson & Van Hamme, 2004). A and B refer to the primary and secondary stars, respectively. Uncertainties are only quoted when they have been robustly assessed by comparison of a full set of alternative solutions.

Parameter	WD2004 name	Value
Control and fixed parameters:		
WD2004 operation mode	MODE	0
Treatment of reflection	MREF	1
Number of reflections	NREF	1
LD law	LD	2 (logarithmic)
Numerical grid size (normal)	N1, N2	60, 60
Numerical grid size (coarse)	N1L, N2L	60, 60
Fixed parameters:		
Mass ratio	RM	1.06
Phase shift	PSHIFT	0.0
Orbital eccentricity	E	0.0
$T_{\rm eff}$ star A (K)	TAVH	6964
$T_{\rm eff}$ star B (K)	TAVC	6840
Bolometric albedos	ALB1, ALB2	1.1, 1.1
Rotation rates	F1, F2	1.0, 1.0
Logarithmic LD coefficients	Y1A, Y2A	0.294, 0.293
Fitted parameters:		
Star A potential	PHSV	5.365 ± 0.044
Star B potential	PHSC	4.867 ± 0.093
Orbital inclination (°)	XINCL	73.912 ± 0.044
Star A gravity darkening	GR1	0.75 ± 0.40
Star B gravity darkening	GR2	1.14 ± 0.40
Star A light contribution	HLUM	5.58 ± 0.12
Star B light contribution	CLUM	7.34 ± 0.12
Star A linear LD coefficient	X1A	0.658 ± 0.019
Star B linear LD coefficient	X2A	0.662 ± 0.013
Fractional radius of star A		0.2344 ± 0.0024
Fractional radius of star B		0.2759 ± 0.0040

Table 3.7: Physical properties measured for the four systems analysed in this work. The units labelled with a 'N' are given in terms of the nominal solar quantities defined in IAU 2015 Resolution B3 (Prša et al., 2016).

Parameter	Star A	Star B
Mass ratio	1.0667 ± 0.0038	
Semimajor axis ($\mathcal{R}_\odot^{\mathrm{N}}$)	10.805 ± 0.019	
Mass ($\mathcal{M}_\odot^{\mathrm{N}}$)	1.749 ± 0.010	1.866 ± 0.010
Radius ($\mathcal{R}_\odot^{\mathrm{N}}$)	2.533 ± 0.026	2.981 ± 0.044
Surface gravity (log[cgs])	3.874 ± 0.009	3.760 ± 0.013
Synchronous velocity ($\mathrm{km\,s^{-1}}$)	59.2 ± 0.6	69.7 ± 1.0
T_{eff} (K)	6964 ± 43	6840 ± 37
Luminosity $\log(L/\mathcal{L}_\odot^{\mathrm{N}})$	1.133 ± 0.014	1.244 ± 0.016
Absolute bolometric magnitude	1.907 ± 0.035	1.631 ± 0.039
$E(B-V)$ (mag)	0.14 ± 0.02	
Distance (pc)	935 ± 13	

et al., 2016) plus the NIST 2018 values for the Newtonian gravitational constant and the Stefan-Boltzmann constant. Errorbars were propagated via a perturbation analysis. The results are given in Table. 3.7.

The distance to the system was determined using optical BV magnitudes from APASS (Henden et al., 2012), near-IR JHK_s magnitudes from 2MASS (Cutri et al., 2003) converted to the Johnson system using the transformations from Carpenter (2001), and surface brightness relations from Kervella et al. (2004). The interstellar reddening was determined by requiring the optical and near-IR distances to match. We found a final distance of $935 \pm 12\,\mathrm{pc}$, which is significantly shorter than the distance of $999 \pm 12\,\mathrm{pc}$ from the *Gaia* DR3 parallax (Gaia Collaboration et al., 2016; Gaia Collaboration, 2021). We have no explanation for this at present, but note that the *Gaia* DR2 and DR3 parallaxes of this object differ by nearly 2σ so might be affected by its binarity.

3.8 Asteroseismic analysis

The pulsation analysis presented in this section was performed by Dr. Timothy Van Reeth; it is included because understanding the seismic properties of KIC 9851944 is an important aspect of this thesis.

3.8.1 Frequency analysis

Following the binary modelling, we continue with the asteroseismic analysis of the target. Because the observed pulsations have much smaller amplitudes than the binary signal, the quality of the TESS and WASP data are insufficient for the asteroseismic analysis, and we limit ourselves to using the residual *Kepler* light curve. This is the merged light curve of all available *Kepler* short-cadence data after subtracting the best-fitting binary model, hereafter referred to as the pulsation light curve. To minimise the impact of outliers and instrumental effects on the asteroseismic analysis of small-amplitude pulsations, we apply additional processing to the data. Firstly, we remove those parts where coronal mass ejections (CMEs) or thermal and pointing changes of the spacecraft, such as at the start of a quarter or after a safe-mode event, have a visible impact on the quality of the light curve. Secondly, we apply preliminary iterative pre-whitening (as described by, e.g., Van Reeth et al., 2023) to build a tentative mathematical model of the 20 most dominant pulsations using a sum of sine waves

$$L(t) = \sum_{i=1}^{N=20} a_i \sin\left(2\pi\left[f_i\left(t - t_0\right) + \phi_i\right]\right), \tag{3.1}$$

where a_i, f_i and ϕ_i are the amplitude, frequency, and phase of the i^{th} sine wave, respectively, and t_0 is the average time stamp of all data points in the pulsation light curve. We then identify individual outliers in the residuals using 5σ clipping, and remove these data points from the pulsation light curve as well.

Next, we use iterative pre-whitening to measure the pulsation frequencies from the resulting cleaned pulsation light curve. Hereby we iteratively fit additional sine

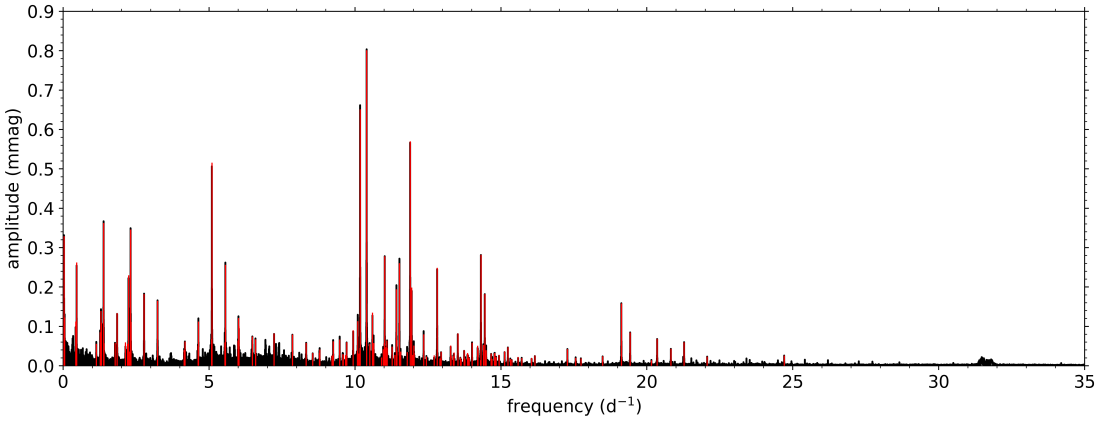

Figure 3.10: Lomb-Scargle periodogram of the short-cadence *Kepler* light curve of KIC 9851944 (black) with the iteratively prewhitened frequencies (full red lines).

waves to the time series, with frequencies that correspond to the dominant amplitudes in the Lomb-Scargle periodogram (Scargle, 1982) of the residual pulsation light curve. However, in the particular case of KIC 9851944, there is a significant amount of red noise present in the data, most likely caused by residual instrumental effects, even after cleaning the pulsation light curve. To ensure that we detect all significant pulsation frequencies (with a signal-to-noise ratio $S/N \geq 5.6$; see e.g. Baran et al. 2015), we customise our approach. Firstly, we split the frequency range between $0\,\mathrm{d}^{-1}$ and the Nyquist frequency ($734.21\,\mathrm{d}^{-1}$) in overlapping parts and apply the iterative prewhitening to these individually: from $0\,\mathrm{d}^{-1}$ to $2\,\mathrm{d}^{-1}$, from $1\,\mathrm{d}^{-1}$ to $6\,\mathrm{d}^{-1}$, from $4\,\mathrm{d}^{-1}$ to $11\,\mathrm{d}^{-1}$, from $9\,\mathrm{d}^{-1}$ to $21\,\mathrm{d}^{-1}$, from $19\,\mathrm{d}^{-1}$ to $51\,\mathrm{d}^{-1}$, from $49\,\mathrm{d}^{-1}$ to $201\,\mathrm{d}^{-1}$, and from $199\,\mathrm{d}^{-1}$ to the Nyquist frequency. In this stage, we measure all frequencies with $S/N \geq 4.0$. Secondly, we merge the different frequency lists, keeping only those frequencies that are dominant in a $2.5\,f_{\mathrm{res}}$-window, where f_{res} is the frequency resolution of the light curve (Loumos & Deeming, 1978) with a value of $0.00208\,\mathrm{d}^{-1}$, and that have $S/N \geq 5.6$. Thirdly, we non-linearly optimise this filtered frequency list using the least-squares minimisation with the trust region reflective method from the `lmfit` python package (Newville et al., 2019). After the optimisation, we redetermined the

S/N that are associated with the different frequencies, again only keeping those with $S/N \geq 5.6$. This leaves us with a final list of 133 measured frequencies in both the p- and g-mode regimes, considerably more than the 89 frequencies reported by Guo et al. (2016). Notably, we formally detect one frequency at $391.5095 \pm 0.0002\,\mathrm{d}^{-1}$ with an amplitude of $6.3 \pm 1.2\,\mu$mag. However, a detailed analysis of this sine wave reveals that it originates from the noise properties of the short-cadence light curve. The signal has a maximal amplitude during the first parts of quarters 13 and 14, but is not detectable in most other parts of the light curve. Hence, we discard this frequency and limit ourselves to the remaining frequencies, with values below $25\,\mathrm{d}^{-1}$. These are illustrated in Fig. 3.10 and listed in Table 3.8.

3.8.2 Tidal perturbation analysis

As already demonstrated by Guo et al. (2016) and illustrated in Fig. 3.11, many of the detected frequencies form orbital-frequency spaced multiplets, also called "tidally split multiplets". In our work, we identify each multiplet by looping over all measured frequencies f_i in order of decreasing amplitude, and consider frequencies f_j to be part of a multiplet around it if

$$|f_i - f_j - n f_{\mathrm{orb}}| < \Delta f, \tag{3.2}$$

where n is an integer chosen to minimise the left-hand side of the Equation, and Δf is a chosen frequency tolerance of $0.002\,\mathrm{d}^{-1}$, that is $\approx f_{\mathrm{res}}$. In each iteration, the considered frequencies f_j have amplitudes a_j that are smaller than the amplitude a_i, associated with f_i, and are not yet associated with a different multiplet.

We identify 13 multiplets that consist of three or more components, as listed in Table 3.8. One of these, with the dominant frequency at $1.386342(4)\,\mathrm{d}^{-1}$, consists of 19 frequencies that match integer multiples of the binary orbital frequency f_{orb} within Δf, and is discussed in detail below in Sect. 3.8.3. In their work, Guo et al. (2016) explained the other multiplets as consequences of *(i)* rotational frequency splitting, and *(ii)* partial occultations of the pulsation mode geometries during the eclipses (e.g.,

Table 3.8: Parameter values associated with the iteratively prewhitened frequencies, which were obtained as described in Sec. 3.8.1. The frequencies are grouped, with the first set consisting of those labelled as independent frequencies, and the following groups consisting of combination frequencies, sorted according to the dominant parent frequency. In the last column, we list the identified combinations. Combination frequencies that are found within the frequency resolution $f_{\rm res}$ but not within 3σ, are indicated with * in the first column and with $\approx$ in the final column.

	frequency f (d^{-1})	amplitude a (mmag)	phase ϕ (2π rad)	signal-to-noise S/N	comments
f_1	0.029864(4)	0.3292(12)	0.4796(6)	20.42	
f_2	0.04104(12)	0.1145(12)	0.246(2)	7.15	
f_3	0.050798(11)	0.1231(12)	-0.482(2)	7.72	
f_4	0.429539(12)	0.1126(12)	-0.412(2)	8.25	
f_6	1.13642(2)	0.0559(12)	0.196(3)	5.68	
f_7	1.26821(2)	0.0855(12)	0.151(2)	9.41	
f_8	1.297029(9)	0.1389(12)	0.044(14)	15.59	
f_{14}	2.1344(2)	0.0598(12)	0.345(3)	10.12	
f_{15}	2.20293(2)	0.0554(12)	-0.028(3)	9.51	
f_{16}	2.239718(6)	0.23(12)	-0.0492(8)	39.16	
f_{17}	2.27839(4)	0.0363(12)	-0.258(5)	6.12	
f_{22}	4.14574(3)	0.04(12)	-0.092(5)	5.63	
f_{27}	5.097165(3)	0.5158(12)	-0.301(4)	55.8	
f_{28}	5.53879(2)	0.0597(13)	-0.271(3)	5.91	
f_{30}	5.99419(2)	0.0644(12)	0.442(3)	5.87	
f_{34}	6.59017(2)	0.0672(12)	0.469(3)	6.12	
f_{35}	7.22671(2)	0.0824(12)	-0.288(2)	8.08	
f_{45}	9.59223(5)	0.0284(12)	-0.486(7)	7.4	
f_{53}	10.176017(2)	0.6515(12)	0.429(3)	172.1	
f_{54}	10.399706(2)	0.8015(12)	-0.2904(2)	221.19	
f_{58}	10.90789(6)	0.0211(12)	0.045(9)	5.79	
f_{60}	11.00533(2)	0.0579(12)	0.059(3)	16.02	
f_{61}	11.018536(5)	0.2785(12)	0.3112(7)	76.68	
f_{63}	11.08192(6)	0.0237(12)	0.408(8)	6.61	
f_{66}	11.27246(3)	0.0487(12)	0.117(4)	13.83	
f_{67}	11.3651(5)	0.0275(12)	-0.247(7)	7.76	
f_{68}	11.41982(7)	0.1941(12)	-0.3938(10)	54.46	
f_{70}	11.43819(3)	0.0376(12)	-0.15(5)	10.57	
f_{71}	11.52234(5)	0.2606(12)	-0.4854(7)	73.33	
f_{74}	11.890477(2)	0.5704(12)	0.1807(3)	164.93	
f_{90}	13.61013(6)	0.0213(12)	0.222(9)	7.7	
f_{93}	13.76588(7)	0.019(12)	0.161(10)	7.05	

Table 3.8 continued.

	frequency f (d^{-1})	amplitude a (mmag)	phase ϕ (2π rad)	signal-to-noise S/N	comments
f_{98}	14.01097(2)	0.0589(12)	-0.244(3)	23.17	
f_{100}	14.21089(3)	0.0417(12)	-0.354(5)	16.79	
f_{102}	14.315077(5)	0.2819(12)	0.4401(7)	115.05	
f_{103}	14.39805(2)	0.0527(12)	-0.117(4)	21.96	
f_{104}	14.448108(7)	0.1824(12)	-0.3085(11)	77.2	
f_{105}	14.4932(3)	0.0396(12)	0.333(5)	16.83	
f_{107}	14.69426(7)	0.0175(12)	0.023(11)	7.6	
f_{111}	14.83253(6)	0.022(12)	0.083(9)	9.79	
f_{125}	19.126701(8)	0.1584(12)	-0.4735(12)	91.81	
f_{126}	19.42779(2)	0.0847(12)	-0.419(2)	47.64	
f_{127}	20.15601(9)	0.0139(12)	-0.124(14)	7.51	
f_{129}	20.82366(3)	0.0432(12)	0.429(4)	21.19	
f_5^*	0.462195(5)	0.2625(12)	-0.3711(7)	19.39	$\approx 1 f_{\rm orb}$
f_{10}^*	1.386342(4)	0.3628(12)	-0.3605(5)	44.54	$\approx 3 f_{\rm orb}$
f_{13}^*	1.848604(10)	0.1336(12)	0.2485(14)	20.41	$\approx 4 f_{\rm orb}$
f_{18}	2.310647(4)	0.3462(12)	0.3839(6)	58.23	$5 f_{\rm orb}$
f_{20}	2.77278(7)	0.1827(12)	0.0065(11)	32.88	$6 f_{\rm orb}$
f_{21}	3.234899(8)	0.1651(12)	-0.3581(12)	29.22	$7 f_{\rm orb}$
f_{24}^*	4.62137(3)	0.051(12)	0.015(4)	6.14	$\approx 10 f_{\rm orb}$
f_{26}^*	5.08347(2)	0.0676(12)	-0.349(3)	7.34	$\approx 11 f_{\rm orb}$
f_{31}^*	6.007556(11)	0.1215(12)	-0.13(2)	11.09	$\approx 13 f_{\rm orb}$
f_{36}^*	7.85624(2)	0.0794(12)	0.441(2)	9.71	$\approx 17 f_{\rm orb}$
f_{39}	8.7805(4)	0.0331(12)	-0.314(6)	7.19	$19 f_{\rm orb}$
f_{52}^*	10.16693(3)	0.0453(12)	-0.448(4)	11.96	$\approx 22 f_{\rm orb}$
f_{64}	11.09106(2)	0.0642(12)	-0.195(3)	17.87	$24 f_{\rm orb}$
f_{77}	12.01533(3)	0.0517(12)	0.058(4)	15.06	$26 f_{\rm orb}$
f_{95}	13.86382(6)	0.021(12)	0.064(9)	7.98	$30 f_{\rm orb}$
f_{109}	14.7881(4)	0.0326(12)	0.314(6)	14.44	$32 f_{\rm orb}$
f_{118}	15.71249(6)	0.0201(12)	-0.435(10)	9.87	$34 f_{\rm orb}$
f_{122}	17.56078(6)	0.0202(12)	-0.407(10)	10.72	$38 f_{\rm orb}$
f_{124}	18.48512(5)	0.0242(12)	-0.172(8)	13.89	$40 f_{\rm orb}$
f_9	1.315491(12)	0.1099(12)	0.252(2)	12.54	f_{16} - $2 f_{\rm orb}$
f_{12}^*	1.77778(2)	0.0577(12)	-0.476(3)	8.7	$\approx f_{16}$ - $f_{\rm orb}$
f_{23}^*	4.17278(2)	0.062(12)	-0.128(3)	8.61	$\approx f_{27}$ - $2 f_{\rm orb}$
f_{25}	4.635033(12)	0.1126(12)	0.394(2)	13.54	f_{27} - $f_{\rm orb}$
f_{29}	5.559303(5)	0.2567(12)	-0.1643(8)	25.3	f_{27} + $f_{\rm orb}$
f_{32}^*	6.021343(13)	0.1002(12)	-0.298(2)	9.15	$\approx f_{27}$ + $2 f_{\rm orb}$

Table 3.8 continued.

	frequency f (d^{-1})	amplitude a (mmag)	phase ϕ (2π rad)	signal-to-noise S/N	comments
f^*_{33}	6.48364(2)	0.0743(12)	0.31(3)	6.72	$\approx f_{27} + 3f_{\rm orb}$
f_{131}	22.06635(5)	0.0237(12)	-0.077(8)	12.1	$f_{52} + f_{73}$
f_{132}	24.70539(5)	0.0264(12)	0.45(7)	14.83	$f_{73} + f_{81}$
f_{11}	1.39562(2)	0.0572(12)	0.312(3)	7.06	f_{53} - $19f_{\rm orb}$
f_{19}	2.319817(12)	0.1116(12)	-0.005(2)	18.75	f_{53} - $17f_{\rm orb}$
f_{37}	8.32746(2)	0.0582(12)	-0.077(3)	9.42	f_{53} - $4f_{\rm orb}$
f_{40}	8.78961(3)	0.0418(12)	0.348(5)	9.09	f_{53} - $3f_{\rm orb}$
f_{42}	9.25174(2)	0.0625(12)	0.162(3)	15.84	f_{53} - $2f_{\rm orb}$
f_{47}	9.71391(2)	0.0599(12)	-0.347(3)	15.77	f_{53} - $f_{\rm orb}$
f_{57}	10.63816(2)	0.058(12)	-0.107(3)	15.93	$f_{53} + f_{\rm orb}$
f^*_{65}	11.10018(3)	0.0449(12)	-0.321(4)	12.47	$\approx f_{53} + 2f_{\rm orb}$
f^*_{72}	11.56252(4)	0.0362(12)	0.098(5)	10.34	$\approx f_{53} + 3f_{\rm orb}$
f_{78}	12.02459(4)	0.0327(12)	-0.062(6)	9.52	$f_{53} + 4f_{\rm orb}$
f_{84}	12.94893(4)	0.0356(12)	0.191(5)	11.25	$f_{53} + 6f_{\rm orb}$
f_{96}	13.87319(5)	0.0283(12)	0.428(7)	10.81	$f_{53} + 8f_{\rm orb}$
f^*_{110}	14.79735(8)	0.0163(12)	-0.299(12)	7.22	$\approx f_{53} + 10f_{\rm orb}$
f^*_{38}	8.55106(4)	0.0327(12)	-0.308(6)	6.3	$\approx f_{54}$ - $4f_{\rm orb}$
f^*_{43}	9.47551(2)	0.067(12)	0.496(3)	17.51	$\approx f_{54}$ - $2f_{\rm orb}$
f_{48}	9.93758(14)	0.0905(12)	0.007(2)	23.92	f_{54} - $f_{\rm orb}$
f^*_{73}	11.78622(4)	0.0348(12)	0.096(6)	10.11	$\approx f_{54} + 3f_{\rm orb}$
f^*_{81}	12.71017(5)	0.0264(12)	0.386(7)	8.21	$\approx f_{54} + 5f_{\rm orb}$
f^*_{91}	13.63457(8)	0.0158(12)	-0.362(12)	5.72	$\approx f_{54} + 7f_{\rm orb}$
f_{49}	10.08101(3)	0.0377(12)	-0.22(5)	9.93	f_{60} - $2f_{\rm orb}$
f_{50}	10.094274(11)	0.1133(12)	0.134(2)	29.92	f_{61} - $2f_{\rm orb}$
f_{75}	11.942814(7)	0.1987(12)	0.13(10)	57.43	$f_{61} + 2f_{\rm orb}$
f_{41}	9.21174(5)	0.0262(12)	0.358(7)	6.61	f_{71} - $5f_{\rm orb}$
f_{46}	9.67396(5)	0.0273(12)	-0.086(7)	7.21	f_{71} - $4f_{\rm orb}$
f_{51}	10.13587(4)	0.0313(12)	-0.405(6)	8.28	f_{71} - $3f_{\rm orb}$
f_{56}	10.598064(10)	0.1353(12)	0.2578(14)	37.3	f_{71} - $2f_{\rm orb}$
f_{62}	11.06027(3)	0.0476(12)	-0.186(4)	13.31	f_{71} - $f_{\rm orb}$
f_{76}	11.9845(5)	0.0274(12)	0.103(7)	8.01	$f_{71} + f_{\rm orb}$
f_{80}	12.44658(5)	0.0237(12)	-0.383(8)	7.04	$f_{71} + 2f_{\rm orb}$
f_{83}	12.90873(7)	0.0189(12)	0.327(10)	5.96	$f_{71} + 3f_{\rm orb}$
f_{87}	13.37075(5)	0.0246(12)	-0.004(8)	8.46	$f_{71} + 4f_{\rm orb}$
f_{101}	14.29517(9)	0.0146(12)	0.283(13)	5.95	$f_{71} + 6f_{\rm orb}$

Table 3.8 continued.

	frequency f (d^{-1})	amplitude a (mmag)	phase ϕ (2π rad)	signal-to-noise S/N	comments
f_{44}	9.58038(4)	0.0297(12)	-0.181(6)	7.74	f_{74} - $5f_{\rm orb}$
f^*_{55}	10.50457(2)	0.0551(12)	0.106(3)	15.18	$\approx f_{74}$ - $3f_{\rm orb}$
f_{59}	10.96637(3)	0.042(12)	-0.292(5)	11.57	f_{74} - $2f_{\rm orb}$
f_{69}	11.42854(2)	0.0649(12)	0.357(3)	18.21	f_{74} - $f_{\rm orb}$
f_{79}	12.35285(2)	0.08(12)	-0.375(2)	23.84	f_{74} + $f_{\rm orb}$
f^*_{82}	12.814957(5)	0.2491(12)	0.0752(8)	77.37	$\approx f_{74}$ + $2f_{\rm orb}$
f_{85}	13.27707(3)	0.0514(12)	-0.101(4)	17.07	f_{74} + $3f_{\rm orb}$
f_{92}	13.73916(3)	0.0399(12)	-0.488(5)	14.76	f_{74} + $4f_{\rm orb}$
f_{99}	14.2014(3)	0.0509(12)	0.167(4)	20.4	f_{74} + $5f_{\rm orb}$
f_{106}	14.66346(4)	0.031(12)	-0.274(6)	13.37	f_{74} + $6f_{\rm orb}$
f_{113}	15.12563(4)	0.0365(12)	0.415(5)	17.04	f_{74} + $7f_{\rm orb}$
f_{117}	15.5876(6)	0.0227(12)	-0.035(8)	11.38	f_{74} + $8f_{\rm orb}$
f_{119}	16.04978(7)	0.0198(12)	-0.329(10)	10.23	f_{74} + $9f_{\rm orb}$
f_{112}	14.93524(5)	0.0278(12)	0.498(7)	12.66	f_{98} + $2f_{\rm orb}$
f_{86}	13.28676(5)	0.0259(12)	0.304(7)	8.65	f_{100} - $2f_{\rm orb}$
f_{88}	13.39085(4)	0.0341(12)	0.204(6)	11.76	f_{102} - $2f_{\rm orb}$
f^*_{94}	13.85328(4)	0.0326(12)	-0.282(6)	12.38	$\approx f_{102}$ - $f_{\rm orb}$
f_{108}	14.77747(4)	0.031(12)	-0.005(6)	13.62	f_{102} + $f_{\rm orb}$
f_{114}	15.2393(3)	0.0473(12)	-0.302(4)	22.42	f_{102} + $2f_{\rm orb}$
f_{120}	16.16355(5)	0.0262(12)	-0.061(7)	13.58	f_{102} + $4f_{\rm orb}$
f_{115}	15.32214(8)	0.0173(12)	-0.351(11)	8.23	f_{103} + $2f_{\rm orb}$
f_{89}	13.52388(2)	0.0822(12)	0.432(2)	29.63	f_{104} - $2f_{\rm orb}$
f_{116}	15.37227(8)	0.0156(12)	-0.108(12)	7.54	f_{104} + $2f_{\rm orb}$
f_{97}	13.90834(6)	0.02(12)	0.279(10)	7.68	f_{111} - $2f_{\rm orb}$
f_{121}	17.27819(3)	0.0423(12)	-0.464(5)	22.4	f_{125} - $4f_{\rm orb}$
f_{123}	17.74024(7)	0.019(12)	0.113(10)	10.38	f_{125} - $3f_{\rm orb}$
f_{128}	20.3521(2)	0.0686(12)	-0.152(3)	35.16	f_{126} + $2f_{\rm orb}$
f_{130}	21.27623(2)	0.0601(12)	-0.429(3)	29.62	f_{126} + $4f_{\rm orb}$

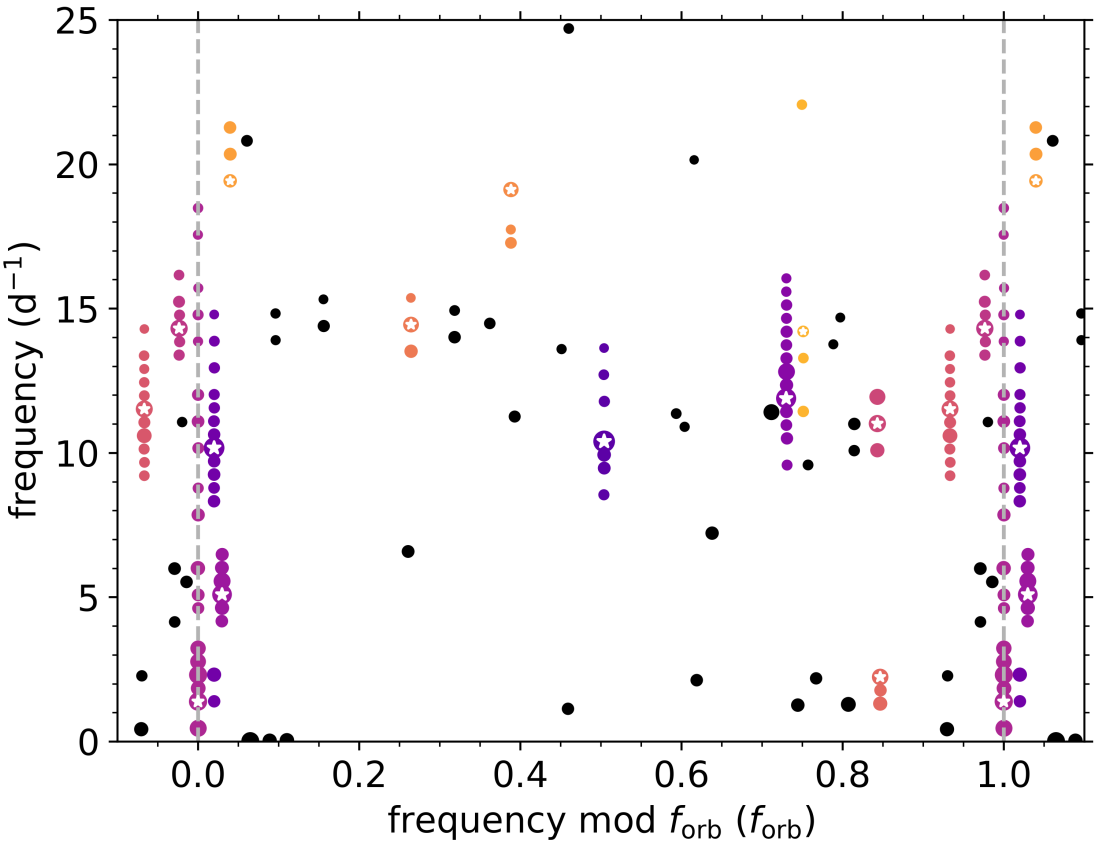

Figure 3.11: Échelle diagram of the prewhitened frequencies of KIC 9851944, folded with the orbital frequency $f_{\rm orb}$. Identified multiplets are indicated in different colours ranging from purple to dark yellow, with a white star marking the dominant frequency of each multiplet. Single frequencies are shown in black. The marker sizes indicate the associated amplitudes.

Reed et al., 2001, 2005; Gamarova et al., 2003; Rodríguez et al., 2004; Gamarova et al., 2005). However, it is now known that pulsation modes are often tidally perturbed (e.g., Samadi Ghadim et al., 2018; Steindl et al., 2021; Van Reeth et al., 2023) or tilted (e.g., Fuller et al., 2020; Handler et al., 2020; Kurtz et al., 2020; Rappaport et al., 2021; Van Reeth et al., 2022) in close binaries.

Hence, to determine the true origin of the detected multiplets, we evaluate their dependence on binary orbital phase in detail. Each multiplet with three or more components is studied individually by removing all measured variability that is not associated with that multiplet from the pulsation light curve, that is, we subtract all sine waves with frequencies that are not in the multiplet from the pulsation light curve. We then fold the residual light curve with the orbital period, split the data in 50 bins, and fit the dominant sine wave of the multiplet to the data, optimising the amplitude and phase for each orbital-phase bin. The reason for this approach is twofold: *(i)* the frequency spacings within the detected multiplets are not always exact multiples of $f_{\rm orb}$, and *(ii)* there can be frequencies missing within the detected multiplets. As a result, the analytical reconstruction from Jayaraman et al. (2022) is not well suited for this star.

The results are illustrated in Fig. 3.12 to 3.24 for all pulsations. In each figure, the relevant frequency multiplet is plotted in the left-hand panel, with a white star marking the dominant frequency. On the right-hand side, the middle and bottom panels show the orbit-phase dependence of the pulsation amplitude and phase, respectively. For reference, the top right panel shows the orbital-phase-folded light curve of the binary. From these figures we can draw several conclusions. Firstly, because most pulsation amplitudes and phases vary significantly at all orbital phases, and the scales of the observed pulsation phase modulations are of the order of 0.5 to 1.5 rad, we can conclude that the observed pulsations are tidally perturbed. While tidally tilted pulsations are expected to have pulsation phase modulations of 0 rad, π rad or 2π rad, which can be smeared out (Fuller et al., 2020), tidal perturbations can result in much smaller pulsation phase modulations (e.g., Van Reeth et al., 2023). Moreover, the observed tidally split multiplets are not perfectly equidistant. This is in contradiction with current the-

oretical predictions made for tidally perturbed (e.g., Smeyers, 2005) and tidally tilted pulsations (Fuller et al., 2020), indicating that aspects that are currently not included in these theoretical frameworks, such as the Coriolis force, also play a role. Secondly, based on the different morphology of the curves for the different pulsations, we can conclude that the pulsations have different mode geometries (Van Reeth et al., 2023). For example, while most observed pulsations are modulated twice per orbit, the amplitude of the pulsation with frequency $f = 5.097165(3)\,\mathrm{d}^{-1}$ only reaches one maximum per orbital cycle. Moreover, for some pulsations the pulsation phase decreases as a function of the orbital phase when the observed amplitudes are maximal, while for others the pulsation phase increases. There is no detectable correlation between these effects and the pulsation frequency, but the tidal modulations are most easily observed for pulsations with higher (average) amplitudes. This suggests that most if not all pulsations in this target are tidally perturbed, but that the S/N of the lower-amplitude pulsations is too low for a detection.

Finally, we can confirm that some pulsations belong to the primary, while others could belong to either the primary or the secondary component, in agreement with the inferences made by Guo et al. (2016) based on asteroseismic models. As seen in Fig. 3.12, the observable amplitude of the p mode with frequency $10.39971\,\mathrm{d}^{-1}$ drops during the primary eclipse, indicating that it belongs to the primary. The higher observed amplitudes just before and after the primary eclipse signifies that the pulsation has a higher amplitude on the side of the primary that is facing the secondary component, similar to what has been observed for g-mode pulsations in V456 Cyg (Van Reeth et al., 2022), and KIC 3228863 and KIC 12785282 (Van Reeth et al., 2023). By contrast, the observable amplitudes of the p modes with frequencies $11.52234\,\mathrm{d}^{-1}$ and $11.89048\,\mathrm{d}^{-1}$ peak during the primary eclipse, as shown in Figs. 3.18 and 3.19. This can either indicate that these pulsations belong to the secondary component, or it can be caused by reduced geometric mode cancellation during the eclipse, depending on the geometry of these pulsation modes. The origin of the observed pulsations can be investigated further using detailed asteroseismic modelling, which would allow us to calculate the probability that specific pulsations belong to one or the other component.

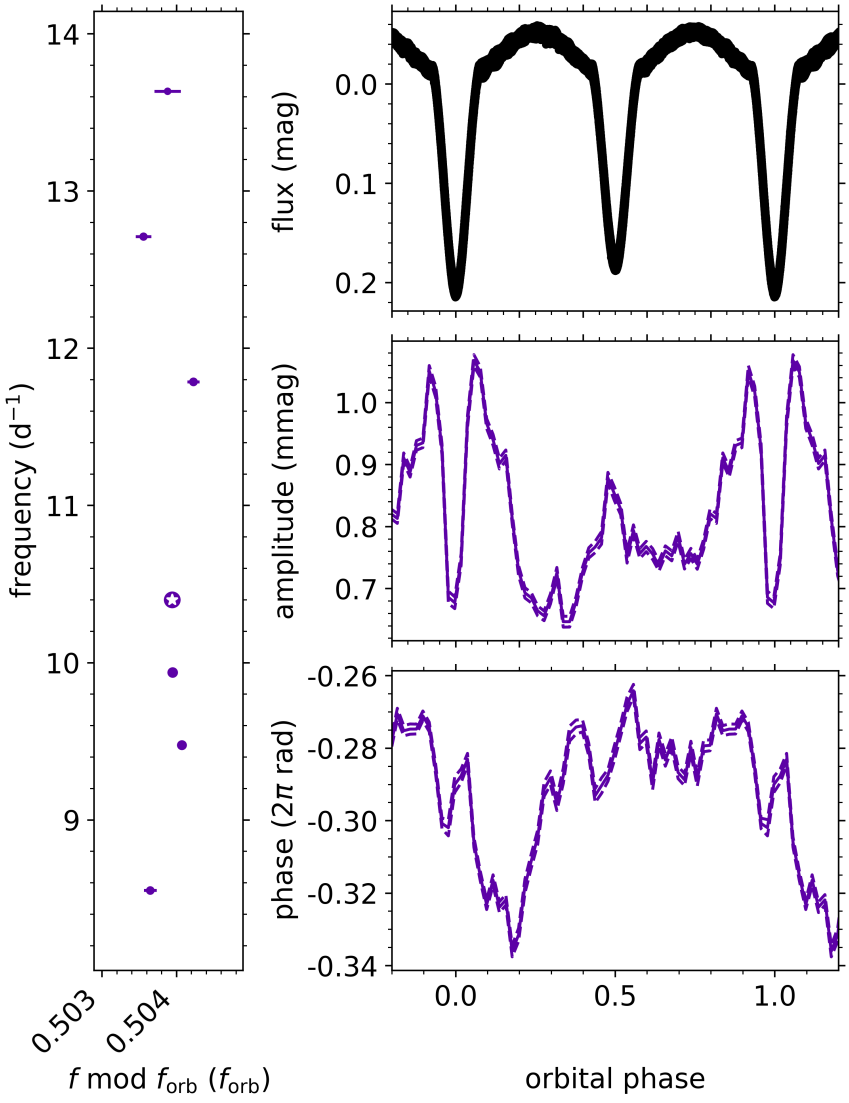

.

Figure 3.12: Tidally perturbed pulsation with frequency $f = 10.399706(2)\,\mathrm{d}^{-1}$. *Left:* Associated frequency multiplet, as shown in Fig. 3.11. The white star marks the dominant frequency of the multiplet. *Top right:* Orbital-phase folded light curve. *Middle right:* Orbital-phase dependent modulations of the pulsation amplitude, calculated in 50 data bins, with the 1σ uncertainty range indicated by the dashed lines. *Bottom right:* Orbital-phase dependent modulations of the pulsation phase, calculated in 50 data bins, with the 1σ uncertainty range indicated by the dashed lines.

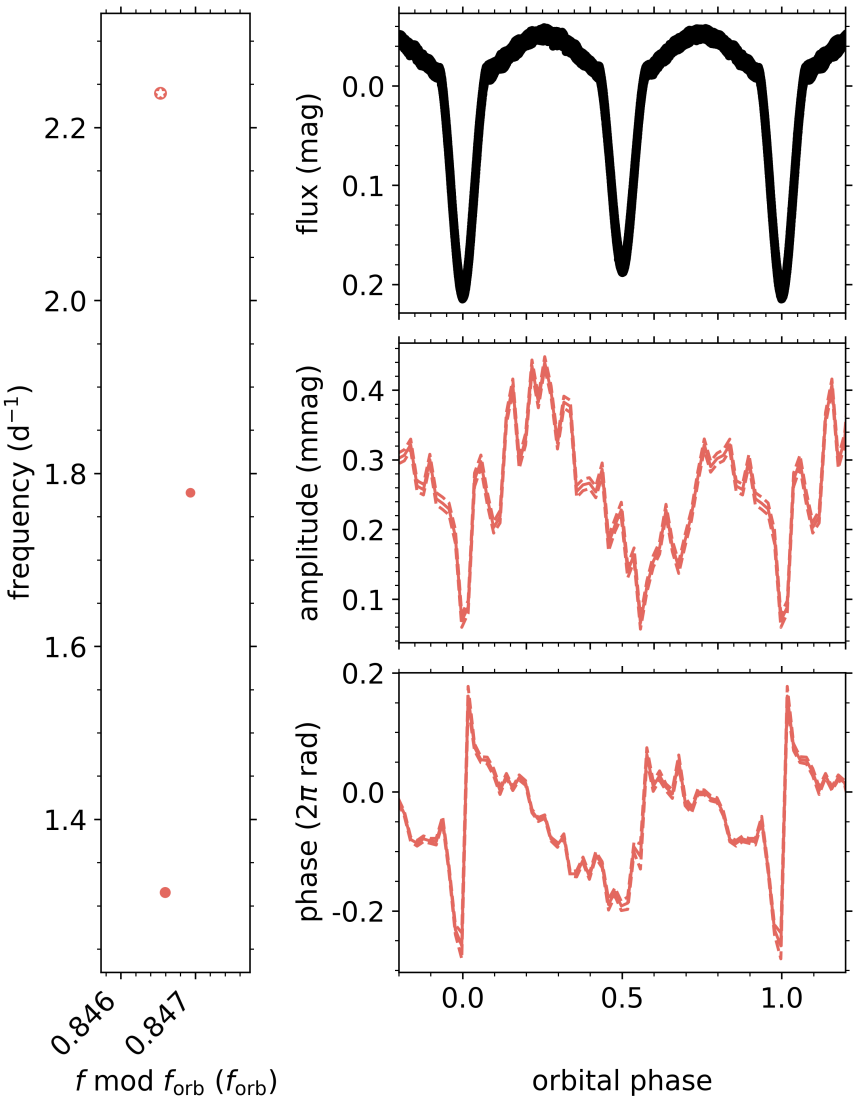

Figure 3.13: Tidally perturbed pulsation with frequency $f = 2.239718(6)\,\mathrm{d}^{-1}$.

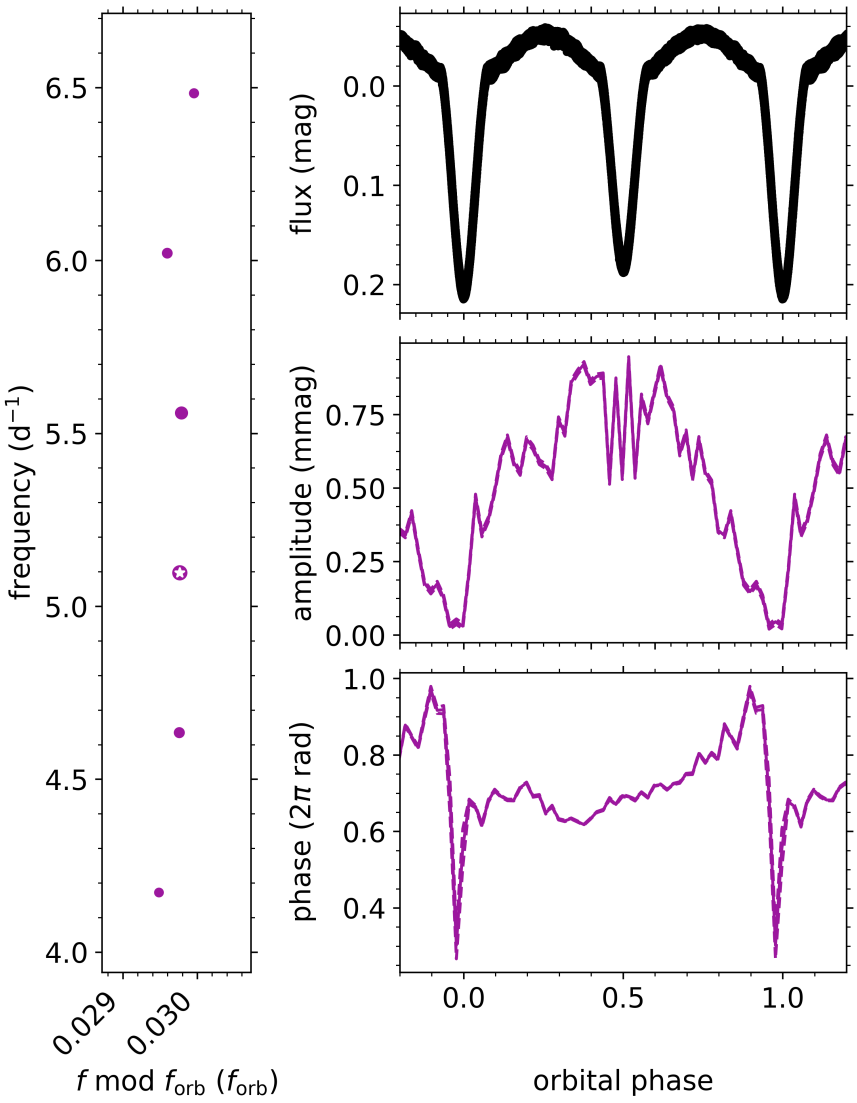

Figure 3.14: Tidally perturbed pulsation with frequency $f = 5.097165(3)\,\mathrm{d}^{-1}$.

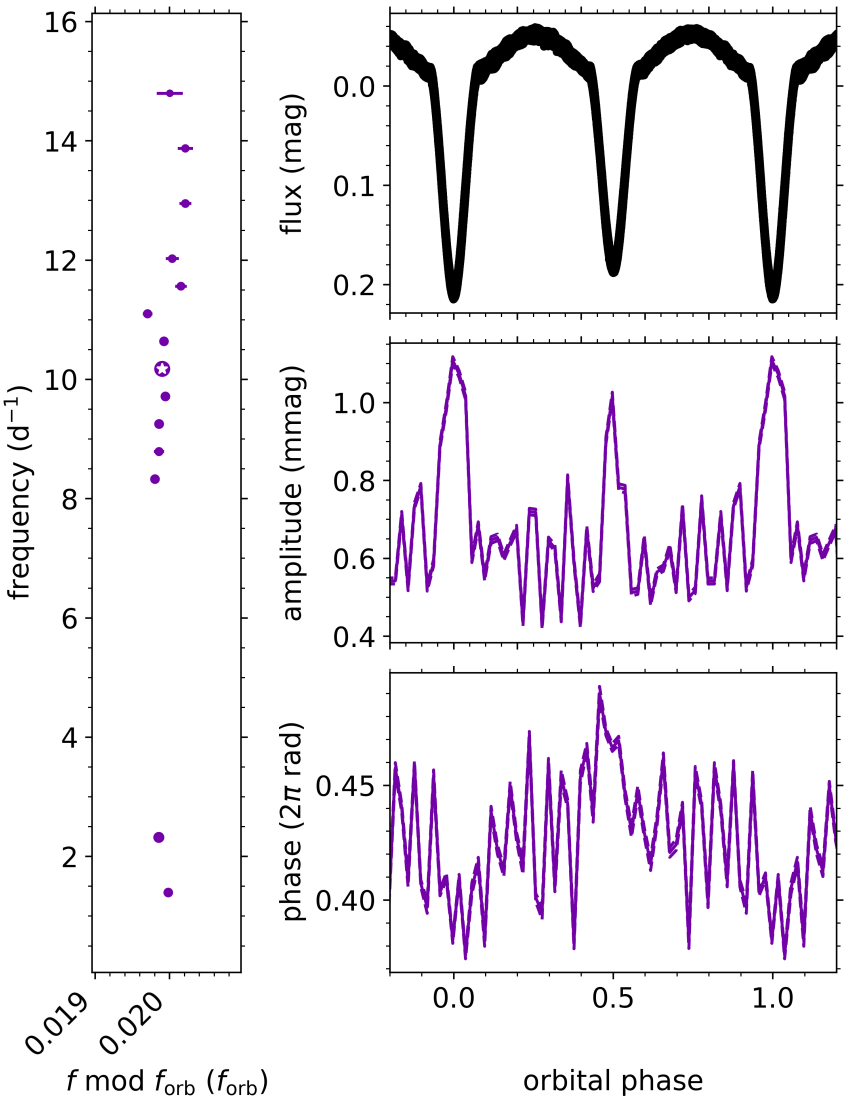

Figure 3.15: Tidally perturbed pulsation with frequency $f = 10.176017(2)\,\mathrm{d}^{-1}$.

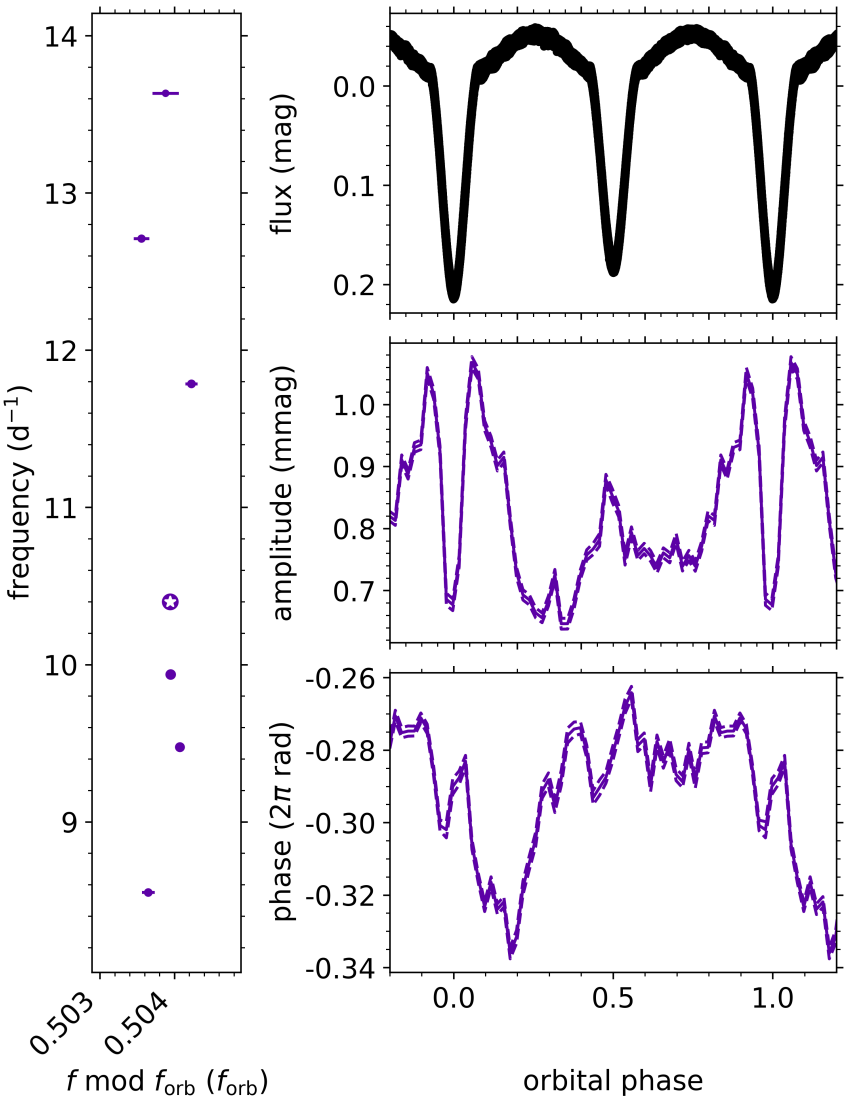

Figure 3.16: Tidally perturbed pulsation with frequency $f = 10.399706(2)\,\mathrm{d}^{-1}$.

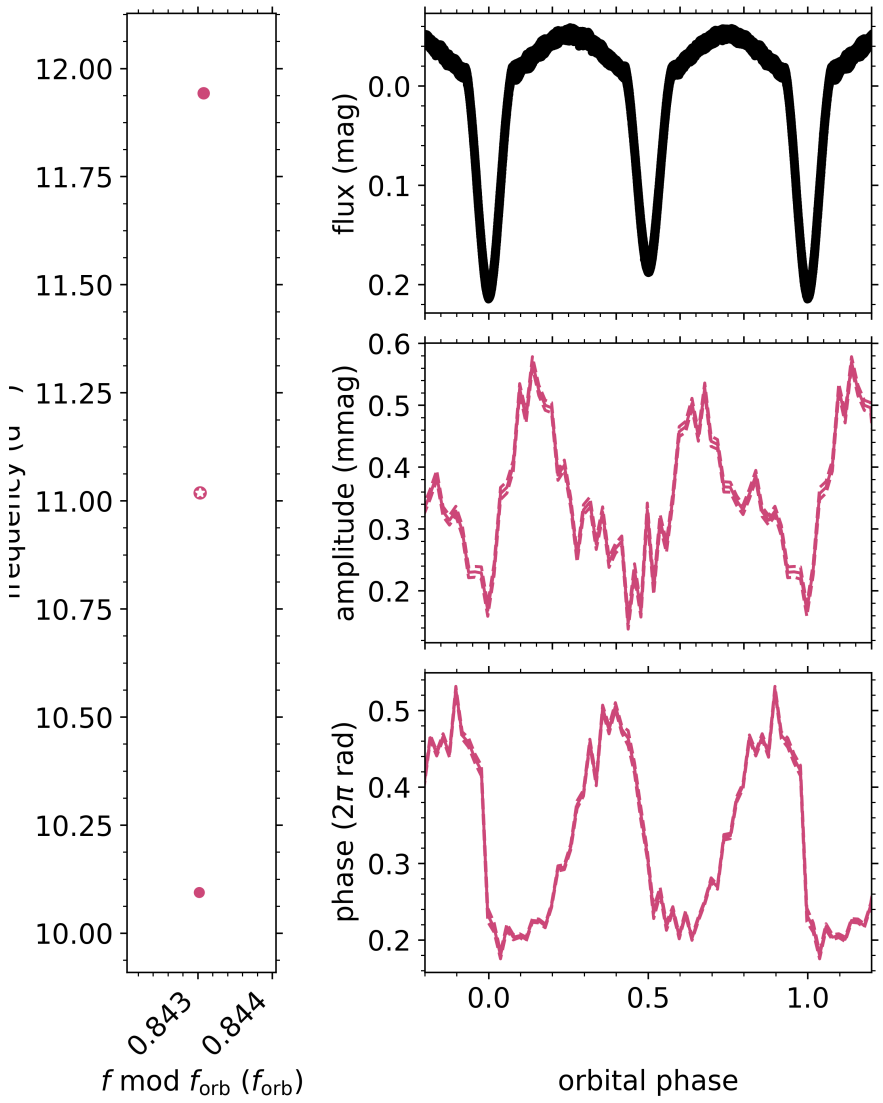

Figure 3.17: Tidally perturbed pulsation with frequency $f = 11.018536(5)\,\mathrm{d}^{-1}$.

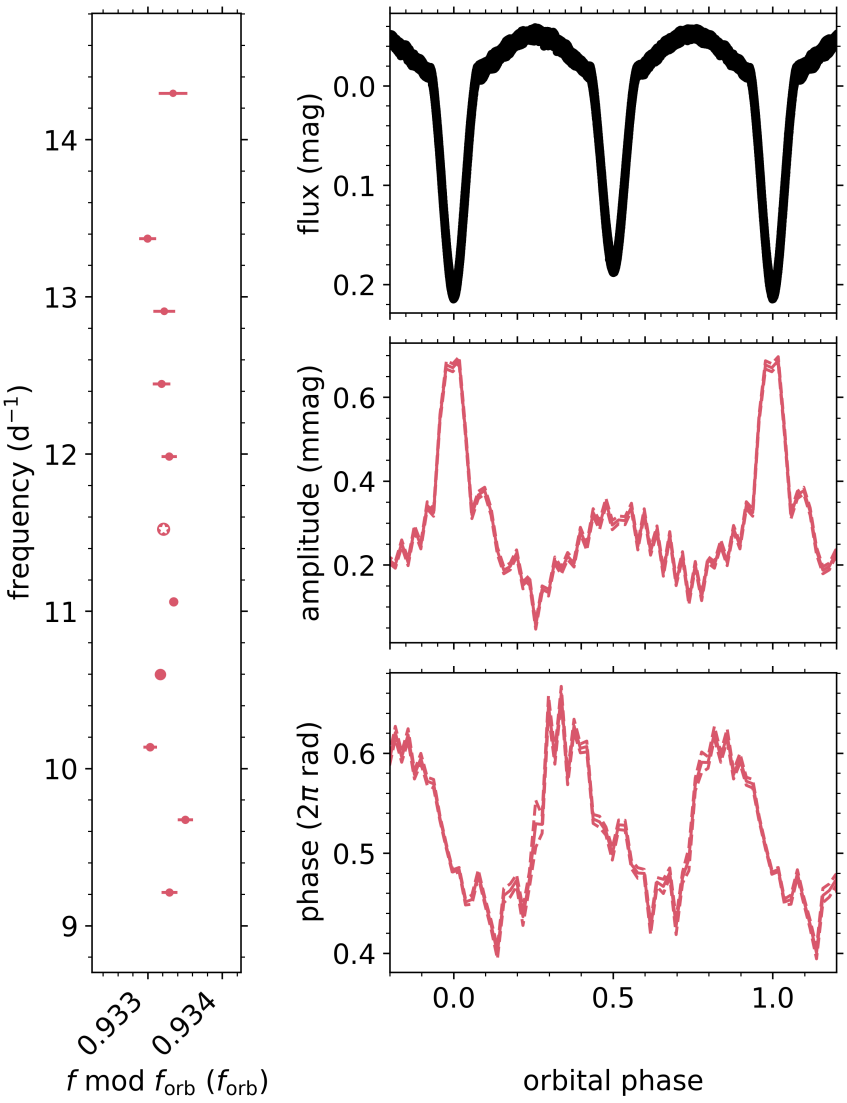

Figure 3.18: Tidally perturbed pulsation with frequency $f = 11.522340(5)\,\mathrm{d}^{-1}$.

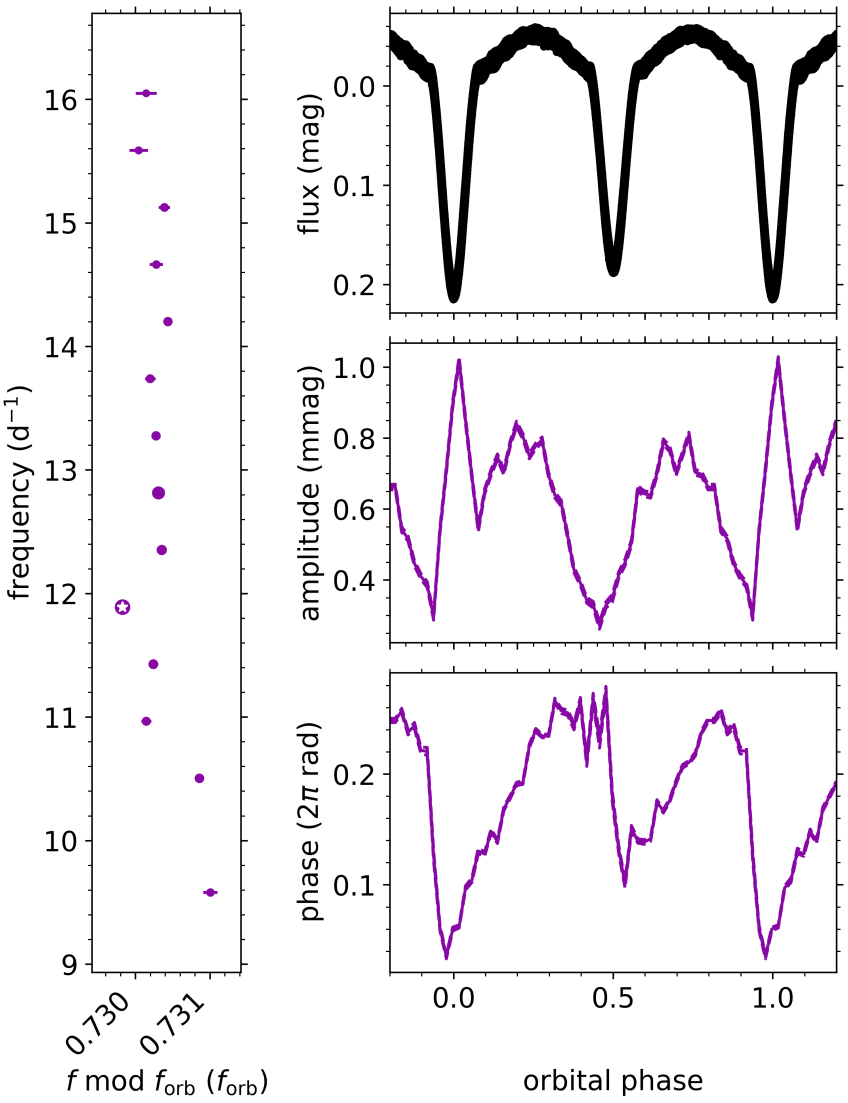

Figure 3.19: Tidally perturbed pulsation with frequency $f = 11.890477(2)\,\mathrm{d}^{-1}$.

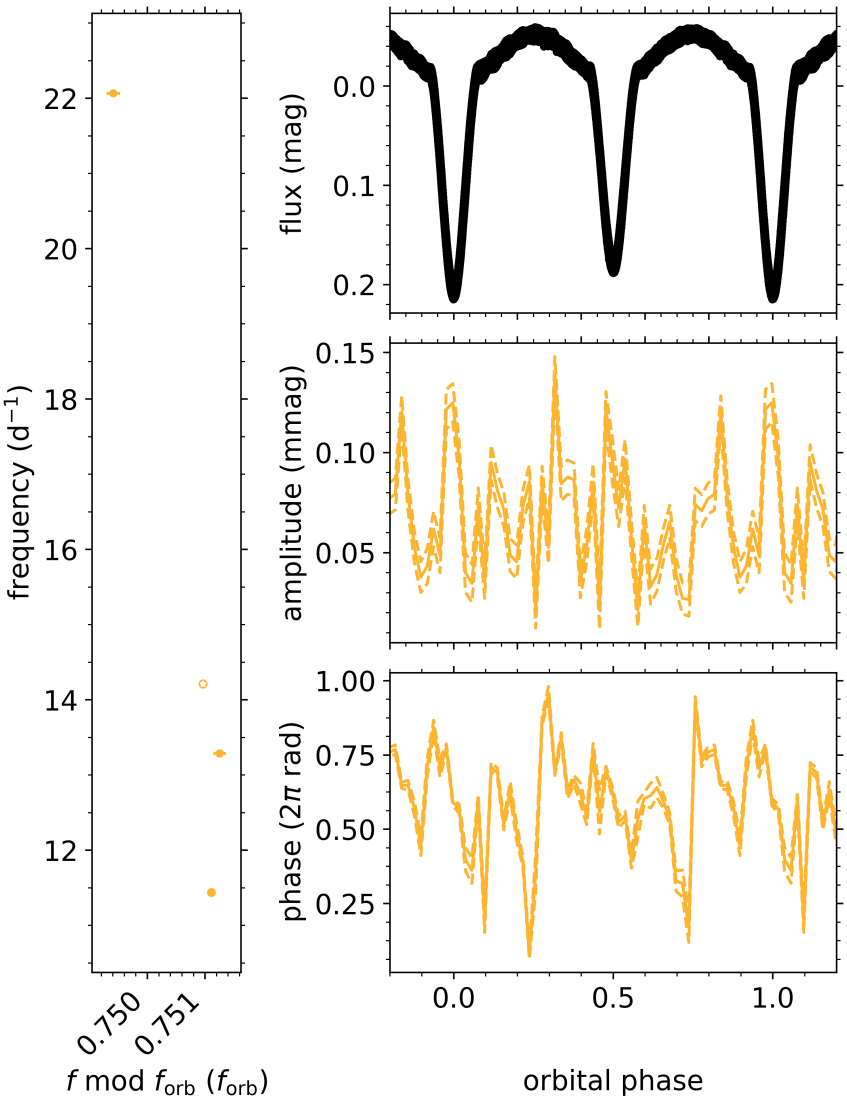

Figure 3.20: Tidally perturbed pulsation with frequency $f = 14.210888(3)\,\mathrm{d}^{-1}$.

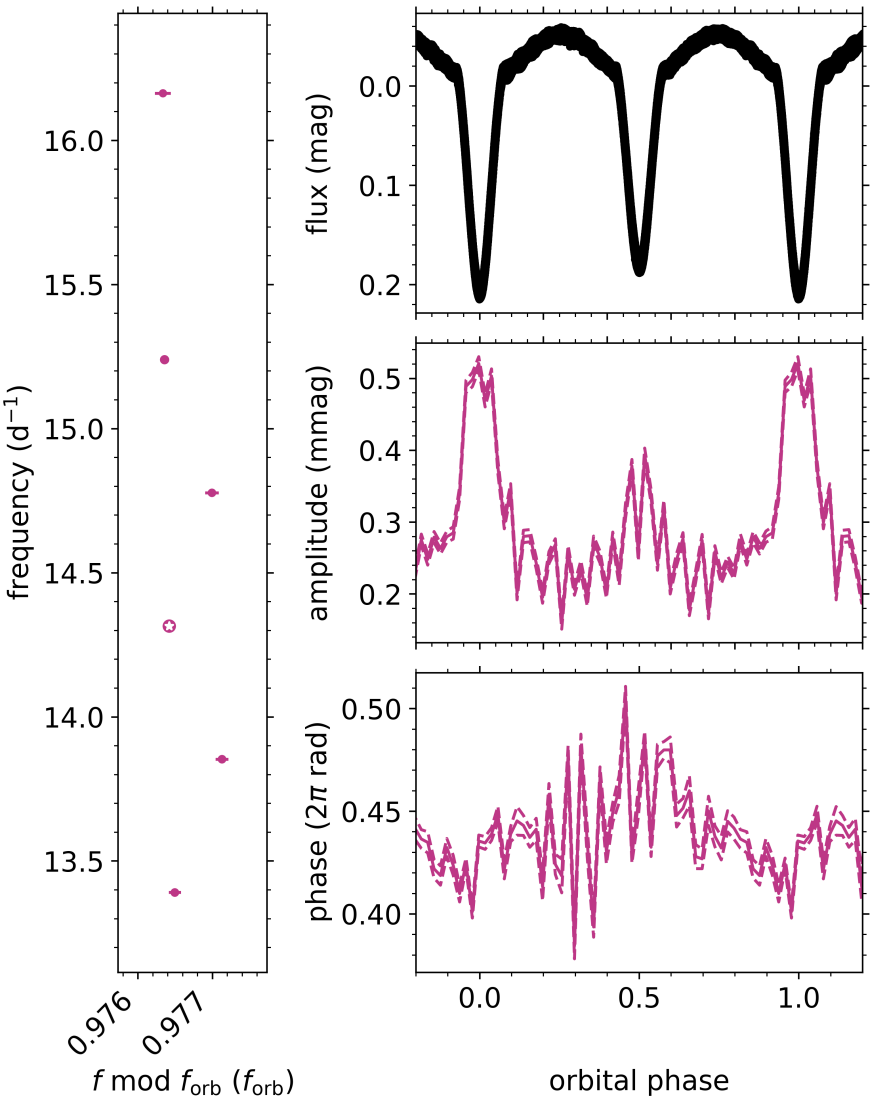

Figure 3.21: Tidally perturbed pulsation with frequency $f = 14.315077(5)\,\mathrm{d}^{-1}$.

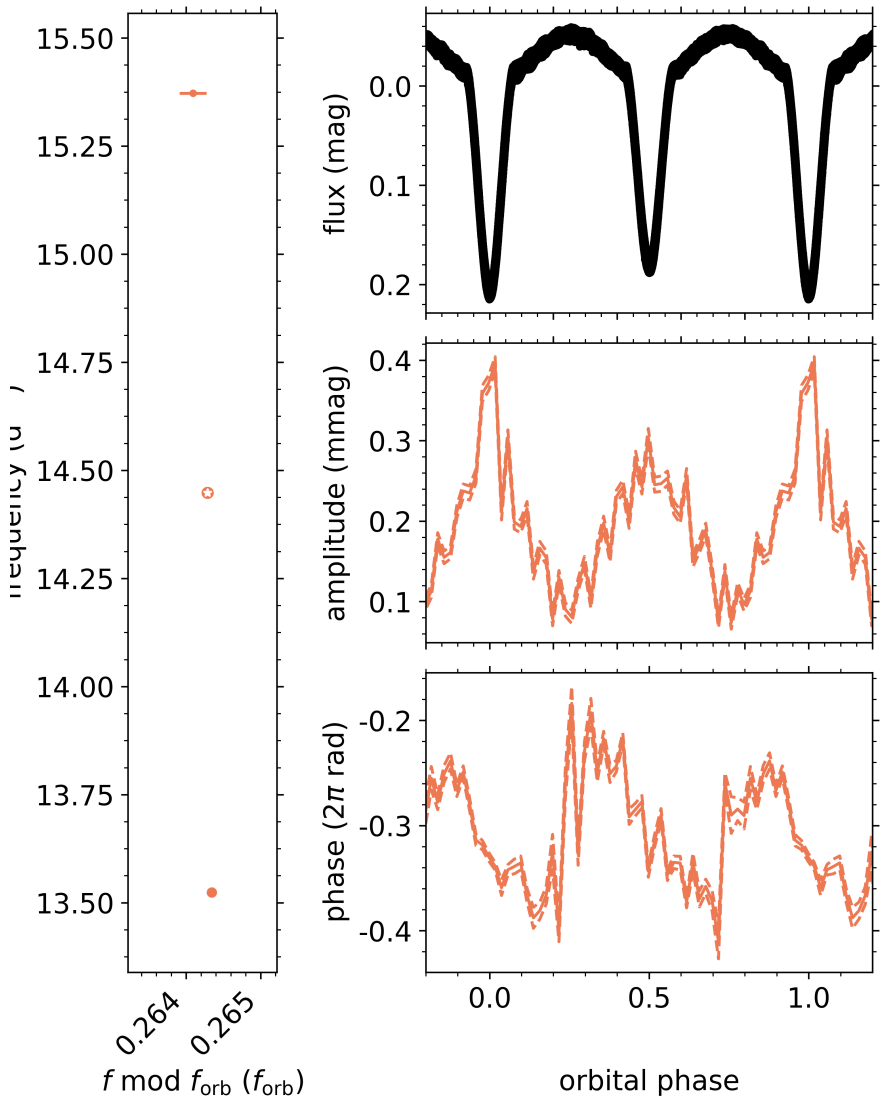

Figure 3.22: Tidally perturbed pulsation with frequency $f = 14.448108(7)\,\mathrm{d}^{-1}$.

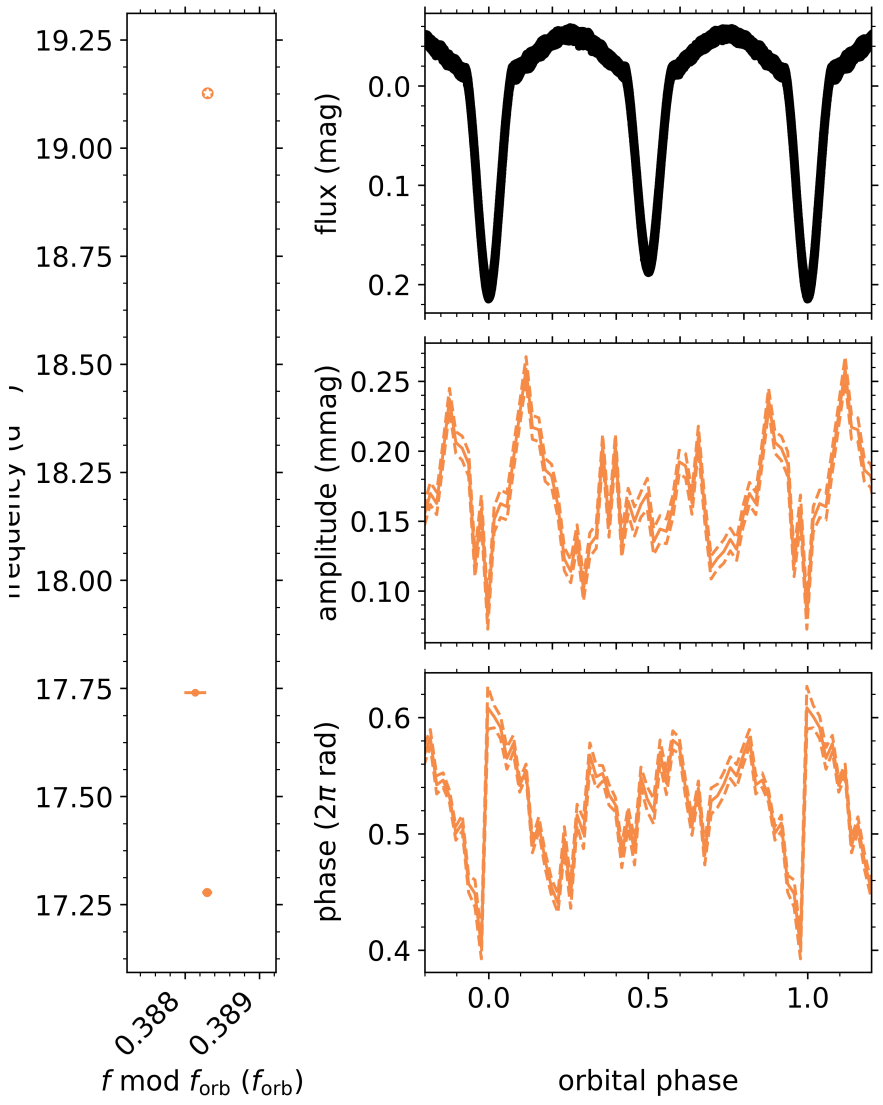

Figure 3.23: Tidally perturbed pulsation with frequency $f = 19.126701(8)\,\mathrm{d}^{-1}$.

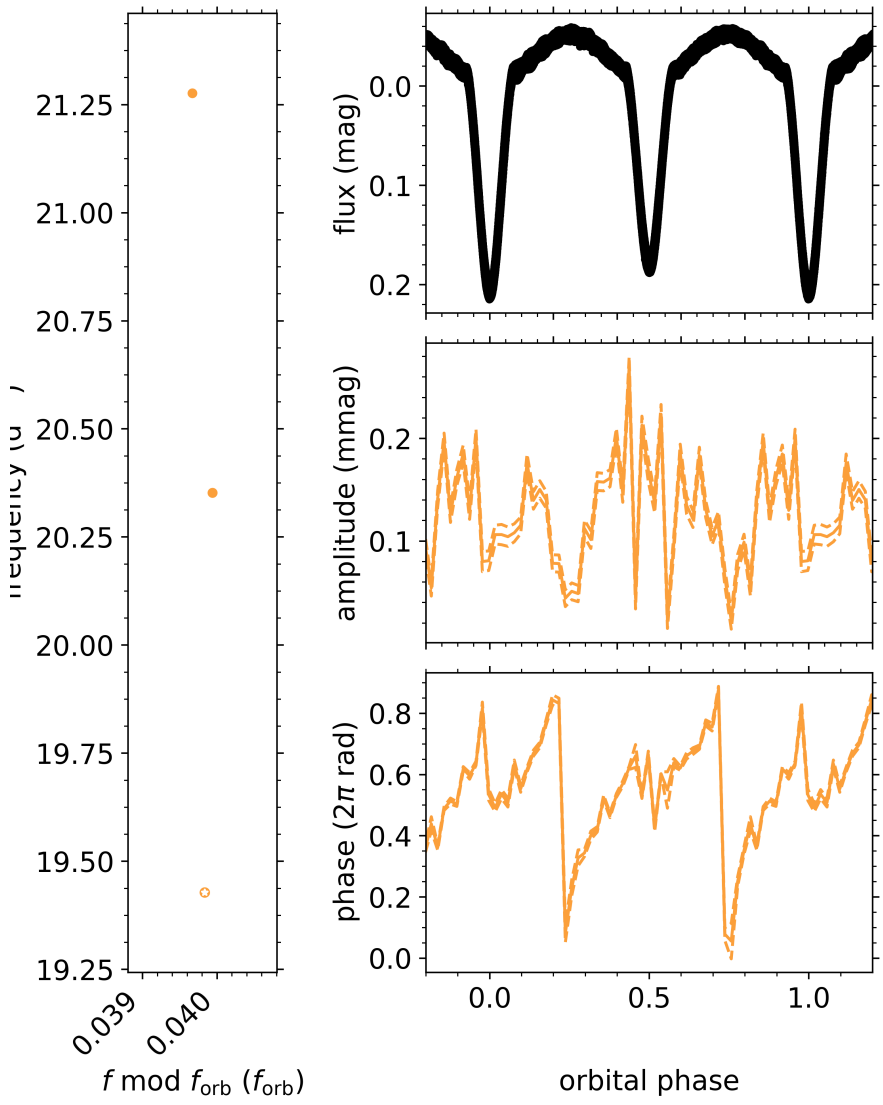

Figure 3.24: Tidally perturbed pulsation with frequency $f = 19.427792(15)\,\mathrm{d}^{-1}$.

However, such a modelling study lies outside the scope of the current work.

3.8.3 Orbital harmonic frequencies

In addition to the tidal perturbation of self-excited pulsations, and in agreement with Guo et al. (2016), we also detect an orbital harmonic frequency comb, illustrated in Fig. 3.25, which can indicate tidally excited oscillations. However, we do not recover the same orbital harmonics as Guo et al. (2016). They reported the detection of $8f_{\rm orb}$, $22f_{\rm orb}$, $46f_{\rm orb}$, and $50f_{\rm orb}$. While our detected orbital harmonic frequency comb consists of 19 frequencies, we only recover $22f_{\rm orb}$. This discrepancy is likely caused by differences between the reduced short- and long-cadence *Kepler* light curves, and between the photometric binary models. Thus, while we confirm the presence of orbital-phase dependent variability in the pulsation light curve, as seen in the bottom right panel of Fig. 3.25, its exact observed characteristics have to be treated with caution.

As pointed out by Guo et al. (2016), the detection of an orbital harmonic frequency comb is somewhat unexpected for synchronised binaries with circular orbits, though it has also been detected for other such systems (da Silva et al., 2014). Because the orbital eccentricity of the binary is zero, the equilibrium tides that are responsible for deforming the star and perturbing the pulsations are considerably larger than the dynamical tides that excite oscillations. Hence, this can indicate that this system has a slightly eccentric orbit or that one or both of the components is asynchronously rotating, within the uncertainty margins of our measurements.

3.8.4 Gravity-mode period-spacing pattern

Finally, we analyse the observed g-mode pulsations in detail. Li et al. (2020b) reported the detection of a short period-spacing pattern of prograde sectoral quadrupole modes, that is with $(k, m) = (0, 2)$, and assigned them to the primary component of the system, based on the stellar masses determined by Guo et al. (2016). In this work, we confirm the pattern detection by Li et al. (2020b) using the methodology from Van Reeth

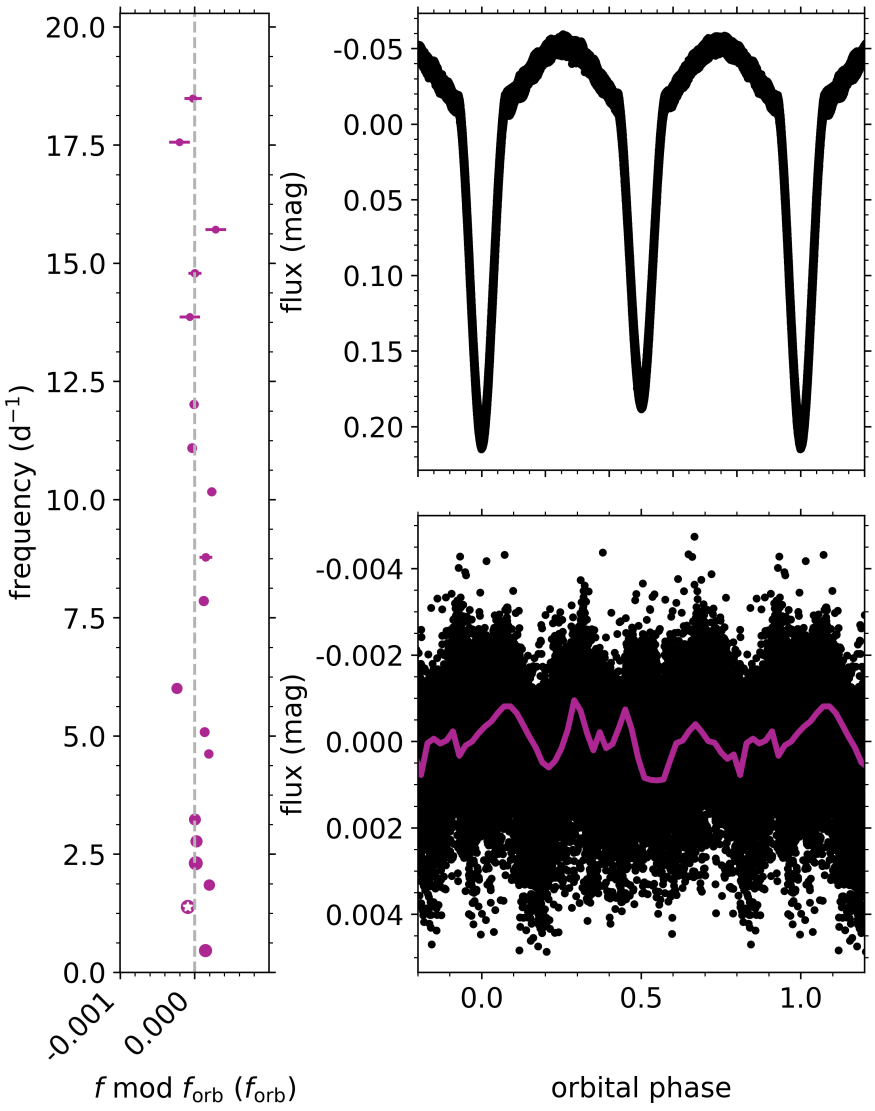

Figure 3.25: Tidally excited oscillations in KIC 9851944. *Left:* Associated frequency multiplet, as shown in Fig. 3.11. The white star marks the dominant frequency of the multiplet. *Top right:* Orbital-phase folded light curve. *Bottom right:* Orbital-phase folded residuals of the light curve after subtraction of the binary model. Individual data points are shown in black. The overplotted purple line shows the average variability as a function of orbital phase, evaluated in 50 equal bins.

et al. (2015b), as shown in Fig. 3.26. Only the g mode with frequency $\sim 0.461\,\mathrm{d}^{-1}$ was not recovered because of the higher signal-to-noise ratio cutoff that we used, that is, $S/N \geq 5.6$ instead of 4.0. Moreover, the dominant g mode in the pattern, with a frequency f of $2.239718(6)\,d^{-1}$, was found to be tidally perturbed and exhibit spatial filtering during the primary eclipse, as shown in Fig. 3.13 and with the corresponding multiplet listed in Table 3.8. These observations confirm that the g modes belong to the primary component of the system: the observed tidal perturbations exhibit a dip in the amplitude and a saw-tooth-like "glitch" in the pulsation phase during the primary eclipse, which can only be explained if the pulsation belongs to the primary (Van Reeth et al., 2022, 2023).

To investigate the potentially asynchronous rotation of the pulsating star, we modelled our detected period-spacing pattern by fitting an asymptotic period-spacing series, following the method described by Van Reeth et al. (2016). We confirmed the pulsation mode identification found by Li et al. (2020b), $(k, m) = (0, 2)$, and found that the star has a buoyancy radius Π_0 of $4370^{+690}_{-660}\,\mathrm{s}$ and a near-core rotation frequency f_{rot} of $0.49^{+0.05}_{-0.06}\,\mathrm{d}^{-1}$. These values agree within 1σ with the results from Li et al. (2020b), who found Π_0 and f_{rot} values of $3500\pm500\,\mathrm{s}$ and $0.41\pm0.05\,\mathrm{d}^{-1}$, respectively. Moreover, both sets of values are consistent with synchronous rotation. However, because the detected pattern is so short, the uncertainties on these f_{rot} values are relatively large. Hence, there is still a possibility that the primary is asynchronously rotating, but insufficiently strongly to be detected with the available data.

3.9 Discussion

We compared the observed properties of the components of KIC 9851944 to isochrones calculated by MIST (Mesa Isochrones and Stellar Tracks) using the MESA code (Paxton et al., 2011, 2013, 2015; Dotter, 2016; Choi et al., 2016; Paxton et al., 2019). We searched for the best MIST isochrone using two methods. For method 1, we interpolated radius, T_{eff} and luminosity as functions of mass. We then estimated these

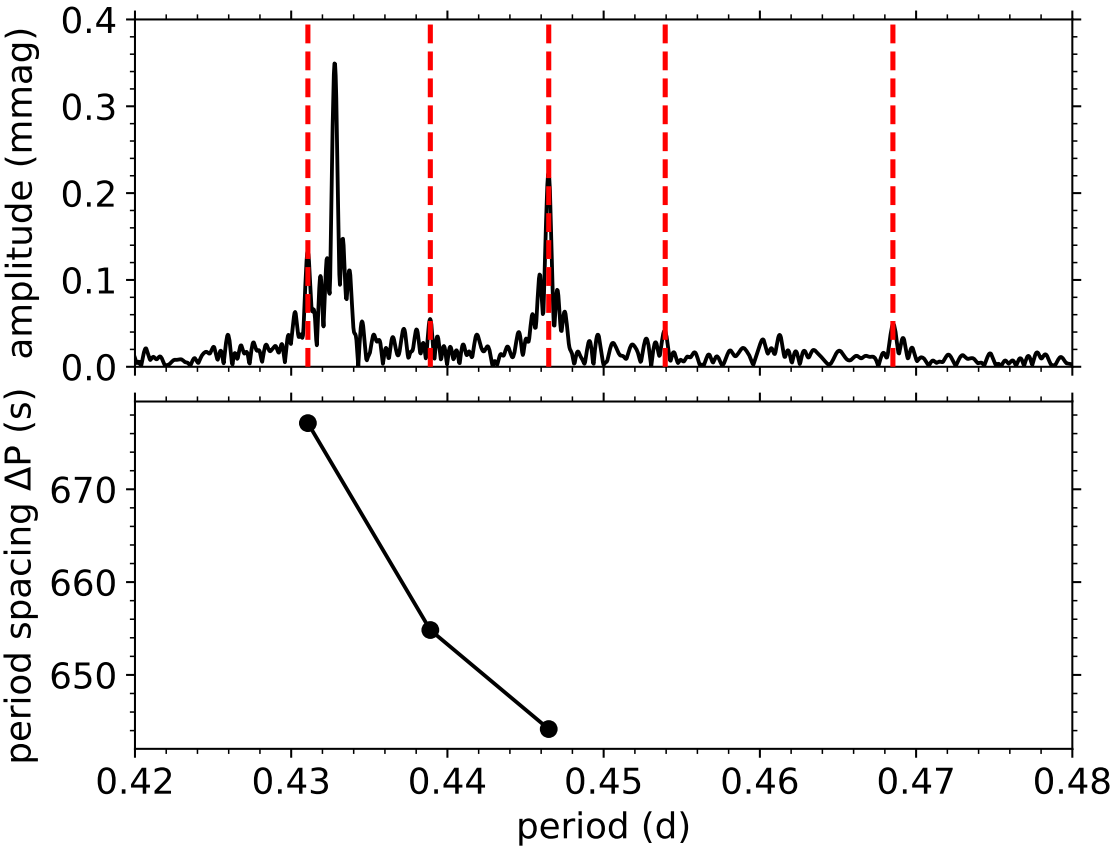

Figure 3.26: Detected period-spacing pattern of g modes with $(k, m) = (0, 2)$ that belong to the primary component of KIC 9851944. *Top:* part of the Lomb-Scargle periodogram of the pulsation light curve (black) with the pulsation periods of the modes that form the pattern (red dashed lines). *Bottom:* the period spacing between consecutive modes in the detected pattern, as a function of the pulsation period. Because there is an undetected mode between the fourth and fifth detected pulsation modes, the fourth period spacing in the pattern is not shown. The error margins are smaller than the symbol sizes.

parameters using the interpolants at our measured masses. The objective function to minimise is then the sum of the quadrature distances between the interpolated and observed locations of the components with age and metallicity as free parameters. For method 2, we included mass in the calculation of the objective function, i.e., masses are not constrained to the observed values. For the minimisation, we used SciPy's implementation of the stochastic differential evolution algorithm (Storn & Price, 1997; Virtanen et al., 2020). Our grid of isochrones spanned from -4.0 to 0.5 dex in [Fe/H] and 0.5 to 10.3 dex in $\log_{10}$(age). The grid spacing in [Fe/H] was 0.05 dex between -0.5 and 0.5 dex and 0.25 dex outside that range up to ± 2 dex, beyond which the grid spacing was 0.5 dex. A grid spacing of 0.05 dex in $\log_{10}$(age) was used through the full grid.

After the best matching coeval isochrone was found, we removed the corresponding metallicity value from our isochrone grid and repeated the procedure to explore the effect of varying [Fe/H] on the predicted age of the system. We did this twice, leading to first, second, and third best matching coeval isochrones, each corresponding to a different metallicity. For method 1, the metallicity values of the first, second and third best matching isochrones were 0.05, 0.1 and 0.0 dex, respectively. For method 2, these values correspond to 0.05, 0.0 and 0.1 dex, i.e., the same set, except the second and third best matches are swapped. In all cases, the predicted age of the system is 1.259 ± 0.073 Gyr. The error on this age estimate is taken to be half the average grid spacing either side of the best fitting isochrone. We note that this age estimation is in excellent agreement with the estimation by Guo et al. (2016) of 1.25 Gyr.

The three best-fitting isochrones are shown in Fig. 3.27 with the observed locations of the objects over-plotted in the $M - \log(T_{\rm eff})$, $M - \log(R)$, $M - \log(L)$ and HR diagrams; also shown are their isochrone neighbours, i.e., $\pm$ the grid spacing in age. For both model comparison methods, the isochrone with [Fe/H] = 0.05 dex yielded the model with the smallest quadrature distance to the observed quantities that were included in the objective functions so we adopt the corresponding model predictions from now on. Those values and their differences relative to the observed values are given in Table 3.9 for both model comparison methods. The locations of these values in the

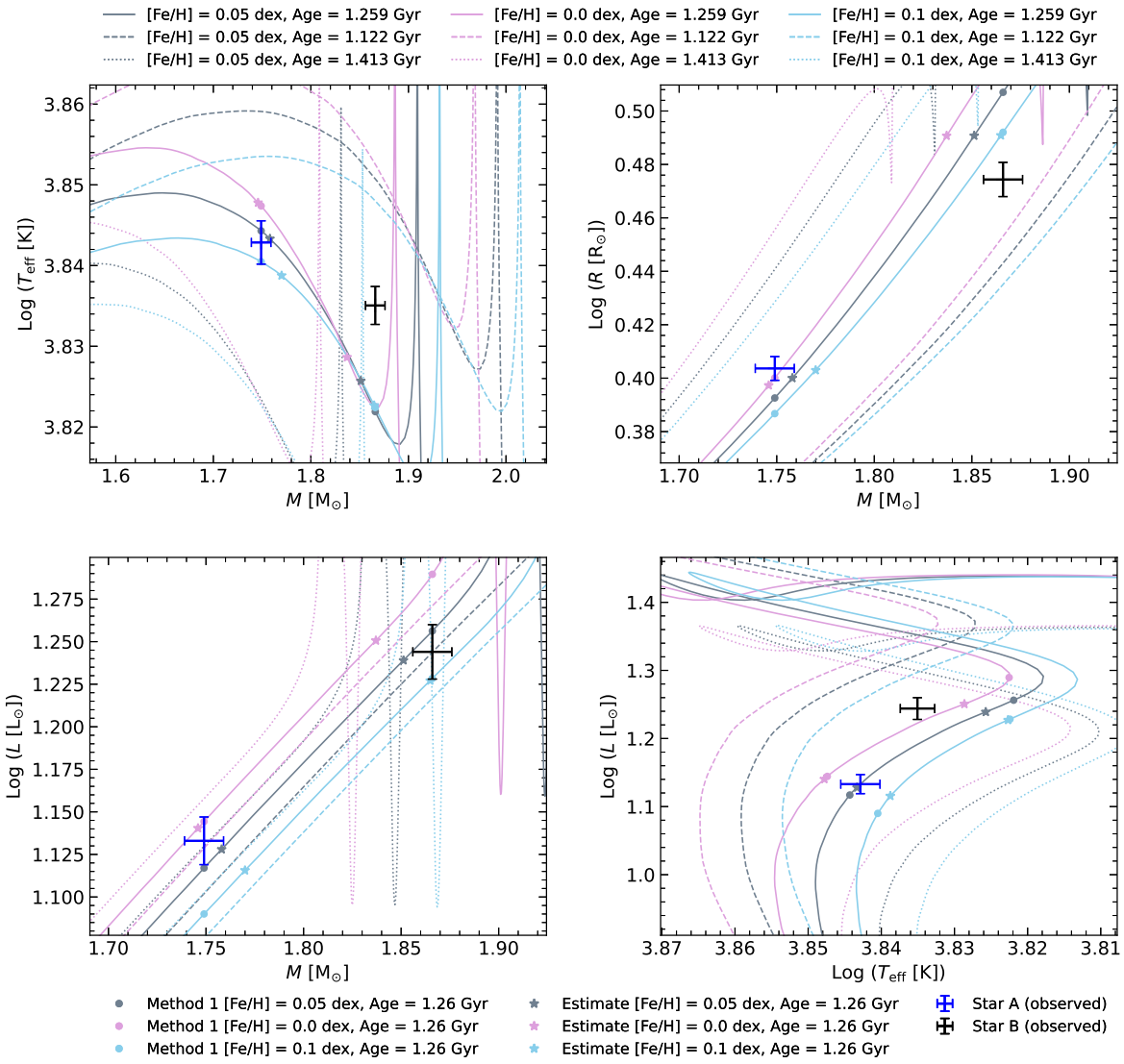

Figure 3.27: The three best fitting isochrones with the observed locations of the objects over-plotted in the $M - \log(T_{\rm eff})$ (top-left), $M - \log(R)$ (top-right), $M - \log(L)$ (bottom-left) and HR (bottom-right) planes. Also plotted are the best fitting isochrone neighbours, i.e., $\pm$ the grid spacing in age. The locations of the isochrones within those planes corresponding to the model with the smallest quadrature distance to the measured quantities that were included in the objective function are indicated for those from both model comparison methods.

Table 3.9: Model parameters of the best fitting isochrone with [Fe/H] = 0.05 dex and an age of 1.259 ± 0.073 Gyr. The results obtained from both comparison methods are given. Also given are the differences Δ between the observations and model for each parameter; we quote this difference in units of the uncertainty associated with the observations in brackets.

Parameter	Method 1		Method 2	
	Value	Δ[%]	Value	Δ[%]
Mass ratio	1.0667	0.0 (0.0σ)	1.0530	-1.2 (3.6σ)
$M_{\rm A}$ [$\rm M_\odot$]	1.749	0.0 (0.0σ)	1.758	0.5 (0.9σ)
$M_{\rm B}$ [$\rm M_\odot$]	1.866	0.0 (0.0σ)	1.851	-0.8 (1.5σ)
$R_{\rm A}$ [$\rm R_\odot$]	2.469	-2.5 (2.5σ)	2.512	-0.8 (0.8σ)
$R_{\rm B}$ [$\rm R_\odot$]	3.214	7.8 (5.3σ)	3.096	3.8 (2.6σ)
$T_{\rm eff,A}$ [K]	6987	0.33 (0.5σ)	6971	0.1 (0.2σ)
$T_{\rm eff,B}$ [K]	6636	-3.0 (5.5σ)	6694	-2.1 (3.9σ)
$\log(L_{\rm A}/\,\rm L_\odot)$	1.117	-1.4 (1.0σ)	1.128	-0.4 (0.4σ)
$\log(L_{\rm B}/\,\rm L_\odot)$	1.256	1.0 (0.8σ)	1.239	-0.4 (0.3σ)

planes of Fig. 3.27 are also shown; note the relative scales of the axes, particularly for $T_{\rm eff}$ where the scale of the axis is much smaller than the scales of the other axes.

Table 3.9 confirms that the luminosity predictions from our best matching isochrone resulting from both comparison methods are accurate for both components and this is also clear in the lower, left panel of Fig. 3.27. The other parameters are also in good agreement for star A, particularly regarding those resulting from method 2 where the agreement is excellent. However, for star B, the radius is underestimated while the $T_{\rm eff}$ is overestimated, and these discrepancies compensate for each other to yield the accurate luminosity prediction.

A possible explanation is that the secondary star is approaching the terminal age main sequence (TAMS), i.e., an evolved stage where the sensitivity of the models increases. Thus, a full evolutionary modelling analysis, such as that carried out by Guo et al. (2016), might yield better model predictions because metallicity and other parameters relating to, e.g., overshooting, are included as free parameters so the model is more flexible. This would also provide the means for a more detailed discussion of

model comparison with observations but is beyond the scope of this paper. Here, we simply searched in grids of pre-computed models, which are limited by the size of the grid steps in metallicity and age, as well as fixed input physics, to estimate the age of the system. The parameter ranges that the isochrone neighbours span in the planes shown in Fig. 3.27 (i.e., about twice the uncertainty), and the agreement with the value determined by Guo et al. (2016), is evidence that this age estimation is accurate.

The evolutionary tracks corresponding to the masses of the models in Table 3.9 are shown in the $T_{\rm eff}$-R, and HR diagrams in Figs. 3.28 and 3.29, respectively, as well as the observed locations of the components. While Guo et al. (2016) find the secondary to be in the hydrogen-shell burning phase for the same age estimate as ours, we find that the secondary has not yet exhausted the hydrogen in its core, and is approaching the TAMS. The scenario found here is more likely to be observed on a statistical basis since the evolution up the HR diagram after the blue loop occurs on a very short timescale. In any case, the secondary is more evolved and thus larger and more massive than the primary, but cooler.

Also shown in those figures are is the blue and red edges of the instability strips for low-order p- (dashed lines), and g-modes (dotted lines) in δ Scuti and γ Doradus stars, respectively, from Xiong et al. (2016). Both stars are well within both instability domains which is in agreement with the findings in Section 3.8 that both components might be pulsating. Guo et al. (2016) find that the secondary is slightly hotter than the blue edge of the γ Doradus instability domain calculated by Dupret et al. (2005). This reflects the fact that the calculations by Xiong et al. (2016) (used here) predict a much broader overlap between the δ Scuti and γ Doradus instability domains so stars with a larger range in $T_{\rm eff}$ are expected to pulsate simultaneously in p- and g-modes, i.e., hybrids are expected to be more common. We also plotted a sub-solar ZAMS ([Fe/H] = -0.25 dex) as well as the ZAMS corresponding to our best matching isochrone ([Fe/H = 0.05 dex] in Fig. 3.28 and Fig. 3.29; this shows how the ZAMS is raised to higher luminosities and radii for higher metallicity.

We present the results previously derived by Guo et al. (2016) in Table 3.10. The 13 spectroscopic observations that the previous authors used to derive their RVs and

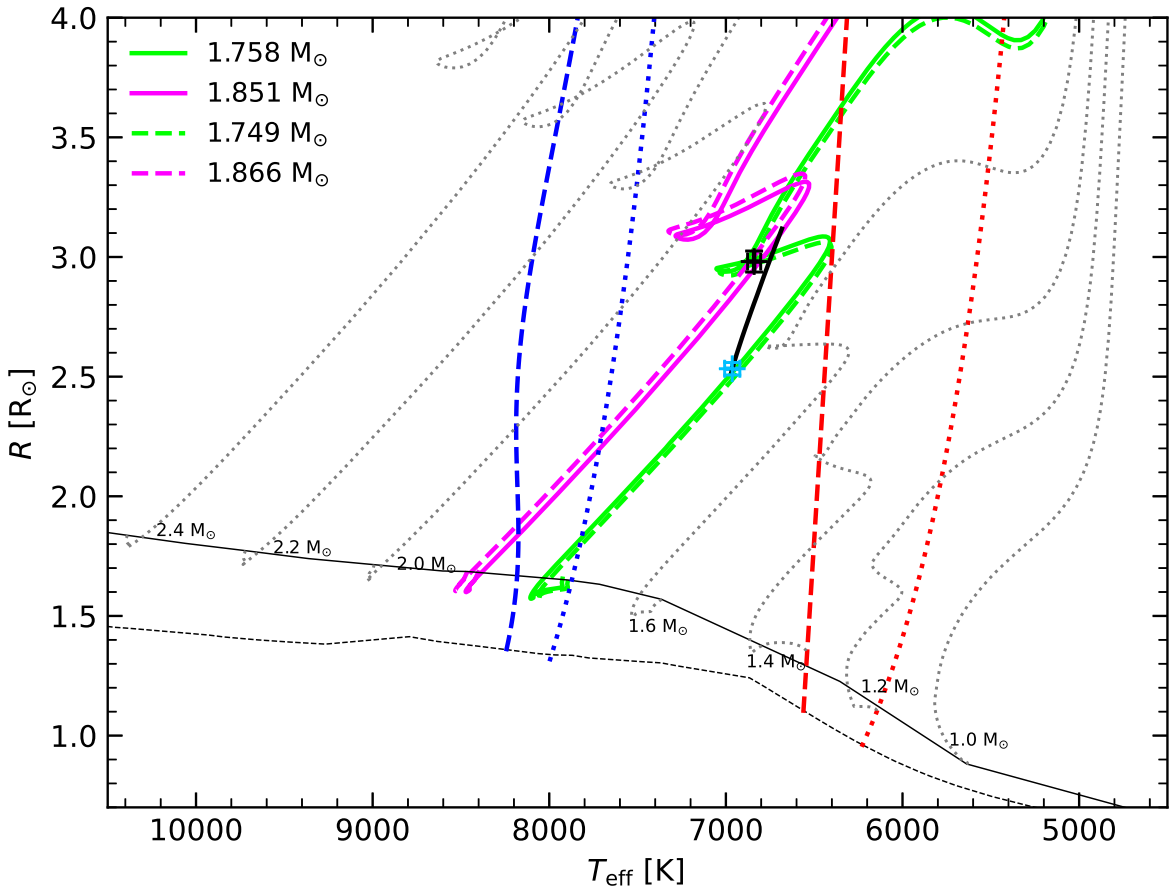

Figure 3.28: The $T_{\rm eff}$-R plane showing the evolutionary tracks corresponding to the models presented in Table 3.9. The evolutionary tracks are shown in green and purple for star A and star B, respectively, and their observed locations are indicated by the blue and black markers. The blue (blue lines) and red (red lines) edges of the instability domains for low-order p- and g-modes calculated by Xiong et al. (2016) for δ Scuti (dashed lines) and γ Doradus (dotted lines) stars are indicated. The thin, black line is the ZAMS corresponding to the models in Table 3.9 ([Fe/H] = 0.05 dex) and the dotted black line is the ZAMS for a metallicity of [Fe/H] = -0.25 dex. The thick, black line represents the best fitting isochrone which is shown as a solid grey line in Fig.3.27. Transparent grey dotted lines show the evolutionary tracks of [Fe/H] = 0.05 dex stars with other labelled masses.

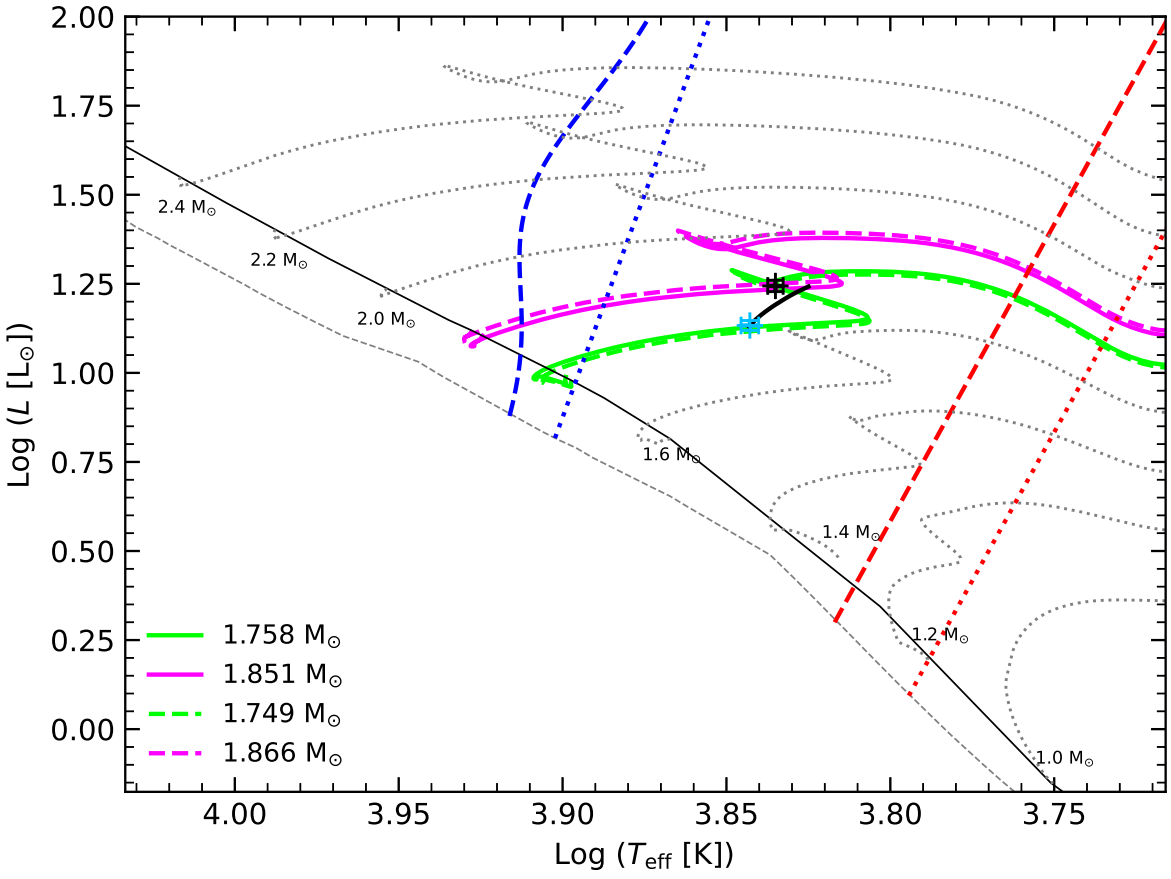

Figure 3.29: Same as Fig. 3.28 but in the Hertzsprung-Russell diagram.

atmospheric parameters have resolutions of $R = 6000$. While it was already discussed in Section 3.5.1 that our atmospheric parameters agree with those derived by Guo et al. (2016), the higher resolution ($R = 60000$) of the spectra, and larger number of observations (33) used in this work yielded a much higher quality RV curve. This is reflected by comparing the reported masses between the two studies; the precision in the mass estimates by Guo et al. (2016) are 4.0% and 3.9% for the primary and secondary, respectively, while we attain precisions of 0.57% and 0.59%. The two sets of mass measurements agree to within $0.2\,\sigma$ for $M_{\rm A}$ and $1.1\,\sigma$ for $M_{\rm B}$. In contrast, our radius measurements differ from those of Guo et al. (2016) by $6.6\,\sigma$ for star A and $3.5\,\sigma$ for star B. However, Guo et al. (2016) note the discrepancy between their values for the radius ratio derived from two spectroscopic methods ($k = 1.22 \pm 0.05$ and $k = 1.27 \pm 0.29$) and the value derived from their light curve modelling (1.41 ± 0.018), where they *tentatively* adopt the radii associated with the latter. The radius ratio derived here agrees with the values derived by Guo et al. (2016) using their spectroscopic methods within $0.8\,\sigma$ and $0.3\,\sigma$, but shows the same discrepancy compared to the value derived from their light curve modelling, for which Guo et al. (2016) note there exists a family of comparable solutions due to the partial nature of the eclipses.

We have assumed a circularised and synchronised orbit for KIC 9851944 because our RV- and light-curve solutions were consistent with a circular orbit, and the values for the component of the synchronous velocity along our line of site are in excellent agreement with the values for $v \sin i$ derived in Section 3.5.1 (see Table 3.4). Further justification was provided by Guo et al. (2016) where they examined the eclipse times by Conroy et al. (2014) and Gies et al. (2015), finding that the median deviation of the phase difference between the primary and secondary eclipses from that of a circular orbit suggests $e \geq 0.0001$. Furthermore, the circularisation time-scale for a binary system like KIC 9851944 is 600 Myr, and the synchronisation timescale is an order of magnitude shorter (Zahn, 1977; Khaliullin & Khaliullina, 2010; Guo et al., 2016); these timescales are shorter than the age of the system reported by both studies.

Our estimations of the near-core and surface rotations reported in Section 3.5.1 and 3.8 suggest KIC 9851944 is rotating rigidly and synchronously. This is similar

to the findings by e.g. Guo et al. (2017b); Guo & Li (2019), that the short-period EBs KIC 9592855 and KIC 7385478 both contain a γ Doradus pulsator that is tidally synchronised at the surface as well as at the near-core regions. Such measurements allow for a calibration of the time-scales for synchronisation at the surface compared to the core, and thus the time-scales associated with angular momentum transport, which further aids in the discrimination among different theories.

In contrast to the above, our detection of the orbital harmonic frequency comb for KIC 9851944 either suggests asynchronous rotation or a non-zero eccentricity that has not been detected due to observational error because these can be indicative of tidally excited oscillations. It is unclear whether the very small value for the lower limit on the eccentricity, i.e., $e > 0.0001$, reported above for this system would be enough to induce tidal excitation of modes at the amplitudes observed here.

The pulsation analysis here complements the study by Guo et al. (2016) who report splittings to some of the pulsation modes. We confirm the detection of tidally split multiplets, and explain their origin; we present evidence to suggest that these are due to perturbations to the pulsation mode cavities, i.e., tidally perturbed pulsations, by investigating their phase and amplitude dependencies with orbital phase. Guo et al. (2016) attempted to interpret the modes by comparing the observations with theoretically computed frequencies, from which they concluded that the observations can be explained by low-order p modes in the primary and the secondary, or the g mode and mixed modes of the secondary (Guo et al., 2016). We confirm that some of the p modes belong to the primary, and others could belong to either the primary or the secondary from modulation of the amplitudes during eclipses. Our evidence suggests the primary is the hybrid, and this is because the saw-tooth-like "glitch" in pulsation phase of the tidally perturbed g mode (see Fig.3.13) can only be explained if the pulsation belongs to the primary (Van Reeth et al., 2022, 2023). Guo et al. (2016) report that mode identification was inconclusive, reflecting the difficulty in identifying the p modes in δ Scuti stars.

Table 3.10: Previously reported results for KIC 9851944 by Guo et al. (2016). Also given are the discrepancies Δ of our results compared to those results, given as a percentage of the previous result as well as units of sigma σ.

Parameter	Star A		Star B	
	Value	Δ [%]	Value	Δ[%]
Mass ($M_\odot$)	1.76 ± 0.07	-0.6 (0.2σ)	1.79 ± 0.07	4.24 (1.1σ)
Radius ($R_\odot$)	2.27 ± 0.03	11.6 (6.6σ)	3.19 ± 0.04	-6.55 (3.5σ)
$\log(g$ [cgs])	3.96 ± 0.03	-2.2 (2.7σ)	3.69 ± 0.03	1.9 (2.1σ)
$v_{\rm sync}$ ($\mathrm{km\,s^{-1}}$)	51.4 ± 0.7	15.2 (8.4σ)	72.1 ± 0.09	-3.3 (2.4σ)
$T_{\rm eff}$ (K)	7026 ± 100	-0.9 (0.6σ)	6902 ± 100	-0.9 (0.6σ)
q	1.01 ± 0.03		5.6 (1.9σ)	
a ($R_\odot$)	10.74 ± 0.014		0.6 (2.8σ)	

3.10 Conclusions

We have determined the physical properties of KIC 9851944, a short-period detached eclipsing binary containing two F-type stars, both of which pulsate. Our analysis is based on 33 échelle spectra plus light curves from the *Kepler* and TESS missions. We measure masses and $T_{\rm eff}$s to 0.6%, radii to 1.0% and 1.5%, and 133 frequencies due to p- and g-mode pulsations. We find no evidence of a third component, apsidal motion, or eccentricity. We estimate the age of the system to be $\sim$1.26 Gyr by comparison of the measured properties to the MIST model isochrones.

We investigated the systematic errors associated with using the cross correlation technique to extract RVs, which arise due to blending between the spectral lines of the components in a binary system. We find that the effect is small when using TODCOR but correcting for the issue is still necessary because the resulting shifts are clearly systematic in nature and have a non-negligible impact on the results. We used three independent spectroscopic methods to determine the light ratio for the system. The results are in agreement with each other and consistent with the value obtained from modelling the light curve which supports the reliability of our light curve solution. We compared our results to those reported by Guo et al. (2016) and find that we have

improved the precision of the measured masses significantly, but the precision in the radius estimates are comparable. Both these outcomes are expected since we use much higher-resolution spectra but the same photometry (primarily *Kepler*).

By analysing the residuals of the light curve model, we confirm the detection of tidally perturbed p mode pulsations, possibly in both components of KIC 9851944. A short period spacing pattern was detected among the g modes and was assigned to the primary component, where perturbations to one of the g modes was detected. Thus, the primary component is a δ Scuti/γ Doradus hybrid. If pulsation mode identification can be performed (as in, e.g., Bedding et al., 2020) on the p modes, KIC 9851944 will become a well-equipped laboratory for stellar physics.

4 Physical Properties of the Hierarchichal Triple KIC 4851217 and Discussion of its Tidally Tilted Pulsations

4.1 Introduction

This chapter presents a comprehensive analysis of KIC 4851217. This object is a detached EB in a close orbit with a period of $\sim$ 2.47 d and shows δ Scuti pulsations, some of which are tidally tilted pulsations (TTPs) meaning that the pulsation axis is aligned with the tidal axis (e.g., Handler et al., 2020; Kurtz et al., 2020; Rappaport et al., 2021). ETVs are detected in the O-C diagram (see Section 4.3.1) which we successfully modelled as a combination of the LTTE due to a third body and apsidal motion of the EB orbit. Thus, the object is an ideal candidate for deriving constraints on stellar structure from its pulsations and dynamically derived fundamental parameters, studying the effects of tides on pulsations from its TTPs, as well as contributing to our understanding of hierarchical systems.

KIC 4851217 was previously studied by Liakos (2020), who presented a detailed light curve, spectroscopic, and seismic analysis using RVs derived by Hełminiak et al. (2019) in their high resolution ($R \sim 50000$) spectroscopic monitoring of 22 bright objects in the *Kepler* eclipsing binary catalogue (KEBC) (Prša et al., 2011; Kirk et al., 2016). A frequency analysis was also performed by Fedurco et al. (2019) on the *Kepler* data. In addition to other previous studies mentioned by Liakos (2020), KIC 4851217 was detected by Gaulme & Guzik (2019) in their systematic search for pulsators in the KEBC; similarly, Chen et al. (2022) detected the object in their search for δ Scuti pulsators in the catalogues of TESS EBs by Prša et al. (2022); Shi et al. (2022). None of these studies report the detection of a tertiary companion. Only a long-term parabolic trend in the primary and secondary ETVs was noted in the studies by Gies et al. (2012, 2015) and Conroy et al. (2014). Our work is complementary to the previous studies. We present and analyse new, higher-resolution ($R = 85000$) spectroscopic

observations, while the inclusion of TESS photometry allows us to report the discovery and characterisation the tertiary component for the first time.

Section 4.2 outlines the observations and in Section 4.3.2 we perform a preliminary analysis of KIC 4851217. We present a detailed spectroscopic analysis in Section 3.5 and analyse the light curves in Section 4.5. In Section 4.6, we perform a simultaneous analysis of RVs, light curves, ETVs and SED (jointly) from which estimations of the components' physical properties follow, as well as determine the physical properties based on the individual modelling of those data. We perform a preliminary investigation of the pulsations in Section 4.7, and give concluding remarks in Section 3.10.

4.2 Observations

4.2.1 Photometry

KIC 4851217 was observed by *Kepler* in seven quarters in SC mode between 2009 June and 2013 May (Q2.3, Q4.2, Q9, Q13, Q15–17), and in 15 quarters in LC mode (Q0–Q5, Q7–Q9, Q11–Q13, Q15–Q17). KIC 4851217 has been observed by TESS in five sectors so far. These are sectors 14 and 15 (2019 July 18 to August 15), 41 (2021 July 23 to August 20), and 54 and 55 (2022 July 9 to September 1). In all cases it was selected for observations in SC mode.

4.2.2 WHT spectoscopy

The WHT spectroscopic observations outlined here were obtained by Dr. Stuart Littlefair (2011) and Dr. Steven Bloemen (2012).

Spectroscopic observations were carried out using the ISIS spectrograph on the 4.2 m William Herschel Telescope (WHT) at La Palma. ISIS has two arms split by a dichroic so can observe two wavelength intervals simultaneously. We used ISIS to

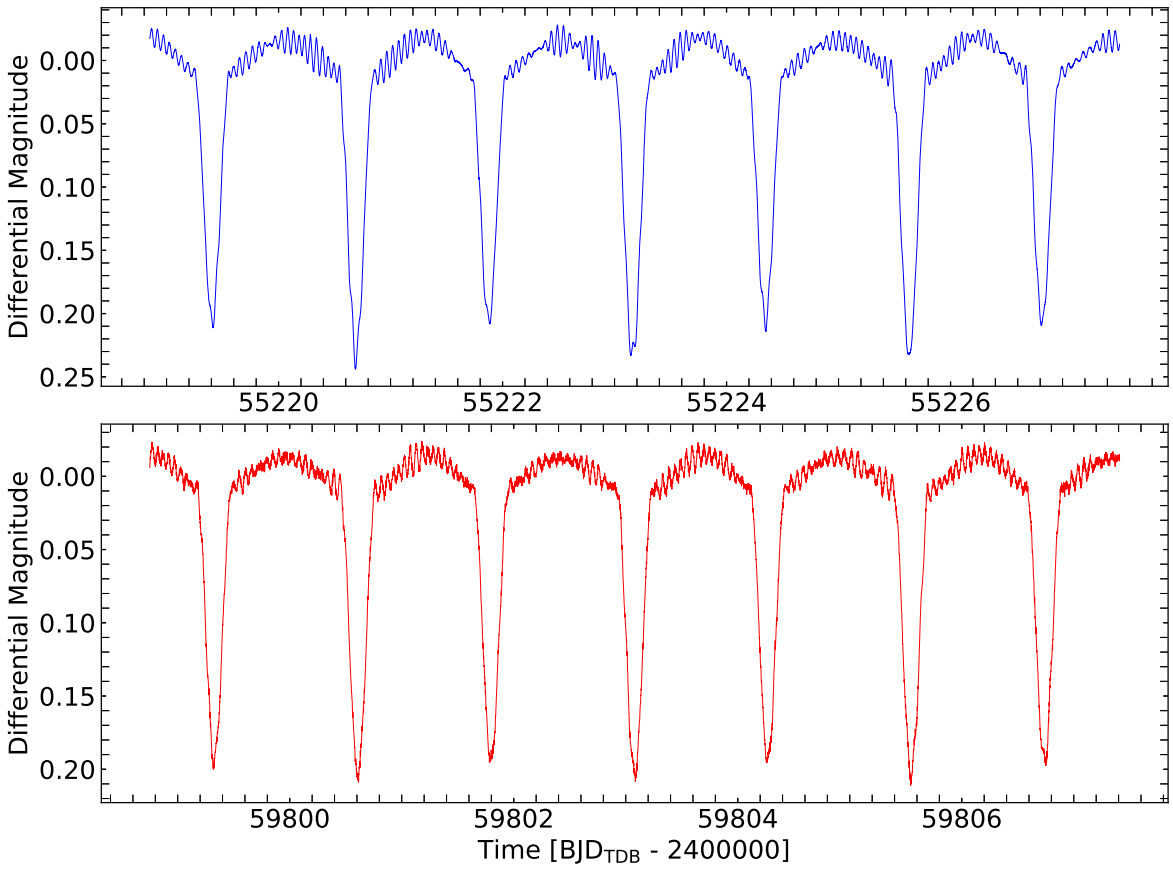

Figure 4.1: Top panel; a cut of the *Kepler* SAP light curve from quarter-4. Bottom panel; same as the top panel but for the TESS sector 55 SAP light curve.

acquire 17 observations in 2011 June (over 4 nights) and 14 observations in 2012 July (over 7 nights).

A 0.5″ slit was used to obtain the highest possible spectral resolution. In the 2011 run the slit width-adjustment mechanism was not working properly so the slit width was set manually to somewhere close to the intended 0.5″.

In the blue arm we used the H2400B grating to obtain spectra covering the 6100–6730 Å wavelength interval. The reciprocal dispersion was 0.11 Å px^{-1} and the resolution was approximately 0.22 Å. The standard 5300 Å dichroic was used to split the blue and red arms.

In the red arm we used the R1200R grating to obtain spectra covering the 4200–4550 Å wavelength interval. The reciprocal dispersion was 0.26 Å px^{-1} and the resolution was approximately 0.52 Å.

4.2.3 HERMES spectoscopy

The HERMES spectroscopic observations following were obtained by Dr. Jonas Debosscher and kindly made available to us by Dr. Timothy Van Reeth.

A total of 41 spectroscopic observations of KIC 4851217 were obtained using the cross-dispersed fibre-fed échelle spectrograph HERMES (High Efficiency and Resolution Mercator Échelle Spectrograph; Raskin et al., 2011) on the 1.2 m Mercator telescope at La Palma. The high-efficiency mode was used, giving spectra with a resolving power of $R = 85\,000$. These observations were obtained between 2011 April and 2012 July.

4.3 Preliminary Analysis

4.3.1 Ephemeris

In all, there were 438 primary and 442 secondary eclipse times extracted from the *Kepler* lightcurves, as well as 54 primary and 50 secondary eclipse times derived from the TESS lightcurves. These data span 13.3 years. The method we used for determining the eclipse mid-times has been discussed in several previous papers (see Borkovits et al., 2015, 2016).

The best fit linear ephemeris for these eclipse times is given by:

$$T_{\mathrm{TDB}}(E) = 2456016.12186(13) + 2.47028992(34)\,E. \tag{4.1}$$

The ETV curve that results from subtracting out this linear ephemeris is shown in Fig. 4.2. We did subtract off 0.042 days from the primary ETV curve so as to bring it

visually closer to the secondary ETV curve, but this was done only after we analyzed the curves for an outer orbit. A cursory look at these ETV curves shows three interesting features: (i) there is clearly non-linear behaviour that likely indicates the presence of a third body; (ii) the two curves drift upward, indicating that our trial linear fit to the eclipse times has some residual term to be fit for; and (iii) the two ETV curves are slowly, but clearly, converging (by $\sim$0.003 days over 13 years), thereby indicating a possible apsidal motion.

4.3.2 Preliminary ETV analysis

We attempted to fit an outer orbit to the ETV curves shown in Fig. 4.2. As noted, in addition to the obvious non-linear behaviour in the ETV curves that likely indicates an outer orbit, the two curves are slightly converging toward each other. If the non-linear behaviour is due to the classic light travel time effect (LTTE)[1], the ETV curves of both the primary and secondary eclipses should run parallel to each other. Since they do not, we take this to tentatively indicate that there is apsidal motion in the EB. Later, we demonstrate that this is too large an effect to be driven by the third body. Therefore, for now we assume that any apsidal motion in the EB is due to the classical effect from mutually induced tides, and treat it as such in our preliminary fit of the ETV curves.

The expression we fit is as follows:

$$\begin{aligned} \mathrm{ETV}(t) &= t_0 + dP(t - t_i)/P_{\mathrm{in}} + \mathrm{LTTE}(t) && (4.2) \\ &\pm \frac{e_{\mathrm{in}} P_{\mathrm{in}}}{\pi} \cos[\omega_{\mathrm{in}}(t_i) + 2\pi(t - t_i)/P_{\mathrm{aps}}] && (4.3) \end{aligned}$$

where t_i is simply defined as the start of the observations on BJD 2454950, and is not a free parameter, and the plus and minus symbol refers to the primary and secondary eclipse times, respectively. In all, there are four terms comprising ten free parameters: (i) an arbitrary offset time for the ETVs, t_0; (ii) a linear term in time that corrects the

[1]Later we show that the dynamical delays are negligible in this system.

EB period, $dP_{\rm in}$; (iii) the LTTE effect that accounts for the outer orbit with five free parameters, $P_{\rm out}$, $a_{\rm out,eb}\,\sin i$[2], $e_{\rm out}$, $\omega_{\rm out}$, and $\tau_{\rm out}$, with their usual meanings; and (iv) the apsidal motion term which has three free parameters: $e_{\rm in}$, $\omega_{\rm in}$, and $P_{\rm aps}$, where the "in" subscript refers to the 'inner orbit", i.e., that of the EB, and $P_{\rm aps}$ is the period of the apsidal motion.

The red curves superposed on each of the ETV curves in Fig. 4.2 are the result of a Levenberg-Marquardt minimisation of χ^2. The best-fit parameters are summarised in Table 4.1, where the cited uncertainties were derived by Prof. Saul Rappaport from an MCMC (Ford, 2005) evaluation of parameter space. The outer orbital period is fairly well determined at 2700 ± 40 days (note that there are nearly two full outer periods in the span of the data train). The outer eccentricity is fairly high at $e_{\rm out} \simeq 0.55 \pm 0.01$. The inferred mass function is $f(M) = 0.0033\,{\rm M}_\odot$, which in turn would indicate that the mass of the third body is about $0.4\,{\rm M}_\odot$ for an assumed outer orbital inclination angle near 90° and total mass of the EB near $4\,{\rm M}_\odot$.

The fit to the apsidal motion yields a well-defined apsidal period for the EB of 160 ± 5 years. Later in this work we show that this is quite a reasonable value given the properties of the two EB stars, and their relatively large values of R/a. An additional bonus from fitting the precise ETV times for apsidal motion is that we also find remarkably precise values of $e_{\rm in}$ and $\omega_{\rm out}$ of 0.03173 ± 0.00005 and $170° \pm 1°$, respectively.

4.3.3 SED fitting

In this section we attempt to see what can be learned about the system parameters using only information from the spectral energy distribution of the triple system (SED); this stage of the analysis was carried out by Prof. Saul Rappaport. We find 25 SED point on the VizieR (Ochsenbein et al. 2000; Simon & Boch: `http://vizier.unistra.fr/vizier/sed/`) SED database between $0.35\,\mu$m and $11.6\,\mu$m. These are shown in

[2]This is the projected semimajor axis of the EB around the centre of mass of the triple system.

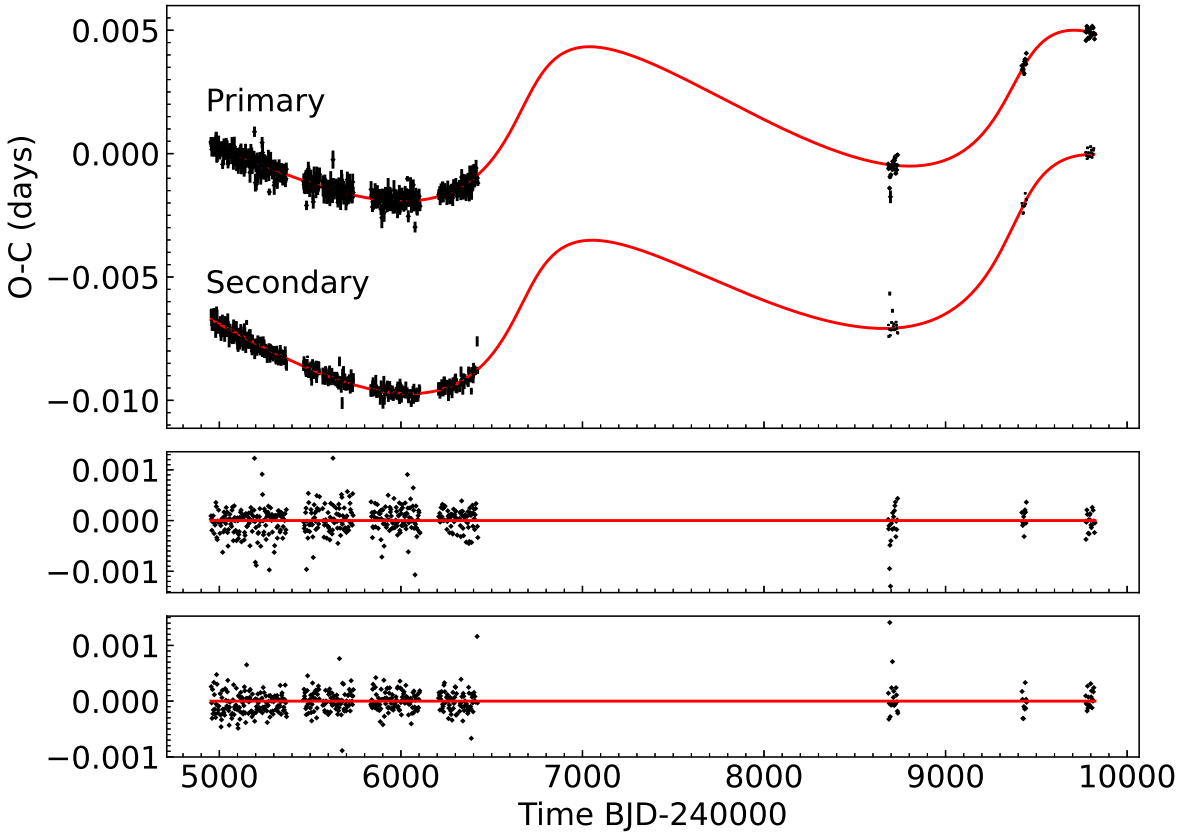

Figure 4.2: Eq.4.2 (red curves) fitted to the primary and secondary eclipse mid-times, where those for the secondary are shifted by -0.042 days.

Table 4.1: Results from the ETV model.

Parameter	Result
$\tau_{\rm out}$ [days]	6747 ± 85
$P_{\rm out}$ [days]	2676 ± 43
$A_{\rm ltte}$ [days]	0.00317 ± 0.00015
$e_{\rm out}$	0.551 ± 0.03
$\omega_{\rm out}$ [°]	21 ± 10
$P_{\rm aps}$ [years]	163 ± 13
$\omega_{\rm in}$ [°]	170.2 ± 1.7
$e_{\rm in}$	0.03174 ± 0.00008
dp [days]	$1.89 \times 10^{-6} \pm 0.10 \times 10^{-6}$

Fig. 4.3. We assign fixed uncertainties of 10% on all fluxes to take into account the fact that there are frequent eclipses of this depth occurring. The purpose of the SED fitting at this stage of the analysis is to provide some initial insights into the system parameters.

In order to fit three stars to a single SED curve it is important to have at least a few other constraints in order to produce anything like a unique solution. Here we adopt the following set of conditions and assumptions: (1) there are three stars in the system with a coeval evolution and with no prior mass transfer events; (2) the tertiary component, star B, contributes $\lesssim 10\%$ of the system light, otherwise it would have been detected in the RV data (see Sect. 3.4); and (3) the hotter primary star in the EB, star Aa, has an approximate temperature ratio with the secondary star, star Ab, of $T_{\rm eff,Ab}/T_{\rm eff,Aa} = 0.975 \pm 0.007$ based on the ratio of eclipse depths. Finally, we note that the large amplitudes of the ellipsoidal variations (ELV) in the lightcurve (of $\sim$4% full amplitude) imply that one or more of the stars must be evolved in radius to produce this ELV. In that case, in order to nudge the solutions in the right direction, we somewhat arbitrarily assume that the cooler star, Ab, is the slightly more massive and evolved star of the pair, with (4) $M_{\rm Aa}/M_{\rm Ab} \lesssim 0.95$ and (5) $R_{\rm Aa}/R_{\rm Ab} \lesssim 0.95$. The details of these latter two constraints are unimportant as long as the best-fit answers for the masses and radii are well away from these constraint boundaries.

The other constraints are (1) we take the *Gaia* distance of 1127 ± 20 pc, and use it as a prior, but with the distance uncertainty increased by a factor of 2 to $\pm$40 pc; (2) we use MIST stellar evolution tracks for an assumed solar composition (Paxton et al. 2011; Paxton et al. 2015; Paxton et al. 2019; Dotter 2016; Choi et al. 2016) to compute the stellar radii and $T_{\rm eff}$ values given the stellar mass and the age of the system; and (3) we utilise stellar atmosphere models from Castelli & Kurucz (2004).

The fitting is done via an MCMC code specifically constructed for this problem as described in Rappaport et al. (2022). There are five fitted parameters which are: $M_{\rm Aa}$, $M_{\rm Ab}$, $M_{\rm B}$, the system age, interstellar extinction (A_V), as well as a consistency check on the distance.

The results of the SED fit are shown in Fig. 4.3 and in Table 4.2. The values in

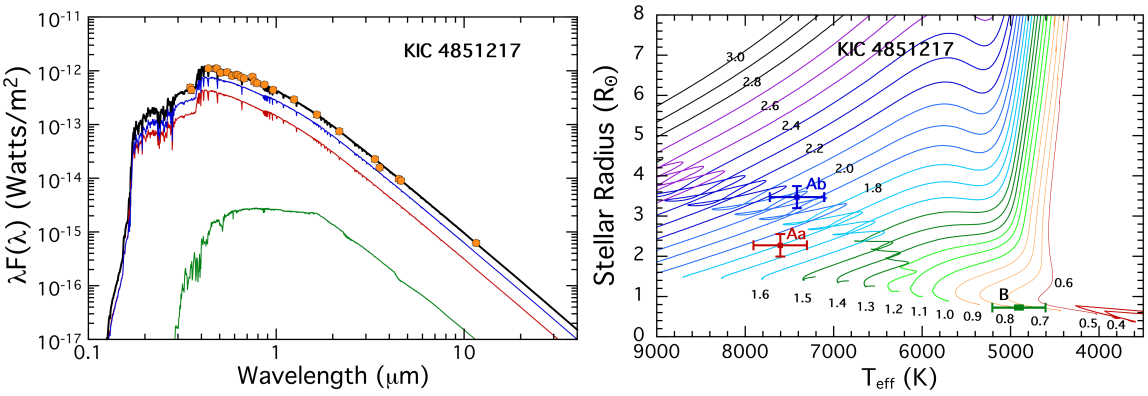

Figure 4.3: *Left panel:* An illustrative SED fit to the KIC 4851217 system. The orange points are the observed SED values take from VizieR (see text), while the blue, red, and green curves are the model SED curves for the secondary, primary, and tertiary stars, respectively. Black is the sum of the individual stellar contributions. *Right panel:* The corresponding locations of the three stars on the MIST stellar evolution tracks (see text). The numbers labeling the tracks are the stellar mass in $M_\odot$. Note that the primary star, Aa, is the hotter, but less massive of the binary pair.

Table 4.2: KIC 4851217 parameters determined from the SED fit only

Parameter	Value	Uncertainty
$M_{\rm Aa}$ [$M_\odot$]	1.93	0.13
$R_{\rm Aa}$ [$R_\odot$]	2.33	0.28
$T_{\rm Aa}$ [K]	8018	300
$M_{\rm Ab}$ [$M_\odot$]	2.12	0.08
$R_{\rm Ab}$ [$R_\odot$]	3.06	0.27
$T_{\rm Ab}$ [K]	7777	300
$M_{\rm B}$ [$M_\odot$]	0.77	0.06
$R_{\rm B}$ [$R_\odot$]	0.71	0.05
$T_{\rm B}$ [K]	4800	300
system age [Myr]	821	120
A_V	0.31	0.10
distance [pc]	1126	17

Table 4.2 are the median values of the posterior distributions, while the error bars are the rms scatter of the posterior distributions around the mean. The fit to the SED points in Fig. 4.3 shows the 25 measured flux values at wavelengths between 0.35 μm and 11.6 μm, as well as the modelled flux for each of the three stars individually (blue, red, and green curves) and the total flux (black curve). In the right panel of Fig. 4.3 we show where the stars with the inferred properties would lie. As can clearly be seen, the secondary star (Ab) is the more massive and evolved, and is in the evolutionary 'loop' corresponding to contraction of the H-depleted core after leaving the main sequence. While the primary star (Aa) has definitely evolved off the ZAMS, it has not yet arrived at the evolutionary 'loop' in the $R - T_{\rm eff}$ plane. We note that the tertiary star is fully consistent with contributing $\lesssim 1\%$ of the system light, and having a mass $\lesssim 1\,{\rm M}_{\odot}$.

Consulting Table 4.2, we see that the masses are determined to $\sim$6% accuracy, about 10% in the radii, and $\sim$300 K for $T_{\rm eff}$. The distance is nicely consistent with the *Gaia* result. The system age of $\sim$800 Myr is what is expected for 2 $\rm M_{\odot}$ stars that are just leaving the MS. It is gratifying to see that our final, much more accurate stellar parameter set for the inner EB, found from all the available data, agree to within the 1σ error bars in Table 4.2.

Overall, the SED fit, with just a few reasonable assumptions and constraints, yields some remarkably useful first estimates of the stellar parameters of the system.

4.4 Spectroscopic Analysis

4.4.1 Radial velocities

The 41 HERMES spectra were reduced and échelle orders were merged with the standard HERMES pipeline. The 31 ISIS spectra were reduced using PAMELA and MOLLY by Dr. John Taylor. Normalisation was carried out using the method of Xu et al. (2019) (see Section 2.2.2.2). Template spectra were synthesised using ISPEC (Blanco-Cuaresma et al., 2014b) for the components of the inner EB; the atmospheric parameters of these

templates were determined from a preliminary analysis of the ISIS spectra and were in agreement with those derived from the SED fitting in Section 4.3.3. Each set of templates was synthesised according to the resolution of either instrument, which in velocity space satisfies 1.56 $\mathrm{km\,s^{-1}}$ for the HERMES spectra and 7.46 $\mathrm{km\,s^{-1}}$ for the ISIS spectra.

Values for $v \sin i$ of each component were estimated following the method outlined in Section 3.4 for the analysis of KIC 9851944. For the HERMES observations, this approach yielded $v \sin i_{\mathrm{Aa}} = 43.9 \pm 0.5$ $\mathrm{km\,s^{-1}}$ and $v \sin i_{\mathrm{Ab}} = 61.6 \pm 0.3$ $\mathrm{km\,s^{-1}}$, which are in excellent agreement with our adopted values derived from the atmospheric analysis of the disentangled HERMES spectra (see Section 4.4.3). For the ISIS observations, this approach yielded $v \sin i_{\mathrm{Aa}} = 31.7 \pm 0.5\,\mathrm{km\,s^{-1}}$ and $v \sin i_{\mathrm{Ab}} = 55.7 \pm 0.7\,\mathrm{km\,s^{-1}}$, where the discrepancy is likely due to the lower velocity resolution. In any case, these are the values that maximise the peaks of the CCFs for each set of templates so we broadened them to these values (Gray, 2005; Czesla et al., 2019).

RVs were measured using our implementation of TODCOR (Zucker & Mazeh, 1994) using the region between 4400 – 4800 Å on the HERMES spectra and between 4380 – 4580 Å on the blue arm of the ISIS observations. These regions were chosen because of the presence of many well resolved lines, which makes them reliable indicators of RV, and the absence of broad lines, i.e., the Balmer series, compared to other regions. We excluded RVs derived from observations taken near phases of conjunction because these RVs contain little or no information about the velocity semi-amplitudes of the components and are prone to yielding anomalous RVs due to severe blending of the spectral lines.

Blending between the main correlation peaks and side lobes introduces systematic shifts in RVs derived from double lined spectra at any phase, and the dependence on phase is expected to be complex (Latham et al., 1996, see Sections 2.2.3.3 and 3.4). As an attempt to mitigate this effect, we performed an initial fit to the extracted RVs using the SciPy package CURVEFIT (Virtanen et al., 2020) and then synthesised the observed orbit by adding synthetic spectra weighted by the relative light contributions of each component, as derived from the TODCOR light ratio, after applying Doppler

Table 4.3: Orbital parameters for KIC 4851217 derived from HERMES and ISIS RVs.

	Primary	Secondary
K ($\mathrm{km\,s^{-1}}$)	130.1 ± 0.1	114.6 ± 0.2
γ ($\mathrm{km\,s^{-1}}$)	-22.5 ± 0.1	
e	0.032 ± 0.001	
ω ($^\circ$)	170.8 ± 2.0	
T_{per} [$\mathrm{BJD_{TDB}}$]	2456016.649 ± 0.013	
rms ($\mathrm{km\,s^{-1}}$)	1.1	1.6

shifts according to the initial fit. We used the exact same procedure to extract the known RVs from the simulated orbit and calculated their discrepancies which were applied to our actual RVs as corrections, as in Section 3.4.

We modelled the corrected RVs from both instruments jointly. The result is shown in Fig. 4.4.1 in the top panel and the corresponding orbital parameters for KIC 4851217 are given in Table 4.3. We attempted to fit for the CM acceleration due to the third body but the results were negligible. This suggests that the third body's influence is negligible over the time-span of the spectroscopic observations. This is expected; the ~ 0.003 day amplitude of the LTTE estimated in Section 4.3.2 translates to a $\sim 2.5\ \mathrm{km\,s^{-1}}$ velocity semi-amplitude of the CM of the EB, while our RVs only span $\sim 15\%$ of the outer orbital period estimated in Section 4.3.2.

Our final values for the light ratio were obtained by repeating the RV extraction using templates corresponding to our adopted atmospheric parameters derived in Section 4.4.3. These values correspond to $\ell_{\mathrm{Ab}}/\ell_{\mathrm{Aa}} = 1.83 \pm 0.02$ and $\ell_{\mathrm{Ab}}/\ell_{\mathrm{Aa}} = 1.95 \pm 0.12$ for the HERMES and ISIS spectra, respectively. Using the updated templates had a negligible impact on the resulting orbital parameters, as expected since RVs depend on the relative locations of spectral lines while $\ell_{\mathrm{Ab}}/\ell_{\mathrm{Aa}}$ is more sensitive to their shapes and depths.

Fig. 4.4.1 shows the corrections that were applied to the RVs as a function of RV in the bottom two panels. Applying the corrections to the HERMES RVs led to a 0.08 % and 0.2 % increase in the velocity semi-amplitude of the primary and

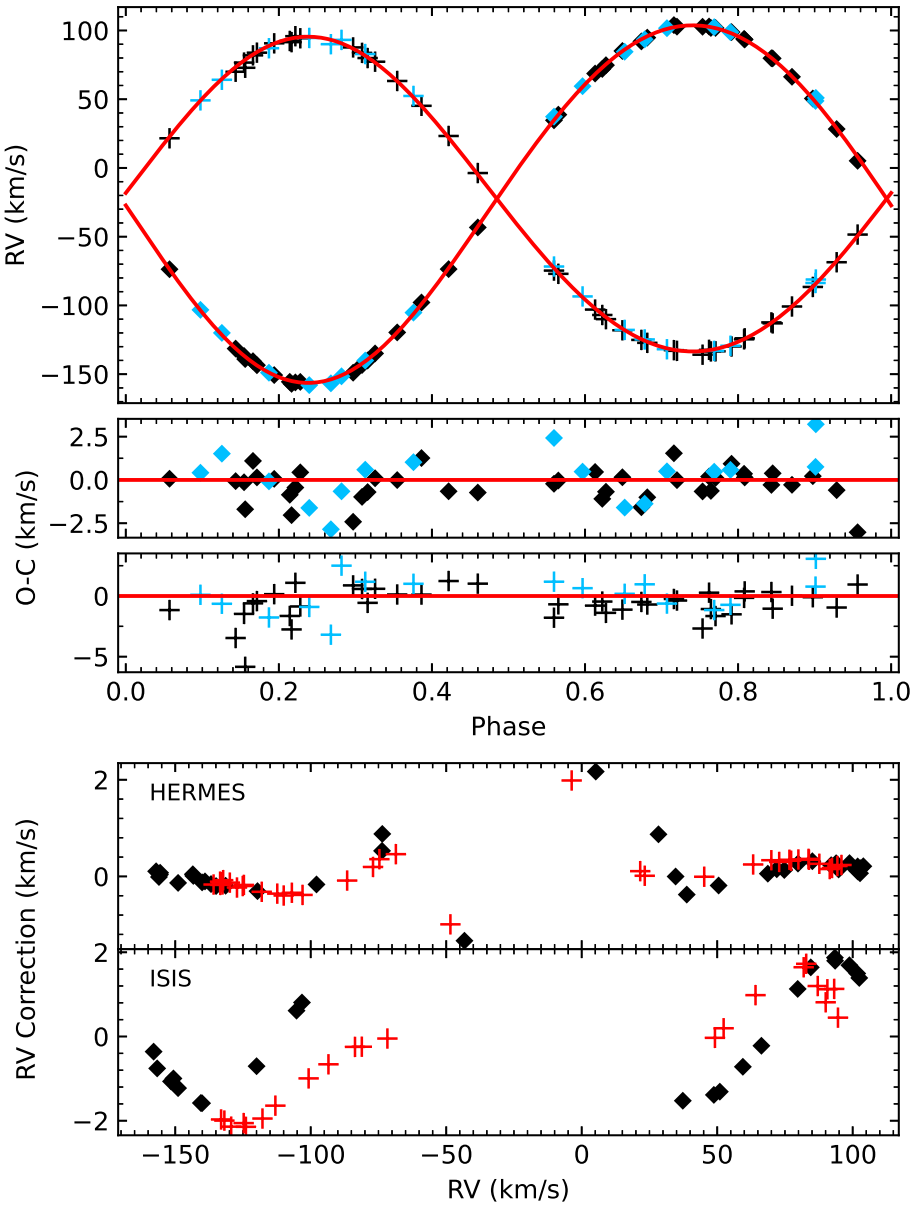

Figure 4.4: Orbital fit to the corrected RVs. Diamonds/crosses indicate the primary/secondary RVs and those corresponding to the HERMES/ISIS instrument are black/blue.

secondary, respectively, where the latter translates to a 0.6 % increase in the mass, which is significant considering that we aim to achieve precisions of $\sim$ 0.5 %. The corresponding values for the ISIS spectra are a 0.5 % and 1.2 % increase in the velocity semi-amplitudes, translating to a 1.5 % and 3.5 % increase in the mass of the primary and secondary stars, respectively, which is very significant.

4.4.2 Spectral disentangling

The spectral disentangling technique allows for the spectra of the individual components to be separated out from the composite binary spectra whilst simultaneously optimising the orbital parameters of the system, as outlined in Sections 2.2.5 and 3.5. We use the implementation FD3 by Ilijic et al. (2004), which works in the Fourier domain, to disentangle the HERMES observations in three spectral regions: (1) 4700 – 5000 Å , which contains the Hβ line of the hydrogen Balmer series, (2) 5050 – 5300Å , which contains the Mg b triplet associated with transitions in neutral magnesium, (3) 6480 – 6640Å , which contains the Hα line of the hydrogen Balmer series. An initial run was performed with initial values for the input parameters taken from Table 4.3 and allowed to vary to within 3 times their error bar to explore the possibility that FD3 might predict different orbital parameters. In all three cases, 100 optimisation runs each consisting of 1000 iterations did not converge to a solution with a smaller χ^2 than at the starting point. We therefore separated the spectra with the orbital parameters fixed to the values in Table 4.3 for subsequent runs. We ignored the presence of the third body since it is not detected spectroscopically as demonstrated in Section 4.4.1.

The absence of observations taken during eclipse requires that we perform disentangling assuming equal light contributions from each of the components and, therefore, the resulting disentangled spectra share a common continuum. For the disentangled spectra to be scaled appropriately relative to their individual continua requires renormalisation as described in Ilijić (2017), which heavily relies on an accurate value for the light ratio of the system. Due to the sensitivity in the TODCOR light ratio on the choice of stellar parameters of the templates (as discussed in Section 3.4) we utilise the

Table 4.4: Results for the light ratio determination.

Wavelength range [Å]	$\ell_{\rm Ab}/\ell_{\rm Aa}$
4400–4800	2.06 ± 0.07
5050–5300	1.96 ± 0.03
5300–5500	1.88 ± 0.06
5500–5700	1.99 ± 0.05
Adopted	1.96 ± 0.11

method used in Section 3.5.2, which we find to be largely insensitive to relatively small differences in the stellar parameters of the templates, to derive an independent value for $\ell_{\rm Ab}/\ell_{\rm Aa}$.

Here, we estimate $\ell_{\rm Ab}/\ell_{\rm Aa}$ by minimising the sum of the square residuals (SSR) between the observed binary spectra and synthetic composite spectra, where the latter were calculated by adding Doppler-shifted synthetic spectra generated by ISPEC weighted by light fractions corresponding to trial values for $\ell_{\rm Ab}/\ell_{\rm Aa}$. For the synthetic spectra, we used the $T_{\rm eff}$ values given in Table 4.2 derived from the analysis of the SED, Doppler shifts corresponded to the RVs derived in Section 3.3, and we searched in a grid of 12 values for $\ell_{\rm Ab}/\ell_{\rm Aa}$ between 1.1 and 2.5. We reiterate that, to ensure optimal normalisation of the raw observations using this method, they are normalised at each iteration of the fit by dividing by a polynomial (second order here) whose coefficients are set as free parameters (see Section 3.5.2).

This process was carried out on a spectral segment within the region used to extract the RVs (4400-4600Å), the Mg b triplet (5050–5300Å) region, as well as regions between 5300-5500Å , and 5500-5700Å because these spectral regions showed a relatively large number of well-resolved lines. We then used the five observations closest to positions of quadrature for each spectral segment and the minimization was carried out using Scipy's MINIMIZE (Virtanen et al., 2020). The results were averaged over the observations for each spectral region and are given in Table 4.4. The optimally normalised observation at phase 0.762 is plotted in Fig. 4.5 with the best fitting composite synthetic spectrum over-plotted for the region containing the Mg b triplet.

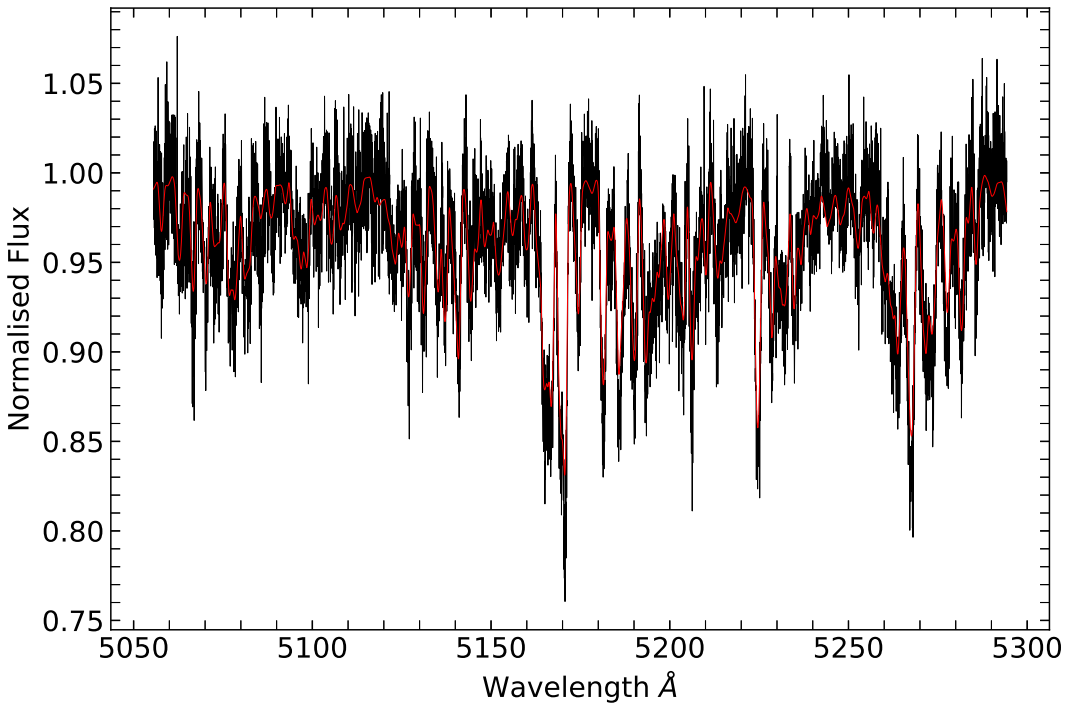

Figure 4.5: The observation at phase 0.762 optimally normalized as described in the text (black) for the spectral region between $5050-5300$Å and the best fitting synthetic spectrum, calculated based on the light ratio reported in Table 4.4, over-plotted (red).

The average of the light ratios estimated from each spectral segment satisfied $\ell_{\rm Ab}/\ell_{\rm Aa} = 1.96 \pm 0.02$. This value is consistent with the TODCOR light ratio derived from the ISIS spectra but inconsistent with that derived from the HERMES spectra. Thus, we inflate the error bar to be consistent with the weighted average of those two values and present this as our adopted value for $\ell_{\rm Ab}/\ell_{\rm Aa}$ in Table 4.4. We then use this value to normalise all observations in the Mg b triplet, Hα, and Hβ regions by optimising the coefficients of a second order polynomial against synthetic templates, as described above.

We performed disentangling as described at the start of this section on the normalised spectra and rescaled the results, as described in Ilijić (2017), using our adopted value for $\ell_{\rm Ab}/\ell_{\rm Aa}$. Our disentangled component spectra for KIC 4851217 are shown in Fig. 4.6 for the Mg b triplet, Hβ, and Hα regions. One of the benefits of spectral disentangling is the increased S/N and this is obvious when comparing the middle panel of Fig. 4.6 to Fig. 4.5.

The normalisation of the observed spectra and the light ratio used to re-scale the disentangled spectra are possible sources of uncertainty that may propagate into the atmospheric analysis. Thus, we computed two more sets of disentangled spectra. For the first set, we normalised the observed spectra by optimising the coefficients of a polynomial against synthetic templates with differing atmospheric parameters, i.e., $\Delta T_{\rm eff} = 150\,{\rm K}$ and $\Delta[{\rm M/H}] = 0.1\,{\rm dex}$. We did not adjust $\log(g)$ because this is reliably determined dynamically and we do not attempt to derive its value from the atmospheric analysis. For the second set of additional disentanged spectra, we varied the value of $\ell_{\rm Ab}/\ell_{\rm Aa}$ used to rescale the spectra within the error bar reported in Table 4.4.

Thus, in this section we have derived an independent value for the light ratio of the EB which we find to be more reliable than the values derived using TODCOR. We then used this light ratio to normalise our observed binary spectra against synthetic spectra, as well as calculate our primary set of disentangled spectra for each component. We also carried out the normalisation and disentangling with adjusted values for the atmospheric parameters of the templates and light ratio, yielding two extra sets of disentangled spectra. These extra sets of disentangled spectra are used to estimate

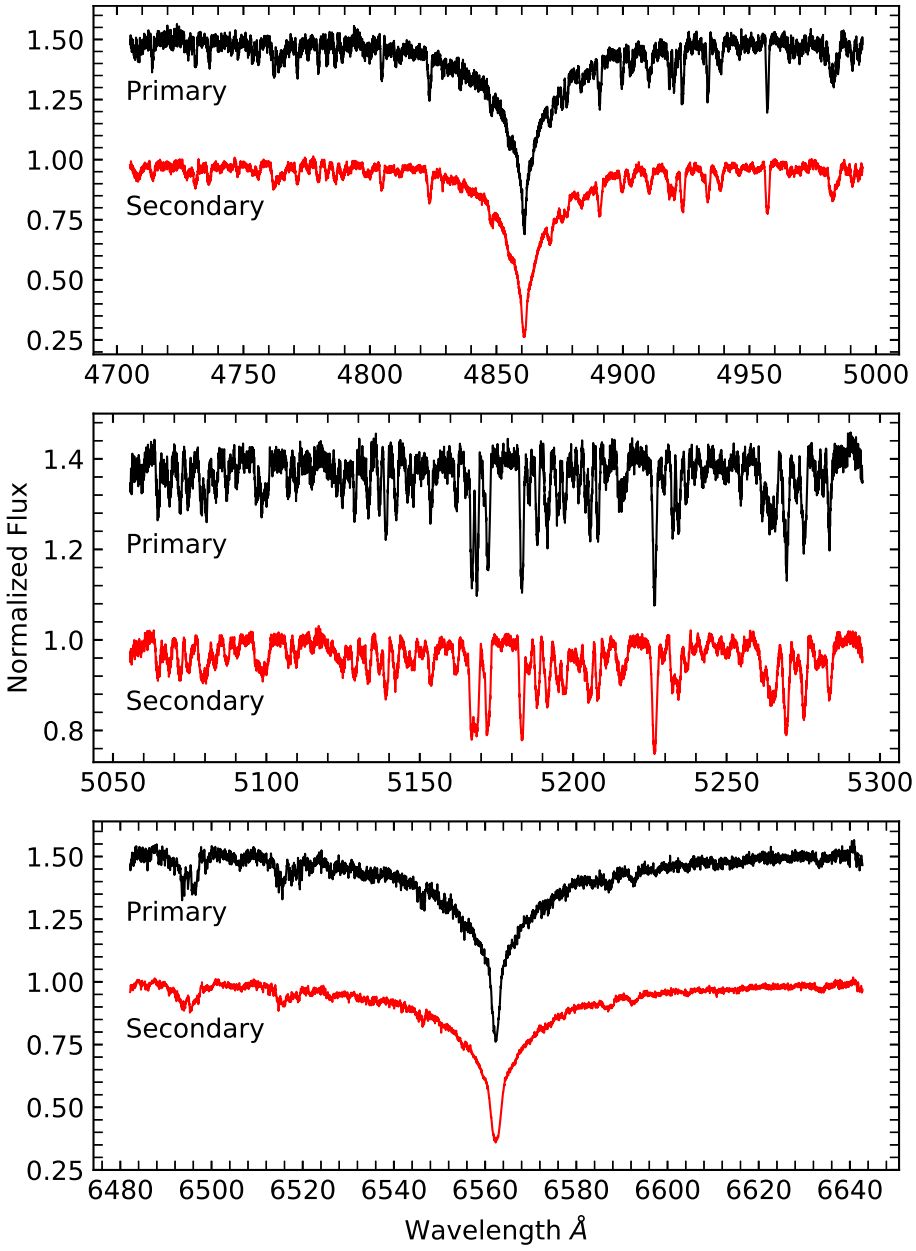

Figure 4.6: Disentangled component spectra for the Hβ, Mg b triplet, and Hα regions shown in the top, middle, and bottom panels, respectively.

systematic uncertainties in the atmospheric parameters which we derive in the next section.

4.4.3 Atmospheric parameters

We used the facilities provided by ISPEC to estimate the S/N of the disentangled component spectra. This led to an average S/N of 82 and 156 for the primary and secondary, respectively. Estimations for the errors on the disentangled fluxes then follow by dividing them by the S/N.

Atmospheric parameters were determined via synthetic spectral fits using the ISPEC framework combined into the ISPEC ZJ wrapper which was described in Section 2.2.6.3. By default, we opted to use the MARCS models (Gustafsson et al., 2008) because these are adequate for dwarf stars (Blanco-Cuaresma et al., 2014b) but we also consider the ATLAS9 models (Kurucz, 2005; Kirby, 2011; Mészáros et al., 2012) to explore wider ranges in $T_{\rm eff}$ and estimate systematic uncertainties. We combined the MARCS models with the solar abundances from Grevesse et al. (2007) to conform with the choice by Blanco-Cuaresma et al. (2014b), where they report better precisions in the resulting parameters, and used the *Gaia* Eso Survey (GES) atomic line list. Our synthesis is only performed on the pre-selected line-masks provided by ISPEC, which are based on the GES atomic linelist, and these only extend down to 4800 Å so part of our Hβ region was not included in the fits.

In all cases, $\log(g)$ is fixed to the dynamical values derived from the combined analysis of the light and RV curves because it is more accurate than the spectroscopic values (Guo et al., 2016). The macroturbulent velocity was fixed to zero for two reasons: (1) the convective envelope is relatively deep in early F/ late A stars, so we we expect granulation signatures to be relatively weak, (2) for surface velocity fields to be directly detectable requires $v \sin i \lesssim 13$ km s^{-1} for stars with $T_{\rm eff} \sim 7500$ K (Landstreet et al., 2009); our estimations for $v \sin i$ are ~ 3 and ~ 5 times this threshold for the primary and secondary, respectively (see Table 4.5).

First, we fitted for the spectral region containing the Mg b triplet (5050 – 5000Å)

Table 4.5: Atmospheric parameters for the components of KIC 4851217. See text for descriptions related to the calculation of the adopted values in column four.

Parameter	Hβ	Hα	Mg b III	Adopted
Wavelength range (Å)	4800–5000Å	6480–6640Å	5050–5300Å	(see text)
Primary				
$T_{\rm eff}$[K]	7810 ± 99	7880 ± 140	7890 ± 330	7833 ± 80
[M/H][dex]	0.0	0.0	0.06 ± 0.23	0.02 ± 0.11
$v_{\rm mic}[\,{\rm km\,s^{-1}}]$	3.2 ± 0.4	5.0 ± 3.2	2.9 ± 0.5	3.1 ± 0.3
$v \sin i$ $[\,{\rm km\,s^{-1}}]$	43.6	43.6	43.6 ± 4.6	43.6 ± 4.6
Secondary				
$T_{\rm eff}$[K]	7715 ± 94	7680 ± 120	7860 ± 390	7701 ± 74
[M/H][dex]	0.0	0.0	-0.03 ± 0.27	-0.10 ± 0.15
$v_{\rm mic}[\,{\rm km\,s^{-1}}]$	3.3 ± 0.3	3.9 ± 1.2	3.1 ± 0.5	3.3 ± 0.3
$v \sin i$ $[\,{\rm km\,s^{-1}}]$	61.6	61.6	61.6 ± 7.0	61.6 ± 7.0

mainly to determine $v \sin i$ because this region is free of strong lines, i.e, the Balmer series where the line profiles are heavily influenced by Stark broadening mechanisms. We then constrained $T_{\rm eff}$ by fitting the Balmer regions with $v \sin i$ fixed. We expect $T_{\rm eff}$ to be better determined from Balmer lines because their profiles are highly temperature sensitive and are insensitive to $\log(g)$ for stars with $T_{\rm eff} \lesssim 8000\,{\rm K}$ (Smalley, 2005; Bowman et al., 2021); we expect the dynamical $\log(g)$ to be accurate but any uncertainties in fixing its value are thus minimised. We also fixed [M/H] to zero in the Balmer regions because our solution from the Mg b triplet region was consistent with solar (see Table 4.5) and, in any case, Balmer lines are less sensitive to the influence of metallicity.

We repeated the fits at each spectral region using the Kurucz, Castelli, and APOGEE ATLAS9 models to investigate the systematic uncertainty associated with our preferred choice of atmospheric model. For $T_{\rm eff}$, the MARCS, Castelli, and APOGEE models give consistent results but the Kurucz models predict larger $T_{\rm eff}$ values by around $\sim$ 150K for both components and in both the Hα and Hβ regions. We also carried out the full process on the two extra sets of disentangled spectra that

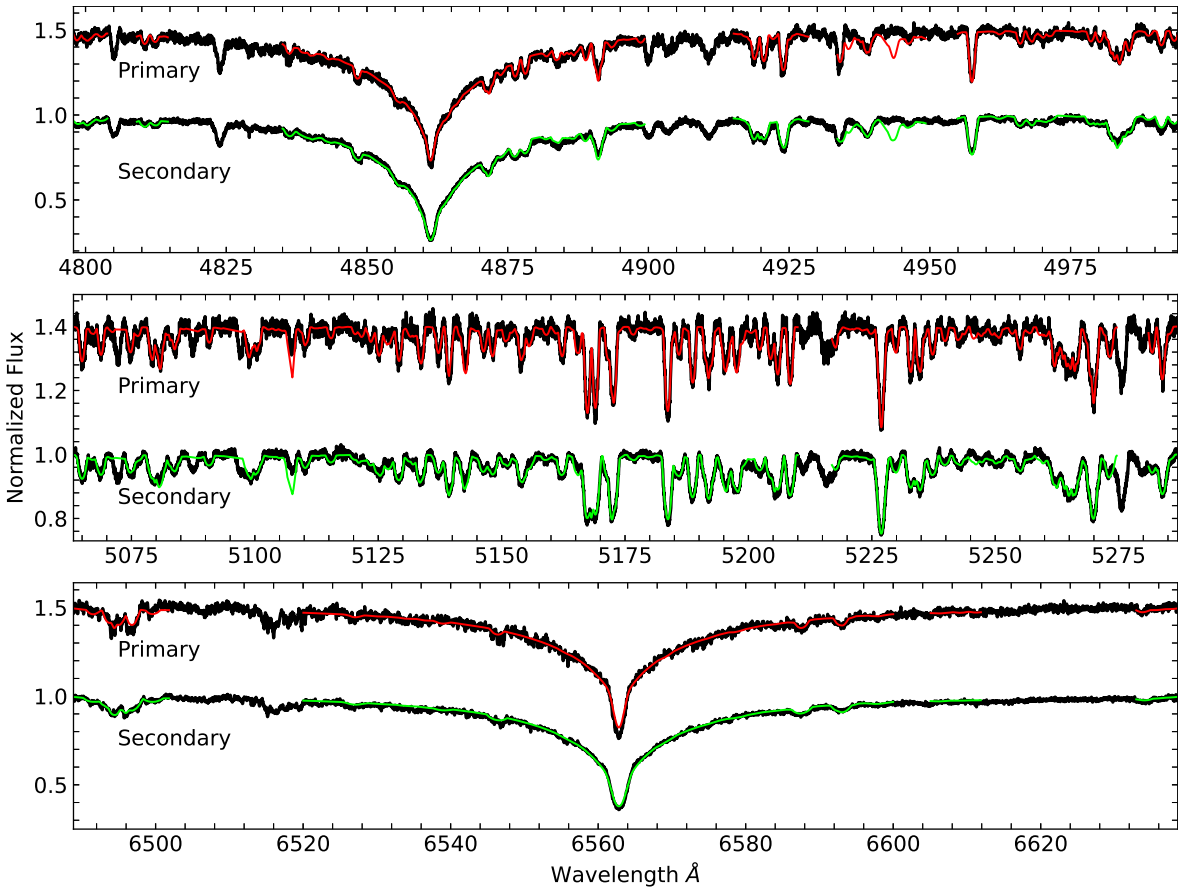

Figure 4.7: Synthetic spectral fits to the Hβ (top), Mg b III (middle), and Hα (bottom) regions. Observed data is shown in black and the best fitting synthetic spectra are shown in red for the primary and green for the secondary. Gaps in the synthetic spectra are because the synthesis was only carried out for spectral regions containing the pre-selected line-masks (see text). The primary data are offset by +0.5 for presentation purposes.

were calculated in the previous section to estimate the uncertainty associated with our estimation for $\ell_{\rm Ab}/\ell_{\rm Aa}$ as well as the the normalisation of the raw observations (see Section 4.4.2). In each investigation, we take the standard deviations of the results as the estimates for the associated systematic uncertainties. Final error bars are then calculated by adding these values in quadrature to the formal error bars from the least squares fits. Results for the fitted parameters from the fits to each spectral region are given in the first three columns of Table 4.5 (fixed parameters are given without an error bar) and Fig. 4.7 displays the best fitting synthetic spectra against the observations.

Values for $T_{\rm eff}$ are poorly constrained in the Mg b triplet region. This could be explained due to correlations between $T_{\rm eff}$ and [M/H] being complicated due to, e.g., line blanketing effects, and this is compounded by the fact both those parameters are correlated with the microturbulent velocity $v_{\rm mic}$. However, these effects are less pronounced for Balmer lines so our adopted values for $T_{\rm eff}$ are the weighted averages of the results from the Hα and Hβ regions. This decision is corroborated by the insensitivity of Balmer lines to $\log(g)$ for stars with $T_{\rm eff} \lesssim 8000\,{\rm K}$. We adopt the weighted average of the results from all three regions for the final value for $v_{\rm mic}$ and finally note that our values for $v \sin i$ are consistent with synchronous rotation. Adopted values for the atmospheric parameters are given in the fourth column of Table 4.5.

The correlations between $T_{\rm eff}$ [M/H] and $v_{\rm mic}$ may be the cause of the large uncertainties in the values for [M/H] derived from the Mg b triplet region. In an attempt to better constrain the values for [M/H], we repeated the fits in the Mg b triplet region except we additionally fixed $T_{\rm eff}$ and $v_{\rm mic}$ to our adopted values. Here we obtain [M/H] $= 0.02 \pm 0.06\,{\rm dex}$ for the primary and [M/H] $= -0.10 \pm 0.05\,{\rm dex}$ for the secondary. The updated metallicity of the secondary is significantly sub-solar compared to the primary, but we also noticed our adopted values for $v_{\rm mic}$ are larger than the empirical values calculated from ISPEC's built-in relation constructed based on *Gaia* FGK benchmark stars (Jofré et al., 2014). These empirical values correspond to 2.5 and $2.4\,{\rm km\,s^{-1}}$ and result in an increase of [M/H] by 0.10 dex and 0.14 dex for the primary and secondary, respectfully. We add these differences in quadrature to the uncertainties on the values for [M/H] reported above and present them as our adopted

values in Table 4.5. These efforts reduced the uncertainties by about a factor of two compared to the previously derived values for [M/H] reported in the third column of Table 4.5, but yield the same conclusions that both components are of solar abundance to within the uncertainty.

In summary, we have derived atmospheric parameters for the components of KIC 4851217 by performing synthetic spectral fits in three spectral regions. Our uncertainties on the parameters take into account those associated with the normalisation of the observations, choice of atmospheric models, and light ratio used to rescale the disentangled spectra. The uncertainties on our adopted values for [M/H] take into account the observed, strong anti-correlation with $v_{\rm mic}$.

4.5 Light curve analysis with the Wilson Devinney Code

The following light curve analysis was carried out by Dr. John Taylor.

To obtain the light curve solution, we considered only the *Kepler* SC observations, as these have a much better time resolution than the *Kepler* LC observations and a lower scatter than the TESS data. We evaluated the orbital phase of each datapoint, sorted them according to phase, and binned them into a total of 352 datapoints. Orbital phases around the eclipses were sampled every 0.001 in phase, whilst those away from the eclipses had a sampling of 0.01 phases. This process removed the shifts in eclipse times (neglecting the extremely small changes over the course of one month), averaged out the pulsation signature, and reduced the number of observations by three orders of magnitude. We analysed the phase-binned light curve using the Wilson-Devinney (WD, Wilson & Devinney, 1971; Wilson, 1979) code. We used the 2004 version of the code driven using the JKTWD wrapper (Southworth et al., 2011).

We quickly arrived at a good solution to the light curve through a process of trying a large number of different modelling options available in WD2004. Our default

solution was obtained in Mode = 0 with a numerical precision of $N = 60$, the mass ratio and $T_{\rm eff}$ values of the stars fixed at the spectroscopic values, synchronous rotation, gravity darkening exponents of 1.0 for both stars, the simple reflection model, limb darkening implemented according to the logarithmic law with the non-lnear coefficients fixed, and using the Cousins R filter as a proxy for the *Kepler* response function. The fitted parameters comprised the potential, albedos, light contributions and linear limb darkening coefficients of the two stars, plus the orbital inclination, eccentricity, argument of periastron, and third light.

The best fit to the light curve corresponds to a light ratio between the components of approximately 1.5, which is in significant disagreement with the spectroscopic value. We therefore forced the solution to agree with the spectroscopic light ratio, finding that the fit is almost as good. For the remainder of this work we use the results for the fixed light ratio to ensure internal consistency between analyses.

The uncertainties in the fitted parameters are dominated by the uncertainty in the spectroscopic light ratio, model choices and the numerical integration limit, because the Poisson noise in the binned light curve is negligible. We evaluated the uncertainties individually for all relevant sources and added them in quadrature for each fitted parameter. The sources include the spectroscopic light ratio, chosen numerical precision, mass ratio, mode of operation of WD2004 (0 or 2), rotation rates (varied by 10%), gravity darkening, whether or not to include third light, choice of limb darkening law (logarithmic versus square-root) and choice of filter (Cousins R versus I).

The best-fitting parameters and uncertainties are given in Table 4.6. Third light is negligible, which places constraints on the brightness of the third component. Of greatest importance is that we have managed to measure the volume-equivalent fractional radii to precisions of approximately 1.5%. Our results differ significantly from those of Hełminiak et al. (2019), who relied on the JKTEBOP code in their work. The eccentricity and argument of periastron also agree well with the spectroscopic value derived in Section 4.3.

A plot of the solution is shown in Fig. 4.8 where significant structure can be seen in the residuals. The short-period wiggles in the residuals during eclipse are likely due

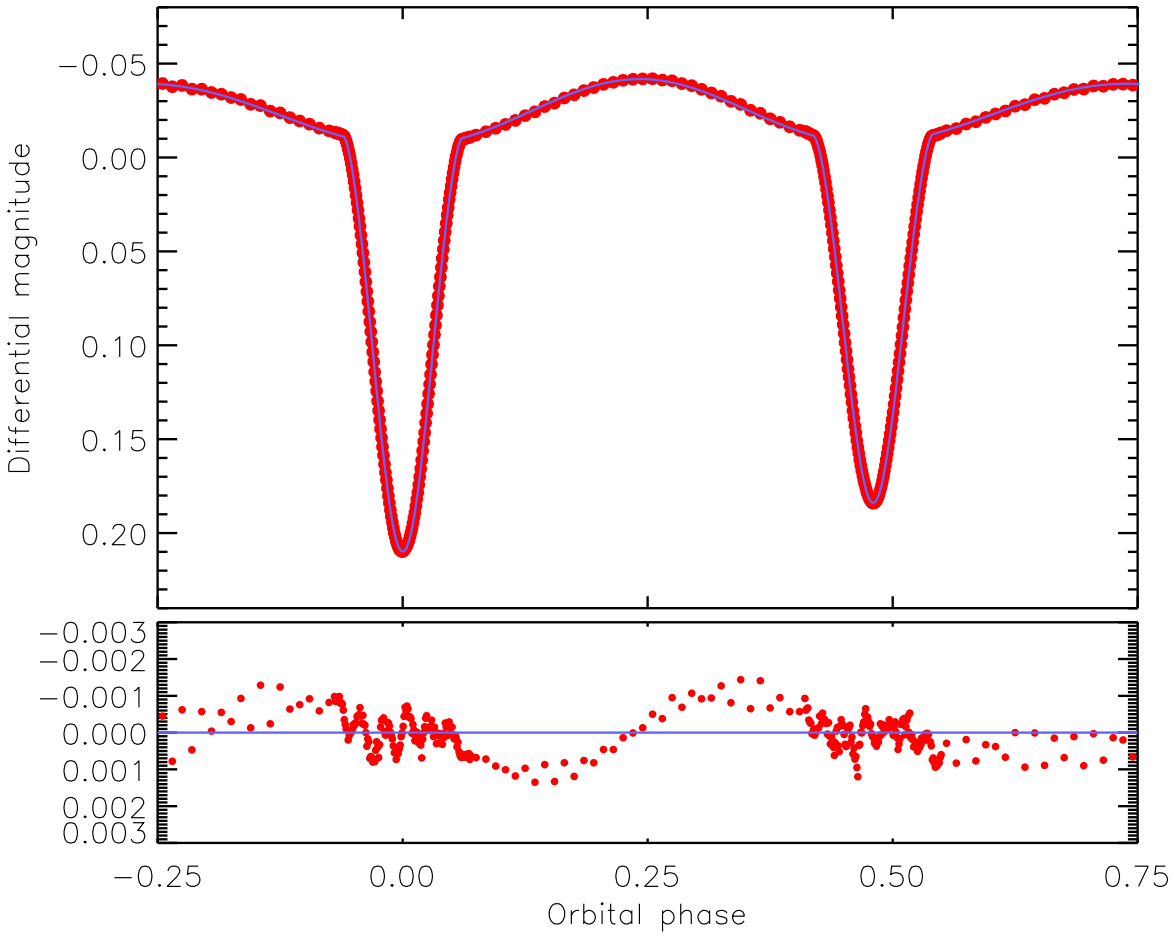

Figure 4.8: The best-fitting WD model (blue line) to the *Kepler* SC phase-binned light curve of KIC 4851217 (red filled circles). The residuals of the fit are plotted in the lower panel using a greatly enlarged y-axis to bring out the detail.

Table 4.6: Summary of the parameters for the WD2004 solution of the phase-binned light curve of KIC 4851217. Detailed descriptions of the control parameters can be found in the WD code user guide (Wilson & Van Hamme, 2004). A and B refer to the primary (hotter) and secondary (cooler) stars, respectively. Uncertainties are only quoted when they have been robustly assessed by comparison of a full set of alternative solutions.

Parameter	WD2004 name	Value
Control and fixed parameters:		
WD2004 operation mode	MODE	0
Treatment of reflection	MREF	1
Number of reflections	NREF	1
LD law	LD	2 (logarithmic)
Numerical grid size (normal)	N1, N2	60
Numerical grid size (coarse)	N1L, N2L	60
Fixed parameters:		
Mass ratio	RM	1.135
Phase shift	PSHIFT	0.0
$T_{\rm eff}$ star A (K)	TAVH	7834
$T_{\rm eff}$ star B (K)	TAVH	7701
Gravity darkening exponents	GR1, GR2	1.0
Rotation rates	F1, F2	1.0, 1.0
Logarithmic LD coefficients	Y1A, Y2A	0.618, 0.628
Fitted parameters:		
Star A potential	PHSV	6.78 ± 0.12
Star B potential	PHSV	5.537 ± 0.061
Orbital inclination (°)	XINCL	76.86 ± 0.12
Orbital eccentricity	E	0.0324 ± 0.0049
Argument of periastron (°)	PERR0	161 ± 19
Bolometric albedo of star A	ALB1	1.4 ± 0.5
Bolometric albedo of star B	ALB2	1.1 ± 0.3
Star A light contribution	HLUM	4.34 ± 0.17
Star B light contribution	CLUM	8.52 ± 0.17
Star A linear LD coefficient	X1A	0.640 ± 0.046
Star B linear LD coefficient	X2A	0.734 ± 0.032
Fractional radius of star A		0.1790 ± 0.0024
Fractional radius of star B		0.2509 ± 0.0032

to spatial resolution of the pulsations plus possible commensurabilities between the orbital period and pulsation periods. The cause of the slower variation seen outside eclipse is unclear but may be related to imperfect treatment of the mutual irradiations of the stars, residual pulsation effects, or Doppler beaming (Zucker et al., 2007).

We found that the albedos of the stars must be fitted to obtain the best solution, although their values are sensitive in particular to the passband used. Or more interest – and concern – is that another source of significant uncertainty was the numerical precision specified. Our exploratory solutions with lower numerical precision ($N = 30$ or 40) had clearly higher residuals, but we also find a significant change in the fitted parameters if the N values are set to 56, 57, 58, 59 or 60. This is unexpected and merits further exploration, but a detailed analysis is beyond the scope of the current work.

4.6 Physical Properties

In this section we undertake a comprehensive and combined analysis of all the various data sets that we have available for this source. This is carried out with the software LIGHTCURVEFACTORY (Borkovits et al., 2013, 2019), and the result is a unified set of all the system parameters, both stellar and orbital. The results of this comprehensive analysis are then compared to the parameters that we were able to extract from various subsets of the data. This approach to extracting information from various parts of the data, vs. what can be done by a single global analysis is instructive for cases where the data sets are not so rich.

4.6.1 An independent, joint light curve, radial velocity curve and ETV analysis with Lightcurvefactory

The contribution to the analysis of KIC 4851217 made in this section was performed by Prof. Tamás Borkovits.

For the independent and combined analysis of all the KIC 4851217 data sets, we used the software package LIGHTCURVEFACTORY (Borkovits et al., 2013, 2019). This code is able to *simultaneously* handle multi-passband light curves, RVs and ETVs of different orbital configurations of hierarchical few body systems, from simple binary stars up to sextuple star systems. Thus, with the use of this software package we analysed KIC 4851217 directly as a hierarchical triple star system. In practice, this means that for each time of the observations, the software calculated the 3D Cartesian coordinates and velocities of all three constituent stars and then synthesised the observable stellar fluxes and RVs of each star accordingly. Moreover, the mid-eclipse times for the ETV curves were also calculated directly from the relative, sky-projected distances of the stellar disks, without the use of any analytic formulae which are often used for fitting RV and/or ETV curves. LIGHTCURVEFACTORY has a built-in numerical integrator to calculate the stars' positions and velocities directly from the perturbed equations of motion. However, in the current situation, due to the large distance of the low-mass tertiary component, we found that the only detectable departure from pure Keplerian motions of both the inner and outer subsystems may come from the constant-rate apsidal motion of the inner pair, which is dominated by the tidal distortions of the inner binary stars. Therefore, instead of numerically integrating the stellar motions, we calculated the stellar positions only with the use of the usual analytic formulae describing the two (inner and outer) Keplerian motions, and with the assumption that the argument of pericentre of the inner orbit varied linearly in time.

This additional analysis, using LIGHTCURVEFACTORY, was also independent in the sense that we used (partly) different sets of the analyzed data. In the first rounds we used folded, binned and averaged *Kepler* SC data, but in the present situation we used 1000 bins of equal in length and, hence, there was no difference in the sampling between the in-eclipse and out-of-eclipse sections of the light curve. Also, we used slightly different primary and secondary ETV curves for the joint analysis than that which was used for the preliminary ETV analysis in 4.3.2. For our purposes we redetermined all mid-eclipse times from both the *Kepler* and *TESS* observations in the same manner as was described in Borkovits et al. (2015, 2016) and used for several cases before. Note,

however, that the two different sets of eclipse times and hence, the ETVs calculated from these data are very similar. Finally, we used the very same RV data which were analyzed before in Sect. 3.4.

For the parameter optimisation, and to explore parameter phase space, we used the built-in MCMC solver contained in the software package. We tried different sets of the stellar and orbital parameters to be adjusted. In our final solutions we adjusted the following parameters:

(i) Eight plus one orbital element related parameters describing the two Keplerian orbits, as follows: $e_1 \cos\omega_1$, $e_1 \sin\omega_1$, and i_1 giving the eccentricity, argument of periastron and the inclination of the inner orbit; furthermore, the parameters of the wide, outer orbit: P_2, $e_2 \cos\omega_2$, $e_2 \sin\omega_2$, i_2, and its periastron passage time, τ_2. Moreover, we also adjusted the constant apsidal advance rate of the inner orbit $\Delta\omega_1$.

(ii) Three parameters connected to the stellar masses: primary star's mass, $m_{\rm Aa}$, the mass ratio of the inner pair, q_1, and, finally the mass function of the outer orbit $f_2(m_{\rm B})$.

(iii) Four mainly light-curve connected parameters: the duration of the primary eclipse ($\Delta t_{\rm pri}$) is an observable which is strongly connected to the sum of the fractional radii of the EB stars; the ratio of the radii and the $T_{\rm eff}$ of the two EB stars ($R_{\rm Ab}/R_{\rm Aa}$; $T_{\rm Ab}/T_{\rm Aa}$), and, finally, the passband-dependent extra (contaminated) light: $\ell_{\rm Kepler}$.

Furthermore, nine additional parameters were internally constrained (or derived), as follows:

(i) The orbital period of the EB, P_1, and the time of an inferior conjunction $\mathcal{T}_1^{\rm inf}$ of the secondary star (i.e., the mid-time of a primary eclipse) were constrained via the ETV curves (see appendix A of Borkovits et al., 2019).

(ii) Even though in the current system, the light contribution of the distant tertiary is negligible, the code needs the $T_{\rm eff}$, $T_{\rm B}$, and the radius, $R_{\rm B}$ of the third

component. These parameters were calculated internally simply according to the main sequence mass-luminosity and mass-radius relations of Tout et al. (1996).

(iii) The systemic radial velocity (γ) was derived internally at the end of each trial step by minimising the value of $\chi^2_{\rm RV}$.

(iv) Finally, note that similar to our previous modelling efforts, we applied a logarithmic limb-darkening law of which the coefficients for each star were interpolated from passband-dependent tables downloaded from the Phoebe 1.0 Legacy page[3]. These tables are based on the Castelli & Kurucz (2004) atmospheric models and were originally implemented in former versions of the PHOEBE software (Prša & Zwitter, 2005).

Finally, the following parameters were kept fixed: the $T_{\rm eff}$ of the primary star was set to $T_{\rm Aa} = 7834\,{\rm K}$, i.e., to the same value which was used in the WD2004 model. Moreover, since both EB members are hot, radiative stars, their gravity darkening exponents and bolometric albedos were set to unity and, opposite to the WD2004 model, all these parameters were fixed.

We also carried out a second type of complex photodynamical modelling with LIGHTCURVEFACTORY, where, besides the above described datasets, we included in the analysis a simultaneous fit of the observed, net SED of the triple system to a model SED. The model SED is constructed from precomputed `PARSEC` tables of stellar evolutionary tracks (Bressan et al., 2012) which are built into LIGHTCURVEFACTORY. In the case of this latter type of analysis, the code calculates the radii, $T_{\rm eff}$ and selected passband magnitudes of each component separately with iteration from the three dimensional grids of [mass; metallicity; age] triplets (see Borkovits et al., 2020, for a detailed description of the process). In this astrophysical model-dependent analysis, naturally, the temperature and stellar radii-related parameters are no longer adjusted

[3] `http://phoebe-project.org/1.0/download`

or, kept fixed, but are interpolated from the PARSEC grids in each trial step. New adjusted parameters are the stellar metallicity $[M/H]$ and (logarithmic) age.[4] Moreover, two additional parameters, the interstellar extinction, $E(B-V)$, and the distance to the system are fit for as well. The former of these is also adjusted in each step, however, the distance calculated at each step is done a posteriori by minimising the value of $\chi^2_{\rm SED}$.

The tabulated results, the median values of the posteriors of the adjusted and several derived parameters, together with their 1σ uncertainties for both kinds of analyses are tabulated in Table 4.7.

4.6.2 Physical properties of the EB from the individual analyses

The results in Table 4.8 were calculated by Dr. John Taylor.

The physical properties of the inner EB of KIC 4851217 can also be determined from the spectroscopic and photometric results derived from the individual analysis of those data, which are presented in Tables 4.3, 4.5 and 4.6. We used the $K_{\rm A}$ and $K_{\rm B}$ values from Table 4.3, the orbital period from Section 4.3.1, and the fractional radii, orbital inclination and eccentricity from Section 4.5. These were fed into the JKTABSDIM code (Southworth et al., 2005b), modified to use the IAU system of nominal solar values (Prša et al., 2016) plus the NIST 2018 values for the Newtonian gravitational constant and the Stefan-Boltzmann constant. Errorbars were propagated via a perturbation analysis. The results are given in Table 4.8.

We determined the distance to the system using optical BV magnitudes from APASS (Henden et al., 2012), near-IR JHK_s magnitudes from 2MASS (Cutri et al., 2003) converted to the Johnson system using the transformations from Carpenter

[4]These parameters, technically, can be set separately for each star, but in practice, we generally assume coeval stellar evolution and, moreover, identical chemical compositions of all the stars in a given multi-stellar system and, hence, we adjust only one global age and metallicity parameter.

Table 4.7: Orbital and astrophysical parameters of KIC 4851217 from the joint photodynamical lightcurve, RV and ETV solution with and without the involvement of the stellar energy distribution and PARSEC isochrone fitting.

	without SED+PARSEC		with SED+PARSEC	
orbital elements				
	subsystem			
	Aa–Ab	A–B	Aa–Ab	A–B
$P_{\rm anom}$ [days]	$2.4703999^{+0.0000027}_{-0.0000027}$	2716^{+26}_{-16}	$2.4703997^{+0.0000026}_{-0.0000029}$	2725^{+16}_{-15}
a [$R_\odot$]	$12.22^{+0.02}_{-0.02}$	1349^{+14}_{-6}	$12.20^{+0.02}_{-0.01}$	1355^{+9}_{-9}
e	$0.03102^{+0.00004}_{-0.00004}$	$0.64^{+0.05}_{-0.04}$	$0.03101^{+0.00004}_{-0.00004}$	$0.67^{+0.03}_{-0.04}$
ω [deg]	$168.4^{+0.6}_{-0.6}$	15^{+3}_{-3}	$168.4^{+0.6}_{-0.5}$	15^{+3}_{-2}
i [deg]	$77.32^{+0.11}_{-0.12}$	70^{+33}_{-14}	$77.24^{+0.07}_{-0.06}$	76^{+20}_{-14}
τ [BJD - 2400000]	$55742.4719^{+0.0031}_{-0.0031}$	56694^{+32}_{-28}	$54951.9443^{+0.0044}_{-0.0037}$	56686^{+27}_{-20}
$\Delta\omega$ [deg/yr]	$2.40^{+0.06}_{-0.06}$	...	$2.39^{+0.06}_{-0.06}$	...
mass ratio [$q = M_{\rm sec}/M_{\rm pri}$]	$1.137^{+0.003}_{-0.003}$	$0.122^{+0.016}_{-0.014}$	$1.140^{+0.003}_{-0.003}$	$0.120^{+0.021}_{-0.011}$
$K_{\rm pri}$ [km s^{-1}]	$129.99^{+0.16}_{-0.12}$	$3.20^{+0.45}_{-0.24}$	$129.94^{+0.09}_{-0.09}$	$3.43^{+0.28}_{-0.32}$
$K_{\rm sec}$ [km s^{-1}]	$114.39^{+0.35}_{-0.34}$	$27.40^{+1.94}_{-3.41}$	$114.02^{+0.29}_{-0.24}$	$28.29^{+1.18}_{-2.86}$
γ [km s^{-1}]	$-22.183^{+0.034}_{-0.034}$		$-22.178^{+0.028}_{-0.032}$	
stellar parameters				
	Aa	Ab	B	Aa	Ab	B
Relative quantities						
fractional radius [R/a]	$0.1719^{+0.0025}_{-0.0024}$	$0.2511^{+0.0010}_{-0.0010}$	$0.00033^{+0.00004}_{-0.00004}$	$0.1728^{+0.0011}_{-0.0010}$	$0.2520^{+0.0006}_{-0.0006}$	$0.00034^{+0.00006}_{-0.00003}$
fractional flux [in *Kepler*-band]	$0.3238^{+0.0092}_{-0.0077}$	$0.6686^{+0.0084}_{-0.0066}$	$0.0007^{+0.0003}_{-0.0002}$	$0.3269^{+0.0032}_{-0.0032}$	$0.6681^{+0.0030}_{-0.0039}$	$0.0005^{+0.0004}_{-0.0001}$
Physical Quantities						
M [$M_\odot$]	$1.876^{+0.012}_{-0.012}$	$2.132^{+0.009}_{-0.009}$	$0.489^{+0.064}_{-0.058}$	$1.865^{+0.011}_{-0.008}$	$2.125^{+0.008}_{-0.005}$	$0.477^{+0.083}_{-0.044}$
R [$R_\odot$]	$2.101^{+0.031}_{-0.031}$	$3.069^{+0.013}_{-0.012}$	$0.448^{+0.061}_{-0.050}$	$2.108^{+0.016}_{-0.013}$	$3.075^{+0.008}_{-0.008}$	$0.461^{+0.083}_{-0.043}$
$T_{\rm eff}$ [K]	7834	7741^{+9}_{-9}	3749^{+98}_{-58}	7997^{+45}_{-45}	7882^{+36}_{-31}	3451^{+224}_{-96}
$L_{\rm bol}$ [$L_\odot$]	$14.92^{+0.45}_{-0.44}$	$30.36^{+0.28}_{-0.28}$	$0.036^{+0.015}_{-0.009}$	$16.28^{+0.51}_{-0.34}$	$32.76^{+0.69}_{-0.58}$	$0.027^{+0.021}_{-0.007}$
$M_{\rm bol}$	$1.81^{+0.03}_{-0.03}$	$1.03^{+0.01}_{-0.01}$	$8.36^{+0.33}_{-0.39}$	$1.74^{+0.02}_{-0.03}$	$0.98^{+0.02}_{-0.02}$	$8.69^{+0.33}_{-0.64}$
M_V	$1.78^{+0.03}_{-0.03}$	$1.01^{+0.01}_{-0.01}$	$9.96^{+0.47}_{-0.60}$	$1.69^{+0.02}_{-0.03}$	$0.91^{+0.02}_{-0.02}$	$10.51^{+0.50}_{-0.97}$
$\log g$ [dex]	$4.068^{+0.012}_{-0.012}$	$3.794^{+0.004}_{-0.004}$	$4.825^{+0.030}_{-0.011}$	$4.060^{+0.004}_{-0.005}$	$3.789^{+0.002}_{-0.002}$	$4.788^{+0.043}_{-0.075}$
log(age) [dex]		–			$8.916^{+0.003}_{-0.005}$	
[M/H] [dex]		–			$0.076^{+0.011}_{-0.011}$	
$E(B-V)$ [mag]		–			$0.133^{+0.008}_{-0.009}$	
extra light ℓ_4 [in *Kepler*-band]		$0.005^{+0.006}_{-0.003}$			$0.005^{+0.004}_{-0.002}$	
$(M_V)_{\rm tot}$		$0.57^{+0.01}_{-0.01}$			$0.48^{+0.02}_{-0.02}$	
distance [pc]		–			1074^{+6}_{-6}	

Table 4.8: Physical properties of KIC 4851217 derived from the independent analysis of the photometric and spectroscopic data. The units labelled with a 'N' are given in terms of the nominal solar quantities defined in IAU 2015 Resolution B3 (Prša et al., 2016). The synchronise rotational velocity $v_{\rm sync}$ is reported for the period of the system and corresponding radii measurements.

Parameter	Star A	Star B
Mass ratio	1.1354 ± 0.0025	
Semimajor axis ($\mathcal{R}^{\rm N}_{\odot}$)	12.263 ± 0.015	
Mass ($\mathcal{M}^{\rm N}_{\odot}$)	1.899 ± 0.008	2.156 ± 0.007
Radius ($\mathcal{R}^{\rm N}_{\odot}$)	2.195 ± 0.030	3.077 ± 0.039
Surface gravity (log[cgs])	4.034 ± 0.011	3.796 ± 0.011
$v_{\rm sync}$ ($\mathrm{km\,s^{-1}}$)	45.0 ± 0.6	63.0 ± 0.8
$T_{\rm eff}$ (K)	7834.0 ± 80.0	7700.9 ± 74.1
Luminosity $\log(L/\mathcal{L}^{\rm N}_{\odot})$	1.214 ± 0.018	1.477 ± 0.018
Absolute bolometric magnitude	1.706 ± 0.046	1.047 ± 0.044
Interstellar extinction $E(B-V)$ (mag)	0.04 ± 0.02	
Distance (pc)	1115 ± 17	

(2001), and surface brightness relations from Kervella et al. (2004). The interstellar reddening was determined by requiring the optical and near-IR distances to match. and is consistent with zero: $E(B-V) = 0.02 \pm 0.02$ mag. We found a final distance of 1115 ± 17 pc, which is in good agreement with the distance of 1127 ± 20 pc from the *Gaia* DR3 parallax (Gaia Collaboration et al., 2016; Gaia Collaboration, 2021), as well as the value from the SED fit in Section 4.3.3.

4.6.3 Comparison of physical properties from the individual and combined analyses

In this work we have done separate and independent analyses for subsets of the system parameters using subsets of the data, including RV data, ETV curves, SED fitting, and lightcurve analysis, in addition to a simultaneous joint analysis of all the data. Here we compare how the results of the analyses of the various subsets of the data compare with those from the joint analysis. Numerical comparisons are given in Table 4.9 both

Table 4.9: Full table of comparisons Δ calculated for both sets of results from the combined analysis against those obtainable from the individual analysis, given as percentages. Also given are these discrepancies in units of the quadrature addition of the uncertainties σ.

	Δ Case 1	Δ Case 2
Orbital parameters from RV analysis		
$K_{\rm Aa}$	-0.09 % (-0.58 σ)	-0.13 % (-1.08 σ)
$K_{\rm Ab}$	-0.18 % (-0.48 σ)	-0.50 % (-1.54 σ)
γ	-1.45 % (2.84 σ)	-1.48 % (2.90 σ)
e	-3.06 % (-0.98 σ)	-3.09 % (-0.99 σ)
ω	-1.41 % (-1.15 σ)	-1.41 % (-1.15 σ)
Parameters from ETV curve analysis		
q	0.14 % (0.41 σ)	0.41 % (1.18 σ)
τ_3	-0.79 % (-0.58 σ)	-0.90 % (-0.68 σ)
P_3	1.50 % (0.80 σ)	1.83 % (1.07 σ)
e_3	16.15 % (1.53 σ)	21.60 % (2.38 σ)
ω_3	-28.57 % (-0.58 σ)	-28.57 % (-0.58 σ)
$P_{\rm aps}$	-7.98 % (-0.96 σ)	-7.59 % (-0.91 σ)
ω	-1.06 % (-0.10 σ)	-1.06 % (-0.10 σ)
e	-2.27 % (-8.05 σ)	-2.30 % (-8.16 σ)
Parameters from SED fitting		
$M_{\rm Aa}$	-2.80 % (-0.41 σ)	-3.37 % (-0.50 σ)
$M_{\rm Ab}$	0.57 % (0.15 σ)	0.24 % (0.06 σ)
M_B	-36.49 % (-3.20 σ)	-38.05 % (-2.86 σ)
$R_{\rm Aa}$	-9.83 % (-0.81 σ)	-9.53 % (-0.79 σ)
$R_{\rm Ab}$	0.29 % (0.03 σ)	0.49 % (0.06 σ)
R_B	-36.90 % (-3.32 σ)	-35.07 % (-2.57 σ)
$T_{\rm eff,Aa}$	-2.30 % (-0.61 σ)	-0.26 % (-0.07 σ)
$T_{\rm eff,Ab}$	-0.46 % (-0.12 σ)	1.35 % (0.35 σ)
$T_{\rm eff,B}$	-21.90 % (-3.33 σ)	-28.10 % (-3.60 σ)
age	N/A	0.37 % (0.03 σ)
distance	N/A	-4.62 % (-2.88 σ)
$E(B-V)$	N/A	33.00 % (1.05 σ)
Parameters from the atmospheric analysis		
$T_{\rm eff,Aa}$	0.00 % (0.00 σ)	2.08 % (1.78 σ)
$T_{\rm eff,Aa}$	0.53 % (0.55 σ)	2.36 % (2.21 σ)
$[{\rm M/H}]_{\rm Aa}$	N/A	406.67 % (0.54 σ)
$[{\rm M/H}]_{\rm Ab}$	N/A	-179.17 % (1.54 σ)
Light curve analysis parameters		
$r_{\rm Aa}$	-3.97 % (-2.05 σ)	-3.46 % (-2.35 σ)
$r_{\rm Ab}$	0.08 % (0.06 σ)	0.44 % (0.34 σ)
Physical properties derived from individual models		
a	-0.35 % (-1.72 σ)	-0.514 % (-2.52 σ)
$M_{\rm Aa}$	-1.21 % (-1.60 σ)	-1.790 % (-2.50 σ)
$M_{\rm Ab}$	-1.11 % (-2.11 σ)	-1.438 % (-2.92 σ)
$R_{\rm Aa}$	-4.28 % (-2.18 σ)	-3.964 % (-2.56 σ)
$R_{\rm Ab}$	-0.26 % (-0.20 σ)	-0.065 % (-0.05 σ)
$\log(g)_{\rm Aa}$	0.84 % (2.09 σ)	0.645 % (2.15 σ)
$\log(g)_{\rm Ab}$	-0.05 % (-0.17 σ)	-0.184 % (-0.63 σ)
$\log(L/{\rm L}_\odot)_{\rm Aa}$	-3.30 % (-1.80 σ)	-0.17 % (-0.09 σ)
$\log(L/{\rm L}_\odot)_{\rm Ab}$	0.340 % (0.27 σ)	2.57 % (1.89 σ)
$E(B-V)$	N/A	232.50 % (4.24 σ)
distance	N/A	-3.68 % (-2.27 σ)

as a percentage difference with respect to the values from the joint analysis and in terms of the mutual sigmas of the two approaches.

In general, for the vast majority of the parameters we find agreement between the results for a subset of the data versus the full joint solution at the $\lesssim 1.5\,\sigma$ level. In some cases the discrepancy for some of the non-essential parameters (e.g., the γ velocity and colour excess) rises to the $3-4\sigma$ level. This provides a caveat that we should not take these particular results too seriously at the exact quoted level of uncertainty. There is one particular parameter, namely the eccentricity of the EB, that is discrepant at the 8-σ level. From our fit to the ETV data alone we found $e_{\rm in} = 0.03174 \pm 0.00008$ while from the joint analysis the result is $e_{\rm in} = 0.03102 \pm 0.00004$. Thus, these differ by 0.00074 ± 0.00009. However, if the actual uncertainty in e is just 0.0004, perhaps due to a tiny systematic error, then there is no significant discrepancy at all. Nonetheless, this provides a warning that super-small error bars are to be viewed with some skepticism.

Table 4.9 presents the full list of comparisons of the results derived from both cases of the combined analyses with those that were derived from the individual subsets of data. The table also serves to summarise the parameters available from each of the subsets of data. Regarding the discrepancies larger than $\sim 1.5\,\sigma$, we note the different levels of constraint that each type of analysis is subject to. For example, the results from the individual modelling of each subset of data are subject to the lowest level of constraint, relatively speaking, while those from case 2 of the combined analysis are subject to the highest level of constraint. In the latter case, all the available observational constraints are imposed but note, the results are not entirely model-independent. Finally, we note the longer list of parameters reported in Table 4.7 for the tertiary component; notably, absolute estimations for its mass follow from the estimation for the outer orbital inclination.

4.7 Pulsation Analysis

Fedurco et al. (2019) were the first to report pulsation in KIC 4851217. They detected

a large number of pulsation frequencies of the δ Scuti type, many of which are spaced by the orbital frequency. These authors interpreted those pulsations as sequences of sectoral modes. Liakos (2020) argued that the highest-amplitude pulsations originate in the secondary star on the basis of a comparison of the amplitudes during primary and secondary eclipse. In what follows, we present an analysis of the pulsations in this system.

4.7.1 Frequency Analysis

The frequency analysis outlined here was performed by Prof. Gerald Handler.

To this end, we used the PERIOD04 software (Lenz & Breger, 2005). This package produces amplitude spectra by Fourier analysis and can also perform multi-frequency least-squares sine-wave fitting. It also includes advanced options, such as the calculation of optimal light-curve fits for multiperiodic signals including harmonic, combination, and equally spaced frequencies which is essential for the analysis to be presented.

We have examined the *Kepler* LC and SC data and chose to analyse the LC data. The SC data do show some peaks at higher frequency than the LC Nyquist frequency. Those lie in the $35 - 40\,\mathrm{d}^{-1}$ range, but can be seen to be, at least primarily, harmonics and combinations of the pulsation modes at half that frequency range. The *Kepler* LC data, which span 1459.5 d after removal of the Q0 and Q2 data that show large drifts, give higher frequency resolution. The higher frequency harmonics and combinations do reflect about the Nyquist down into the lower frequency range, where they lie in the $10 - 15\,\mathrm{d}^{-1}$ range, but at lower amplitude than we are analysing and hence can be neglected. The *Kepler* data are more precise than, and of longer time span than the TESS data ($\Delta T = 1140.9$ d). Minor complications of using those data are that KIC 4851217 shows pulsational amplitude variations during the 4-year time base of *Kepler* observations, as do a large fraction of δ Scuti pulsators (e.g., Bowman et al., 2016), and that there are ETVs (Sect.4.3.1).

The first step in the analysis therefore is to determine the average value of the

orbital frequency during the time of *Kepler* observations, and then to fit a harmonic series to remove that as a heuristic representation of the orbital light variations from the LC data. The average orbital frequency obtained was $\nu_{orb} = 0.40481179(2)\,\mathrm{d}^{-1}$.

Owing to the ETVs and amplitude variations, we have subdivided the data set into four parts (with comparable time bases and numbers of data points): [Q1,Q3–5], Q7–Q9, Q11-Q13, Q15–Q17. We established the frequencies using the full data set for best accuracy, but then determined the amplitudes and phases of the signals from the four data subsets. For the detection of additional frequencies we then merged the residuals of those four data subsets into a single light curve and computed residual Fourier spectra, mostly free of artifacts from pulsational amplitude variations, from it. During this process it became clear that there is a multitude of pulsational signals, often spaced by multiples of the orbital frequency.

In such a situation one needs to be careful about the application of signal to noise criteria regarding frequency detection, as this may lead to overly optimistic numbers of detections (Balona, 2014b). In a first step, we therefore accepted signals with amplitudes exceeding 0.05 mmag, corresponding to $S/N = 25$ following Breger et al. (1993) only. We then computed an Échelle Diagram using those frequencies with respect to the orbital frequency (see Jayaraman et al. (2022) for an explanation) and looked for additional possible components of the emerging multiplet structures. For multiplet components to be accepted, we demanded them to be exactly[5] equally spaced in frequency by multiples of the orbital frequency within Period04, and that their amplitude exceeds 0.012 mmag ($S/N = 6$). The Échelle Diagram obtained in this way is shown in Fig. 4.7.1, and the list of pulsation frequencies in Table 4.10.

The complicated échelle Diagram is an indication of tidally tilted pulsation (e.g., Handler et al., 2020; Kurtz et al., 2020; Fuller et al., 2020; Rappaport et al., 2021). To examine this possibility, we reconstructed the runs of the pulsation amplitudes and phases of individual modes from the list of pulsation frequencies (Table 4.10) using the

[5]This is in contrast to the analysis of the TPPs in KIC 9851944, where multiplet components were demanded to be spaced by multiples of the orbital frequency to within a given threshold (see Section 3.8).

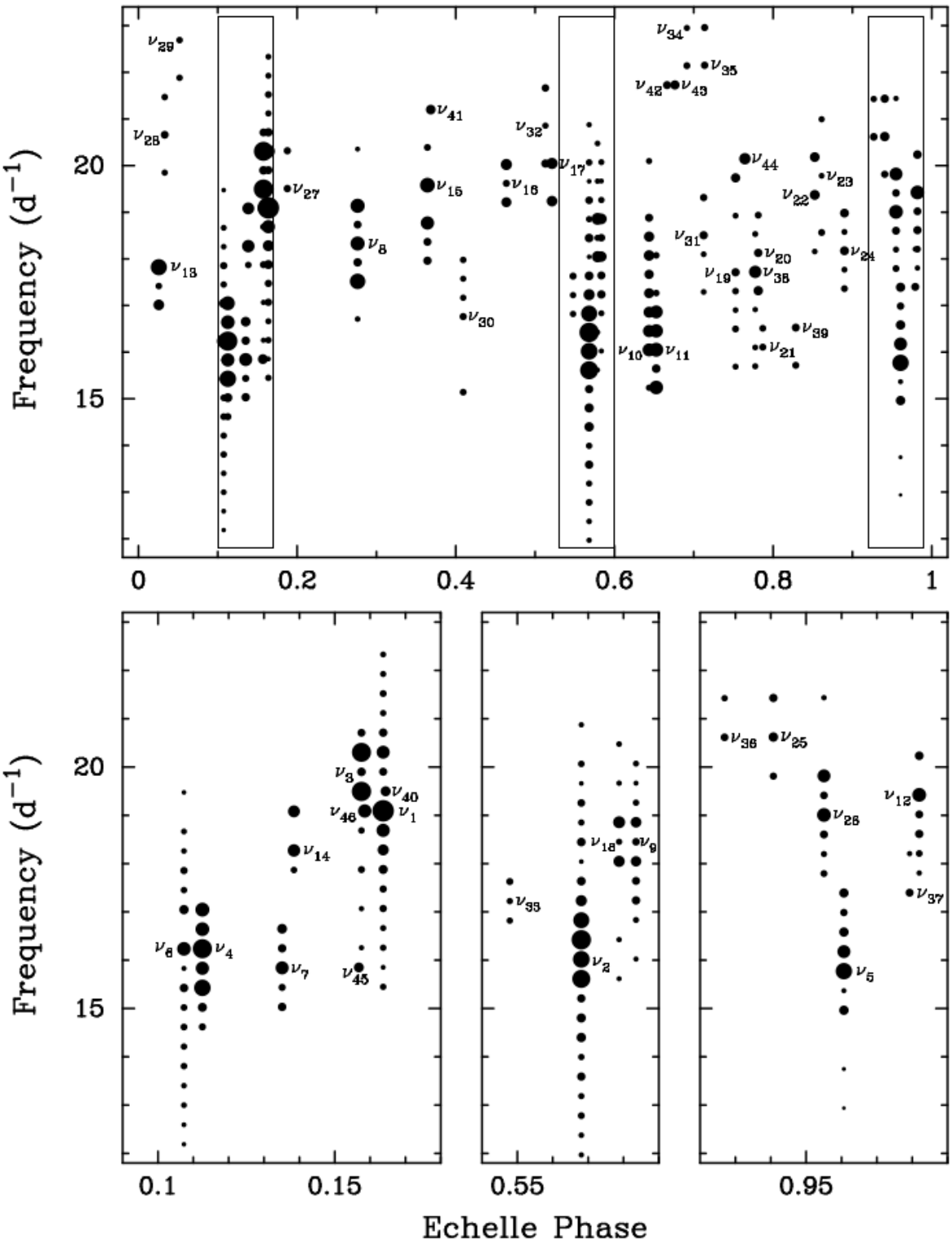

Figure 4.9: The échelle Diagram of the pulsations. The lower panels are zooms into the most crowded regions. The size of the plot symbols is proportional to the amplitude of the signals.

expressions given by Jayaraman et al. (2022).

4.7.2 Interpretation of the Modes

We examine the results of the reconstructed pulsation amplitudes and phases of individual modes in an attempt to understand the nature of the pulsations. To aid this examination, Prof. Saul Rappaport simulated light curves of KIC 4851217 assuming that Star Aa is the pulsator, and that it pulsates in a single tidally tilted mode with a typical period of 0.051 days. The simulations were carried out assuming tidally tilted dipole and quadrupole modes with Ylm = Y10, Y11, Y20 and Y22, but for varied inclinations in order to investigate how the line of site with respect to the tidal axis affects the observations. I plotted these data in Fig. 4.10 for inclination values of 75° and 80° along with the corresponding pulsation amplitudes and phases as functions of time; the effect of such a slight change in the inclination is most obvious by comparing the peak heights of the sectoral modes ($m = l$).

The easiest nonradial mode to understand is the axisymetric dipole mode (Y10). If the pulsation axis is aligned with the tidal axis, then we expect the amplitude of the Y10 pulsation to modulate with the orbit because at phases of quadrature, both hemispheres (with respect to the pulsation axis) are observed to pulsate with an anti-phase relationship, so the variability is cancelled out. Hence, the maximum of the modulation occurs during conjunction when only a single hemisphere with respect to the pulsation axis is visible. Thus, we observe the product of the pulsations and some modulation, which for the Y10 mode is sinusoidal with the orbital frequency and the Fourier transform is two delta functions which are shifted relative to the central frequency of the pulsation mode by ± the orbital frequency (see Fig. 4.10). Multiplying the pulsation by the modulating term also accounts mathematically for the associated pulsation phase changes, which occur at the nulls of the modulation (i.e., phases of quadrature for the Y10 mode when the hemisphere that is visible changes) and are integer multiples of π. Similar but more complicated arguments lead to the results for the Y11, Y20 and Y22 modes in Fig. 4.10 (see, e.g., Jayaraman et al., 2022).

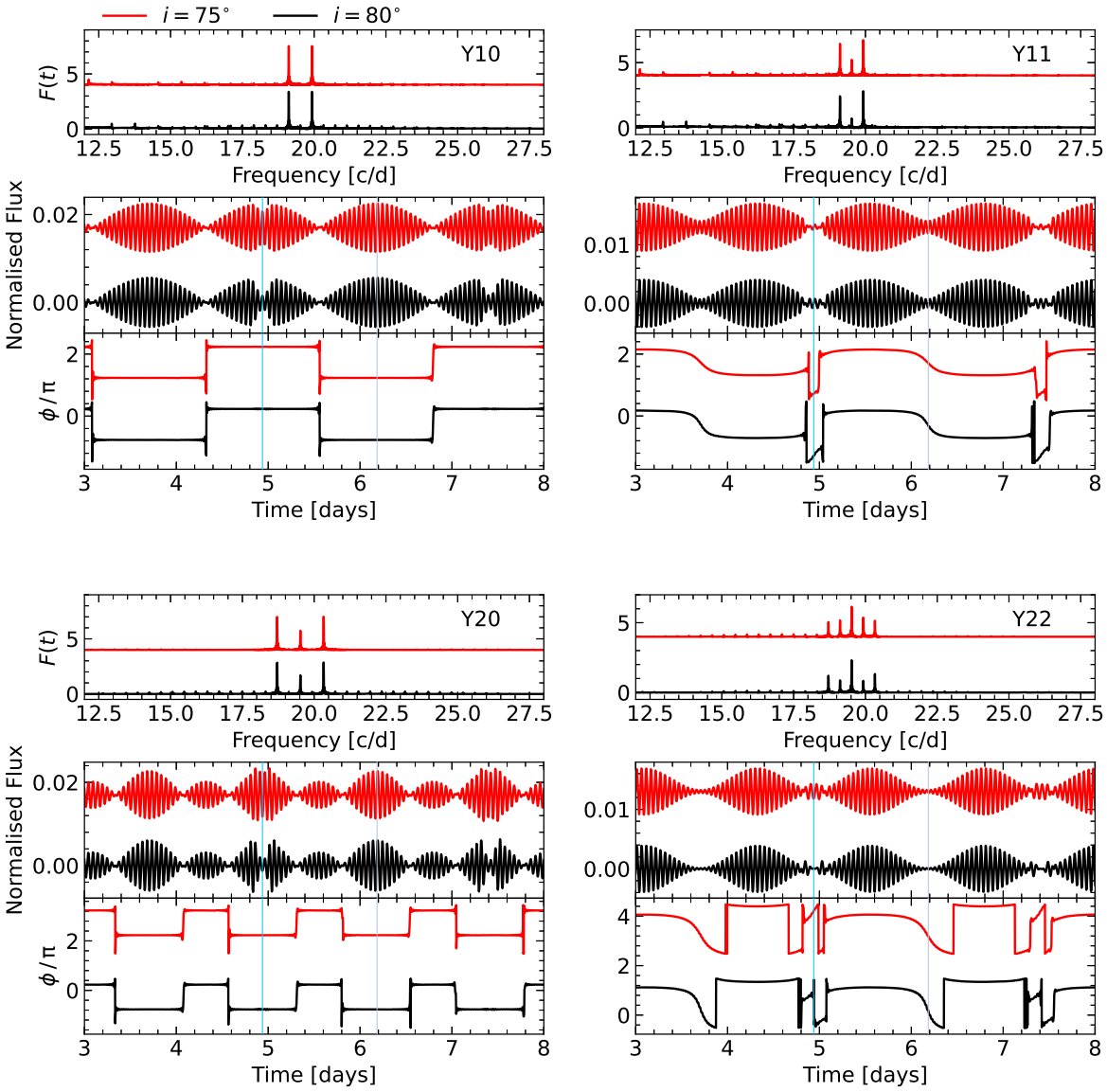

Figure 4.10: Simulations of the KIC 4851217 light curve except for inclination angles which were adjusted to $i = 75°$ (red) and $i = 80°$ (black). The primary component is assumed to pulsate in a single tidally tilted Y10 (top left), Y11 (top right), Y20 (bottom left) and Y22 (bottom right) mode. Indicated are the the times of primary (blue) and secondary (grey) eclipses.

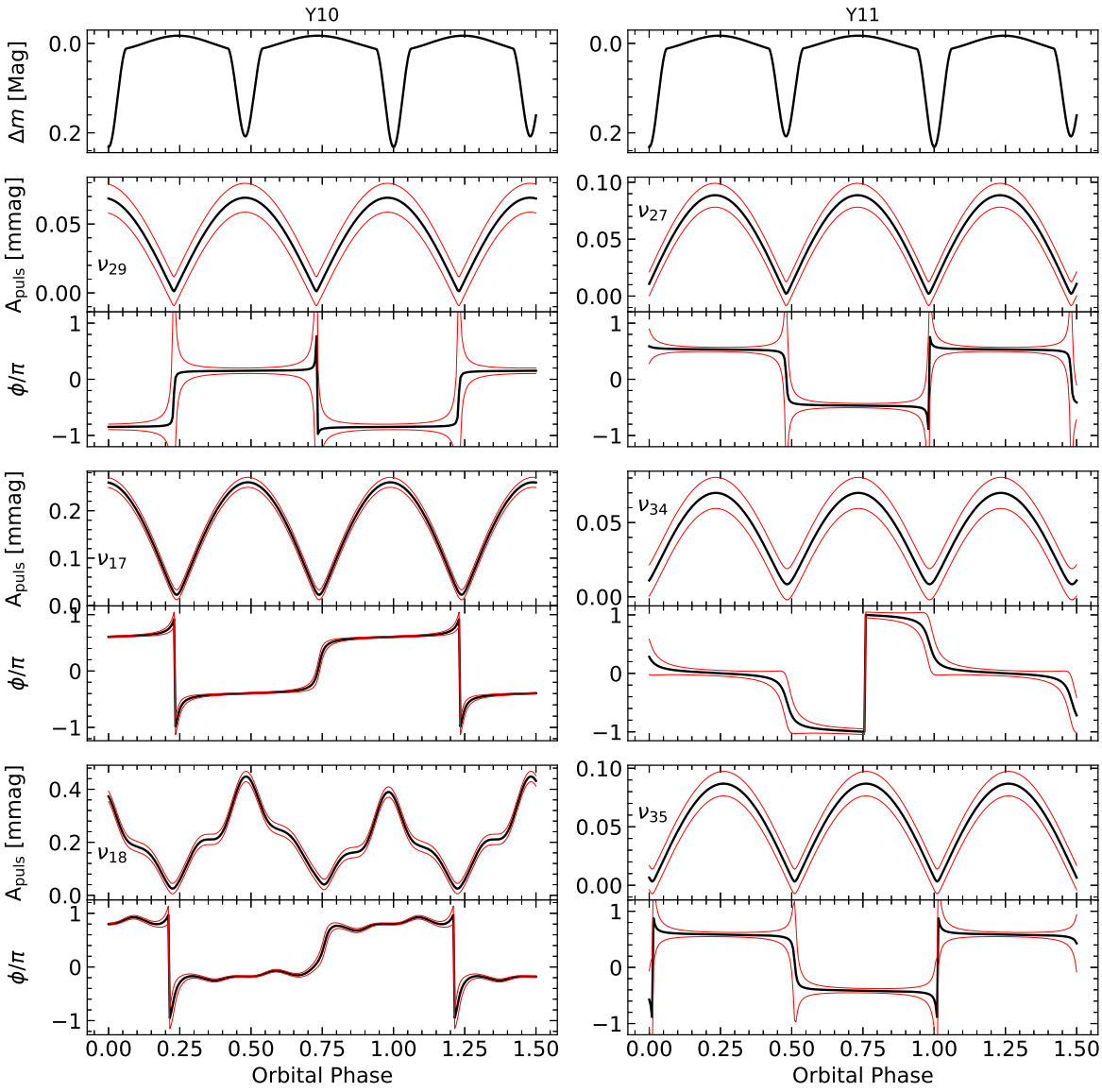

Figure 4.11: Pulsation phase and amplitudes of modes identified as Y10 (left column) and Y11 (right column). The red curves indicate the size of the formal error. The orbital light curve is plotted in two panels at the top of each column for reference.

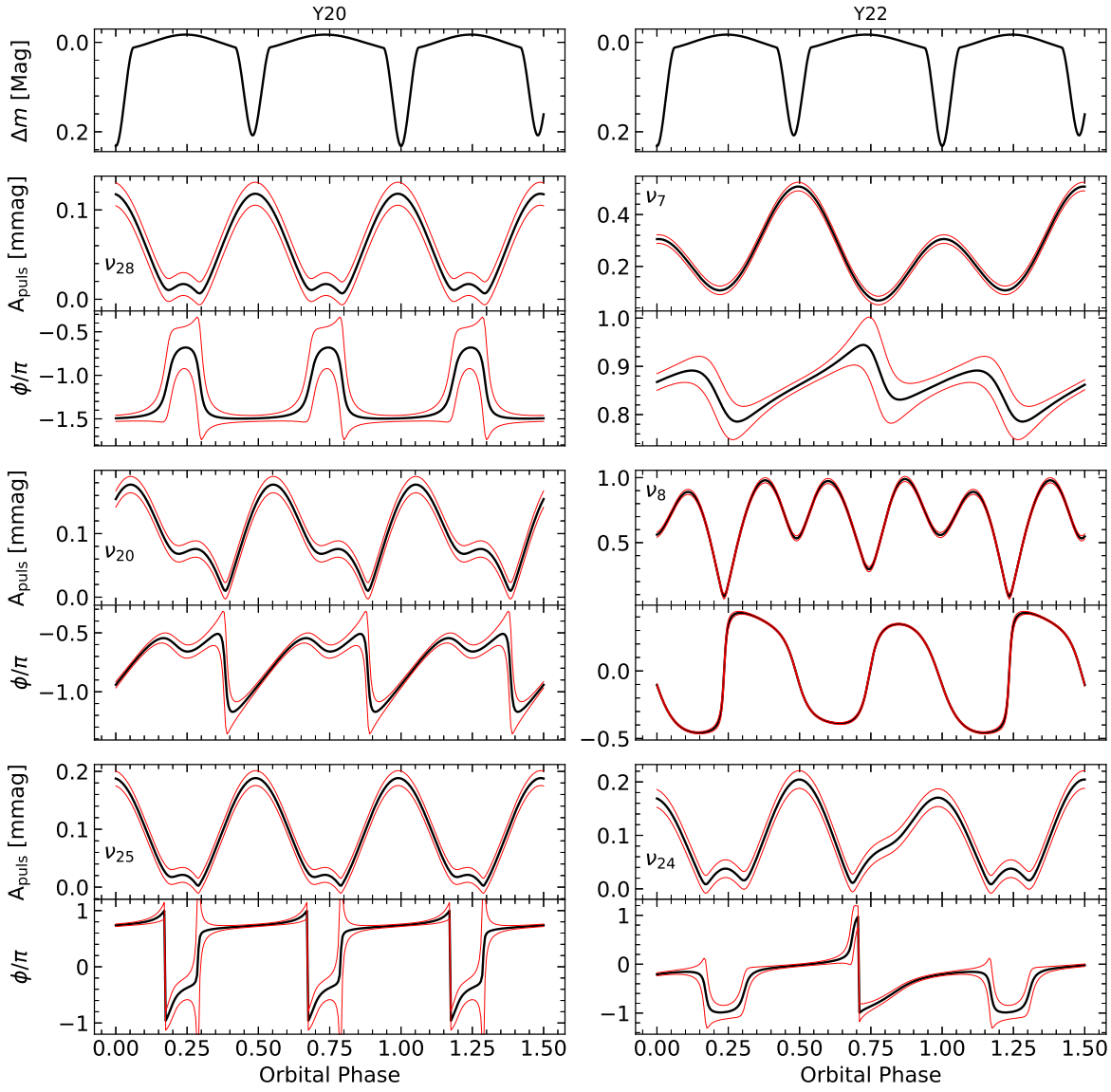

Figure 4.12: Same as Fig. 4.11 but for modes identified as Y20 (left) and Y22 (right).

For this thesis, 12 of the échelle ridges in Fig. 4.7.1 are selected for which the corresponding mode can be identified relatively simply and explained in terms of the TTP hypothesis by comparison of the multiplet structures, pulsations phases and amplitudes, with the simulated results in Fig. 4.10. The reconstructed runs of phases and amplitudes of these 12 modes are plotted in Fig. 4.11 and Fig. 4.12. The left and right columns of Fig. 4.11 shows the runs for modes that we identify as Y10 and Y11 dipole modes, respectively. The left and right columns of Fig. 4.12 show the runs for modes that we identify as Y20 and Y22 quadrupole modes, respectively. The first step in identifying l and m for these modes is to compare the multiplet structures for the frequencies in Fig. 4.7.1 to the simulated Fourier transforms (FTs) in Fig. 4.10. For example, the quintuplet due to ν_7 clearly matches the FTs of the Y22 mode. The doublets due to ν_{29} and ν_{17} match the FTs of the Y10 mode. For the latter, good matches are also observed in terms of the pulsation phase and amplitude modulations. This is almost the case for the ν_{18} mode, except its runs of phase and amplitude show wiggles. These are related to the spatial filtering effect during eclipse, which results in extra multiplet components (see Fig. 4.7.1); this is similarly the case for the Y20 quadrupole mode at ν_{20}. Notice that for the Y11 modes, the amplitude maxima of the pulsations and the corresponding phase changes are shifted to occur during conjunction. For the quadrupole Y20 modes in Fig. 4.12 (left column), we observe twice as many amplitude maxima as well as twice as many phase shifts compared the dipole modes, as expected from the simulations in Fig. 4.10.

These identifications and the phase shifts corresponding to integer multiples of π are compounded by the multiplet components being spaced *exactly* by integer multiples of the orbital frequency in suggesting that these modes are tidally tilted. The caveat in these identifications of l and m is that low amplitudes means additional components could be lost in the noise and thus they are not present in the échelle. However, the fact that such additional components were not detected argues that the modes have been described accurately. Many of the échelle ridges in Fig. 4.7.1 (e.g., ν_6, ν_9, ν_{12}, ν_{19}, ν_{26}, ν_6, ν_{30}, ν_{31}, and ν_{38}) require further investigations due to them being complicated in nature. We mentioned above that the pulsations of KIC 4851217 are subject to higher

degrees of complexity owing to ETVs and the other contributions to the amplitude modulation observed in δ Scuti pulsators. This is in addition to spatial filtering effects. We note that the results for the selected modes presented in the right panel of Fig. 4.12 were tentatively identified as Y22 quadrupole modes based on the FTs; the phase and amplitude runs are less convincing. The topic of TTPs is still in its infancy and more studies are required for a complete understanding and accurate interpretation of every observed signature. To that end, a detailed investigation into every mode displayed in Fig. 4.7.1 is in preparation.

We finally consider the mode at ν_3 (see Fig. 4.13), which was previously investigated by Fedurco et al. (2019) with the interpretation that the mode is a tidally locked (TPP) sectoral mode. We note the similarity between the amplitude and phase modulations for this mode to those of a mode in the tidally tilted subdwarf B star HD 265435 (ν_{03} in Jayaraman et al., 2022), where those authors identified the mode to be a Y22 quadruple mode. We suggest that the identification by Fedurco et al. (2019) is correct, but the interpretation is incorrect, and ν_3 is a tidally tilted mode.

The insights into the modes discussed in this this section benefited largely from conversations with Saul Rappaport, Donald Kurtz, Gerald Handler and Jim Fuller.

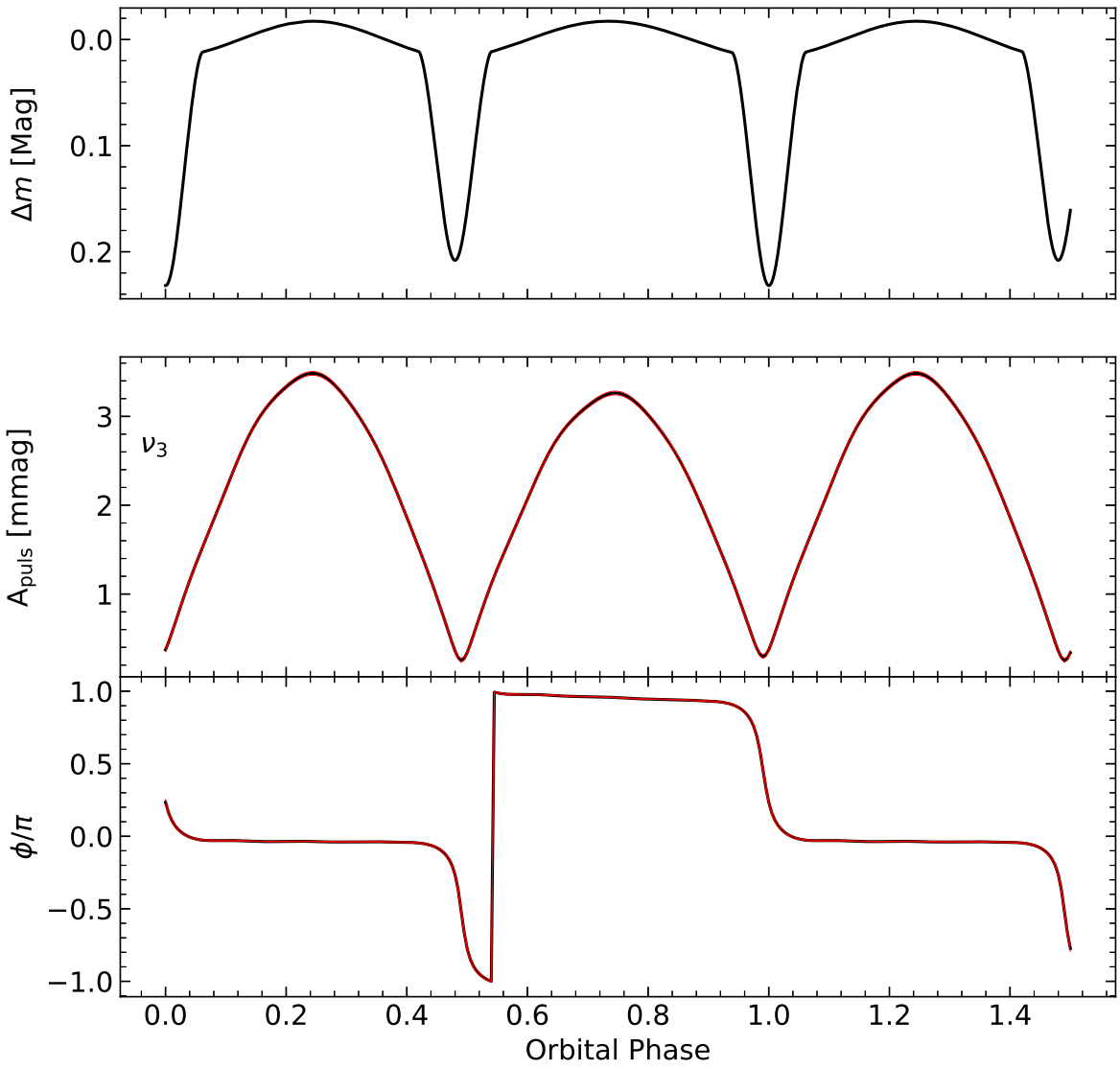

Figure 4.13: Same as Fig.4.11 but only considering the mode at ν_3.

Table 4.10: Multiple pulsation frequency solution for the *Kepler* 30-min photometry of KIC 4851217. The phases are calculated with respect to a time of primary minimum of $\mathrm{BJD_{TDB}}$ 2454953.900333. The formal errors on the frequencies and phases (Montgomery & O'Donoghue, 1999) are given in brackets in units of the last significant digit; the formal errors on the amplitudes are ±0.008 mmag.

ID	Freq. ($\mathrm{d^{-1}}$)	Ampl. (mmag)	Phase (rad)	ID	Freq. ($\mathrm{d^{-1}}$)	Ampl. (mmag)	Phase (rad)
$\nu_1-9\nu_{orb}$	15.449121	0.033	1.8(3)	$\nu_6-10\nu_{orb}$	12.18782	0.019	1.4(5)
$\nu_1-8\nu_{orb}$	15.853932	0.021	1.8(5)	$\nu_6-9\nu_{orb}$	12.59263	0.021	−0.2(4)
$\nu_1-7\nu_{orb}$	16.258744	0.033	1.8(3)	$\nu_6-8\nu_{orb}$	12.99744	0.027	1.5(3)
$\nu_1-6\nu_{orb}$	16.663556	0.030	1.7(3)	$\nu_6-7\nu_{orb}$	13.40225	0.026	0.0(3)
$\nu_1-5\nu_{orb}$	17.068368	0.044	1.8(2)	$\nu_6-6\nu_{orb}$	13.80706	0.035	1.6(2)
$\nu_1-4\nu_{orb}$	17.47318	0.043	2.0(2)	$\nu_6-5\nu_{orb}$	14.21188	0.033	0.1(2)
$\nu_1-3\nu_{orb}$	17.877991	0.076	1.5(1)	$\nu_6-4\nu_{orb}$	14.61669	0.038	1.7(2)
$\nu_1-2\nu_{orb}$	18.282803	0.135	−0.03(6)	$\nu_6-3\nu_{orb}$	15.0215	0.036	0.2(2)
$\nu_1-\nu_{orb}$	18.687615	0.266	1.75(3)	$\nu_6-2\nu_{orb}$	15.426311	0.063	1.7(1)
ν_1	19.092427(1)	3.410	1.703(3)	$\nu_6-\nu_{orb}$	15.83112	0.022	0.5(4)
$\nu_1+2\nu_{orb}$	19.90205	0.055	0.5(2)	ν_6	16.23593(1)	0.303	1.93(3)
$\nu_1+3\nu_{orb}$	20.306862	0.248	1.86(3)	$\nu_6+2\nu_{orb}$	17.04556	0.082	1.8(1)
$\nu_1+4\nu_{orb}$	20.711674	0.062	1.8(2)	$\nu_6+3\nu_{orb}$	17.45037	0.034	0.6(3)
$\nu_1+5\nu_{orb}$	21.116486	0.032	1.9(4)	$\nu_6+4\nu_{orb}$	17.85518	0.043	1.7(2)
$\nu_1+6\nu_{orb}$	21.521298	0.039	1.8(3)	$\nu_6+5\nu_{orb}$	18.25999	0.026	0.8(4)
$\nu_1+7\nu_{orb}$	21.926109	0.030	1.7(4)	$\nu_6+6\nu_{orb}$	18.66481	0.028	2.2(4)
$\nu_1+8\nu_{orb}$	22.330921	0.028	1.9(4)	$\nu_6+8\nu_{orb}$	19.47443	0.019	−0.7(5)
$\nu_2-10\nu_{orb}$	11.96951	0.024	1.6(5)	$\nu_7-2\nu_{orb}$	15.03273	0.062	1.4(1)
$\nu_2-9\nu_{orb}$	12.374322	0.026	2.2(4)	$\nu_7-\nu_{orb}$	15.43754	0.042	−0.4(2)
$\nu_2-8\nu_{orb}$	12.779134	0.038	1.7(3)	ν_7	15.842351(1)	0.251	1.35(3)
$\nu_2-7\nu_{orb}$	13.183946	0.031	2.2(3)	$\nu_7+\nu_{orb}$	16.24716	0.062	−0.1(1)
$\nu_2-6\nu_{orb}$	13.588757	0.060	1.7(2)	$\nu_7+2\nu_{orb}$	16.65197	0.093	1.4(1)
$\nu_2-5\nu_{orb}$	13.993569	0.033	2.2(3)	$\nu_8-4\nu_{orb}$	16.70908	0.026	−0.5(4)
$\nu_2-4\nu_{orb}$	14.398381	0.084	1.8(1)	$\nu_8-2\nu_{orb}$	17.5187	0.535	−0.11(2)
$\nu_2-3\nu_{orb}$	14.803193	0.077	1.9(1)	$\nu_8-\nu_{orb}$	17.92351	0.062	2.1(1)
$\nu_2-2\nu_{orb}$	15.208005	0.059	−0.8(2)	ν_8	18.32832(1)	0.346	−0.03(3)
$\nu_2-\nu_{orb}$	15.612816	1.176	1.876(7)	$\nu_8+\nu_{orb}$	18.73314	0.051	0.7(2)
ν_2	16.017628(2)	0.784	1.80(1)	$\nu_8+2\nu_{orb}$	19.13795	0.356	1.59(3)
$\nu_2+\nu_{orb}$	16.422440	1.829	1.946(5)	$\nu_8+5\nu_{orb}$	20.35238	0.022	0.0(5)

Table 4.10 continued.

ID	Freq. (d^{-1})	Ampl. (mmag)	Phase (rad)	ID	Freq. (d^{-1})	Ampl. (mmag)	Phase (rad)
$\nu_2+2\nu_{orb}$	16.827252	0.630	2.06(1)	$\nu_9-6\nu_{orb}$	16.02389	0.023	1.0(5)
$\nu_2+3\nu_{orb}$	17.232064	0.139	2.04(6)	$\nu_9-4\nu_{orb}$	16.83352	0.030	1.3(4)
$\nu_2+4\nu_{orb}$	17.636875	0.069	2.1(1)	$\nu_9-3\nu_{orb}$	17.23832	0.061	−0.4(1)
$\nu_2+5\nu_{orb}$	18.041687	0.020	1.7(6)	$\nu_9-2\nu_{orb}$	17.64314	0.055	1.3(2)
$\nu_2+6\nu_{orb}$	18.446499	0.066	2.1(1)	$\nu_9-\nu_{orb}$	18.04795	0.112	−0.3(1)
$\nu_2+7\nu_{orb}$	18.851311	0.033	1.6(3)	ν_9	18.45276(3)	0.048	1.5(2)
$\nu_2+8\nu_{orb}$	19.256123	0.049	2.1(2)	$\nu_9+\nu_{orb}$	18.85757	0.123	−0.2(1)
$\nu_2+9\nu_{orb}$	19.660934	0.020	1.6(6)	$\nu_9+2\nu_{orb}$	19.26239	0.033	1.7(3)
$\nu_2+10\nu_{orb}$	20.065746	0.035	2.1(3)	$\nu_9+3\nu_{orb}$	19.6672	0.022	0.3(4)
$\nu_2+12\nu_{orb}$	20.87537	0.024	2.1(5)	$\nu_9+4\nu_{orb}$	20.07201	0.029	1.7(3)
$\nu_3-7\nu_{orb}$	16.256245	0.023	0.7(5)	$\nu_{10}-2\nu_{orb}$	15.23858	0.032	0.0(3)
$\nu_3-5\nu_{orb}$	17.065869	0.024	0.4(5)	ν_{10}	16.04820(1)	0.246	−0.35(4)
$\nu_3-3\nu_{orb}$	17.875493	0.040	0.5(3)	$\nu_{10}+\nu_{orb}$	16.45301	0.193	−0.56(5)
$\nu_3-2\nu_{orb}$	18.685116	0.034	0.7(3)	$\nu_{10}+2\nu_{orb}$	16.85783	0.136	1.01(7)
$\nu_3-\nu_{orb}$	19.494740(2)	1.761	0.693(5)	$\nu_{10}+3\nu_{orb}$	17.26264	0.099	−0.72(9)
ν_3	19.899552	0.065	0.2(1)	$\nu_{10}+4\nu_{orb}$	17.66745	0.081	0.6(1)
$\nu_3+\nu_{orb}$	20.304363	1.606	2.323(5)	$\nu_{10}+5\nu_{orb}$	18.07226	0.119	−0.10(8)
$\nu_3+2\nu_{orb}$	20.709175	0.053	1.6(1)	$\nu_{10}+6\nu_{orb}$	18.47707	0.106	2.24(8)
$\nu_4-4\nu_{orb}$	14.618782	0.042	0.8(3)	$\nu_{10}+7\nu_{orb}$	18.88188	0.056	−0.1(1)
$\nu_4-3\nu_{orb}$	15.023594	0.074	2.1(1)	$\nu_{10}+10\nu_{orb}$	20.09632	0.031	0.8(3)
$\nu_4-2\nu_{orb}$	15.428406	0.727	−0.76(1)	$\nu_{11}-2\nu_{orb}$	15.24229	0.307	−0.20(3)
$\nu_4-\nu_{orb}$	15.833218	0.268	−0.72(3)	$\nu_{11}-\nu_{orb}$	15.6471	0.066	−0.7(1)
ν_4	16.238029(2)	1.676	0.816(5)	ν_{11}	16.05191(1)	0.342	−0.01(3)
$\nu_4+\nu_{orb}$	16.642841	0.310	0.68(3)	$\nu_{11}+\nu_{orb}$	16.45672	0.282	0.36(3)
$\nu_4+2\nu_{orb}$	17.047653	0.333	−0.64(3)	$\nu_{11}+2\nu_{orb}$	16.86154	0.248	1.49(4)
$\nu_5-7\nu_{orb}$	12.938057	0.014	1.9(6)	$\nu_{11}+3\nu_{orb}$	17.26635	0.035	−0.4(3)
$\nu_5-5\nu_{orb}$	13.74768	0.016	1.9(6)	$\nu_{11}+5\nu_{orb}$	18.07597	0.036	−0.3(3)
$\nu_5-2\nu_{orb}$	14.962116	0.084	1.2(1)	$\nu_{12}-4\nu_{orb}$	17.80443	0.024	2.0(4)
$\nu_5-\nu_{orb}$	15.366927	0.022	0.4(4)	$\nu_{12}-3\nu_{orb}$	18.20924	0.037	−0.2(3)
ν_5	15.771739(5)	0.715	1.22(1)	$\nu_{12}-2\nu_{orb}$	18.61406	0.059	0.9(2)
$\nu_5+\nu_{orb}$	16.176551	0.244	1.11(3)	$\nu_{12}-\nu_{orb}$	19.01887	0.052	0.2(2)
$\nu_5+2\nu_{orb}$	16.581363	0.083	−0.42(9)	ν_{12}	19.42368(1)	0.318	−0.77(3)
$\nu_5+3\nu_{orb}$	16.986175	0.045	−0.5(2)	$\nu_{12}+2\nu_{orb}$	20.2333	0.066	1.0(1)
$\nu_5+4\nu_{orb}$	17.390986	0.080	−0.1(1)				

Table 4.10 continued.

ID	Freq. (d^{-1})	Ampl. (mmag)	Phase (rad)	ID	Freq. (d^{-1})	Ampl. (mmag)	Phase (rad)
$\nu_{13}-2\nu_{orb}$	17.012433	0.122	0.41(7)	$\nu_{26}-3\nu_{orb}$	17.79352	0.038	0.4(2)
$\nu_{13}-\nu_{orb}$	17.417245	0.035	-0.6(3)	$\nu_{26}-2\nu_{orb}$	18.19833	0.030	1.9(3)
ν_{13}	17.822057(5)	0.650	0.38(1)	$\nu_{26}-\nu_{orb}$	18.60314	0.055	-0.3(2)
$\nu_{14}-\nu_{orb}$	17.86777	0.035	0.3(3)	ν_{26}	19.00795(1)	0.316	0.49(3)
ν_{14}	18.27258(2)	0.211	0.68(4)	$\nu_{26}+\nu_{orb}$	19.41277	0.049	2.2(2)
$\nu_{14}+2\nu_{orb}$	19.08220	0.176	-0.77(5)	$\nu_{26}+2\nu_{orb}$	19.81758	0.243	2.06(4)
$\nu_{15}-4\nu_{orb}$	17.959205	0.059	1.2(1)	$\nu_{26}+6\nu_{orb}$	21.43682	0.024	2.2(4)
$\nu_{15}-3\nu_{orb}$	18.364016	0.054	0.5(1)	ν_{27}	19.50695(7)	0.045	1.6(2)
$\nu_{15}-2\nu_{orb}$	18.768828	0.272	-0.16(3)	$\nu_{27}+2\nu_{orb}$	20.31658	0.043	0.1(2)
ν_{15}	19.578452(8)	0.431	-0.07(2)	$\nu_{28}-2\nu_{orb}$	19.84917	0.032	0.7(3)
$\nu_{15}+2\nu_{orb}$	20.388075	0.039	1.6(2)	ν_{28}	20.65880(6)	0.052	0.8(2)
$\nu_{16}-\nu_{orb}$	19.21393	0.099	1.17(9)	$\nu_{28}+2\nu_{orb}$	21.46842	0.035	0.8(3)
ν_{16}	19.61874(2)	0.041	-0.1(2)	$\nu_{29}-2\nu_{orb}$	21.88076	0.034	1.7(3)
$\nu_{16}+\nu_{orb}$	20.02355	0.140	1.28(7)	ν_{29}	22.69038(9)	0.035	1.9(3)
$\nu_{17}-2\nu_{orb}$	19.23716	0.119	0.91(8)	$\nu_{30}-4\nu_{orb}$	15.14377	0.037	0.1(3)
ν_{17}	20.04678(2)	0.141	0.98(7)	ν_{30}	16.76302(8)	0.042	0.2(2)
$\nu_{18}-7\nu_{orb}$	15.61714	0.022	0.8(4)	$\nu_{30}+\nu_{orb}$	17.16783	0.032	1.9(3)
$\nu_{18}-5\nu_{orb}$	16.42676	0.024	1.0(4)	$\nu_{30}+2\nu_{orb}$	17.57264	0.031	0.2(3)
$\nu_{18}-\nu_{orb}$	18.04601	0.142	1.26(6)	$\nu_{30}+3\nu_{orb}$	17.97746	0.034	-0.2(3)
ν_{18}	18.45082(2)	0.032	-0.1(3)	$\nu_{31}-3\nu_{orb}$	17.29054	0.027	1.1(3)
$\nu_{18}+\nu_{orb}$	18.85563	0.180	1.32(5)	$\nu_{31}-\nu_{orb}$	18.10016	0.027	-0.6(3)
$\nu_{18}+3\nu_{orb}$	19.66526	0.025	1.4(4)	ν_{31}	18.50497(6)	0.060	-0.4(2)
$\nu_{18}+5\nu_{orb}$	20.47488	0.027	1.5(3)	$\nu_{31}+2\nu_{orb}$	19.31460	0.044	1.3(2)
$\nu_{19}-10\nu_{orb}$	15.68755	0.030	-0.6(3)	$\nu_{32}-2\nu_{orb}$	20.04343	0.059	1.9(2)
$\nu_{19}-8\nu_{orb}$	16.49718	0.039	1.5(2)	ν_{32}	20.85306(6)	0.032	2.1(3)
$\nu_{19}-7\nu_{orb}$	16.90199	0.027	0.9(3)	$\nu_{32}+2\nu_{orb}$	21.66268	0.046	0.4(2)
$\nu_{19}-6\nu_{orb}$	17.30680	0.036	-0.3(3)	$\nu_{33}-\nu_{orb}$	16.81905	0.033	-0.6(3)
$\nu_{19}-5\nu_{orb}$	17.71161	0.059	1.2(2)	ν_{33}	17.22387(8)	0.032	1.2(3)
$\nu_{19}-2\nu_{orb}$	18.92605	0.028	1.6(3)	$\nu_{33}+\nu_{orb}$	17.62868	0.041	-0.4(2)
ν_{19}	19.73567(4)	0.081	1.7(1)	$\nu_{34}-2\nu_{orb}$	22.13968	0.039	0.7(2)
$\nu_{20}-2\nu_{orb}$	17.31839	0.083	2.0(1)	ν_{34}	22.94931(8)	0.031	-0.7(3)
ν_{20}	18.12801(4)	0.061	1.4(1)	$\nu_{35}-2\nu_{orb}$	22.14875	0.045	1.7(2)
$\nu_{20}+2\nu_{orb}$	18.93764	0.038	1.4(2)	ν_{35}	22.95838(7)	0.042	0.1(2)
ν_{21}	16.10628(8)	0.040	-0.4(2)	ν_{36}	20.61582(7)	0.050	2.0(2)
$\nu_{21}+\nu_{orb}$	16.51109	0.037	1.1(2)	$\nu_{36}+2\nu_{orb}$	21.42545	0.033	2.0(3)

Table 4.10 continued.

ID	Freq. (d^{-1})	Ampl. (mmag)	Phase (rad)	ID	Freq. (d^{-1})	Ampl. (mmag)	Phase (rad)
$\nu_{22}-3\nu_{orb}$	18.15684	0.027	1.9(3)	ν_{37}	17.39852(7)	0.054	-0.3(2)
ν_{22}	19.37128(3)	0.099	0.46(9)	$\nu_{37}+2\nu_{orb}$	18.20814	0.024	1.3(4)
$\nu_{22}+2\nu_{orb}$	20.18090	0.094	1.96(9)	$\nu_{38}-5\nu_{orb}$	15.69757	0.030	0.6(3)
ν_{23}-$3\nu_{orb}$	18.56518	0.039	-0.7(2)	$\nu_{38}-4\nu_{orb}$	16.10238	0.028	2.3(3)
ν_{23}	19.77961(8)	0.027	0.9(3)	$\nu_{38}-2\nu_{orb}$	16.91200	0.024	-0.7(4)
$\nu_{23}+3\nu_{orb}$	20.99405	0.031	-0.4(3)	ν_{38}	17.72163(2)	0.207	-0.48(4)
$\nu_{24}-2\nu_{orb}$	17.36238	0.038	-0.1(2)	$\nu_{38}+2\nu_{orb}$	18.53125	0.029	-0.5(3)
$\nu_{24}-\nu_{orb}$	17.76720	0.029	1.9(3)	$\nu_{39}-2\nu_{orb}$	15.71829	0.040	1.8(2)
ν_{24}	18.17201(5)	0.072	-0.3(1)	ν_{39}	16.52792(6)	0.054	2.1(2)
$\nu_{24}+\nu_{orb}$	18.57682	0.029	2.1(3)	ν_{40}	19.49752(3)	0.100	0.89(9)
$\nu_{24}+2\nu_{orb}$	18.98163	0.071	-0.1(1)	ν_{41}	21.19934(4)	0.091	1.7(1)
$\nu_{25}-2\nu_{orb}$	19.81179	0.043	1.1(2)	ν_{42}	21.72483(6)	0.056	1.4(2)
ν_{25}	20.62141(4)	0.085	1.2(1)	ν_{43}	21.72880(4)	0.079	-0.7(1)
$\nu_{25}+2\nu_{orb}$	21.43104	0.061	1.2(1)	ν_{44}	20.14523(2)	0.152	1.56(6)
				ν_{45}	15.85114(3)	0.096	0.1(1)
				ν_{46}	19.09031(1)	0.275	-0.09(3)

4.8 Conclusion

Considering our model-independent methods of analysis of the photometric and spectroscopic data (i.e., using the results from the individual modelling of the data subsets and their joint analysis via method 1 in Section 4.6.1), we measured the masses of the components of the inner EB to 0.5% and 0.4% on average for star Aa and Star Ab, respectively; their radii were measured to 1.4% and 0.8% on average. We measured both their $T_{\rm eff}$s to $\sim 1\%$ via the atmospheric analysis of the components' disentangled spectra in Section 4.4.3. Both model-dependent methods, i.e., the SED fitting in Section 4.3.3 and method 2 of the combined analysis are consistent with an age of 0.82 Gyr. The secondary is larger and more massive than the primary, but cooler as it is evolving off the MS (see Fig. 4.3). This study has highlighted the results obtainable from the modelling of the individual subsets of spectroscopic and photometric data, and compared those with the results of their combined analysis; in general, we find

good agreement.

We have reported the detection of a tertiary companion (star B) in the KIC 4851217 system from the analysis of the primary and secondary mid-eclipse times of the inner EB, which were measured from *Kepler* and TESS light curves and show ETVs due to an outer orbit and apsidal motion of the EB orbit. The relatively low amplitude of the ETV signatures mean that the outer orbit is undetected in the time-span of our spectroscopic observations, and is another example of the advantages associated with the high precision, long time-base monitoring of stars provided by such space missions. We analysed the ETVs jointly with the light curves and RVs measured from high (HERMES; R $\sim$ 85000) and moderate (ISIS; R $\sim$ 10000) resolution spectra to yield estimates for the mass, radius and $T_{\rm eff}$ of star B to 15%, 16% and 5%, precisions on average, respectively.

We analysed the *Kepler* LC light curves and extracted a list of pulsation frequencies which we present in Table 4.10. Many of these frequencies are spaced by multiples of the orbital frequency and form ridges in the échelle diagram of Fig. 4.7.1 plotted with respect to the orbital frequency. An examination of the reconstructed pulsation phases and amplitudes of the individual modes suggests that these are TTPs, which has allowed for the identification of l and m for a selection of these modes. The TTP hypothesis is further supported by the fact that we only accepted components to belong to a multiplet if they were spaced exactly by the orbital frequency. This is in contrast to the detection of TPPs in Section 3.8.2. We also note that the phase modulations of the TPPs in KIC 9851944 were of the order 0.5 – 1.5 rad rather than integer multiples of π expected for TTPs and observed here.

Until the detection of TTPs in the subdwarf B star HD 265435 by Jayaraman et al. (2022), there were only three conclusively identified TTPs reported in the literature (Handler et al., 2020; Kurtz et al., 2020; Rappaport et al., 2021), with each of them being δ Scuti stars. Thus, the former precludes the possibility that tidal tilting of the pulsation axis is a phenomenon unique to δ Scuti stars, and this is in line with theory (Fuller et al., 2020). This study contributes another δ Scuti TTP to the literature and the precisely derived physical properties make KIC 4851217 an ideal candidate for de-

veloping our understanding of the TTP phenomenon via pulsation modelling. Indeed, full investigations into the complicated pulsations of KIC 4851217 are on-going and plans are in place to carry out a detailed modelling of this object's pulsations. Tidally tilted pulsations are a relatively new discovery and hence the lack of reported detections in the literature. To advance our understanding of this phenomenon, we need to detect and model more TTPs; it is noteworthy that while some stars exhibit TTPs, others display TPPs. KIC 4851217 is a precisely-characterised δ Scuti star so its contribution to the literature also aligns with the broader objective to derive constraints on the internal structures of intermediate mass stars.

5 Revising the properties of low mass eclipsing binary stars using TESS light curves

The work outlined in this chapter was published in the Monthy Notices of the Royal Astronomical Society (MNRAS) main journal (Jennings et al., 2023a).

5.1 Introduction

Thirteen EBLMs considered in this study have been observed using ground-based photometry. Such data are sufficient to detect and measure the properties of EBLMs, but the observational scatter often limits the precision of the mass and radius measurements. The situation can be greatly improved by using space-based photometry due to its competitive precision coupled with improved time sampling over longer periods of continuous monitoring. The use of photometry from space satellites has revolutionised the study of EBs (Southworth, 2021).

The Transiting Exoplanet Survey Satellite (TESS, Ricker et al. 2015) is the most useful mission in the context of this project because it has observed the great majority of the sky in both hemispheres. In this work, we use light curves from TESS and published RVs to obtain new measurements of the physical properties of a set of known EBLMs. The aim is to provide improved constraints on theoretical models of low-mass stars and thus more accurately address the uncertainties surrounding the interior structure of these objects for which we refer to Section 1.1.5.3. We also present new ground-based high-precision light curves of two objects obtained in four passbands simultaneously.

Basic information regarding the systems studied in this work are given in Table 5.1. These objects were chosen with the aim to include all EBLMs with published RVs and previously unstudied TESS light curves. However, we explicitly excluded objects in the EBLM series of papers (see Triaud et al., 2017) as these are currently being analysed by others.

In Section 5.2 a description of the observations and data used in this work is presented. Section 5.3 outlines the analysis techniques, and the results for each system are presented in Section 5.4. A discussion and concluding remarks are presented in Section 5.5.

5.2 Observations

5.2.1 TESS observations

TESS has observed over 200 000 selected main sequence dwarfs in 2-minute cadence (SC) mode and many more in the 30-minute cadence (LC) mode in which the data are saved as a full-frame-image (FFI). We account for the sparser sampling of the latter using numerical integration (see Section 5.3).

The TESS-point web tool[1] was used to determine which and how many sectors the targets had been observed in. For SC data, both simple aperture photometric (SAP) and pre-search data conditioned SAP (PDCSAP) data (Jenkins et al., 2016b) were inspected before choosing one of them as the most suitable. This is necessary since the PDC reduction pipeline usually yields more precise data but can introduce unwanted artefacts in targets dissimilar to those that the routine is tailored to.

For targets observed in LC mode, the data were extracted from the FFIs using custom routines. Aperture photometry was performed using apertures whose size and position were adjusted manually for each target to optimally extract the flux of each target while minimsing background flux from neighbours. The surrounding field was investigated by first querying the *Vizier*[2] database for all objects within a 3.5 arcminute radius from the target with an apparent *Gaia* G magnitude of less than 16 in the *Gaia* DR2 catalogue (Gaia Collaboration, 2018). A threshold magnitude of $G = 16$ was chosen since objects fainter than this are not expected to be bright enough to have

[1] `https://heasarc.gsfc.nasa.gov/wsgi-scripts/TESS/TESS-point_Web_Tool/TESS-point_Web_Tool/wtv_v2.0.py/`

[2] `https://vizier.cds.unistra.fr/`

Table 5.1: Basic parameters for the EBLMs included in this work. Values for $T_{\rm eff}$ were taken from the literature when such analysis was reliable. In other cases, indicated with an asterisk next to the $T_{\rm eff}$, the values were determined from a SED fit as described in Section 5.3.2.

Identifiers						
This work	TIC	Published	Reference(s)	V mag	TESS sectors	Temperature (K)
TYC 2755-36-1	305982045	HAT-TR-205-013	Beatty et al. (2007); Latham et al. (2009)	10.72	–	6617±200*
HAT-TR-205-003	115686059	HAT-TR-205-003	Latham et al. (2009)	12.48	16	6363±150*
T-Aur0-13378	122104276	T-Aur0-13378	Fernandez et al. (2009)	13.35	19	6675±125*
TYC 3576-2035-1	295803225	T-Cyg1-01385	Fernandez et al. (2009)	10.70	14, 15	5887±125*
TYC 3473-673-1	148781497	T-Boo0-00080	Fernandez et al. (2009)	10.30	16, 23	6254±125*
TYC 3545-371-1	48450535	T-Lyr1-01662	Fernandez et al. (2009)	11.30	14, 15	6956±125*
TYC 3121-1659-1	394178587	T-Lyr0-08070	Fernandez et al. (2009)	12.30	14	6633±125*
TYC 7096-222-1	53059882	TYC 7096-222-1	Bentley et al. (2009)	10.28	6, 7, 33, 34	7600 ± 300
TYC 2855-585-1	192587088	TYC 2855-585-1	Koo et al. (2012)	11.31	18	6500 ± 250
TYC 9535-351-1	451596415	TYC 9535-351-1	Wang et al. (2014); Crouzet et al. (2012)	10.12	13,27,39	6663±125*
TYC 6493-290-1	32606889	HATS 551-019	Zhou et al. (2014)	12.06	5, 6, 32, 33	6380 ± 170
GSC 06493-00315	32677675	HATS 551-021	Zhou et al. (2014)	13.11	5, 6, 32, 33	6670 ± 220
GSC 05946-00892	59751429	HATS 553-001	Zhou et al. (2014)	13.19	33	6230 ± 250
GSC 06465-00602	594723	HATS 550-016	Zhou et al. (2014)	13.61	32	6420 ± 90
TYC 3700-1739-1	645967562	TYC 3700-1739-1	Eigmüller et al. (2016)	11.77	18	7350 ± 250

any effect on the observations (Southworth et al., 2020). The positions of these objects were then marked on the 200th frame of the target, chosen due to early frames in the time series being contaminated by scattered light from Earth near perigee. Verifying the locations of neighbouring objects also aided the choice of the size and location of the aperture. The positions of any marked contaminants in *Gaia* DR2 were further confirmed using the Two Micron All Sky Survey (2MASS; Skrutskie et al. 2006) as a reference when available. In a few cases where a 2MASS image was unavailable, we used images from the ESO Digitised Sky Survey (DSS) instead. The level of contaminant flux captured within the aperture of LC targets was investigated by plotting the position of the centroid of the target in the x and y planes of the target pixel file against time. Shifts in the position of the centroids occur during eclipses when contamination is serious.

All LC and SC data were normalised by dividing the flux and error by the median flux value. Quasi-periodic variations present in most light curves were attributed to starspots in the primary component and divided out. Before dividing out the magnetic activity, it was necessary to mask the eclipses. Astropy's implementation of the box least squares algorithm (Astropy Collaboration et al., 2013, 2018), which models a transit as a periodic upside-down top hat with four simple parameters, was used to develop a mask for the primary eclipses. The parameters of the model are the transit midpoint, duration, period and depth, where the first three of these were used in the masking process. The secondary eclipses were masked manually.

The variations were then modelled via two methods and divided out. The most effective method based on a visual inspection of the resulting light curve was chosen. The first method used Astropy's implementation of Lomb-Scargle periodograms in order to model the observed variations with a combination of sinusoids. The second method applied a Savitsky-Golay filter, as implemented by the python package LIGHTKURVE (Lightkurve Collaboration et al., 2018), to the masked time series, fitting successive subsets of adjacent datapoints with a low-degree polynomial by linear least squares. Trial values for the degree of polynomial were used and the best result carried forward for comparison with the first method.

Some objects were observed by TESS in more than one sector. In these cases, the data from each sector were concatenated into a single data file after the above process was carried out individually for each sector. The phase-folded TESS data are shown in Fig. 5.1.

5.2.2 Ground-based observations

The following ground based observations and data reductions were carried out by Dr. John Taylor, Dr Pierre Maxted and Dr Luigi Mancini.

One transit each of TYC 2755-36-1 and TYC 3121-1659-1 was observed simultaneously in four passbands using the Bonn University Simultaneous CAmera (BUSCA) four-band imaging photometer (Reif et al., 1999) on the 2.2 m telescope at Calar Alto, Spain (Fig. 5.2). Due to the brightness of TYC 2755-36-1 we elected to observe through the intermediate-band Strömgren *uby* and Johnson I filters. TYC 3121-1659-1 is significantly fainter and was observed through the Strömgren v, Gunn g and r, and Johnson I filters. In both cases we operated with the telescope defocussed following the approach of Southworth et al. (2009), and were able to extract good light curves in all four passbands.

One more transit of TYC 3121-1659-1 was obtained through a Cousins I filter using the 1.23 m telescope at Calar Alto and the DLR-MKIII CCD camera. The telescope was operated out of focus as before.

The data were reduced using the DEFOT pipeline (Southworth et al., 2009, 2014), which depends on the NASA ASTROLIB library[3] IDL[4] implementation of the APER photometry routine from DAOPHOT (Stetson, 1987). We specified software apertures by hand and chose the aperture radii that minimised the scatter in the final light curve. Differential-magnitude light curves were generated versus an ensemble comparison star containing the weighted flux sum of all good comparison stars. A low-order polynomial

[3] `http://idlastro.gsfc.nasa.gov/`

[4] `http://www.harrisgeospatial.com/SoftwareTechnology/ IDL.aspx`

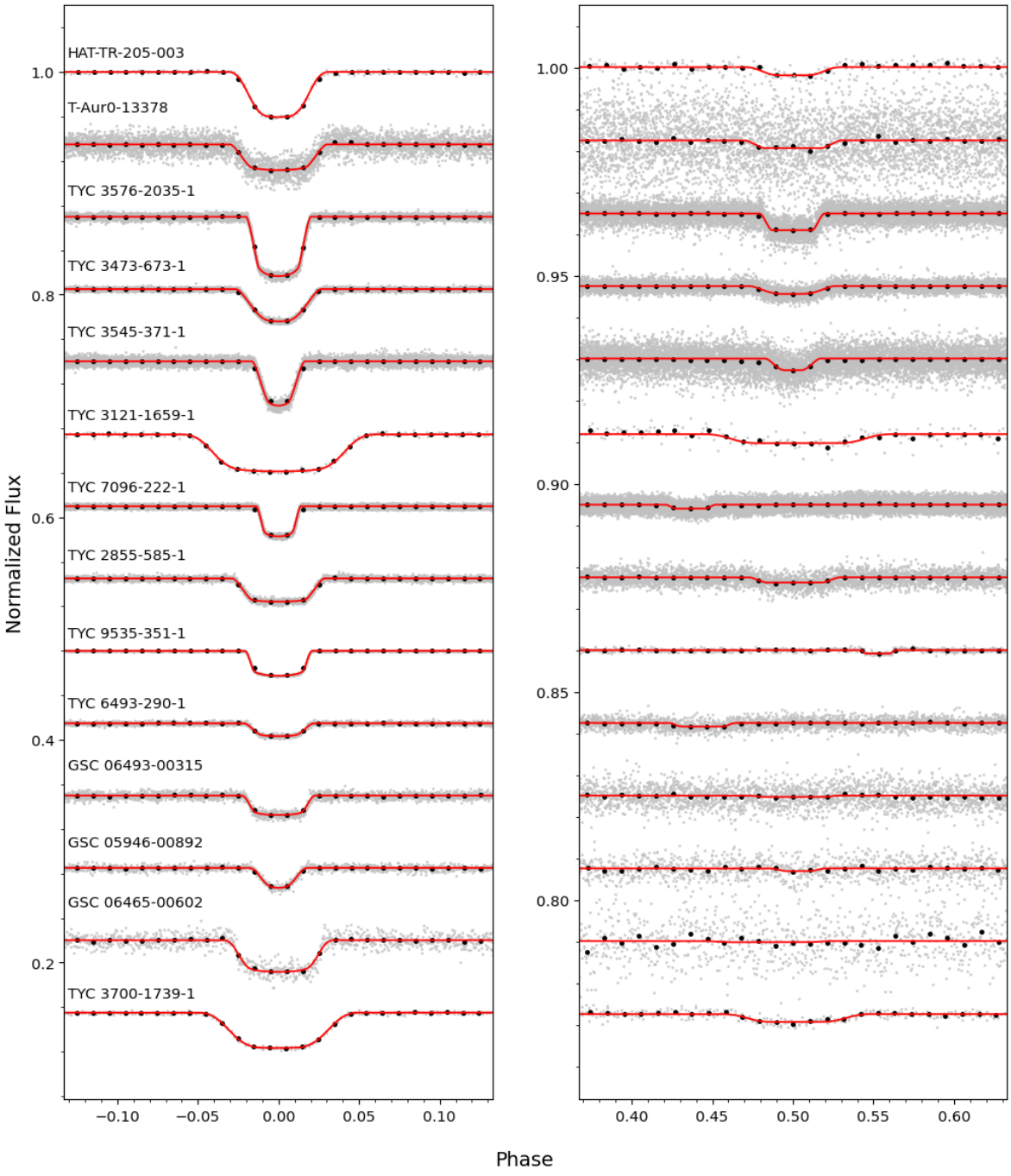

Figure 5.1: The TESS light curves for our targets around primary eclipse (left) and secondary eclipse (right) compared to the fitted model (lines). Binned data (black) is plotted over the raw (grey) data. The system TYC 2755-36-1 is not included because no TESS data are available for it.

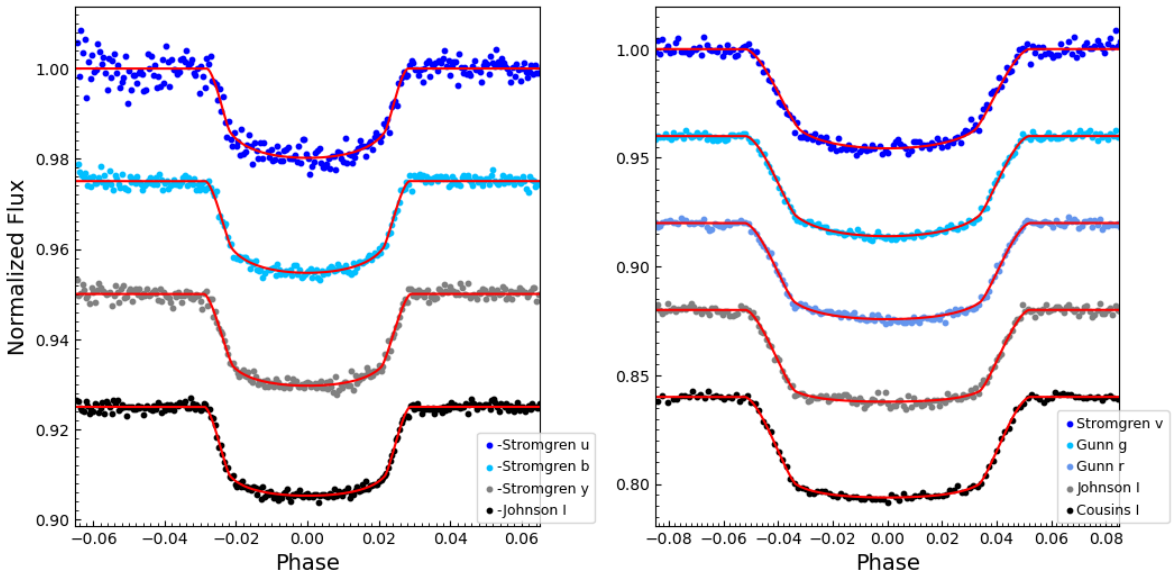

Figure 5.2: The ground-based light curves presented in this work for TYC 2755-36-1 (left) and TYC 3121-1659-1 (right). The filters are labelled in the legends. The red lines show the fitted models.

was also fitted to the observations outside transit and subtracted to shift the final light curve to zero differential magnitude. The timestamps were converted to the midpoint of the exposure on the $\mathrm{BJD_{TDB}}$ timescale (Eastman et al., 2010).

5.3 Analysis methods

5.3.1 Light and RV curve modelling

The light curves and published RVs were modelled using the JKTEBOP code (Southworth, 2012, 2013) after converting the fluxes and errors to magnitudes and converting the time stamps from Barycentric TESS Julian Day (BTJD) to BJD. The components of the binary systems were modelled as spheres under the assumption that distortion from tidal effects would be negligible in EBLMs. We investigated the validity of this assumption by quantifying the amount of distortion expected along the lines of cen-

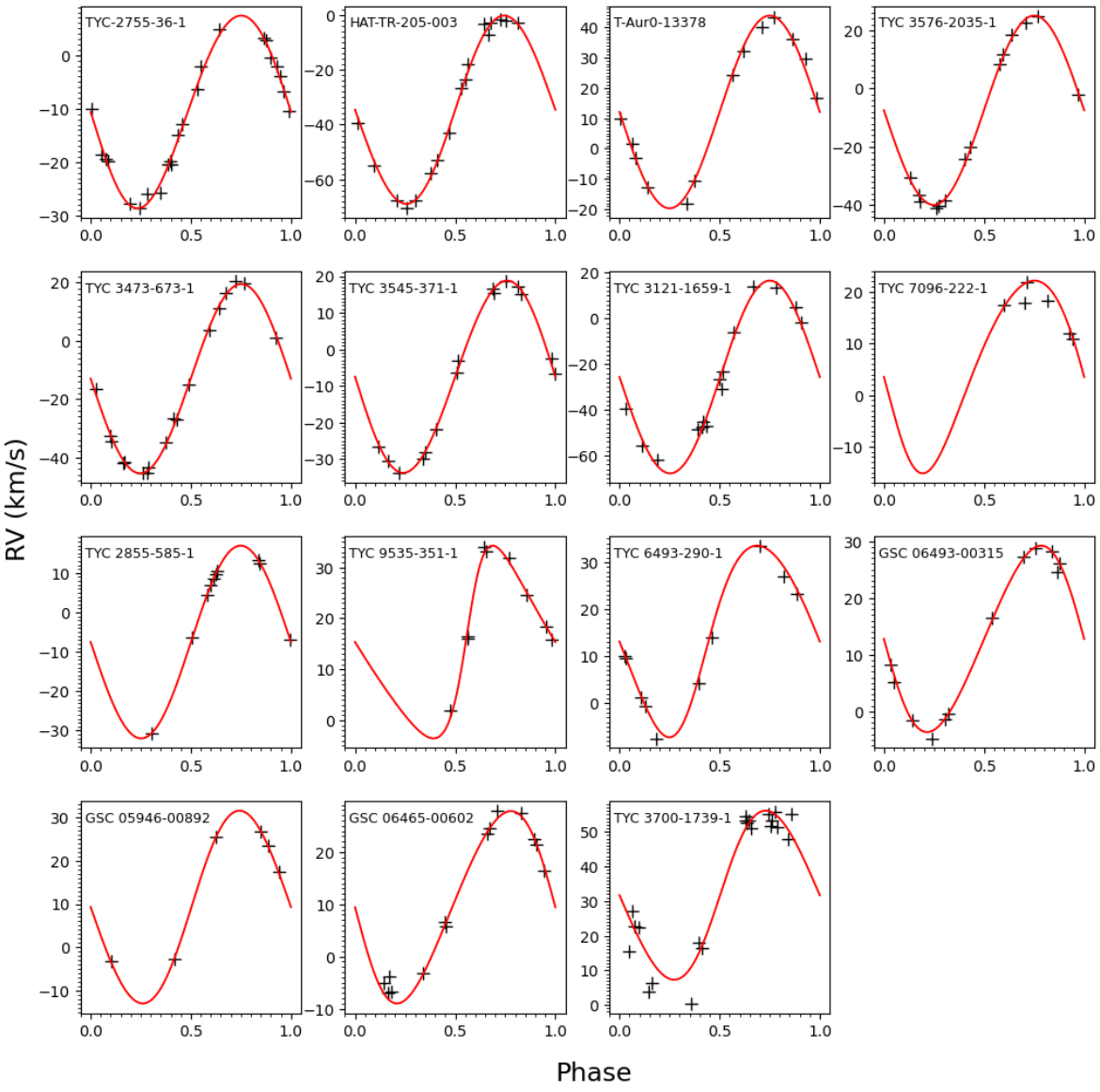

Figure 5.3: Fits to the RV data for each object. Object names are shown in the top left of each plot.

tres of the stars following Sterne (1941) and Beech (1985) and using the parameters derived in later sections. Assuming synchronous rotation, the average distortion expected among our list of targets is $\approx 0.36\%$. The average ratio of the uncertainty in the final radii values against the uncertainty expected from distortion is ≈ 35 with all but one object having a ratio of at least 9. For all but one of our targets, the expected deformation is therefore insignificant compared to the size of the uncertainty on the final radii measurement. For TYC 3121-1659-1, the distortion reaches a value of 1.6%. This is expected given the relatively larger value of r_1 for this object (see Table 5.4).

Parameters fitted for all targets with JKTEBOP were the period P, the ratio of the radii $k = R_2/R_1$, the inclination i, the sum of the radii normalised by the semi-major axis of the orbit, $r_1 + r_2$, the time of primary minimum T_0 and a magnitude scale factor. All targets were fitted for their surface brightness ratio J, except TYC 2755-36-1 for which only data for the primary eclipse is available so we assumed $J = 0$. The Poincaré elements, $e\cos\omega$ and $e\sin\omega$, where e is the orbital eccentricity and ω the argument of periastron, were also included for all targets. The quadratic limb darkening law was used to model limb darkening where as many coefficients were included in the fit as possible subject to the condition that their fitted values remained between 0 and 1. Where this condition was not satisfied, the values were taken from Claret (2017). A parameter to account for any contaminating light sources, L_3, was included as a fitted parameter but was only found to be needed for TYC 2855-585-1. For the remaining targets, we found that L_3 had either a negative value or a value smaller than its errorbar, so we fixed it at zero. Our ability to extract measurements of L_3 from the light curves is limited due to the shallowness of the secondary eclipses.

We included in our analysis all available published ground-based light curves that were well sampled, covered the full primary eclipse and were obtained with a $\gtrsim 1\,\mathrm{m}$ telescope. Data satisfying these criteria are available for TYC 2755-36-1, TYC 3576-2035-1, TYC 3473-673-1 and GSC 06465-00602. For the remaining objects, only the published reference time of primary minimum was included to constrain the orbital ephemeris, under the assumption of a constant orbital period. We ensured each was converted to $\mathrm{BJD_{TDB}}$. Combining the published RV measurements within the fits

allowed for the primary velocity semi-amplitude, K_1, and the systemic velocity, γ, to be included as free parameters and to further constrain P, T_0, the eccentricity e and argument of periastron ω. RV measurements published in HJD were converted to BJD using Wright & Eastman (2014). For ground-based data where photometry was obtained in more than one passband simultaneously, that with the highest quality was chosen to be fitted with the RVs.

The low sampling cadence for the LC data was accounted for using numerical integration implemented within JKTEBOP (Southworth, 2010). The model was evaluated at seven points evenly spaced within an 1800 s interval, and the average of these points was used to compare to the observed brightness measurement.

Errors in the fitted parameters were determined via both Monte Carlo and residual permutation algorithms (Southworth, 2008). The larger of the two errorbars was chosen for each parameter. For targets observed through more than one passband, a weighted average of the photometric parameters was taken. The resulting ephemerides and spectroscopic orbits are given in Table 5.3, and the photometric parameters in Table 5.4. The JKTEBOP fits to the TESS data are shown in Fig. 5.1, and for the ground-based data in Fig. 5.2. Fits to the RV measurements are shown in Fig. 5.3.

5.3.2 Physical properties

The physical properties of the systems were determined using the values of r_1, r_2, i, e, K_1 and P found above. This analysis also used measurements of $T_{\rm eff}$, as given in Table 5.1, as well as published values for the metallicity, if those values were measured from high resolution spectra, e.g., at least $R \sim 20000$. For cases where such a measurement is absent, we adopted [Fe/H] $= -0.1 \pm 0.2$ as a representative value in the solar neighbourhood (Haywood, 2001, their fig. 3). Table 5.2 presents the values for [Fe/H] for objects where we used the previously published value, as well as the spectrograph and resolution used to obtain the measurement.

Those values for $T_{\rm eff}$ in Table 5.1 are taken from the corresponding reference also given in that table when the analysis is deemed reliable, such as those determined

Table 5.2: Previously reported values for [Fe/H] for objects where the value was measured from spectral observations with $R \gtrsim 20000$. Also given is the spectrograph and resolution used to obtain the measurement.

Object	[Fe/H]	R	Spectrograph
TYC-7096-222-1	0.08 ± 0.13	60000	CORALIE
TYC-6493-290-1	-0.4 ± 0.1	24000	ANU 2.3m Échelle
GSC-06493-00315	-0.4 ± 0.1	24000	ANU 2.3m Échelle
GSC-05946-00892	-0.1 ± 0.2	24000	ANU 2.3m Échelle
GSC-06465-00602	-0.60 ± 0.06	24000	ANU 2.3m Échelle
TYC-3700-1739-1	-0.05 ± 0.17	32000	Tautenburg 2m Échelle

from high-resolution échelle spectra. In other cases, the $T_{\rm eff}$ values correspond to those calculated by us from a fit to the spectral energy distribution (SED), using the VOSA software (Bayo et al., 2008) to obtain photometric flux values as well as perform the fit. Values of the colour excess, $E(B-V)$, were determined using the STILISM tool (Lallement et al., 2018) and a value of $R_V = 3.1$ was used as the canonical value in the diffuse interstellar medium (Schlafly & Finkbeiner, 2011) resulting in extinction coefficients, A_V, to be included in the SED fit and allowed to adjust to within their error bar for each target. In most cases, the error was taken as half the grid step in the models that the χ^2 fit was calculated against and is 125 K in $T_{\rm eff}$. For TYC 2755-36-1 and HAT-TR-205-003 this value was increased to 200 K and 150 K, respectively, in order to remain consistent with *Gaia* and TESS predictions. An asterisk next to the quoted $T_{\rm eff}$ in Table 5.1 indicates that the value was determined via this SED fitting process.

The physical properties were then determined using an isochrone fitting method by Dr. John Taylor. For each object, we first estimated a suitable value of the velocity semi-amplitude of the secondary component (K_2) and then calculated the physical properties of the system. This initial value of K_2 was iteratively refined to maximise the agreement between the measured $T_{\rm eff}$ and calculated radius of the primary star, and the predictions of theoretical models for a given mass and [Fe/H]. This was done over a

grid of age values to determine the overall best mass and age for the system, and then over a set of five different sets of theoretical models (Southworth, 2009; Southworth, 2010). The model sets used were the Yonsei-Yale (Demarque et al., 2004), Teramo (Pietrinferni et al., 2004), VRSS (VandenBerg et al., 2006), Dartmouth (Dotter et al., 2008), and an extension to lower masses of the models from Claret (2004).

Random errors from the input parameters were propagated by perturbation. Systematic errors were quantified by calculating the largest difference in values for a given parameter between the results using the five sets of theoretical models. The resulting properties are given in Table 5.5 for the primary components and Table 5.6 for the secondary components of our target EBLMs.

We determined the $T_{\rm eff}$ value of each secondary star as follows. We interpolated a synthetic spectrum for the primary star using its $T_{\rm eff}$ and surface gravity, and the BT-Settl synthetic spectral grid from Allard et al. (2001). We then did the same for a grid of $T_{\rm eff}$ values for the secondary star covering 2600 K to 6000 K. All spectra were then convolved with the TESS passband response function from Ricker et al. (2015) and the predicted surface brightness ratio within the TESS passband was calculated by dividing the secondary star spectra by the primary star spectrum. The $T_{\rm eff}$ of the secondary star was then obtained by interpolating the grid of surface brightness ratios to the value measured from the light curve. Errors in the measured surface brightness ratio and primary star $T_{\rm eff}$ were propagated and added in quadrature. These calculations to derive $T_{\rm eff}$ values for the each of the secondary stars were also carried out by Dr. John Taylor.

We did not make use of any *Gaia* information in our analysis. This is because six of our objects have a renormalised unit weight error (RUWE) much larger than the maximum value of 1.4 for a reliable astrometric solution (Gaia Collaboration, 2021). However, we did cross-check our results against the distances obtained from simple inversion of the *Gaia* EDR3 parallax values. To do this we adopted the physical properties determined in this work, apparent magnitudes from Høg et al. (2000) and Skrutskie et al. (2006), interstellar extinction values from Lallement et al. (2018) and bolometric corrections from Girardi et al. (2002). We found good agreement in all cases,

but this is not a strong conclusion because of the significant correlation between $T_{\rm eff}$ and reddening, and the uncertainty of the JHK apparent magnitudes and passband definitions.

5.4 Results for each system

5.4.1 TYC 2755-36-1

TYC 2755-36-1 was observed by the HATNet (Hungarian-made Automatic Telescope Network) wide angle survey and identified as a planetary candidate by both Beatty et al. (2007) and Latham et al. (2009). Both studies reported the object to be an EB with a faint component following reconnaissance spectroscopy. The 23 RV measurements published by Latham et al. (2009) are identical to those obtained by Beatty et al. (2007). These measurements are presented in their table 1 and were utilised in the current study (Fig. 5.3).

Stellar parameters were also reported by both Beatty et al. (2007) and Latham et al. (2009) for TYC 2755-36-1 via cross correlation of the observed spectra against a library of synthetic spectra. A full characterisation of the system was performed by Beatty et al. (2007) using the assumption that the system is synchronised and combining their spectroscopic measurements with those derived from the modelling of follow-up light curves. The resulting masses and radii from their study can be found in Table 5.7 along with the previous literature estimations of these parameters for all other objects included in this work.

The radii reported by Beatty et al. (2007) for both components of TYC 2755-36-1 agree with our estimations within 1σ. The masses are larger by 19% (1.2σ) and 12% (1.2σ) for the primary and secondary, respectively. The previous authors report an M dwarf radius inflated by 11% while the current study finds that the magnitude of inflation is 5% when compared to the corresponding Baraffe et al. (2015) (BCAH15, hereafter) isochrone for its age estimation given in Table 5.5.

Table 5.3: The orbital ephemerides and spectroscopic orbital parameters for the objects studied in the current work. Quantities in brackets represent the uncertainties in the final digits of the preceding number.

Object	P (days)	T_0 ($\mathrm{BJD_{TDB}}$)	K_1 (km/s)	γ (km/s)	e	ω ($^\circ$)
TYC 2755-36-1	2.230728 (13)	55433.49613 (13)	18.28 ± 0.38	-9.91 ± 0.21	0.037 ± 0.016	131.5 ± 26.8
HAT-TR-205-003	2.179235216 (69)	58744.907830 (19)	34.48 ± 0.59	-34.54 ± 0.42	0.018 ± 0.022	270.2 ± 64.3
T-Aur0-13378	3.54176081 (49)	58820.744570 (62)	31.78 ± 0.71	12.09 ± 0.47	0.000 ± 0.000	0.0 ± 0.0
TYC 3576-2035-1	6.56016357 (28)	58702.610279 (71)	32.46 ± 0.33	-7.41 ± 0.27	0.003 ± 0.004	107.6 ± 79.0
TYC 3473-673-1	2.539880435 (95)	58945.441688 (45)	32.52 ± 0.38	-12.97 ± 0.25	0.008 ± 0.007	95.4 ± 73.4
TYC 3545-371-1	4.23382530 (21)	58715.411745 (10)	26.25 ± 0.26	-7.43 ± 0.22	0.023 ± 0.015	90.3 ± 1.2
TYC 3121-1659-1	1.184756213 (71)	58686.003373 (19)	42.21 ± 1.25	-25.81 ± 0.73	0.006 ± 0.019	321.3 ± 115.7
TYC 7096-222-1	8.95819901 (44)	58493.788560 (84)	18.62 ± 0.82	5.39 ± 2.97	0.134 ± 0.021	138.0 ± 9.7
TYC 2855-585-1	2.40590630 (11)	58792.98841 (11)	24.46 ± 0.10	-7.55 ± 0.07	0.005 ± 0.003	285.0 ± 10.2
TYC 9535-351-1	9.92610416 (55)	58663.10479 (14)	18.90 ± 0.50	13.86 ± 1.47	0.337 ± 0.025	283.5 ± 1.2
TYC 6493-290-1	4.68679718 (63)	58454.98281 (34)	20.36 ± 0.19	14.93 ± 0.98	0.131 ± 0.055	227.9 ± 46.0
GSC 06493-00315	3.636496 (13)	58454.82048 (66)	16.43 ± 0.10	12.78 ± 0.70	0.109 ± 0.049	89.6 ± 9.7
GSC 05946-00892	3.80408653 (53)	58483.00490 (46)	22.24 ± 0.16	9.20 ± 0.10	0.028 ± 0.006	280.2 ± 6.4
GSC 06465-00602	2.05180453 (54)	59175.066023 (55)	18.40 ± 0.71	9.85 ± 2.71	0.111 ± 0.088	102.3 ± 84.1
TYC 3700-1739-1	1.351204584 (48)	58800.808307 (13)	24.41 ± 1.01	31.61 ± 1.69	0.069 ± 0.055	272.8 ± 92.5

Table 5.4: Results of the JKTEBOP analysis for the objects studied in Chapter 5.

Object	r_1	r_2	Light ratio	k	i (°)	J	L_3
TYC 2755-36-1	0.166 ± 0.002	0.0218 ± 0.0004	–	0.1313 ± 0.0006	86.5 ± 0.4	0.0 fixed	0.0 fixed
HAT-TR-205-003	0.169 ± 0.007	0.0340 ± 0.0015	0.001964 ± 0.000423	0.2000 ± 0.0034	83.2 ± 0.8	0.056 ± 0.014	0.0 fixed
T-Aur0-13378	0.198 ± 0.010	0.0296 ± 0.0018	0.002154 ± 0.000243	0.1492 ± 0.0020	82.4 ± 1.0	0.108 ± 0.014	0.0 fixed
TYC 3576-2035-1	0.107 ± 0.0006	0.0233 ± 0.0002	0.004020 ± 0.000057	0.2182 ± 0.0005	88.2 ± 0.1	0.096 ± 0.029	0.0 fixed
TYC 3473-673-1	0.191 ± 0.001	0.0330 ± 0.0003	0.001904 ± 0.000042	0.1730 ± 0.0003	81.2 ± 0.1	0.068 ± 0.002	0.0 fixed
TYC 3545-371-1	0.109 ± 0.005	0.0216 ± 0.0014	0.002843 ± 0.000995	0.1984 ± 0.0247	85.4 ± 0.4	0.075 ± 0.004	0.0 fixed
TYC 3121-1659-1	0.282 ± 0.003	0.0559 ± 0.0006	0.002276 ± 0.000012	0.1983 ± 0.0008	85.3 ± 0.7	0.078 ± 0.013	0.0 fixed
TYC 7096-222-1	0.092 ± 0.003	0.0145 ± 0.0005	0.000936 ± 0.000050	0.1580 ± 0.0004	86.9 ± 0.2	0.041 ± 0.002	0.0 fixed
TYC 2855-585-1	0.179 ± 0.014	0.0287 ± 0.0025	0.001639 ± 0.000574	0.1607 ± 0.0264	83.7 ± 1.4	0.072 ± 0.004	0.22±0.20
TYC 9535-351-1	0.081 ± 0.002	0.0114 ± 0.0003	0.000838 ± 0.000063	0.1409 ± 0.0006	89.6 ± 0.3	0.045 ± 0.004	0.0 fixed
TYC 6493-290-1	0.149 ± 0.015	0.0160 ± 0.0016	0.000872 ± 0.000105	0.1079 ± 0.0010	84.0 ± 1.3	0.080 ± 0.010	0.0 fixed
GSC 06493-00315	0.130 ± 0.008	0.0161 ± 0.0010	0.000344 ± 0.000206	0.1244 ± 0.0010	89.9 ± 1.9	0.024 ± 0.014	0.0 fixed
GSC 05946-00892	0.127 ± 0.006	0.0175 ± 0.0010	0.000692 ± 0.000241	0.1379 ± 0.0025	84.1 ± 0.4	0.039 ± 0.013	0.0 fixed
GSC 06465-00602	0.161 ± 0.005	0.0199 ± 0.0007	0.000282 ± 0.000564	0.1264 ± 0.0007	90.0 ± 1.1	0.012 ± 0.024	0.0 fixed
TYC 3700-1739-1	0.262 ± 0.023	0.0468 ± 0.0040	0.001877 ± 0.000310	0.1784 ± 0.0015	79.8 ± 1.8	0.068 ± 0.012	0.0 fixed

Table 5.5: The physical properties determined in the current work for the primary stars. For these calculations we used the nominal physical constants and solar quantities defined by the IAU (Prša et al., 2016).

Object	M_1 ($M_\odot$)	R_1 ($R_\odot$)	$\log g_1$ (cgs)	ρ_1 ($\rho_\odot$)	Age (Gyr)
TYC 2755-36-1	1.241 ± 0.085	1.312 ± 0.038	4.296 ± 0.019	0.549 ± 0.030	$1.6^{+1.5}_{-0.6}$
HAT-TR-205-003	1.150 ± 0.074	1.343 ± 0.062	4.243 ± 0.037	0.475 ± 0.059	$3.2^{+1.6}_{-0.7}$
T-Aur0-13378	1.270 ± 0.071	2.26 ± 0.12	3.835 ± 0.045	0.111 ± 0.017	$1.9^{+1.0}_{-0.4}$
TYC 3576-2035-1	1.046 ± 0.061	1.767 ± 0.035	3.963 ± 0.013	0.189 ± 0.005	$6.8^{+1.4}_{-1.1}$
TYC 3473-673-1	1.161 ± 0.061	1.686 ± 0.033	4.050 ± 0.012	0.242 ± 0.008	$4.5^{+1.2}_{-0.3}$
TYC 3545-371-1	1.350 ± 0.069	1.283 ± 0.067	4.352 ± 0.045	0.640 ± 0.098	$0.2^{+0.5}_{-0.2}$
TYC 3121-1659-1	1.271 ± 0.063	1.545 ± 0.029	4.165 ± 0.012	0.345 ± 0.011	$2.4^{+0.7}_{-0.6}$
TYC 7096-222-1	1.67 ± 0.11	2.087 ± 0.083	4.022 ± 0.030	0.184 ± 0.018	$0.5^{+0.4}_{-0.2}$
TYC 2855-585-1	1.20 ± 0.11	1.51 ± 0.13	4.159 ± 0.069	0.348 ± 0.083	$2.9^{+1.9}_{-1.1}$
TYC 9535-351-1	1.263 ± 0.072	1.778 ± 0.055	4.040 ± 0.024	0.225 ± 0.017	$2.2^{+0.6}_{-0.6}$
TYC 6493-290-1	1.071 ± 0.078	1.90 ± 0.20	3.913 ± 0.088	0.157 ± 0.049	$4.6^{+2.1}_{-0.7}$
GSC 06493-00315	1.169 ± 0.087	1.416 ± 0.094	4.204 ± 0.055	0.412 ± 0.077	$2.6^{+1.8}_{-0.8}$
GSC 05946-00892	1.11 ± 0.11	1.423 ± 0.080	4.176 ± 0.043	0.384 ± 0.055	$4.6^{+3.0}_{-0.7}$
GSC 06465-00602	1.003 ± 0.053	1.26 ± 0.18	4.24 ± 0.13	0.51 ± 0.24	$4.9^{+1.9}_{-1.3}$
TYC 3700-1739-1	1.53 ± 0.12	1.61 ± 0.15	4.208 ± 0.077	0.364 ± 0.098	$0.4^{+0.5}_{-0.2}$

The M dwarf in this system is the densest and has the smallest radius out of all objects included in the current study. It has the second largest surface gravity and is the second least massive. There are no spots identified in the light curve of the host system, and this would oppose the hypothesis that enhanced magnetic fields due to faster rotation induced by synchronisation are the cause for inflation (Beatty et al., 2007).

5.4.2 HAT-TR-205-003

HAT-TR-205-003 was also observed by the HATNet survey and identified as a planetary transit candidate by Latham et al. (2009). A spectroscopic reconnaissance confirmed the nature of the companion to be stellar. Seventeen RV measurements were obtained from single-order échelle spectra and used to obtain a preliminary orbital solution.

Table 5.6: Same as Table 5.5 but for the secondary components.

Object	M_2 ($M_\odot$)	R_2 ($R_\odot$)	$\log g_2$ (cgs)	ρ_2 ($\rho_\odot$)	a ($R_\odot$)	$T_{\rm eff,2}$ (K)
TYC 2755-36-1	0.139 ± 0.007	0.172 ± 0.005	5.111 ± 0.019	29.1 ± 1.8	8.00 ± 0.17	–
HAT-TR-205-003	0.267 ± 0.012	0.270 ± 0.013	5.001 ± 0.039	14.4 ± 1.9	7.95 ± 0.16	3243 ± 184
T-Aur0-13378	0.312 ± 0.013	0.337 ± 0.021	4.876 ± 0.054	8.6 ± 1.6	11.40 ± 0.20	3808 ± 128
TYC 3576-2035-1	0.358 ± 0.013	0.385 ± 0.007	4.822 ± 0.009	6.7 ± 0.2	16.52 ± 0.29	3440 ± 235
TYC 3473-673-1	0.267 ± 0.009	0.291 ± 0.005	4.937 ± 0.009	11.5 ± 0.4	8.83 ± 0.15	3335 ± 69
TYC 3545-371-1	0.277 ± 0.009	0.316 ± 0.019	4.880 ± 0.051	9.3 ± 1.6	12.96 ± 0.19	3614 ± 77
TYC 3121-1659-1	0.282 ± 0.013	0.303 ± 0.006	4.925 ± 0.016	10.7 ± 0.5	5.46 ± 0.10	3546 ± 141
TYC 7096-222-1	0.281 ± 0.018	0.329 ± 0.013	4.853 ± 0.036	8.4 ± 1.0	22.69 ± 0.50	3347 ± 136
TYC 2855-585-1	0.193 ± 0.011	0.242 ± 0.022	4.956 ± 0.078	14.5 ± 3.9	8.44 ± 0.24	3449 ± 137
TYC 9535-351-1	0.231 ± 0.013	0.251 ± 0.006	5.001 ± 0.022	15.5 ± 1.0	22.22 ± 0.38	3191 ± 81
TYC 6493-290-1	0.186 ± 0.009	0.204 ± 0.021	5.090 ± 0.090	23.4 ± 7.3	12.72 ± 0.28	3483 ± 126
GSC 06493-00315	0.141 ± 0.007	0.175 ± 0.012	5.100 ± 0.055	27.9 ± 5.3	10.89 ± 0.25	2859 ± 343
GSC 05946-00892	0.196 ± 0.012	0.196 ± 0.013	5.145 ± 0.050	27.6 ± 4.8	11.21 ± 0.33	3003 ± 226
GSC 06465-00602	0.118 ± 0.006	0.199 ± 0.029	4.911 ± 0.137	15.9 ± 7.4	7.06 ± 0.15	2551 ± 593
TYC 3700-1739-1	0.184 ± 0.012	0.288 ± 0.026	4.784 ± 0.078	8.2 ± 2.2	6.16 ± 0.16	3646 ± 190

Table 5.7: Results from previous authors. For TYC 7096-222-1, the quoted value for M_2 is in the middle of the range off possible values reported by the previous authors and the given uncertainty satisfies both ends of this range.

Object	M_1 ($\mathrm{M}_\odot$)	M_2 ($\mathrm{M}_\odot$)	R_1 ($\mathrm{R}_\odot$)	R_2 ($\mathrm{R}_\odot$)
TYC 2755-36-1	1.04 ± 0.14	0.124 ± 0.011	1.28 ± 0.04	0.169 ± 0.006
T-Aur0-13378	1.60 ± 0.13	0.37 ± 0.03	2.40 ± 0.10	0.37 ± 0.02
TYC 3576-2035-1	0.91 ± 0.15	0.345 ± 0.034	1.63 ± 0.08	0.360 ± 0.017
TYC 3473-673-1	1.49 ± 0.07	0.315 ± 0.010	1.83 ± 0.03	0.325 ± 0.005
TYC 3545-371-1	0.77 ± 0.08	0.198 ± 0.012	1.14 ± 0.03	0.238 ± 0.007
TYC 3121-1659-1	0.95 ± 0.11	0.240 ± 0.019	1.36 ± 0.05	0.265 ± 0.010
TYC 7096-222-1	1.735 ± 0.054	0.435 ± 0.165	1.662 ± 0.092	0.263 ± 0.046
TYC 2855-585-1	1.26 ± 0.11	0.20 ± 0.02	1.30 ± 0.05	0.17 ± 0.01
TYC 6493-290-1	1.10 ± 0.07	0.17 ± 0.01	1.70 ± 0.09	0.18 ± 0.01
GSC 06493-00315	1.1 ± 0.1	0.132 ± 0.01	1.20 ± 0.05	0.154 ± 0.007
GSC 05946-00892	1.2 ± 0.1	0.20 ± 0.02	1.58 ± 0.06	0.22 ± 0.01
GSC 06465-00602	0.97 ± 0.06	0.110 ± 0.006	1.22 ± 0.03	0.147 ± 0.004
TYC 3700-1739-1	1.493 ± 0.073	0.188 ± 0.014	1.474 ± 0.040	0.234 ± 0.009

These RV measurements are presented in table 2 of their paper.

By cross-correlating the observed spectra against a library of synthetic spectra, Latham et al. (2009) were able to derive estimates for the $T_{\rm eff}$, $v \sin i$ and $\log(g)$ assuming solar metallicity, but aside from a preliminary estimation of R_1, no further characterization of the object was carried out as their study concentrated on candidate transiting planets.

Our results are the first measurements of the fundamental parameters for this object. The radius of the companion in this system, $R_2 = 0.270 \pm 0.013\,\mathrm{R}_\odot$, is found to agree with the BCAH15 theoretical predictions for its mass ($M_2 = 0.267 \pm 0.012\,\mathrm{M}_\odot$) and age ($3.2^{+1.6}_{-0.7}$ Gyr).

5.4.3 T-Aur0-13378

The transit events for T-Aur0-13378, as well as the objects described in the following four subsections, were detected by the Trans-Atlantic Exoplanet Survey (TrES) and

the companion in each was confirmed to be stellar by Fernandez et al. (2009) via a spectroscopic reconnaissance. Thirteen RVs were measured for each object from single-order échelle spectra along with estimations for $T_{\rm eff}$, $v \sin i$ and $\log(g)$. The RVs are presented in their tables 2–6. The stellar parameters were derived for four fixed metallicities, -1, -0.5, 0.0 and $+0.5$ dex, resulting in four sets of parameters. Binary parameters were obtained from the analysis of follow-up light curves.

Combining binary and spectroscopic parameters allowed for the derivation of physical parameters via isochrone fitting following the procedure of Torres et al. (2008). Physical parameters were also derived independently by invoking the assumption that the orbits are synchronised. Both methods were carried out for each set of atmospheric parameters corresponding to the four fixed metallicities described above. The expectation was that one of the fixed metallicities would yield agreeable solutions between the two methods.

For T-Aur0-13378, no good solution was found for any of the input metallicities, opposing the idea that the system is synchronised, so the results from isochrone fitting with solar abundance were adopted. It was necessary to fix $e = 0$ in our study to obtain the optimum solution and this indicates that the system is at least older than the circularisation timescale. However, Fernandez et al. (2009) calculated the ratio of the orbital and rotational angular momentum, α, for the objects in their study and for each of them, this resulted in a value larger than 70, which means that the timescales for synchronisation and alignment are expected to be shorter than that for circularisation.

Fernandez et al. (2009) hypothesise a possible reason for the system not being synchronised but circularised is that the primary component in the system is evolved. As the primary component expands, its rotational velocity decreases in order to conserve angular momentum and this process may dominate over tidal forces acting to synchronize the system. The current results support this hypothesis with small values for the surface gravity and density for a relatively massive star among Table 5.5, along with the relatively large surface brightness ratio reported in Table 5.4.

The masses derived here are smaller than those reported by the previous authors,

and given in Table 5.7, by 21% (2.2σ) and 16% (1.8σ) for the primary and secondary components, respectively. The estimated radius for the primary component is consistent between both studies within 1σ but our measurement of the M dwarf radius is 9% (1.1σ) smaller. A marginal inconsistency in the radius of the M dwarf was observed by Fernandez et al. (2009) when compared to the theory in the direction of inflation. The current results demonstrate inflation by 12% relative to the BCAH15 isochrone for its age.

5.4.4 TYC 3576-2035-1

The study by Fernandez et al. (2009) also included the system TYC 3576-2035-1. For this system, there was a metallicity range where the two methods of characterization agreed and a value of [Fe/H] $= -0.5 \pm 0.2$ dex was adopted. For systems where an acceptable solution was found, Fernandez et al. (2009) adopted the one derived via the assumption of synchronisation.

The primary star and M dwarf masses from that solution are both in agreement with the parameters derived here within 1σ. Our estimations for the radii are 8% (1.6σ) and 7% (1.4σ) larger compared to those of Fernandez et al. (2009) for R_1 and R_2, respectively. The previous authors find their estimation for the radius of the M dwarf to be marginally inflated compared to isochrones. We observe a radius 11% larger than the BCAH15 theoretical prediction for its age.

The secondary eclipse of about 0.0025 mag deep is clearly visible and, combined with the good phase coverage in the RV measurements, provides a strong constraint on the eccentricity for this system of $e = 0.003 \pm 0.004$ (Table 5.3). This is consistent with a circular orbit and shows that circularisation timescales have been satisfied by the age of this system. Given the value of $\alpha > 70$ reported by Fernandez et al. (2009), the system is expected to be synchronised.

As Fernandez et al. (2009) state, synchronisation is not always guaranteed when evidence is strong (e.g, Pont et al. 2006) and the consistency between their synchronised and model-dependent solutions is ultimately dependent on the adopted atmospheric

parameters. The disagreement between our results for the radii and those of the synchronised solution reported by Fernandez et al. (2009) may therefore be explained by the difference in metal abundance and $T_{\rm eff}$ adopted between the studies.

5.4.5 TYC 3473-673-1

For TYC 3473-673-1, Fernandez et al. (2009) deduced a metallicity of [Fe/H] = 0.5±0.2 dex along with the parameters corresponding to a synchronised orbit. The primary and secondary masses derived here are 22% (3.5σ) and 15% (3.6σ) smaller compared to the values derived by Fernandez et al. (2009) while the radii are 8% (3.2σ) and 10% (4.8σ) smaller.

Again, good phase coverage in RV measurements and a visible secondary eclipse leads to a well-constrained orbit for this system with $e = 0.008 \pm 0.007$. This is consistent with a circular orbit (Lucy & Sweeney, 1971), so the assumption of synchronisation invoked by Fernandez et al. (2009) is valid given $\alpha > 70$. The arguments explained in the previous subsection apply and may explain the disagreement in the resulting parameters of the two studies. The finding that the M dwarf is inflated compared to models is, however, in agreement with our findings, where we find that its radius is 7% larger than the BCAH15 predictions.

5.4.6 TYC 3545-371-1

A solution corresponding to a synchronised orbit was adopted by Fernandez et al. (2009) for TYC 3545-371-1 on the basis that the resulting parameters agreed with those from isochrone fitting for a metallicity of [Fe/H] $= -0.5 \pm 0.2$ dex. Our results are larger by 75% (5.5σ) and 40% (5.3σ) in mass and 13% (2.0σ) and 33% (3.9σ) in radius for the primary and secondary, respectively. These are large discrepancies and are probably caused by differences in the assumed $T_{\rm eff}$ values between the two studies. We adopted a $T_{\rm eff}$ value 756 K hotter than that of the model-dependent solution derived by Fernandez

et al. (2009), which matched the synchronised solution that they adopted. Also, the difference in metal abundance is 0.5 dex.

Their result for R_2 was found to disagree within error with theoretical predictions in the direction of radius inflation. The prediction here is that the M dwarf radius is inflated compared to theory for a pre-MS age of $\sim$0.2 Gyr (reported in Table 5.5). The error bar for the age estimation of this object, however, spans the entire pre-main-sequence; it is therefore unclear how reliably the inflation status of this star can be determined given the size of the variation in the predicted radius over the lower range of its age uncertainty. This is shown by comparing the position of the 0.05 Gyr and 0.3 Gyr isochrones in Fig. 5.5.

A significant value for third light of $L_3 = 0.37 \pm 0.13$ was found in our first analysis. However, this leads to an unphysically small r_1 so we instead present a solution with $L_3 = 0$. The $T_{\rm eff}$ we use has a noticeable effect on the age estimate for this target – a lower $T_{\rm eff}$ of 6500 K gives a solution with a larger age of $1.5^{+0.5}_{-0.6}$ Gyr and a significantly lower M_1 of $1.29 \pm 0.06\,{\rm M}_\odot$. A high-quality spectrum of this target would be useful for checking and confirming its $T_{\rm eff}$.

5.4.7 TYC 3121-1659-1

The fifth and final object studied by Fernandez et al. (2009) is TYC 3121-1659-1. A synchronised solution, matched to a model-dependent solution with [Fe/H] $= -0.5 \pm 0.2$ dex, was adopted. Our estimates of the fundamental parameters for this object were again in conflict with those derived by Fernandez et al. (2009). For the primary and secondary, this amounted to a 34% (2.5σ) and 18% (1.8σ) increase in mass accompanied by a 14% (3.2σ) and 14% (3.3σ) increase in radius. The previous authors observed the M dwarf radius to be marginally inflated, in agreement with our findings that its radius is 8.2% inflated compared to the BCAH15 models. The results obtained by Fernandez et al. (2009) are given in Table 5.7 for comparison. We also calculated the properties of the system after accounting for the distortion of the primary star and found that they changed by much less than their errorbars. We therefore elected to present the results

Table 5.8: Comparison of the results obtained for TYC 3121-1659-1.

Passband	r_1	r_2	k	i (°)
TESS	0.296 ± 0.018	0.0522 ± 0.0040	0.176 ± 0.003	81.8 ± 2.6
Cousins I	0.280 ± 0.004	0.0571 ± 0.0012	0.204 ± 0.001	86.9 ± 2.4
Gunn r	0.283 ± 0.005	0.0554 ± 0.0012	0.196 ± 0.002	86.5 ± 1.8
Gunn g	0.282 ± 0.005	0.0557 ± 0.0013	0.198 ± 0.002	86.2 ± 1.6
Johnson i	0.281 ± 0.005	0.0553 ± 0.0011	0.197 ± 0.002	86.5 ± 1.7
Strömgren v	0.290 ± 0.008	0.0578 ± 0.0020	0.199 ± 0.003	83.5 ± 1.5
Adopted	0.282 ± 0.003	0.0559 ± 0.0006	0.198 ± 0.001	85.3 ± 0.7

obtained without accounting for distortion, for consistency with the other objects in the current work.

For this object, our ground-based light curves (Section 5.2) were used in the photometric analysis. Table 5.8 shows the results from the different light curves for the photometric parameters. The resulting values for i and k are significantly smaller from the TESS band compared to the other passbands. This may be due to the combined effect of the under-sampling of positions of contact across the primary eclipse from the TESS 30-minute cadence mode, as well as some third light being collected in the larger TESS pixels. An alternative explanation for the inclination being different is that the orbital plane has undergone precession due to exterior forcing, such as a third body. However, since the radius ratio is also affected, the former explanation is more likely.

5.4.8 TYC 7096-222-1

This object was identified as an EB using photometry collected by WASP-South and was characterised by Bentley et al. (2009). RVs were derived from grating spectra, and stellar parameters of the primary were determined from synthetic spectral fits to high-resolution échelle spectra ($R \sim 60000$). Their value for [Fe/H] of 0.08 ± 0.13 was adopted in the current work.

By combining the results from their spectral and light curve analysis, Bentley

et al. (2009) derived full system parameters following the results of the primary mass, which was obtained from isochrone fitting. The mass of the secondary was found to depend on the eccentricity, which was not well constrained by the available RVs. Bentley et al. (2009) obtained limiting values of $0.29 \pm 0.02\,\mathrm{M}_\odot$ for $e = 0$, and $0.54 \pm 0.06\,\mathrm{M}_\odot$ for $e = 0.75$.

Our analysis is able to rectify this issue because the secondary eclipse is detectable in the TESS observations. We find a significant eccentricity of $e = 0.134 \pm 0.021$. Our estimate of $M_2 = 0.281 \pm 0.018\,\mathrm{M}_\odot$ agrees with the value quoted by Bentley et al. (2009) for an orbit of zero or modest eccentricity while our estimate for M_1 is also in agreement within 1σ. The primary and secondary radii derived here are both 25% larger than those calculated by Bentley et al. (2009), corresponding to 3.4σ and 1.4σ, respectively.

Bentley et al. (2009) find their estimation for the M dwarf radius to agree with theoretical predictions. We find that the system is inflated by 19.3%, which is comparable to the 25% increase in our R_2 compared to Bentley et al.'s value, explaining the different conclusions regarding the object's inflation status.

The primary star is of approximately A8/F0 spectral type and such stars are expected to have rotational velocities of $\approx 200\,\mathrm{km\,s^{-1}}$ (Gray, 2005). Bentley et al. (2009) suggest that the object is a fairly typical Am star given its relatively slow rotation ($v \sin i = 35 \pm 0.5\,\mathrm{km\,s^{-1}}$); Am stars are thought to have been spun down by a companion. The previous authors determine that the rotation of the primary is still larger than that of the secondary, showing that the synchronisation process is ongoing, suggesting an upper limit to the age of the system of ≈ 0.92 Gyr, calculated as the synchronisation timescale by Bentley et al. (2009). The current age estimation of $0.5^{+0.4}_{-0.2}$ Gyr supports these statements. It is also noted that the newly derived estimate for the eccentricity shows that circularisation time-scales are also yet to be satisfied. This also supports our young age estimate for this system.

5.4.9 TYC 2855-585-1

Koo et al. (2012) identified transit-like variations in the photometric data of Lee et al. (2008) for the object TYC 2855-585-1. High-resolution multi-epoch échelle spectra were obtained from which six RVs were derived. Follow-up photometry was modelled and the absolute dimensions were computed by applying the photometric and spectroscopic measurements to the mass–radius and mass–$T_{\rm eff}$ relations for EBs from Southworth (2009).

The current estimations for the masses of the components agree with those by Koo et al. (2012) within 1σ but the radii are 16% (1.5σ) and 42% (3.0σ) larger for the primary and secondary, respectively. There was no discussion of the system parameters in the context of the radius discrepancy in low mass stars by Koo et al. (2012), but here we find that the radius is 14.6% inflated compared to its corresponding BCAH15 isochrone.

This object is the only system where we did not fix third light at zero. We find a value of $L_3 = 0.22 \pm 0.20$, which is not significant and has little effect on the results.

5.4.10 TYC 9535-351-1

TYC 9535-351-1 was identified by Crouzet et al. (2012) and Wang et al. (2014) as a potential planetary candidate. Follow-up RV observations were conducted by both authors and the RVs derived confirmed the object to be an EB in both cases. Five RV measurements were provided to us by Wang et al. (2014) and four were obtained from Crouzet et al. (2012).

The current study is the first time that a full characterization has been performed for the object and as such contributes another M dwarf with precise mass and radius measurements to the literature. The orbit for this system is the most eccentric in this study, with $e = 0.337 \pm 0.025$. We find that the system is 4.3% inflated compared to the BCAH15 isochrone for its mass and age given in Tables 5.6 and 5.5, respectively.

5.4.11 TYC 6493-290-1

TYC 6493-290-1 was identified from photometric observations by the HATSouth global network and characterised by Zhou et al. (2014). Spectroscopic analysis yielded ten RVs as well as atmospheric parameters of the primary. A global fit to the RVs and available light curves was performed simultaneously. The masses and radii of the components were derived at each iteration by combining the assumption of synchronisation with an isochrone fitting method. For TYC 6493-290-1, their photometric follow-up data consisted of only a partial primary eclipse and so is heavily reliant on the discovery data.

Our estimation for the primary mass agrees with the estimation from Zhou et al. (2014) within 1σ but our value for the M dwarf mass is 9% (1.2σ) larger. The radii predictions between the two studies for both components in this system are in agreement within 1σ. However, a comparison of our values to those of Zhou et al. (2014) is limited by the precision of the published values, so the discussion of the agreement in radii is based on rounding ours to the same precision. Zhou et al. (2014) find the radius of the M dwarf to agree with theoretical predictions, as do we. We find the system to be eccentric, $e = 0.131 \pm 0.055$, with an estimated age of ≈ 4.6 Gyr.

5.4.12 GSC 06493-00315

The study by Zhou et al. (2014) also included the system GSC 06493-00315. The identification and characterization of the object were carried out in the same way as for TYC 6493-290-1. For this object, they obtained 12 RV measurements but no follow-up light curves. The characterization was thus reliant on the discovery data alone.

Our results for the masses of the components are in agreement with those of Zhou et al. (2014) within 1σ but our radius measurements are 18% (2σ) and 14% (1.5σ) larger for the primary and secondary, respectively. Again, we find a marginally significant eccentricity, $e = 0.109 \pm 0.049$, which means the assumption of synchronisation (Zhou et al., 2014) is questionable. Zhou et al. (2014) found their measured R_2 to agree with

theoretical models within the uncertainty. Our results confirm this.

5.4.13 GSC 05946-00892

GSC 05946-00892 is another object that was previously characterised in the study by Zhou et al. (2014), who obtained six RV measurements. Excellent agreement is found between their estimations and our measurements of the masses of the components, amounting to less than 0.3σ for the secondary. Our radii are smaller by 10% (1.6σ) and 11% (1.5σ). Zhou et al. (2014) derived and adopted a chemical abundance consistent with solar, [Fe/H] $= -0.1 \pm 0.2$ dex, which is in agreement with our approach.

Zhou et al. (2014) found that R_2 agrees with theoretical models to within its errorbar. We find that the R_2 value is 8.6% lower than the predicted value from the BCAH15 isochrones. Whilst the error bars of the R_2 values from each study encompass the other, the sum of the uncertainties is $\approx 11\%$ so is larger than the size of the under-inflation observed in the current study.

5.4.14 GSC 06465-00602

The fourth and final object characterised by Zhou et al. (2014) is GSC 06465-00602, for which they obtained 14 RV measurements. Our measurement for the M dwarf radius is the only one that differs with that found by Zhou et al. (2014), and by an amount of 35% (1.8σ); all other values are in agreement within 1σ. Zhou et al. (2014) found that their radius estimation for the secondary is inflated by $\approx 13\%$ when compared to theoretical models. We find that the M dwarf is inflated by 39%. Looking at Fig. 5.5, the M dwarf is seen to lie on the 0.1 Gyr isochrone.

The reported age in Table 5.6 is estimated as $4.9^{+1.9}_{-1.3}$ Gyr on the MS but an alternative solution that we derived, assuming solar metallicity, yields an age estimation with a lower boundary of the uncertainty that spans the pre-MS, where contraction is ongoing. This scenario would suggest that the location of the object in Fig. 5.5 relative to the 0.1 Gyr isochrone might be correct, in which case the M dwarf is not inflated.

This may be important given the unusually low metallicity of [Fe/H] $= -0.6 \pm 0.06$ reported by Zhou et al. (2015) that was also adopted in our final solution.

The secondary component of this system has the smallest mass out of all objects included in the current study as well as the smallest surface brightness ratio. We find a marginally significant eccentricity for this system of $e = 0.111 \pm 0.088$, so the assumption of synchronisation invoked by Zhou et al. (2014) may not be valid.

5.4.15 TYC 3700-1739-1

TYC 3700-1739-1 was detected in the Berlin Exoplanet Search Telescope (BEST) and Tautenburg Exoplanet Search Telescope (TEST) surveys as an exoplanetary candidate and the object was published as an uncharacterised Algol type by Pasternacki et al. (2011) after its planetary status was deemed false. Eigmüller et al. (2016) later combined the data from both surveys in their study of the binary star system. Spectroscopic follow-up observations were performed resulting in 21 échelle spectra and RV measurements. A simultaneous fit to the RVs and photometric data from the two surveys was performed and the resulting binary parameters are presented in their table 4. By co-adding the individual observations corrected for their orbital motion, they were able to obtain a high-S/N spectrum which was used to derive the stellar parameters of the primary component. Full system parameters were derived via isochrones in combination with the stellar parameters of the primary and 2MASS apparent magnitudes. The resulting parameters are in agreement with our findings to within 1σ except for R_2, where our estimation is 23% larger, corresponding to 2.0σ.

Comparisons to theoretical models by the previous authors indicate that the secondary has an inflated radius even when correcting the isochrones for 5% of the discrepancy observed among low-mass stars. This might be due to the fact that the system is young; Eigmüller et al. (2016) estimate a synchronisation factor of $P_{\rm rot}/P_{\rm orb} = 0.43 \pm 0.05$ leading to an upper limit to the age of this system of 120–250 Myr via synchronisation timescales. Those authors also derive a statistically insignificant value for the eccentricity, $e = 0.070 \pm 0.063$, in agreement with our value (Table 5.3). This

suggests that the system is at least older than the time taken to circularise and, coupled with the upper limit suggested above, tightly constrains its age.

This upper limit on the age of the system is encompassed by the uncertainty in the current age estimation of $0.4\,^{+0.5}_{-0.2}$. The current study estimates that the M dwarf is 41% inflated compared to a 0.3 Gyr BCAH15 isochrone. This value is suspiciously large. Looking at Fig. 5.5, we see that the BCAH15 isochrones predict a rapid phase of contraction from 0.05 Gyr to 0.3 Gyr. Lowering the current age estimation within its uncertainty would account for much of the 41% inflation as well as obey the upper age limit suggested above. Then, given the size of the uncertainty on the M dwarf's age about a phase of such rapid contraction means that the inflation status of this object can not be reliably discerned, while the evidence does suggest a younger age and a lesser amount of inflation. Further support that the system is young is also provided by the overestimate of the M dwarf $T_{\rm eff}$ compared to the models (see Fig. 5.5), since radius inflation is commonly observed together with a lower $T_{\rm eff}$.

5.5 Discussion

We have characterised 15 EBLM stars using new light curves and published RVs. We used light curves from the TESS mission for 14 of them, and our own high-precision multi-band ground-based light curves for two of them. Two of the EBLMs had not previously been analysed in detail so our results represent the first measurements of their physical properties. Regarding those that were previously characterised, the precision in 19 of the 26 masses has been improved. Although the overall precision in the radius measurements from both studies were comparable ($\sim 3\%$), only 8 of the 26 radii have improved in precision, despite the much better data available, which suggests that some of the published errorbars are underestimated.

In order to convert the light curve and RV results into the physical parameters of the two stars, we needed a value for the metal abundance of each system. We have assumed a value representative of the solar neighbourhood in all cases as these are

nearby stars, except where the previously published value was measured from high resolution spectroscopy. In the latter case, we deemed the result reliable and adopted its value. Metallicity values were published for some of the other objects, but were either derived from low-resolution spectra or have large uncertainties.

Revised metallicity measurements from high-resolution and high-S/N échelle spectra would be valuable in most cases. Inaccuracies in the adopted metallicity leads to inaccuracies in the stellar models used in determining the physical parameters, and adds further uncertainty to the systematic uncertainty already inherent to the model-dependent results. See Southworth (2009) for a discussion of the nature in which systematic uncertainties propagate into the resulting parameters. Reliable estimations for $T_{\rm eff}$ could also be derived from such spectra. While the choice of metallicity affects the model used in each iteration, the choice of $T_{\rm eff}$ affects the best-matching solution that is returned because the solution is compared to the $T_{\rm eff}$ (and calculated radius) at each iteration. It is therefore important that this value is accurate such that the final best-fitting match is indeed that which corresponds to the true system parameters.

We find that in the absence of such measurements for $T_{\rm eff}$ and [Fe/H], the detection of the secondary eclipse as well as the use of high-precision space photometry still allows for significantly increased accuracy and reliability of the measured properties. This is especially the case for objects whose previous estimates for eccentricity were vague, e.g. TYC 7096-222-1. The literature value of [Fe/H] for this system, which we adopted, was also derived from the highest resolution échelle spectra among our targets, along with a value for $T_{\rm eff}$. The resulting parameters reported in Tables 5.5 and 5.6 for this object may therefore be considered the most reliable.

Reliability as well as precision in the measurement of the fundamental properties of M dwarfs is important in order to address uncertainties surrounding the interior physics governing the evolution of them. Fig. 5.5 displays the objects plotted in the mass-radius plane along with all M dwarfs with radii previously determined to better than 10% as catalogued by Parsons et al. (2018). The figure also displays BCAH15 isochrones for 0.05, 0.1, 0.3 Gyr and 10 Gyr. Notice the rapid contraction between 0.05 and 0.3 Gyr as the model evolves toward the main sequence. In the main sequence,

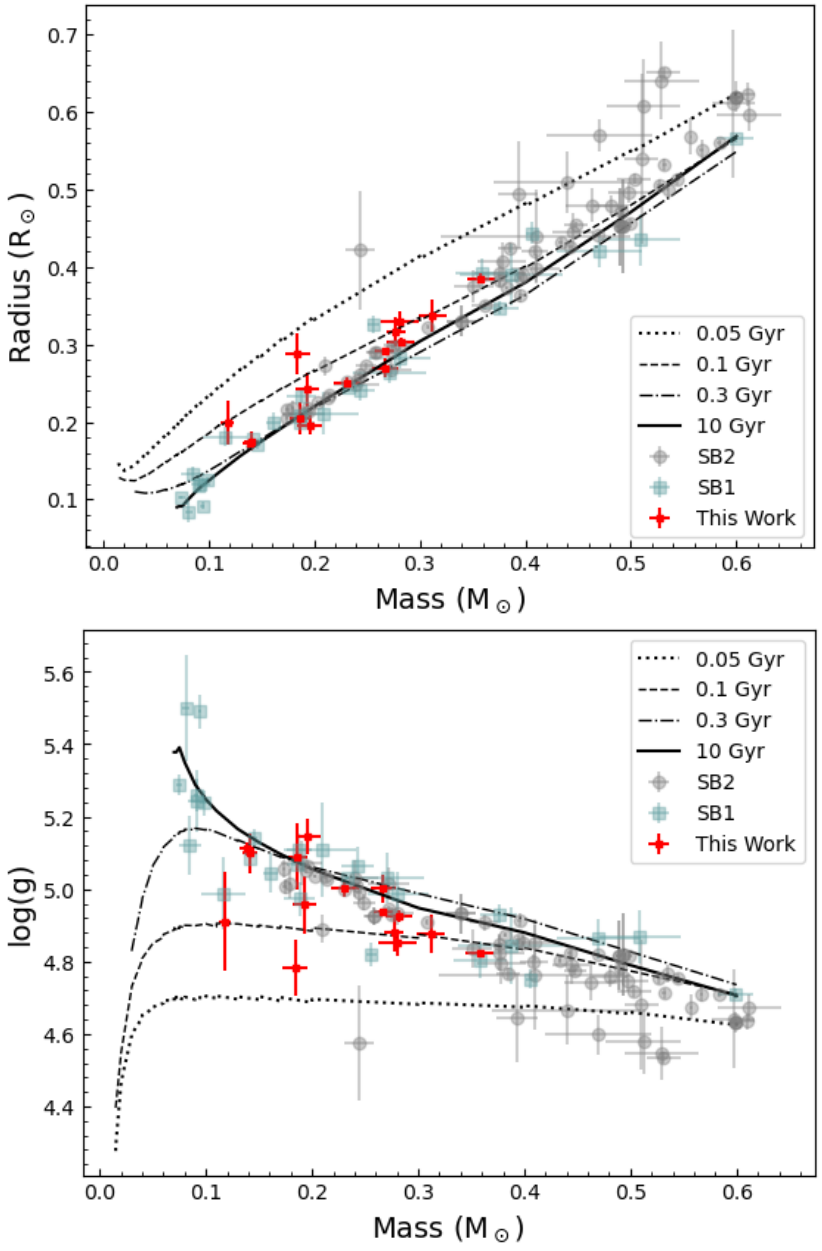

Figure 5.4: Top; BCAH15 isochrones for 0.05, 0.1, 0.3 and 10 Gyr plotted in the mass-radius plane with the locations of the current objects overplotted in red. M dwarfs from Parsons et al. (2018) are also shown where SB2 M-dwarfs are plotted in grey and SB1 M-dwarfs are plotted in blue. Bottom; Same as top but in the mass-log(g) plane.

between 0.3 and 10 Gyr, theory systematically underestimates M dwarf radii. This conclusion is verified in Fig. 5.5, where surface gravity is used instead of radius; the surface gravity of the M-dwarf is derived from the light-curve and RVs alone (Southworth et al., 2007), so is not dependent on the models. We also show the same objects in the mass-$T_{\rm eff}$ plane with the same isochrones. The SB2 systems suggest that temperatures are overestimated by the models. We note that our M-dwarf $T_{\rm eff}$ predictions appear to conform to the general trend set by SB2 M-dwarfs better than other SB1 M-dwarf determinations for this parameter.

It has been claimed that a correlation exists where inflated radii are accompanied by a cooler $T_{\rm eff}$ such that luminosity is unaffected (e.g. Torres, 2007). We investigated this by plotting the two discrepancies relative to BCAH15 isochrones for the objects studied in this work in Fig. 5.6. The discrepancies were calculated relative to the corresponding isochrones for each object's age, so this was not possible for the rest of the objects in Fig. 5.5. Below the dashed blue line, objects show overestimated $T_{\rm eff}$s by the models, and to the right of the red dashed line, objects are inflated, i.e., underestimated by the models. It does not appear that inflated radii are accompanied by an overestimated $T_{\rm eff}$ from this sample. This is in contrast to the majority of SB2 systems that do show overestimated $T_{\rm eff}$s by the models in Fig. 5.5. It is possible that different physical processes due to the brighter companion, such as global redistribution of a larger amount of incident radiation, may affect the adequacy of using SB1 systems to test the constant luminosity hypothesis, and this could be why the radius, as well as the $T_{\rm eff}$, is underestimated by the models for five of the objects in this study. Furthermore, the constant luminosity hypothesis requires a gradient of -0.5, which is represented by the black dash-dotted line in Fig. 5.6. We found that removing the outlier, GSC-06465-00602 (bottom right in the figure), from the investigation yields a linear fit to the remaining objects that satisfied a gradient of $+0.42$; the weighted Pearson correlation coefficient of 0.217, however, indicates that this is only a weak correlation.

TYC 3700-1739-1B shows the largest amount of inflation compared to the models but note that this is a young system, as estimated by the previous authors as well as the

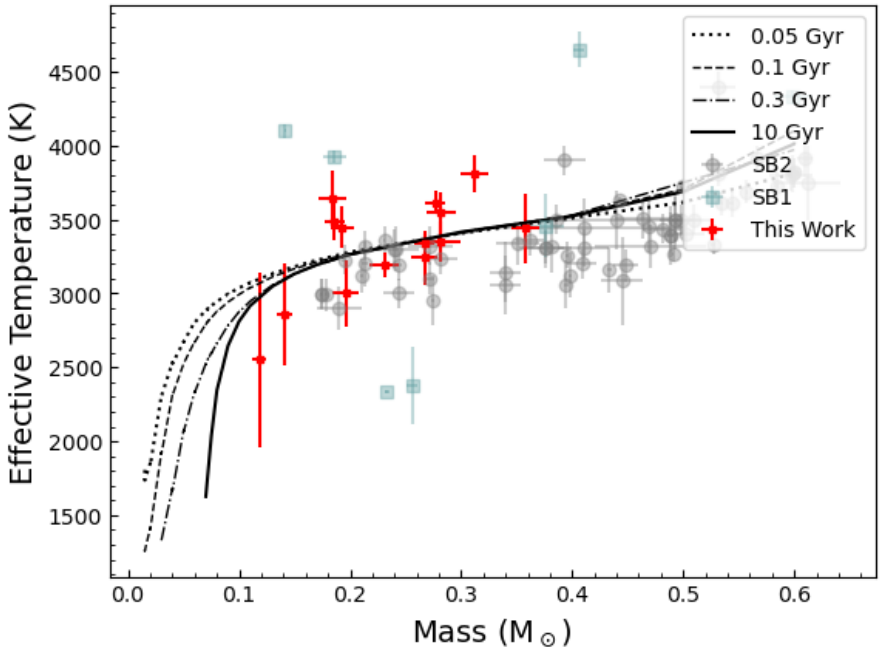

Figure 5.5: Same as Fig. 5.5 but in the mass-$T_{\rm eff}$ plane.

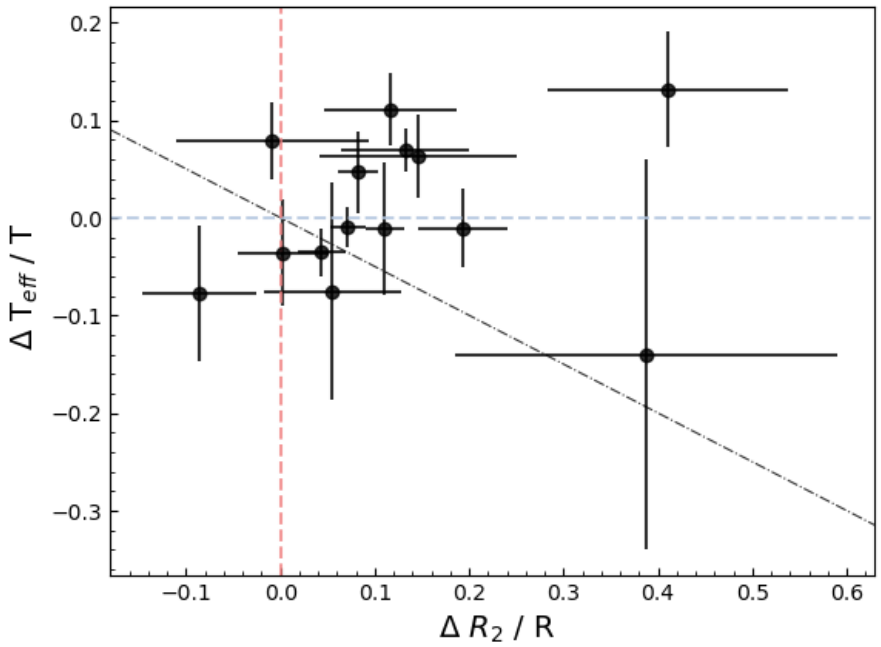

Figure 5.6: The fractional radius and $T_{\rm eff}$ discrepancies relative to theoretical predictions of BCAH15. Below the dashed blue line, objects show overestimated temperatures by the models for the corresponding age and to the right of the red dashed line, objects are inflated. The constant luminosity hypothesis is represented by the black dash-dotted line.

current study. The margin of uncertainty in the current age estimate for this system encompasses the entire pre-main sequence phase, where the models show the largest and most rapid variation in radius. Taking the lower limit of the age estimation in the determination of its inflation status leads to the conclusion that the object is under-inflated after previously being stated to be inflated by 41%. It is therefore vital that precise age estimates are obtained for young stars in order to be able to accurately compare their properties to theory. The same scenario is observed for GSC 06465-00602, where it is observed to be inflated by a large amount while the uncertainty in its age spans the pre-main sequence. It is concluded that the inflation status of an M dwarf cannot be accurately addressed if the uncertainty in its age estimate allows a pre-main-sequence solution, where small changes in the object's age would change the result. This necessity for precise age estimations due to rapid evolutionary changes makes these young objects valuable tests for our theoretical understanding.

Large uncertainties in age estimations are common but this has a much smaller effect on the predicted radius of a main sequence M dwarf. Inflation observed well within the main sequence is therefore likely accurate. The contraction of the core throughout the main sequence due to an increasing mean molecular weight results in a slight increase in the star's radius but most M dwarfs are found to be inflated beyond this. This is demonstrated in Fig. 5.5 by the gap between the 0.3 and 10 Gyr BCAH15 isochrones, where most M dwarfs lie above it.

A widely discussed hypothesis is related to the binarity of the majority of M dwarfs with measured radii precise to 10%. Increased rotational velocity induced via synchronisation between the orbital and rotational periods speeds up the internal dynamo, increasing magnetic activity and decreasing the efficiency of convection (Fernandez et al., 2009). This may cause the radius to expand (Mullan & MacDonald, 2001; López-Morales, 2007). However, the dynamos may operate differently in fully convective stars (Zhou et al., 2014) so the relationship between rotation and activity regarding such systems and its relevance to radius inflation is unclear. As stated in Section 1.1.5.3, the explanation needs not to be restricted to binary stars due field stars measured via interferometry demonstrating the same discrepancy compared to models;

field stars rotate slowly due to magnetic braking.

Berger et al. (2006) found the disagreement to be larger for metal rich stars, concluding that an opacity component missing from the models may lead to larger radii for stars with larger metallicity. Then it is interesting that two of the M dwarfs (TYC 6493-290-1 and GSC 06493-00315), found to agree with their isochrones in the current work, were previously found to have sub-solar metallicity by their previous authors, Zhou et al. (2014) and Fernandez et al. (2009). It is of particular interest to determine whether the remaining M dwarf which agrees with isochrones, HAT-TR-205-003, is also metal-poor. This would support the hypothesis of Berger et al. (2006) and other authors who have suggested the treatment of metallicity in the models as a source for inflation.

On the other hand, von Boetticher et al. (2019) found a correlation between radius residual with solar isochrones and estimated metallicity, such that for objects with values for [Fe/H] $\neq 0$, accounting for it in the isochrones would act to reduce the observed inflation or remove it. Estimations for [Fe/H] derived from high resolution échelle spectra would therefore be particularly valuable because it would mean that the radius residuals against the solar isochrones can be corrected for it as well as being able to include the value for [Fe/H] in the derivation of the empirical M dwarf radius. We note, since GSC-06465-00602 is the only inflated object in the current study with a significantly sub-solar, and potentially reliable value for metallicity, the reliability of the investigation into the size of the discrepancy might be improved by using a non-solar metallicity isochrone, rather than the solar BCAH15 isochrones.

GSC 05946-00892 is the only object in the current study found to be under-inflated compared to models. This object also has the largest surface gravity estimation among the other objects included in this work.

We have used the BCAH15 isochrones to determine how inflated the M dwarfs are in each system. However, these models may have a different age scale from the models used to determine the properties of the primary stars. The difference between the age scales is at most 0.2 Gyr, so should not affect our conclusions.

5.6 Conclusion

We have presented determinations of the physical properties of a set of 15 EBLMs using TESS and new ground-based light curves plus published RVs. Photometric data were modelled simultaneously with the RVs using JKTEBOP and physical parameters were calculated using an isochrone fitting method, yielding masses and radii of both components as well as the orbital semimajor axis and age of the systems. Our results are the first measurements of these properties for two of the systems. Our results improve and extend the catalogue of available physical properties of low-mass stars.

The full phase coverage of the TESS light curves means that the secondary eclipse for 14 of these objects has been observed and analysed for the first time, allowing for an estimation of the surface brightness ratio and $T_{\rm eff}$ of the M dwarf, whilst also reliably constraining the eccentricity of the systems. Our M dwarf $T_{\rm eff}$ predictions appear to be more reliable than previous attempts to estimate this value for M dwarfs in SB1 systems.

Estimated $T_{\rm eff}$ values for the M dwarfs allowed for the objects to be displayed in the mass-$T_{\rm eff}$ plane as well as the mass-radius diagram, among other well-characterised M dwarfs, and discussed in the context of radius inflation. It was discovered that exquisite precision in the age estimate of young stars is required in order to reliably address their inflation status. Neglecting such objects (TYC 3545-371-1, TYC 3700-1739-1) from the following statistic due to the uncertainty in the determination of its inflation status, 10 out of the 13 remaining objects were found to be inflated, by 11.4% on average. We do not find evidence from our SB1 sample of M-dwarfs that luminosity is unaffected by inflation; however, we note that our sample of objects with inflated radii is relatively small compared to the amount of SB2 M dwarfs in Fig. 5.5 where $T_{\rm eff}$ is overpredicted by models.

Precise measurements of the metallicity and $T_{\rm eff}$ for these systems would improve the reliability of the results and possibly remove ambiguity regarding some of the disagreements between the current and previous results. These would ideally be based on new high-quality échelle spectra. Additional RV measurements would be useful

for many of the systems, and TESS continues to observe the objects we have studied. Our work is therefore an important improvement, but not the final word, in our understanding of these objects.

6 Conclusion

6.1 Overview

Through the analysis of EBs we are able to measure the properties of stars to high precision and in a model-independent way that enables us to constrain our understanding of stellar theory. Asteroseismology is used to probe the interiors of pulsating stars and this allows us to go deeper in the level of intricacy to which we can aim to calibrate stellar models when pulsating stars exist in EBs. Measuring the physical properties of pulsating stars in EBs (e.g., Chapter 3 and Chapter 4) is an indispensable complement to stellar astrophysics, as is the characterisation of EBs in general (e.g., Chapter 5).

Thus, our complete understanding of celestial mechanics and gravity (in the Newtonion limit) provides the backbone for advancement in stellar astrophysics, and the advancement leads to investigations of phenomena associated with binaries (e.g., apsidal motion, tidal friction, binary evolution) as well as discoveries such as tertiary (or multiple) components. Given dynamical constraints from binarity, which act to reduce the parameter space of seismic models and remove degeneracies, asteroseismology simply relies on our ability to measure pulsation frequencies accurately; being able to reproduce them hinges on the advancement of stellar astrophysics.

Our ability to measure pulsation frequencies accurately increased significantly with the advent of the *Kepler* space mission; as outlined in Section 2.1.2, *Kepler* revealed that hybrids, such as KIC 9851944, are common. Furthermore, the combination of the *Kepler* and TESS time base, as well as the high photometric precision of these space missions, allowed us to the discover the tertiary component in KIC 4851217. These statements boast the success of these space missions which have played a pivotal role in the entirety of this work; their data are a central feature.

It is important to note that this thesis presents characterisations and analyses of objects already studied by previous authors. This work aimed to complement and build on those studies by presenting the analysis of new data and utilizing previously reported

results. Similarly, our work acts as an additional stepping stone in the advancement of stellar astrophysics, and lays the foundations for further studies of the objects. Additionally, we present the first characterisations of three M-dwarfs; HAT-TR-205-003B, TYC 9535-351-1B, and the tertiary component gravitationally bound to the EB KIC 4851217, where for the latter we report its discovery.

6.2 Project Comparison

There are two aims outlined in the title of this thesis and those are to determine the physical properties of intermediate- and low-mass stars, each with the broader aim of contributing to the advancement of stellar theory in those mass-regimes. In Chapter 3 and Chapter 4, we concentrate on the first of these objectives, while Chapter 5 is centred on the latter. Notably, in Chapter 5, we present the analysis of 15 *non-pulsating* EBLMs. The inadequacy of the models in the low-mass regime is discernible from conventional constraints alone (see Fig. 5.5). In contrast, we focus on single objects in Chapter 3 and Chapter 4, each of which contains a pulsating star, and the intention is that in future, a comprehensive seismic analysis will be conducted. These approaches underscore the completeness of stellar theory in the intermediate-mass regime compared to the low-mass regime.

KIC 9851944 and KIC 4851217 are similar objects for two reasons in particular. First, they have a comparable mass ratio near unity ($1.05 < q < 1.15$) and secondly, they are situated at comparable stages in their evolution, where in each system the secondary is evolving off the main sequence owing to its slightly larger mass. This makes both objects equally valuable in testing stellar theory at a critical transitional phase of evolution. Such rare examples of significant differential evolution in equal mass binaries are rare, and can be very informative (Torres et al., 2010).

Aside from the fact that KIC 4851217 is hierarchichal triple system, the difference between the inner EBs mainly lies within the pulsations. While both dominantly boast δ Scuti signatures, KIC 9851944 is a δ Scuti/γ Doradus hybrid. Furthermore, while

both the systems' pulsations are influenced by tides, the pulsations of KIC 9851944 are TPPs and those of KIC 4851217 are TTPs. Thus, this work reports the detection of both types of tidally influenced pulsations, as well as evidence for TEO's in KIC 9851944. The detection of TEOs is evidence of a non-eccentric orbit, which is against both our photometric and spectroscopic values of $e = 0$ for KIC 9851944, because TEOs are driven by the dynamical tide. The KIC 9851944 system might be eccentric (or a non-synchronous rotator) below our observational limit for detection, but it is not clear whether such a small value would be enough to excite TEOs at the observed amplitudes; this observation is not understood. In contrast, the eccentricity of the KIC 4851217 system is small but significant ($e \sim 0.032$).

The KIC 4851217 and KIC 9851944 EBs are both partially eclipsing ($i \sim 77°$), which introduces degeneracies in the eclipse model, particularly among the radius ratio and light ratio. The effect was observed for both systems and the light ratio was difficult to constrain. This was outlined in detail throughout Chapter 3, where we adopted three spectroscopic methods to determine the light ratio of the KIC 9851944 system. Likewise, the light ratio was not well constrained from photometry alone for the KIC 4851217 EB with similarly good fits to the light curve returning solutions with light ratios of ~ 1.5 and ~ 1.9. We adopted the latter based on our spectroscopic method (see Sections 3.5.2 and 4.4.2) which depends on template spectra but with less sensitivity on their atmospheric parameters than the TODCOR light ratio. We conclude that the TODCOR light ratio should be treated tentatively if the atmospheric parameters of the input templates are not reliable (i.e., preliminary estimations), which is in contrast to the RVs which are quite robust against the choice of template parameters.

We have extracted RVs from spectroscopic observations corresponding to a range of resolving power using TODCOR and estimated systematic corrections associated to them, as outlined in Section 2.2.3.3. The magnitude of these corrections has been shown to be smaller for larger resolving power. The WHT/ISIS observations ($R \approx 11000$) led to RV corrections translating to as high as 1.5% and 3.5% in mass for the primary and secondary, respectively. These values are as low as 0.24% and 0.6% for the HERMES observations ($R \approx 85000$), and somewhat in between at 0.6% and 0.9% for

the Hamilton observations ($R \approx 60000$). We determined the masses of the components of the KIC 9851944 and KIC 4851217 EBs to $\sim 0.5\%$ precision so it might be sensible only to bypass the velocity correction procedure for resolutions comparable to the HERMES spectrograph and slow rotators; we suggest that the significant corrections estimated for the HERMES RVs for the secondary component of the KIC 4851217 EB are the result of its larger $v \sin i$ value compared to that of the primary's.

Each of the three projects presented in Chapters 3, 4 and 5 utilized data from the *Kepler* and/or TESS space missions and benefitted from the advantages associated with continuous and long timebase monitoring of stars. This is notable from a seismic perspective and the discovery of the tertiary component in KIC 4851217. In addition, the resulting full phase coverage of the EBLMs studied in Chapter 5 removed ambiguity in the eccentricity of these systems as well as allowing for first estimations of the M-dwarf's $T_{\rm eff}$ values in most cases.

High precision is another advantage of the data collected from the *Kepler* and TESS space missions. However, ground based telescopes can attain competitive precisions. We considered ground based observations obtained from > 1 m class telescopes in our analysis of TYC 2755-36-1 and TYC 3121-1659-1 in Chapter 5 because such data are likely to be of comparable or better precision than the TESS data. There is the additional benefit of higher cadence during eclipse when only the long cadence space data are available (e.g., TYC 3121-1659-1). This is not the case for ground based telescopes with smaller apertures, e.g., WASP data which were only used as constraints on the times of mid eclipse to obtain the preliminary light curve solution for KIC 9851944 from *Kepler* and TESS light curves.

Consideration of the orbital configurations of the objects studied in this thesis influenced our approaches to the light curve modelling. We assumed that the distortion from tidal effects is negligible in EBLMs, and justified this assumption in Section 5.3.1. Thus, the JKTEBOP code is reliable in this circumstance so is the preferred choice compared to, e.g., the WD code, because JKTEBOP is faster. On the other hand, the difficulty in reaching a robust light curve solution for the KIC 9851944 and KIC 4851217 EBs is compounded by their close proximity and associated deformation, rendering the

JKTEBOP code plausible only for preliminary investigations, and the WD code was used for the final solution.

6.3 Future Work

The heightened sensitivity of models at evolved stages makes the KIC 9851944 and KIC 4851217 systems particularly well suited for comprehensive evolutionary modelling (e.g., del Burgo & Allende Prieto, 2018) where a successful model would need to predict the MS properties of the primary simultaneously with the TAMS properties of the secondary for a single age and metallicity (see section 1.1.5). The difficulty in reproducing the observations for these objects would be compounded by the inclusion of the observed pulsation frequencies in the modelling. Accurate seismic modelling of these relatively fast-rotating stars relies on sufficiently accurate equilibrium structure models being used and the ability to identify the pulsation modes. Thus, future work will be focused on identifying the pulsation modes in these stars and satisfying one of the main motives for studying such systems, which is to combine seismic and conventional constraints in the modelling. It is expected that the equilibrium structure models for the calculation of the pulsation frequencies will advance with increasing numbers of such studies.

It is important to continue characterising more pulsating EBs because their is a lack of studies taking advantage of the joint analysis of dynamical and seismic data (Sekaran et al., 2020; Liakos, 2021). The number of ideal candidates is increasing thanks to systematic searches for pulsators in EBs observed by *Kepler* (Gaulme & Guzik, 2019) and TESS (Chen et al., 2022) with emphasis of the detection of δ Scuti EBs in the southern TESS field by Kahraman Aliçavuş et al. (2023). In particular, this will lead to more well-characterised hybrid pulsators, which are arguably considered our most valuable objects for constraining stellar theory; a statistically large sample of hybrid pulsators is required to advance our knowledge of mode excitation mechanisms which would improve our understanding of convection, rotation, tidal interactions and

nonlinearity on pulsations (Guo et al., 2016).

Regarding the tidal influence on the pulsations of KIC 9851944 and KIC 4851217, it is noteworthy to ask why the former exhibits TPPs and the latter exhibits TTPs. It was noted in Section 4.8 that the topic of TTPs is still in its infancy and there are only four TTP systems which have been conclusively identified, three of which are δ Scuti stars. The detection and modelling of more TTPs is crucial for advancement on this front. Therefore, one might propose for systematic searches for TPP and TTP candidates, with emphasis on the latter, in the catalogues of pulsating EBs reported above.

Studies must also continue which involve measuring the properties of low-mass stars for progress to advance on this front and for models to overcome the radius inflation problem. This is important for the broader objective to advance stellar astrophysics, but also from a planet hunting perspective. Planets are easily detected around small stars (Ricker et al., 2015), i.e., M-dwarfs, and understanding a planet's host is important for accurate characterisation of the planet. The PLanetary Transits and Oscillations of stars (PLATO) satellite is due launch in 2026 with the aim of detecting and characterising planets as well as their hosts using asteroseismology (Rauer et al., 2022). The PLATO mission is set to provide highly relevant data for future research in line with the overarching goals of this thesis.

A Orbital Dynamics Appendix

A.1 The Two Body Problem

The point mass approximation used in the Roche model is also useful when studying the dynamical relationships among the orbiting bodies in a binary system because Newton's second theorem states that the gravitational force of a spherical body of mass m is equivalent to that of a point mass m located at the centre of the sphere. The theorem breaks down under certain conditions but is a sufficiently valid assumption in most cases since stars are centrally condensed objects (Hilditch, 2001). In this approximation, the motion of the components about the centre of mass in a binary system constitutes a classical two-body problem (Prša, 2018).

Assuming an isolated system, the only force experienced by either body results from the gravitational field of the other component, and the total force equates to zero; the centre of mass of the system moves through space at constant velocity, as demonstrated in, e.g., Hilditch (2001). The difference between the equations of motion that are implied by the gravitational acceleration experienced by each body, and described with respect to an arbitrary coordinate system (see Fig. A.1), results in a description for the motion of the stars relative to each other, i.e.,

$$\ddot{\boldsymbol{r}} = \ddot{\boldsymbol{r_1}} - \ddot{\boldsymbol{r_2}} = -\frac{GM_2}{r^2}\hat{r} + \frac{GM_1}{r^2}(-\hat{r}) = -\frac{G(M_1+M_2)}{r^2}\hat{r}, \tag{A.1}$$

for $\boldsymbol{r_1}$ and $\boldsymbol{r_2}$ the position vectors of the bodies located at P_1 and P_2, respectfully, in Fig. A.1, $\hat{r}$ is a unit vector in the direction of their separation r, and $M_{1,2}$ are the masses of the components. Multiplying this result by the *reduced mass* $\mu = M_1M_2/(M_1+M_2)$ yields,

$$\mu\ddot{\boldsymbol{r}} = -\frac{G(M_1+M_2)}{r^2}\mu\hat{r} = -\frac{GM_1M_2}{r^2}\hat{r}, \tag{A.2}$$

which is equivalent to the *force* acting on either body. This demonstrates that the relative motion of the bodies is equivalent to a single body of mass μ orbiting a central mass that corresponds to the total mass of the system (Prša, 2018; Hilditch, 2001);

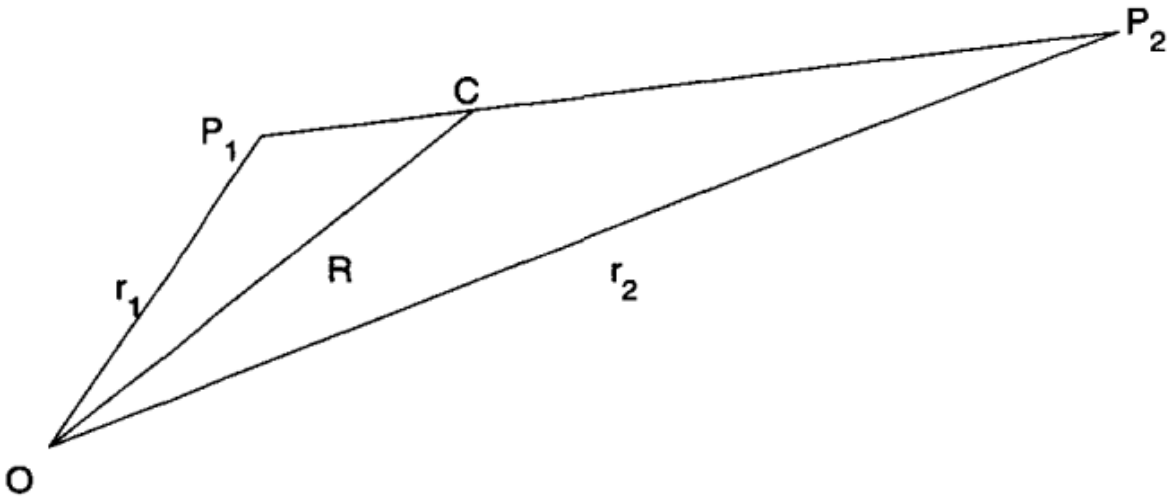

Figure A.1: Arbitrary coordinate system describing the positions of the components in an EB. From Hilditch (2001).

this is the *relative orbit*. The classical two body problem can be solved by reducing it to a single body in this orbit (Prša, 2018).

The Hamiltonian describing the total energy is then,

$$H = \frac{1}{2}\mu\dot{r}^2 - \frac{GM_1M_2}{r}, \tag{A.3}$$

where $\dot{r}$ is the speed of a fictitious body of mass μ, i.e., the relative speed of the two components. The solution for $r(t)$ is not analytical so we solve for $r(\nu)$, where ν is the angle measured from *periastron* to the position of the star about the focal point of the orbit (see Section 1.1.2.3); by definition, periastron is the location of the orbit at which the two components are closest to each other. The solution for $r(\nu)$ satisfies a conic section and is the *polar equation of orbit*,

$$r(\nu) = \frac{a(1-e^2)}{1+e\cos\nu}, \tag{A.4}$$

where the semi-major axis,

$$a = \frac{J^2}{\mu GM_1M_2(1-e^2)}, \tag{A.5}$$

and eccentricity,

$$e = \left(1 + \frac{2HJ^2}{\mu G^2 M_1^2 M_2^2}\right)^{1/2}, \tag{A.6}$$

are the constants of integration. Here, H is the total energy, as in Eq. A.3, and J is the total angular momentum of the system.

Kepler's second law shows that the *specific* angular momentum $L = r^2\dot{\nu}$ is constant, and can be expressed as (see Appendix E.1.1),

$$L = \frac{4\pi^2 a^3}{P^2} a(1-e^2) = M(1-e^2), \tag{A.7}$$

where we recognise M is the mass term from Keplers third law, which depends on the orbit in consideration (see below). Differentiating Eq. A.4, and using the previous expression for L, results in the following equation for the speed,

$$\dot{r}^2 = M\left[\frac{2}{r} - \frac{1}{a}\right]. \tag{A.8}$$

Since mass is inseparable from the gravitational constant G in orbital motion calculations, the M in Eq. A.8 corresponds to $G(M_1 + M_2)$ for the relative orbit, i.e., Eq. A.2, where the gravitational acceleration is due to the total mass of the system $(M_1 + M_2)$.

Using this mass term and plugging Eq. A.8 into Eq. A.3 leads to the following expression for the total energy of the relative orbit,

$$H = -\frac{1}{2}\frac{GM_1M_2}{a}, \tag{A.9}$$

which is constant since no forces are acting on the system. For $H > 0$, the bodies are not bound, and the orbit is hyperbolic with $e > 1$. Parabolic orbits are the result of $H = 0$, $e = 1$, and elliptical orbits have $H < 0$, $e < 1$. The total angular momentum of the system J is found by adding up the angular momentum of the two *barycentric* orbits. This can be expressed in terms of the specific angular momentum of the relative orbit as follows,

$$J = M_1\frac{M_2^2}{(M_1+M_2)^2}L + M_2\frac{M_1^2}{(M_1+M_2)^2}L, \tag{A.10}$$

which leads to,

$$J = \mu\omega a^2\sqrt{1-e^2}, \tag{A.11}$$

where $\omega = 2\pi/P$ is the orbital frequency, within which, we have introduce the period P of the binary system. The value of J is another constant of the orbit since the potential is central (Prša, 2018) [1]. This is also implicit through Kepler's second law which states that the radius vector sweeps out equal areas in equal intervals of time. The consequence of this is that bodies move faster when they get closer (Hilditch, 2001).

A.2 Barycentric Orbits

We need to relate the orbit of the fictitious body in the *relative* orbit to the *barycentric* orbits where each body is in motion about the centre of mass, denoted C in Fig. A.1. The vector describing the position of C in *any* coordinate system is given by (Prša, 2018),

$$\boldsymbol{R} = \frac{M_1\boldsymbol{r_1} + M_2\boldsymbol{r_2}}{M_1 + M_2}, \tag{A.12}$$

for distance vectors $\boldsymbol{r}_{1,2}$ of each component from the origin, as before. Denoting $\boldsymbol{R}_{1,2}$ the distance vectors describing the position of each component relative to C, and $\boldsymbol{r}$ their position relative to each other, then we can write,

$$\boldsymbol{r_1} = \boldsymbol{R} + \boldsymbol{R_1}; \quad \boldsymbol{r_2} = \boldsymbol{R} + \boldsymbol{R_2}; \quad \boldsymbol{r} = \boldsymbol{r_1} - \boldsymbol{r_2} = \boldsymbol{R_1} - \boldsymbol{R_2}. \tag{A.13}$$

Using Eq. A.12 and Eq. A.13 we can show $M_1\boldsymbol{R_1} + M_2\boldsymbol{R_2} = 0$ (see Appendix E.1.3). Hence, we can write (see Appendix E.1.4),

$$\begin{aligned} \boldsymbol{R_1} &= +\frac{\mu}{M_1}\boldsymbol{r}, \\ \boldsymbol{R_2} &= -\frac{\mu}{M_2}\boldsymbol{r}, \end{aligned} \tag{A.14}$$

[1] The potential is central because the only force acting is along the line connecting the stars. The force and distance vectors are parallel and the torque acting on the system $\boldsymbol{\tau} = \boldsymbol{r} \times \boldsymbol{F}$ is zero, i.e., no rotational acceleration or deceleration; angular momentum is conserved.

which implies that the barycentric orbits are equivalent to the orbit of the fictitious orbit, except they are in opposite directions, and scaled by $\mu/M_{1,2}$. The equations of motion for the barycentric orbits are then derived using the expressions for $\ddot{\boldsymbol{r}}_{\mathbf{1}}$ and $\ddot{\boldsymbol{r}}_{\mathbf{2}}$ in Eq. A.1, as well as the expressions in Eq. A.13 and Eq. A.14 as (see Appendix E.1.5),

$$\ddot{\boldsymbol{R}}_{\mathbf{1}} = -\frac{GM_2^3}{(M_1+M_2)^2}\frac{\boldsymbol{R_1}}{\boldsymbol{R}_{\mathbf{1}}^3}; \quad \ddot{\boldsymbol{R}}_{\mathbf{2}} = -\frac{GM_1^3}{(M_1+M_2)^2}\frac{\boldsymbol{R_2}}{\boldsymbol{R}_{\mathbf{2}}^3}, \tag{A.15}$$

where the mass terms for the barycentric orbits are now apparent, i.e, $GM_2^3/(M_1+M_2)^2$ and $M_1^3/(M_1+M2)^2$ for the star of mass M_1 and M_2, respectively.

A.3 Derivation of Kepler's Equation

Following (Prša, 2018), the coordinates of the star's position on the auxiliary circle are $x_p = ae + r\cos\nu$ and $y_p = r\sin\nu$. The coordinates of Q are $x_Q = a\cos E$ and $y_Q = a\sin E$. It is then clear from Fig. 1.3, that the distance from position T to position S is,

$$|TS| = ae - a\cos E = r\cos(\pi - \nu) = -r\cos\nu. \tag{A.16}$$

Rearranging for $\cos\nu$ and subbing into the polar equation of orbit, i.e., Eq. A.4, leads to the equation of orbit in terms of the eccentric anomaly (see Appendix E.1.6),

$$r(E) = a(1 - e\cos E). \tag{A.17}$$

Now is a good time to take note of the following identities,

$$\begin{aligned} x_P = x_Q \quad &: \quad ae + a(1-e\cos E)\cos\nu = a\cos E, \\ ay_p = by_q \, : \quad &ar\sin\nu = ba\sin E, \end{aligned} \tag{A.18}$$

where b denotes the semi-minor axis of the barycentric orbit. The derivative of the reciprocal of the polar equation of orbit leads to an equation for the specific angular momentum that reads (see Appendix E.21),

$$r^2\dot{\nu} = \frac{a(1-e^2)\dot{r}}{e\sin\nu} = \omega a^2\sqrt{1-e^2}, \tag{A.19}$$

where we have equated the result to Eq. A.11/μ and, again, $\omega = 2\pi/P$ is the orbital angular frequency. The derivative of Eq. A.17 satisfies,

$$\dot{r} = ae \sin E \dot{E}, \tag{A.20}$$

which we equate to Eq. A.19 via $\dot{r}$ and rearrange to find,

$$\dot{E} = \frac{a\omega \sin \nu}{a \sin E \sqrt{1-e^2}} = \frac{a\omega \sin \nu}{b \sin E} = \frac{a\omega}{r} = \frac{a\omega}{a(1 - e\cos E)}, \tag{A.21}$$

where we used $b = a\sqrt{1-e^2}$, the y-component of the alignment in Eq. A.18, and subbed for r using Eq. A.17. Writing $\dot{E}$ as dE/dt and cancelling the a's, we can now integrate as follows,

$$\int (1 - e\cos E)\, \mathrm{d}E = \int \omega \, \mathrm{d}t \Rightarrow E - e \sin E = \omega t + C, \tag{A.22}$$

where $C = -\omega t_{\mathrm{per}}$ due to the condition that $E|_{t=t_{\mathrm{per}}} = 0$. The result is *Keplers equation*,

$$E - e \sin E = \omega(t - t_{per}) = \mathcal{M}, \tag{A.23}$$

which describes the star's position as a function of time by relating the the eccentric anomaly (*position dependence*) to the mean anomaly (*time dependence*).

From the identities in Eq. A.18 (see Appendix E.1.8),

$$\cos E = \frac{e + cos\nu}{1 + e\cos\nu}, \quad \sin E = \frac{\sqrt{1-e^2}}{1 + e\cos\nu} \sin\nu. \tag{A.24}$$

Dividing these equations leads to the relationship between the true and eccentric anomalies as,

$$\tan E = \frac{\sqrt{1-e^2}\sin\nu}{e + \cos\nu}, \tag{A.25}$$

which can be converted using half angle identities to a more practical form (Smart & Green, 1977),

$$\tan\frac{E}{2} = \sqrt{\frac{1-e}{1+e}} \tan\frac{\nu}{2}. \tag{A.26}$$

Thus, for some time t, we can calculate E from $\mathcal{M}$ and this can be used to compute ν. We can then use Eq. A.4 to specify the position as a function of time $r(t)$.

A.4 Velocity along the line of site

From Eq. A.18,

$$\begin{aligned} \dot{x} &= -a\dot{E}\sin E, \\ \dot{y} &= b\dot{E}\cos E. \end{aligned} \tag{A.27}$$

From Kepler's equation,

$$\dot{E} = \omega + e\cos E\dot{E} = \frac{\omega}{1 - e\cos E} \tag{A.28}$$

so,

$$\dot{x} = -\frac{a_1\omega\sin E}{1 - e\cos E}; \quad \dot{y} = \frac{b_1\omega\cos E}{1 - e\cos E}. \tag{A.29}$$

Using the following transformation from the orbital plane to our line site from Prša (2018),

$$\dot{z} = \sin i\sin\omega\dot{x} + \sin i\cos\omega\dot{y}, \tag{A.30}$$

and plugging in for $\dot{x}$ and $\dot{y}$ yields,

$$\dot{z} = \frac{a_1\omega\sin i}{1 - e\cos E}(\sqrt{1 - e^2}\cos\omega\cos E - \sin\omega\sin E). \tag{A.31}$$

B Radiation Basics

Consider an arbitrarily chosen surface within a star, the specific intensity I_ν is the energy emitted per area $\mathrm{d}A$ and per solid angle $\mathrm{d}\omega$ in a direction θ measured from the surface normal, within a frequency and time interval $\mathrm{d}\nu$ and $\mathrm{d}t$, respectfully (see Fig. B.1). Thus,

$$\begin{aligned} I_\nu &= \lim \frac{\Delta E_\nu}{\cos\theta \Delta A \Delta\omega \Delta t \Delta\nu}, \\ I_\nu &= \frac{\mathrm{d}E_\nu}{\cos\theta\, \mathrm{d}A\, \mathrm{d}\omega\, \mathrm{d}t\, \mathrm{d}\nu}, \end{aligned} \tag{B.1}$$

which is easily converted to a function of wavelength λ using $I_\nu\, \mathrm{d}\nu = I_\lambda\, \mathrm{d}\lambda$.

As light propagates toward the surface of a star, the photons endure a *random walk*, which consists of various absorption and scattering processes, as well as emission. The net *extinction* to the intensity of a photon beam due to these processes is expressed as,

$$\mathrm{d}I_\nu = -\kappa_\nu \rho I_\nu\, \mathrm{d}l + j_\nu \rho\, \mathrm{d}l, \tag{B.2}$$

where κ_ν is the *continuous* absorption coefficient and j_ν is the *continuous* emission coefficient (Gray, 2005; Prša, 2018). Defining the *optical depth*,

$$\mathrm{d}\tau = -\kappa_\nu \rho\, \mathrm{d}l, \tag{B.3}$$

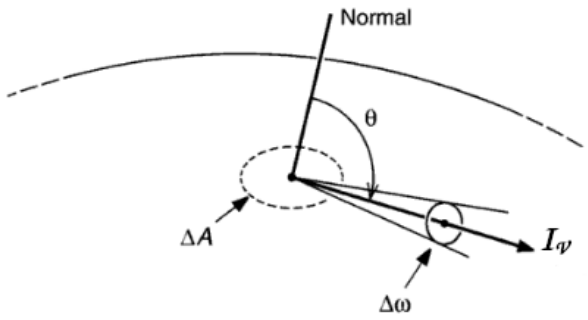

Figure B.1: A depiction of a photon beam, i.e., the specific intensity from Gray (2005).

which refers to the opacity ($\kappa_\nu \rho$) along the path traversed ($\mathrm{d}l$) by a photon, allows us to reformulate Eq. B.2 and express the *radiative transfer equation* as,

$$\frac{\mathrm{d}I_\nu}{\mathrm{d}\tau_\nu} = -I_\nu + S_\nu, \tag{B.4}$$

where $S_\nu = j_\nu/\kappa_\nu$ is the ratio of emission to absorption, i.e., the *source function*. Solving Eq. B.4 yields the specific intensity at a given location; this is how model atmospheres are calculated.

The *monochromatic flux* F_ν is the specific intensity integrated over all solid angles, but projected along the surface normal [1],

$$F_\nu = \oint I_\nu \cos\theta \, \mathrm{d}\omega = \int_0^\pi \int_0^{2\pi} I_\nu \cos\theta \, \mathrm{d}\phi \sin\theta \, \mathrm{d}\theta, \tag{B.5}$$

where ϕ is measured clockwise about the dashed circle in Fig. B.1. Since F_ν is a measure of the net flow of energy through the area $\mathrm{d}A$, then, $F_\nu = F_\nu^{in} + F_\nu^{out}$, where,

$$\begin{aligned} F_\nu^{\mathrm{in}} &= \int_0^{2\pi} \int_{\pi/2}^{\pi} I_\nu \cos \, \mathrm{d}\phi\theta \sin\theta \, \mathrm{d}\theta. \\ F_\nu^{\mathrm{out}} &= \int_0^{2\pi} \int_0^{\pi/2} I_\nu \cos \, \mathrm{d}\phi\theta \sin\theta \, \mathrm{d}\theta, \end{aligned} \tag{B.6}$$

(see Fig. B.1). Indeed, the surface containing $\mathrm{d}A$ may be one that corresponds to the physical boundary of the star, in which case, $F_\nu = F_\nu^{\mathrm{out}}$.

Assuming that I_ν is not sensitive to *rings* of constant θ, i.e., no ϕ dependence, then at the *stellar surface* (Gray, 2005),

$$F_\nu = F_\nu^{out} = 2\pi \int_0^{\pi/2} I_\nu \cos\theta \sin\theta \, \mathrm{d}\theta. \tag{B.7}$$

Integrating Eq. B.7 over the entire area of the star and over all frequencies yields the luminosity,

$$L = 4\pi R^2 \int_0^\infty F_\nu \, \mathrm{d}\nu, \tag{B.8}$$

[1] The light we receive at the telescope is the component of the specific intensity in the direction of the projected area of the star ΔA integrated over all solid angles, i.e., we measure the flux corresponding to some frequency interval $\Delta\nu$- the photometric pass band- and time interval Δt- the exposure time.

which is the total power output from the star. If the star was approximated as a black body radiator with the same power output as the star, the distribution I_ν is described by the Plank function,

$$B_\nu = \frac{2h\nu^3}{c^2}\frac{1}{\exp\frac{h\nu}{kT}-1}, \tag{B.9}$$

which leads to[2] (Gray, 2005),

$$L = 4\pi R^2 \sigma T_{\text{eff}}^4, \tag{B.10}$$

where T_{eff} is the *effective temperature* and σ is the Stephen Boltzman constant. The effective temperature T_{eff} is therefore the temperature of a black body with the same power output L as the star (Smalley, 2005).

The distribution I_ν at the surface of the star is more complex than the Plank function; to predict I_ν, atmospheric models must solve the radiative transfer equation (Eq. B.4) in the upper atmospheric layers to the photosphere, taking into account continuous and line opacity variations along the photons path. However, the value of T_{eff} serves as a characteristic temperature of the stellar *photosphere*.

[2]If I_ν is not direction dependent then from Eq. B.7, $F_\nu = \pi I_\nu = \pi B_\nu$ and $\int_0^{\pi/2} F_\nu \mathrm{d}\nu = \pi \int_0^{\pi/2} \mathrm{B}_\nu \mathrm{d}\nu = \sigma \mathrm{T}^4$. This is the *Stephan-Boltzmann law*.

C Stellar Structure

C.1 Equations of Hydrodynamics

Stars consist of ionised gas (plasma) within which, the constituents behave collectively as a fluid. Thus, the equations describing the structure of a star are the equations of hydrodynamics. The associated properties are the local density $\rho(\boldsymbol{r}, t)$, local pressure $p(\boldsymbol{r}, t)$ and local, instantaneous velocity $\boldsymbol{v}(\boldsymbol{r}, t)$, of the gas inside the star, expressed as functions of time t and position relative to some stationary point $\boldsymbol{r}$[1](Aerts, 2021).

The equation of continuity,

$$\frac{\mathrm{d}\rho}{\mathrm{d}t} + \mathrm{div}(\rho \boldsymbol{v}) = 0, \tag{C.1}$$

expresses that mass in conserved; the rate of change of mass in a volume is balanced by the flux of mass into the volume V (Aerts et al., 2010). The equation of motion,

$$\rho \frac{\mathrm{d}\boldsymbol{v}}{\mathrm{d}t} = -\nabla p - \rho \nabla \Phi, \tag{C.2}$$

expresses momentum conservation, where Φ is the local gravitational potential; the only forces considered to act on a volume of gas are due to pressure and gravity, i.e., other forces such the centrifugal and magnetic forces are neglected. The Laplacian ∇^2 of the gravitational field is proportional to the mass density via the *Poisson equation*,

$$\nabla^2 \Phi = 4\pi G \rho, \tag{C.3}$$

where G is the Newtonion gravitational constant. Finally, conservation of energy is expressed by the first law of thermodynamics,

$$\frac{\mathrm{d}q}{\mathrm{d}t} = \frac{\mathrm{d}E}{\mathrm{d}t} + p\frac{\mathrm{d}V}{\mathrm{d}t}, \tag{C.4}$$

where $\mathrm{d}q/\,\mathrm{d}t$ is the heating term, E is the internal energy of the system, and the last term on the right is the work done by the system in expanding or compressing the gas.

[1]Our definition for $\boldsymbol{r}$ means our description of the stellar hydrodynamical properties is what is seen by a stationary observer, so is *Eulerian*. Alternatively, in a Lagrangian description, the quantities are defined such that the observer follows the motion of the gas (Aerts et al., 2010).

C.2 Diffusion Approximation

The heating term in Eq. C.4 depends on the energy generation per unit mass ϵ and the flux $\boldsymbol{F}$ via (Aerts et al., 2010; Aerts, 2021),

$$\rho \frac{\mathrm{d}q}{\mathrm{d}t} = \rho\epsilon - \mathrm{div}\boldsymbol{F}. \tag{C.5}$$

To calculate the flux (Eq. B.5), one needs to determine the specific intensity which is derived by solving the radiative transfer equation (Eq. B.4). A simplification arises at large optical depths (i.e., interior regions where $\tau >> 1$), where the *mean free path* of a photon is small compared to the distance scales over which the temperature changes, because the local temperature can be directly associated to the thermodynamic properties of the local plasma; the system is in *local thermodynamic equilibrium* (LTE). The specific intensity assuming LTE is equivalent to the Plank distribution B_ν, which leads to the following approximation for the flux,

$$\boldsymbol{F} = -\frac{4\pi}{3\kappa_\nu \rho}\nabla B = -\frac{4acT^3}{3\kappa_\nu \rho}\nabla T \tag{C.6}$$

Eq. C.6 is called the *diffusion approximation* for radiative energy transfer.

C.3 Standard Stellar Models

The so called *standard stellar models* assume that the stellar structure is static, spherically symmetric (i.e., depends only on the radial distance r from the centre) and that there are no velocities (Aerts et al., 2010). The continuity equation (Eq. C.1) becomes trivial in this situation, and the equation of motion (Eq. C.2) reduces to that of *hydrostatic equilibrium*,

$$\frac{\mathrm{d}p}{\mathrm{d}r} = -g(r)\rho(r), \tag{C.7}$$

where g is the gravitational acceleration and the first integral of the Poisson equation,

$$g(r) = G\int_0^r 4\pi\rho(r)\,\mathrm{d}r = \frac{G}{r^2}\int_0^r 4\pi\rho(r)r^2\,\mathrm{d}r = \frac{GM(r)}{r^2}, \tag{C.8}$$

where the following identification,

$$M(r) = \int_0^r 4\pi\rho(r)r^2 dr, \tag{C.9}$$

ensures mass is conserved. Since the flux is directed radially outward in a spherically symmetric model and $\mathrm{d}q/\,\mathrm{d}t = 0$ in LTE, from Eq. C.5,

$$\rho\epsilon = \frac{1}{r^2}\frac{\mathrm{d}}{\mathrm{d}r}(r^2F(r)) = \frac{1}{4\pi r^2}\frac{\mathrm{d}L(r)}{\mathrm{d}r}, \tag{C.10}$$

where $L = 4\pi r^2 F(r)$; L is the total flow of energy over the entire sphere of radius r from the centre. Hence,

$$\frac{\mathrm{d}L}{\mathrm{d}r} = 4\pi r^2\rho(r)\epsilon, \tag{C.11}$$

which expresses energy conservation. We can also use $F = L/4\pi r^2$ to express the diffusion approximation as,

$$\frac{\mathrm{d}T}{\mathrm{d}r} = -\frac{3\kappa_\nu\rho(r)}{16\pi r^2 acT^3}L(r). \tag{C.12}$$

Eqs. C.7, C.9, C.11, and C.12 are the *standard equations of stellar structure* (MacDonald, 2015; Lamers, 2017).

C.4 Convection

Convection involves the transfer of heat via the motions of the fluid itself, distinct from radiative transfer. The mixing length theory[2] (MLT) (Böhm-Vitense, 1960) is a simplified and time-independent treatment of convection. It is commonly used due to limited understanding surrounding the turbulent, time-dependent nature of convective elements which prevents a complete hydrodynamical description (i.e., one that accounts for both radiative and convective energy transport). In this sense, convection is treated

[2]The MLT describes the average length scale, *the mixing length* l_{ml}, over which convective elements traverse before before dissipating in thermodynamic equilibrium, and is usually parameterised by the *mixing length parameter* α_{ml} multiplied by the pressure scale height H_{p}. See Joyce & Tayar (2023) for a review of the MLT of convection in 1D stellar modelling.

as a separate contribution to the flux in Eq. C.5 and Eq. C.12 is modified in convectively unstable regions (Aerts et al., 2010).

A region is unstable to convection if convective energy transport is more efficient than radiative energy transport in that region. This is assessed by calculating the temperature gradients associated with either transport mechanism. The adiabatic temperature gradient inside convective cells is used to evaluate the efficiency of convection (convection is an adiabatic process). It is convenient to express this gradient against pressure as,

$$\nabla_{\rm adi} = \left(\frac{{\rm d}\ln T}{{\rm d}\ln P}\right)_{\rm adi} = \left(\frac{\gamma - 1}{\gamma}\right), \tag{C.13}$$

where γ is the ratio of specific heats $c_{\rm p}$ and $c_{\rm V}$ at constant pressure and volume, respectively (LeBlanc, 2010). From Eq. C.7 and Eq. C.12, the radiative temperature gradient then follows (see Appendix E.2.1),

$$\nabla_{\rm rad} = \left(\frac{{\rm d}\ln T}{{\rm d}\ln P}\right)_{\rm rad} = \frac{3\kappa_\nu p}{16\pi acGT^4}\frac{L(r)}{M(r)}. \tag{C.14}$$

The gradient in the mean molecular weight μ is also important because convective cells rise due to buoyancy; a decrease in μ would act to increase stability against convection. This leads to the *Ledoux criterion* for convective instability,

$$\nabla_{\rm rad} > \nabla_{\rm ad} + \nabla_\mu; \tag{C.15}$$

the *Schwarzchild criterion* simplifies the assessment by neglecting ∇_μ.

The top panel of Fig. C.1 shows the extent of the convective envelope as a function of $T_{\rm eff}$ and the lower panel shows the contribution of convection to the total flux along the zero-age main-sequence (ZAMS) calculated using the MLT. The figure demonstrates that convection is an efficient energy transport mechanism throughout the envelopes of low- and intermediate-mass stars up to $T_{\rm eff} \sim 7000K$, at which point the convection zone splits into contributing components at shallower and deeper geometrical depths; these are the first and second ionization zones of helium, respectively. Ionization zones lead to convection because of the associated increase in opacity; from

Eq. C.14 and Eq. C.15, convective stability decreases with increasing opacity. Eq. C.14 is also proportional to the flow of energy per unit mass in the region of interest, i.e., $L(r)/M(r)$. Since the energy generation in stars with masses exceeding $\sim 1.2\,\mathrm{M}_{\odot}$ is strongly concentrated in the core (oweing to the temperature sensitivity of the CNO cycle), this leads to a convective core (Naur & Osterbrock, 1953).

C.5 Mixing

Convective turnover time-scales are on the order of months or years (Landin et al., 2010) so convective regions can be regarded as fully mixed with uniform composition. In radiative regions, the rate of change of the abundance X of an element k follows,

$$\frac{\partial X_k}{\partial t} = R_k + \frac{\partial}{\partial M}\left(D_k \frac{\partial X_k}{\partial M}\right) + \frac{\partial}{\partial M}(V_k X_k). \tag{C.16}$$

The abundance X_k is expressed as the mass fraction of element k, R_k is the rate of change of X_k due to nuclear reactions and D_k and V_k are the diffusion coefficient and settling constant, respectfully, for element k (Aerts et al., 2010). Heavier elements tend to settle near the stellar center due to gravity, resulting in a negative molecular gradient $\Delta\mu$. However, radiative levitation and diffusive mixing processes act to oppose gravitational settling, leading to *chemical peculiarity* in stars.

Rotational, magnetic, and pulsational effects also contribute to the mixing of chemical species but, due to limited understanding, are approximated as diffusive and usually wrapped in D_k (Aerts et al., 2010, 2018; Aerts, 2021). Stellar models are often simplified further by assuming mixing only occurs in convective regions, leading to uncertainties in the composition profiles of radiative regions. These uncertainties are compounded by those associated to the MLT. Addressing such uncertainties by deriving constraints on the individual processes is one of the goals of asteroseismology.

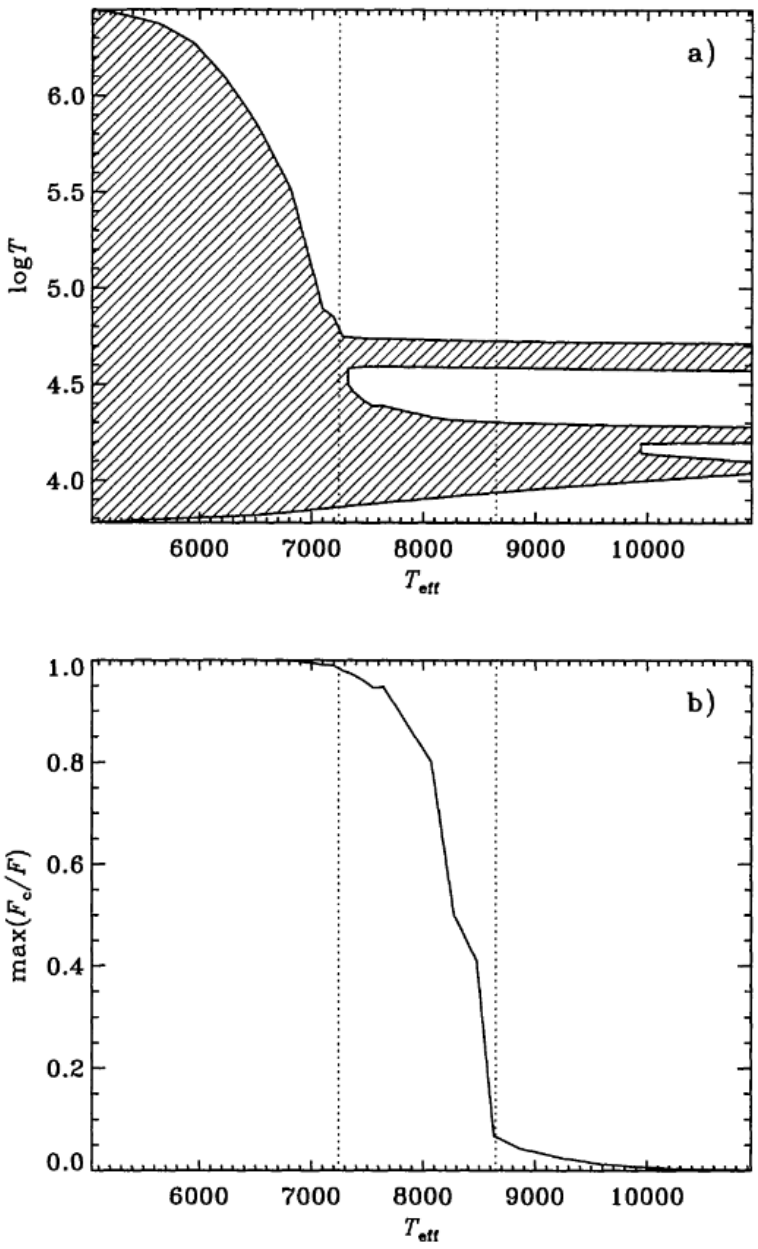

Figure C.1: Extent of the envelope convection zone as a function of $T_{\rm eff}$. The dashed vertical lines, within which this "splitting" occurs, indicate the limits of the *classical instability strip*. The δ Scuti instability domain is located within the classical instability strip (see section 1.2.3.1) so these convection zones are relevant in δ Scuti stars ($6500 < T_{\rm eff} < 9500$).(Christensen-Dalsgaard, 2000).

C.6 Micro-physics

Hydrostatic equilibrium, energy transfer, stratification and mixing describe *macro-physical* processes. Descriptions for the properties of stellar matter itself are contained in the micro-physics and the micro-physics influences the macro-physics.

The equation of state determines the thermodynamic properties of the plasma and so the way it behaves. An *ideal* gas is composed of non-interacting particles and leads to the familiar ideal gas equation of state obeying Maxwell-Boltzmann statistics (LeBlanc, 2010),

$$P = \frac{\rho k_B T}{\mu m_u}, \tag{C.17}$$

where k_B is the Boltzmann's constant and m_u is the atomic mass unit. The ideal gas approximation is usually valid in stars (LeBlanc, 2010), in which case the the various states of ionisation and the relative populations of states can be calculated using the Saha and Boltzman equations, respectively. The approximation breaks down at high densities when *degeneracy* sets in and the appropriate equation of state needs to consider *degeneracy pressure*. Non-ideal effects can also be important when the flux of radiation is large enough that radiation pressure becomes significant, or when energy densities are so large that relativistic effects are important.

Opacity calculations require knowledge of the ionisation and excitation states, as well as other thermodynamic properties associated to the equation of state. To consider each individual frequency across the distribution κ_ν is complex, making it difficult to draw general conclusions (LeBlanc, 2010). The *Rosseland mean opacity*, obtained as a harmonic mean of the frequency-dependent opacity (Aerts et al., 2010), is a suitable average which significantly reduces the complexity of stellar model calculations where the diffusion approximation is valid. Opacity subtracts from the photon beam (Eq.B.4) so evidently impacts radiative energy transfer.

A precise comprehension of Coulomb interactions among particles, quantum phenomena like tunneling, and reaction rates is essential to accurately integrate the nuclear processes responsible for a star's energy into stellar models. These nuclear reactions

influence stellar structure; for instance, whether reactions adhere to the p-p chain or the CNO cycle dictates the manner in which energy is emitted from the core. These factors carry heightened significance in determining the stages of stellar evolution.

We finally note that atomic diffusion and settling also occurs on a microscopic level, as a pose to the macrosopic description in section C.5. This leads to a further level of detail in the complexity of stellar model calculations.

D Stellar Oscillation Equations

D.1 Linear-Adiabatic Oscillations

The stellar oscillation equations are linearised by neglecting terms of order higher than unity (Aerts et al., 2010; Aerts, 2021). The radial displacement variation of the stellar plasma due to linear adiabatic oscillations is given by,

$$\frac{\mathrm{d}\xi_r}{\mathrm{d}r} = -\Big(\frac{2}{r} + \frac{1}{\Gamma_1 p}\frac{\mathrm{d}p}{\mathrm{d}r}\Big)\xi_r + \frac{1}{\rho c^2}\Big(\frac{S_l^2}{\omega^2} - 1\Big)p' + \frac{l(l+1)}{\omega^2 r^2}\Phi', \tag{D.1}$$

where, ρ is the density, c is the speed of light, $\omega = 2\pi\nu$ is the *angular frequency* (García & Ballot, 2019), Φ' is the perturbation to the gravitational potential Φ, p' is the perturbation to the pressure p, Γ_1 is the first adiabatic exponent, and the characteristic acoustic frequency S_l is given by,

$$S_l^2 = \frac{l(l+1)c^2}{r^2} = k_h^2 c^2, \tag{D.2}$$

where k_h is the horizontal wavenumber. The pressure perturbation varies as,

$$\frac{\mathrm{d}p'}{\mathrm{d}r} = \rho(\omega^2 - N^2)\xi_r + \frac{1}{\Gamma_1 p}\frac{\mathrm{d}p}{\mathrm{d}r}p' - \rho\frac{\mathrm{d}\Phi'}{\mathrm{d}r}, \tag{D.3}$$

where N is the buoyancy, or Brunt-Väisällä, frequency, given by,

$$N^2 = g\Big(\frac{1}{\Gamma_1 p}\frac{\mathrm{d}p}{\mathrm{d}r} - \frac{1}{p}\frac{\mathrm{d}\rho}{\mathrm{d}r}\Big), \tag{D.4}$$

with g the unperturbed acceleration due to gravity. Finally, the derivative of the perturbation to the gravitational potential (i.e., the perturbed gravitational acceleration) is expressed as,

$$\frac{1}{r^2}\frac{\mathrm{d}}{\mathrm{d}r}\Big(r^2\frac{\mathrm{d}\Phi'}{\mathrm{d}r}\Big) = 4\pi G\Big(\frac{p'}{c^2} + \frac{\rho\xi_r}{g}N^2\Big) + \frac{l(l+1)}{r^2}\Phi'. \tag{D.5}$$

This fourth order system of ordinary differential equations (Eqs. D.1; D.3; D.5) is a complete set describing linear, adiabatic, non-radial oscillations in the perturbed quantities ξ_r, p', Φ' and $\mathrm{d}\Phi'/\mathrm{d}r$ (Aerts et al., 2010).

E Extra Derivations

E.1 Orbital Mechanics

E.1.1 Kepler's Second Law shows L is constant

Keplers second law states equal areas are swept out in equal periods of time by the radius vector of a component in an elliptic orbit. The infinitesimal area $\mathrm{d}A$ swept by the radius vector r after traversing the angle $\mathrm{d}\theta$ in over the time $\mathrm{d}t$ is given by,

$$\frac{\mathrm{d}A}{\mathrm{d}t} = \frac{r^2}{2}\frac{\mathrm{d}\theta}{\mathrm{d}t}. \tag{E.1}$$

Over a full period then, the full area of the ellipse $A = \pi ab$ is traced, so,

$$\frac{r^2}{2}\frac{\mathrm{d}\theta}{\mathrm{d}t} = \frac{\pi ab}{P}, \tag{E.2}$$

where a and b are the semi-major and -minor axes of the ellipse. Therefore,

$$r^2\frac{\mathrm{d}\theta}{\mathrm{d}t} = \frac{2\pi ab}{P} = constant. \tag{E.3}$$

The definition of angular momentum is $m\boldsymbol{r} \times \dot{\boldsymbol{r}}$ with a magnitude in polar coordinates of $mr^2\dot{\theta}$. Thus, Eq. E.3 shows specific angular momentum is constant and expressed by $2\pi ab/P$.

E.1.2 Derivation of Eq.A.9

Plugging Eq. A.8 into Eq. A.3, using $G(M_1+M_2)$ as the mass term in the relative orbit, we have,

$$\begin{aligned} H &= \frac{1}{2}\mu G(M_1+M_2)\left[\frac{2}{r}-\frac{1}{a}\right]-\frac{GM_1M_2}{r} \\ &= \frac{1}{2}\frac{M_1M_2}{(M_1+M_2)}G(M_1+M_2)\left[\frac{2}{r}-\frac{1}{a}\right]-\frac{GM_1M_2}{r} \\ &= \frac{GM_1M_2}{2}\left[\frac{2}{r}-\frac{1}{a}\right]-\frac{GM_1M_2}{r} \\ &= \frac{GM_1M_2}{2}\left[\frac{2}{r}-\frac{1}{a}-\frac{2}{r}\right] \\ &= -\frac{1}{2}\frac{GM_1M_2}{a}. \end{aligned} \tag{E.4}$$

E.1.3 Derivation of M1R1 + M2R2 = 0

To show $M_1\boldsymbol{r_1}+M_2\boldsymbol{r_2}=0$, consider Eq. A.12 and Eq. A.13,

$$\begin{aligned} M_1\boldsymbol{R_1} &= M_1(\boldsymbol{r_1}-\boldsymbol{R}) \\ &= M_1\boldsymbol{r_1}-M_1\left(\frac{M_1\boldsymbol{r_1}+M_2\boldsymbol{r_2}}{(M_1+M_2)}\right) \\ &= M_1\boldsymbol{r_1}-\left(\frac{M_1^2\boldsymbol{r_1}+M_1M_2\boldsymbol{r_2}}{(M_1+M_2)}\right) \\ &= \frac{(M_1^2\boldsymbol{r_1}+M_1M_2\boldsymbol{r_1})-(M_1^2\boldsymbol{r_1}+M_1M_2\boldsymbol{r_2})}{(M_1+M_2)} \\ &= \frac{M_1M_2\boldsymbol{r_1}-M_1M_2\boldsymbol{r_2}}{(M_1+M_2)}. \end{aligned} \tag{E.5}$$

Now do the same for the same for $M_2\boldsymbol{r_2}$,

$$\begin{aligned} M_2\boldsymbol{R_2} &= M_2(\boldsymbol{r_2} - \boldsymbol{R}) \\ &= M_2\boldsymbol{r_2} - M_2\left(\frac{M_1\boldsymbol{r_1} + M_2\boldsymbol{r_2}}{(M_1+M_2)}\right) \\ &= M_2\boldsymbol{r_2} - \left(\frac{M_1M_2\boldsymbol{r_1} + M_2^2\boldsymbol{r_2}}{(M_1+M_2)}\right) \\ &= \frac{(M_2^2\boldsymbol{r_2} + M_1M_2\boldsymbol{r_2}) - (M_1M_2\boldsymbol{r_1} + M_2^2\boldsymbol{r_2})}{(M_1+M_2)} \\ &= \frac{M_1M_2\boldsymbol{r_2} - M_1M_2\boldsymbol{r_1}}{(M_1+M_2)}. \end{aligned} \tag{E.6}$$

Therefore,

$$\begin{aligned} M_1\boldsymbol{R_1} + M_2\boldsymbol{R_2} &= \frac{M_1M_2\boldsymbol{r_1} - M_1M_2\boldsymbol{r_2}}{(M_1+M_2)} + \frac{M_1M_2\boldsymbol{r_2} - M_1M_2\boldsymbol{r_1}}{(M_1+M_2)} \\ &= \frac{M_1M_2\boldsymbol{r_1} - M_1M_2\boldsymbol{r_2} + M_1M_2\boldsymbol{r_2} - M_1M_2\boldsymbol{r_1}}{(M_1+M_2)} \\ &= 0. \end{aligned} \tag{E.7}$$

E.1.4 Derivation of Eq.A.14

Use the fact that $M_1\boldsymbol{r_1} + M_2\boldsymbol{r_2} = 0$ and Eq. A.13,

$$\boldsymbol{R_1} = -\frac{M_2\boldsymbol{R_2}}{M_1}, \tag{E.8}$$

and therefore,

$$\begin{aligned} \boldsymbol{r} = \boldsymbol{R_1} - \boldsymbol{R_2} &= -\frac{M2\boldsymbol{R_2}}{M_1} - \boldsymbol{R_2} \\ &= -\boldsymbol{R_2}\left(\frac{M2}{M1} + 1\right) \\ &= -\boldsymbol{R_2}\left(\frac{M_2 + M_1}{M_1}\right). \end{aligned} \tag{E.9}$$

Using $\mu = M_1M_2/(M_1+M_2)$,

$$\boldsymbol{R_2} = -\boldsymbol{r}\left(\frac{M_1}{M_1+M_2}\right) = -\frac{\mu}{M_2}\boldsymbol{r}. \tag{E.10}$$

Similarly, using $\boldsymbol{R_2} = -M_1\boldsymbol{R_1}/M_2$,

$$\boldsymbol{R_1} = \boldsymbol{r}\left(\frac{M_2}{M_1+M_2}\right) = \frac{\mu}{M_1}\boldsymbol{r}. \tag{E.11}$$

E.1.5 Derivation of Barycentric Equations of Motions

First, take the equation of motion for component 1 from Eq. A.1, which was described in an arbitrary coordinate system, i.e.,

$$\ddot{\boldsymbol{r_1}} = -\frac{GM_2}{r^2}\hat{r} = -\frac{GM_2}{r^3}\boldsymbol{r}, \tag{E.12}$$

where we used $\hat{r} = \boldsymbol{r}/r$. Using Eq. A.13, we can also write,

$$\ddot{\boldsymbol{r_1}} = -\frac{GM_2}{r^3}(\boldsymbol{R_1} - \boldsymbol{R_2}). \tag{E.13}$$

We also have from Eq. A.14 (derived in Appendix E.1.4) that,

$$\boldsymbol{r} = r\hat{r} = \boldsymbol{R_1}\frac{(M_1+M_2)}{M_2} = R_1\frac{(M_1+M_2)}{M_2}\hat{r}, \tag{E.14}$$

since $\boldsymbol{R_1}$ and $\boldsymbol{r}$ are in the same direction, i.e., the CM is in the line connecting the star's and there are not external forces acting on the system. Thus,

$$r^3 = \frac{(M_1+M_2)^3}{M_2^3}R_1^3, \tag{E.15}$$

which we sub back into Eq. E.13 to yield,

$$\ddot{\boldsymbol{r_1}} = -\frac{GM_2^4}{(M_1+M_2)^3}\frac{(\boldsymbol{R_1} - \boldsymbol{R_2})}{R_1^3}. \tag{E.16}$$

From Aection A.2 $M_1\boldsymbol{R_1} + M_2\boldsymbol{R_2} = 0$ so,

$$\begin{aligned}
\ddot{\boldsymbol{r_1}} &= -\frac{GM_2^4}{(M_1+M_2)^3}\frac{(\boldsymbol{R_1} + M_1\boldsymbol{R_1}/M_2)}{R_1^3}, \\
&= -\frac{GM_2^4}{(M_1+M_2)^3}\frac{(1+M_1/M_2)\boldsymbol{R_1}}{R_1^3}, \\
&= -\frac{GM_2^4}{(M_1+M_2)^3}\frac{(M_2+M_1)}{M_2}\frac{\boldsymbol{R_1}}{R_1^3}, \\
&= -\frac{GM_2^3}{(M_1+M_2)^2}\frac{\boldsymbol{R_1}}{R_1^3}.
\end{aligned} \tag{E.17}$$

Finally, since there are no external forces acting on the system, the CM acceleration is zero, i.e., $\ddot{\boldsymbol{R}} = 0$, and $\ddot{\boldsymbol{r_1}} = \ddot{\boldsymbol{R}}_{\boldsymbol{1}}$ so,

$$\ddot{\boldsymbol{R}}_{\boldsymbol{1}} = -\frac{GM_2^3}{(M_1+M_2)^2}\frac{\boldsymbol{R_1}}{R_1^3}. \tag{E.18}$$

The derivation is the same for $\ddot{\boldsymbol{R}}_{\boldsymbol{2}}$.

E.1.6 Derivation of Eqation of Orbit in terms of E

Using,

$$\cos\nu = \frac{a(e-\cos E)}{-r}, \tag{E.19}$$

then,

$$\begin{aligned}
r &= \frac{a(1-e^2)}{1+e\cos\nu} \\
r &= \frac{a(1-e^2)}{1+e\frac{a(e-\cos E)}{-r}} \\
r\Big[1+\frac{ea(e-\cos E)}{-r}\Big] &= a(1-e^2) \\
r - a(e^2 - e\cos E) &= a(1-e^2) \\
r &= a(1-e^2) + a(e^2 - e\cos E) \\
r(E) &= a(1-e\cos E).
\end{aligned} \tag{E.20}$$

E.1.7 Specific Angular Momentum from Polar Orbit

$$\begin{aligned}
\frac{1}{r} &= \frac{1+e\cos\nu}{a(1-e^2)} \\
-r^{-2}\dot{r} &= -\frac{e\sin\nu\dot{\nu}}{a(1-e^2)} \\
r^2\dot{\nu} &= \frac{a(1-e^2)\dot{r}}{e\sin\nu}.
\end{aligned} \tag{E.21}$$

Now since the total angular momentum is,

$$J = \mu\omega a^2\sqrt{1-e^2}, \tag{E.22}$$

we can divide by μ and write the specific angular momentum as,

$$r^2\dot{\nu} = \frac{a(1-e^2)\dot{r}}{e\sin\nu} = \omega a^2\sqrt{1-e^2}, \tag{E.23}$$

where $\omega = 2\pi/P$ is the orbital frequency.

E.1.8 Derivation of expressions for cos(E) and sin(E)

Begin with the identities in Eq.A.18,

$$\begin{aligned}
\cos E &= e + (1 - e\cos E)\cos\nu \\
\cos E &= e + \cos\nu - e\cos E\cos\nu \\
\cos E + e\cos E\cos\nu &= e + \cos\nu \\
\cos E(1 + e\cos\nu) &= e + \cos\nu \\
\cos E &= \frac{e+\cos\nu}{1+e\cos\nu}.
\end{aligned} \tag{E.24}$$

Now for $\sin E$, from Eq. A.18,

$$\begin{aligned}
\sin E &= \frac{r\sin\nu}{b} \\
\sin E &= \frac{r\sin\nu}{a\sqrt{1-e^2}},
\end{aligned} \tag{E.25}$$

where we used $b = \sqrt{1-e^2}$. Subbing in for r using Eq. A.4,

$$\begin{aligned}
\sin E &= \frac{a(1-e^2)}{1+e\cos\nu}\frac{\sin\nu}{a\sqrt{1-e^2}} \\
\sin E &= \frac{\sqrt{1-e^2}}{1+e\cos\nu}\sin\nu.
\end{aligned} \tag{E.26}$$

E.2 Stellar Theory

E.2.1 Derivation of Radiative Temperature Gradient

From Eq. C.7,

$$\mathrm{d}r = -\frac{\mathrm{d}p}{g(r)\rho}, \tag{E.27}$$

and from Eq. C.12,

$$\mathrm{d}r = -\frac{16\pi r^2 acT^3}{3\kappa\rho L(r)}\,\mathrm{d}T, \tag{E.28}$$

so,

$$\frac{\mathrm{d}T}{\mathrm{d}p} = \frac{3\kappa\rho L(r)}{16\pi r^2 acT^3 g(r)\rho} = \frac{3\kappa L(r)}{16\pi acT^3 GM(r)}. \tag{E.29}$$

and,

$$\frac{\mathrm{d}\ln T}{\mathrm{d}\ln p} = \frac{\mathrm{d}T/T}{\mathrm{d}p/p} = \frac{3\kappa p L(r)}{16\pi acGT^4 M(r)}. \tag{E.30}$$

Bibliography

Abazajian K., et al., 2003, The Astronomical Journal, 126, 2081

Abazajian K., et al., 2004, The Astronomical Journal, 128, 502

Aerts C., 2021, Reviews of Modern Physics, 93, 015001

Aerts C., Christensen-Dalsgaard J., Kurtz D. W., 2010, Asteroseismology. Springer Netherlands

Aerts C., Van Reeth T., Tkachenko A., 2017, ApJL, 847, L7

Aerts C., et al., 2018, ApJS, 237, 15

Aerts C., Mathis S., Rogers T. M., 2019, ARA&A, 57, 35

Ahlers J. P., et al., 2020, The Astronomical Journal, 160, 4

Allard F., Hauschildt P. H., Alexander D. R., Tamanai A., Schweitzer A., 2001, ApJ, 556, 357

Alvarez R., Plez B., 1998, A&A, 330, 1109

Ambastha A., 2010, Solar Interior. pp 15–34, doi:10.1007/978-3-642-11341-3˙2

Andersen J., 1975a, A&A, 44, 355

Andersen J., 1975b, A&A, 45, 203

Andersen J., 1991, A&A Rv, 3, 91

Andersen J., Clausen J. V., Nordstrom B., 1990, ApJL, 363, L33

Antoci V., et al., 2014, ApJ, 796, 118

Astropy Collaboration et al., 2013, A&A, 558, A33

Astropy Collaboration et al., 2018, AJ, 156, 123

Auvergne M., et al., 2009, A&A, 506, 411

Baglin A., Auvergne M., Barge P., Deleuil M., Catala C., Michel E., Weiss W., COROT Team 2006, in Fridlund M., Baglin A., Lochard J., Conroy L., eds, ESA Special Publication Vol. 1306, The CoRoT Mission Pre-Launch Status - Stellar Seismology and Planet Finding. p. 33

Baglin A., Auvergne M., Barge P., Deleuil M., Michel E., 2008, Proceedings of the International Astronomical Union, 4, 71–81

Balona L. A., 2010, Challenges In Stellar Pulsation

Balona L. A., 2014a, MNRAS, 437, 1476

Balona L. A., 2014b, MNRAS, 439, 3453

Balona L. A., 2018, MNRAS, 476, 4840

Balona L. A., Dziembowski W. A., 2011, MNRAS, 417, 591

Balona L. A., Guzik J. A., Uytterhoeven K., Smith J. C., Tenenbaum P., Twicken J. D., 2011, MNRAS, 415, 3531

Balona L. A., Daszyńska-Daszkiewicz J., Pamyatnykh A. A., 2015, MNRAS, 452, 3073

Baraffe I., Homeier D., Allard F., Chabrier G., 2015, A&A, 577, A42

Baran A. S., Koen C., Pokrzywka B., 2015, MNRAS, 448, L16

Batalha N. M., et al., 2010, The Astrophysical Journal Letters, 713, L109

Bayo A., Rodrigo C., Barrado Y Navascués D., Solano E., Gutiérrez R., Morales-Calderón M., Allard F., 2008, A&A, 492, 277

Beatty T. G., et al., 2007, ApJ, 663, 573

Bedding T. R., Murphy S. J., Colman I. L., Kurtz D. W., 2015, in European Physical Journal Web of Conferences. p. 01005 (arXiv:1411.1883), doi:10.1051/epjconf/201510101005

Bedding T. R., et al., 2020, Nature, 581, 147

Beech M., 1985, Ap&SS, 117, 69

Bell S. A., Malcolm G. J., 1987, MNRAS, 226, 899

Bentley S. J., et al., 2009, A&A, 508, 391

Berger D. H., et al., 2006, ApJ, 644, 475

Bessell M. S., 2005, ARA&A, 43, 293

Binnendijk L., 1960, Properties of double stars; a survey of parallaxes and orbits.

Bíró I. B., Nuspl J., 2011, Monthly Notices of the Royal Astronomical Society, 416, 1601

Blackman R. B., Tukey J. W., 1958, The measurement of power spectra from the point of view of communications engineering — Part I, doi:10.1002/j.1538-7305.1958.tb03874.x

Blanco-Cuaresma S., Soubiran C., Jofré P., Heiter U., 2014a, A&A, 566, A98

Blanco-Cuaresma S., Soubiran C., Heiter U., Jofré P., 2014b, A&A, 569, A111

Boffin H. M. J., Jones D., 2019, The Importance of Binaries in the Formation and Evolution of Planetary Nebulae, doi:10.1007/978-3-030-25059-1.

Böhm-Vitense E., 1960, in Thomas R. N., ed., Vol. 12, Aerodynamic Phenomena in Stellar Atmospheres. pp 338–345

Borkovits T., 2022, Galaxies, 10, 9

Borkovits T., et al., 2013, MNRAS, 428, 1656

Borkovits T., Rappaport S., Hajdu T., Sztakovics J., 2015, MNRAS, 448, 946

Borkovits T., Hajdu T., Sztakovics J., Rappaport S., Levine A., Bíró I. B., Klagyivik P., 2016, MNRAS, 455, 4136

Borkovits T., et al., 2019, MNRAS, 483, 1934

Borkovits T., Rappaport S. A., Hajdu T., Maxted P. F. L., Pál A., Forgács-Dajka E., Klagyivik P., Mitnyan T., 2020, MNRAS, 493, 5005

Borucki W. J., et al., 2010, Science, 327, 977

Bouabid M. P., Dupret M. A., Salmon S., Montalbán J., Miglio A., Noels A., 2013, MNRAS, 429, 2500

Bowman D. M., 2017, Amplitude Modulation of Pulsation Modes in Delta Scuti Stars. Springer, doi:10.1007/978-3-319-66649-5

Bowman D. M., Kurtz D. W., 2018, MNRAS, 476, 3169

Bowman D. M., Kurtz D. W., Breger M., Murphy S. J., Holdsworth D. L., 2016, MNRAS, 460, 1970

Bowman D. M., Johnston C., Tkachenko A., Mkrtichian D. E., Gunsriwiwat K., Aerts C., 2019, ApJL, 883, L26

Bowman D. M., Hermans J., Daszyńska-Daszkiewicz J., Holdsworth D. L., Tkachenko A., Murphy S. J., Smalley B., Kurtz D. W., 2021, MNRAS, 504, 4039

Bradley P. A., Guzik J. A., Miles L. F., Uytterhoeven K., Jackiewicz J., Kinemuchi K., 2015, AJ, 149, 68

Brassard P., Charpinet S., 2008, Ap&SS, 316, 107

Breger M., 1979, PASP, 91, 5

Breger M., 2000, in Breger M., Montgomery M., eds, Astronomical Society of the Pacific Conference Series Vol. 210, Delta Scuti and Related Stars. p. 3

Breger M., Beichbuchner F., 1996, A&A, 313, 851

Breger M., et al., 1993, A&A, 271, 482

Bressan A., Marigo P., Girardi L., Salasnich B., Dal Cero C., Rubele S., Nanni A., 2012, Monthly Notices of the Royal Astronomical Society, 427, 127

Butters O. W., et al., 2010, A&A, 520, L10

Canterna R., 1976, AJ, 81, 228

Carnall A. C., 2017, arXiv e-prints, p. arXiv:1705.05165

Carpenter J. M., 2001, AJ, 121, 2851

Casas R., Moya A., Suárez J. C., Martín-Ruíz S., Amado P. J., Rodríguez-López C., Garrido R., 2009, ApJ, 697, 522

Castelli F., Kurucz R. L., 2004, New Grids of ATLAS9 Model Atmospheres (`arXiv:astro-ph/0405087`)

Chabrier G., Baraffe I., 1997, A&A, 327, 1039

Chabrier G., Baraffe I., 2000, ARA&A, 38, 337

Chabrier G., Gallardo J., Baraffe I., 2007, A&A, 472, L17

Chapellier E., Mathias P., 2013, A&A, 556, A87

Chaplin W. J., Miglio A., 2013, ARA&A, 51, 353

Chen X. H., Li Y., Lai X. J., Wu T., 2016, A&A, 593, A69

Chen X., et al., 2022, ApJS, 263, 34

Choi J., Dotter A., Conroy C., Cantiello M., Paxton B., Johnson B. D., 2016, ApJ, 823, 102

Christensen-Dalsgaard J., 2000, in Breger M., Montgomery M., eds, Astronomical Society of the Pacific Conference Series Vol. 210, Delta Scuti and Related Stars. p. 187

Christensen-Dalsgaard J., 2008, Ap&SS, 316, 113

Claret A., 1999, in Gimenez A., Guinan E. F., Montesinos B., eds, Astronomical Society of the Pacific Conference Series Vol. 173, Stellar Structure: Theory and Test of Connective Energy Transport. p. 277

Claret A., 2000, A&A, 363, 1081

Claret A., 2004, A&A, 424, 919

Claret A., 2007, A&A, 475, 1019

Claret A., 2017, A&A, 600, A30

Claret A., Bloemen S., 2011, A&A, 529, A75

Claret A., Torres G., 2016, A&A, 592, A15

Claret A., Torres G., 2017, ApJ, 849, 18

Claret A., Torres G., 2018, ApJ, 859, 100

Claret A., Torres G., 2019, ApJ, 876, 134

Claret A., Giménez A., Baroch D., Ribas I., Morales J. C., Anglada-Escudé G., 2021, A&A, 654, A17

Clausen J. V., Torres G., Bruntt H., Andersen J., Nordström B., Stefanik R. P., Latham D. W., Southworth J., 2008, A&A, 487, 1095

Cleveland W. S., 1979, Journal of the American Statistical Association, 74, 829

Collins K. A., et al., 2018, AJ, 156, 234

Conroy K. E., Prša A., Stassun K. G., Orosz J. A., Fabrycky D. C., Welsh W. F., 2014, AJ, 147, 45

Cousins A. W. J., 1976, MmRAS, 81, 25

Cox J. P., 1967, in Thomas R. N., ed., 28 Vol. 28, Aerodynamic Phenomena in Stellar Atmospheres. p. 3

Cox J. P., 1974, Reports on Progress in Physics, 37, 563

Crouzet N., et al., 2012, Astrophysics from Antarctica, IAU Symposium, 8, 226–230

Cutri R. M., et al., 2003, 2MASS All Sky Catalogue of Point Sources. The IRSA 2MASS All-Sky Point Source Catalogue, NASA/IPAC Infrared Science Archive, Caltech, US

Czesla S., Schröter S., Schneider C. P., Huber K. F., Pfeifer F., Andreasen D. T., Zechmeister M., 2019, PyA: Python astronomy-related packages (ascl:1906.010)

Debosscher J., et al., 2013, A&A, 556, A56

Degroote P., et al., 2009, A&A, 506, 111

Degroote P., et al., 2010, Nature, 464, 259

Deleuil M., et al., 2018, A&A, 619, A97

Demarque P., Woo J.-H., Kim Y.-C., Yi S. K., 2004, ApJS, 155, 667

Deupree R. G., 2011, ApJ, 742, 9

Deupree R. G., Castañeda D., Peña F., Short C. I., 2012, ApJ, 753, 20

Dotson J., 2012, NASA - Kepler Guest Observer Program, `https://nexsci.caltech.edu/workshop/2012/keplergo/PyKEprimerLCs.shtml`

Dotter A., 2016, ApJS, 222, 8

Dotter A., Chaboyer B., Jevremović D., Kostov V., Baron E., Ferguson J. W., 2008, ApJS, 178, 89

Draine B. T., 2003, ARA&A, 41, 241

Duchêne G., Kraus A., 2013, ARA&A, 51, 269

Dupret M. A., Grigahcène A., Garrido R., Gabriel M., Scuflaire R., 2004, A&A, 414, L17

Dupret M. A., Grigahcène A., Garrido R., Gabriel M., Scuflaire R., 2005, A&A, 435, 927

Eastman J., Siverd R., Gaudi B. S., 2010, PASP, 122, 935

Edelsbrunner H., Kirkpatrick D., Seidel R., 1983, IEEE Transactions on Information Theory, 29, 551

Eigmüller P., et al., 2016, The Astronomical Journal, 151, 84

Enoch B., Collier Cameron A., Parley N. R., Hebb L., 2010, A&A, 516, A33

Espinosa Lara F., Rieutord M., 2011, A&A, 533, A43

Etzel P. B., 1975, PhD thesis

Fedurco M., Parimucha Š., Gajdoš P., 2019, in Griffin R. E., ed., 339 Vol. 14, Southern Horizons in Time-Domain Astronomy. pp 295–298, doi:10.1017/S1743921318002806

Fernandez J. M., et al., 2009, ApJ, 701, 764

Fischer D. A., Marcy G. W., Spronck J. F. P., 2014, ApJS, 210, 5

Ford E. B., 2005, AJ, 129, 1706

Foreman-Mackey D., Hogg D. W., Lang D., Goodman J., 2013, PASP, 125, 306

Fuller J., 2017, MNRAS, 472, 1538

Fuller J., Kurtz D. W., Handler G., Rappaport S., 2020, MNRAS, 498, 5730

Fulton B. J., Petigura E. A., Blunt S., Sinukoff E., 2018, PASP, 130, 044504

Gaia Collaboration 2018, A&A, 616, A1

Gaia Collaboration 2021, A&A, 649, A1

Gaia Collaboration et al., 2016, A&A, 595, A1

Gamarova A. Y., Mkrtichian D. E., Rodriguez E., Costa V., Lopez-Gonzalez M. J., 2003, in Sterken C., ed., Astronomical Society of the Pacific Conference Series Vol. 292, Interplay of Periodic, Cyclic and Stochastic Variability in Selected Areas of the H-R Diagram. p. 369

Gamarova A. Y., Mkrtichian D. E., Rodríguez E., 2005, in Claret A., Giménez A., Zahn J. P., eds, Astronomical Society of the Pacific Conference Series Vol. 333, Tidal Evolution and Oscillations in Binary Stars. p. 258

García R. A., Ballot J., 2019, Living Reviews in Solar Physics, 16, 4

Gaulme P., Guzik J. A., 2019, A&A, 630, A106

Gies D. R., Williams S. J., Matson R. A., Guo Z., Thomas S. M., Orosz J. A., Peters G. J., 2012, AJ, 143, 137

Gies D. R., Matson R. A., Guo Z., Lester K. V., Orosz J. A., Peters G. J., 2015, AJ, 150, 178

Gilliland R. L., et al., 2010a, PASP, 122, 131

Gilliland R. L., et al., 2010b, ApJL, 713, L160

Girardi L., Bertelli G., Bressan A., Chiosi C., Groenewegen M. A. T., Marigo P., Salasnich B., Weiss A., 2002, A&A, 391, 195

Goldreich P., Nicholson P. D., 1989, ApJ, 342, 1079

Gontcharov G. A., 2016, Astrophysics, 59, 548

Goodman J., Weare J., 2010, Communications in Applied Mathematics and Computational Science, 5, 65

Goupil M. J., Dupret M. A., Samadi R., Boehm T., Alecian E., Suarez J. C., Lebreton Y., Catala C., 2005, Journal of Astrophysics and Astronomy, 26, 249

Grassitelli L., Fossati L., Langer N., Miglio A., Istrate A. G., Sanyal D., 2015, A&A, 584, L2

Gray D. F., 2005, The Observation and Analysis of Stellar Photospheres, 3 edn. Cambridge University Press, doi:10.1017/CBO9781316036570

Gray R. O., Corbally C. J., 1994, AJ, 107, 742

Grevesse N., Asplund M., Sauval A. J., 2007, SSRv, 130, 105

Grigahcène A., et al., 2010, ApJL, 713, L192

Guo Z., 2021, Frontiers in Astronomy and Space Sciences, 8, 67

Guo Z., Li G., 2019, ApJL, 882, L5

Guo Z., Gies D. R., Matson R. A., García Hernández A., 2016, ApJ, 826, 69

Guo Z., Gies D. R., Fuller J., 2017a, ApJ, 834, 59

Guo Z., Gies D. R., Matson R. A., 2017b, ApJ, 851, 39

Guo Z., Fuller J., Shporer A., Li G., Hambleton K., Manuel J., Murphy S., Isaacson H., 2019, ApJ, 885, 46

Gustafsson B., Edvardsson B., Eriksson K., Jørgensen U. G., Nordlund Å., Plez B., 2008, A&A, 486, 951

Guzik J. A., 2021, Frontiers in Astronomy and Space Sciences, 8, 55

Guzik J. A., Kaye A. B., Bradley P. A., Cox A. N., Neuforge C., 2000, ApJL, 542, L57

Hadrava P., 1995, A&AS, 114, 393

Hadrava P., 2009, arXiv e-prints, p. arXiv:0909.0172

Halbwachs J. L., et al., 2020, MNRAS, 496, 1355

Halbwachs J.-L., et al., 2023, A&A, 674, A9

Hambleton K. M., et al., 2013, MNRAS, 434, 925

Handler G., 2009a, MNRAS, 398, 1339

Handler G., 2009b, in Guzik J. A., Bradley P. A., eds, American Institute of Physics Conference Series Vol. 1170, Stellar Pulsation: Challenges for Theory and Observation. pp 403–409 (arXiv:2110.09806), doi:10.1063/1.3246528

Handler G., 2013, in Oswalt T. D., Barstow M. A., eds, , Vol. 4, Planets, Stars and Stellar Systems. Volume 4: Stellar Structure and Evolution. Springer Neverlands, p. 207, doi:10.1007/978-94-007-5615-1˙4

Handler G., Shobbrook R. R., 2002, MNRAS, 333, 251

Handler G., et al., 2020, Nature Astronomy, 4, 684

Handler G., Jayaraman R., Kurtz D. W., Fuller J., Rappaport S. A., 2022, Tidally Tilted Pulsators (arXiv:2201.01722)

Harris C. R., et al., 2020, Nature, 585, 357

Hartman J. D., et al., 2015, AJ, 149, 166

Hastie T., 2009, The Elements of Statistical Learning Data Mining, Inference, and Prediction, Second Edition, 2nd ed. 2009. edn. Springer Series in Statistics, Springer New York, New York, NY

Hawley S., Reid I. N., Gizis J., 2000, in Griffith C. A., Marley M. S., eds, Astronomical Society of the Pacific Conference Series Vol. 212, From Giant Planets to Cool Stars. p. 252

Haywood M., 2001, MNRAS, 325, 1365

Hełminiak K. G., Konacki M., Maehara H., Kambe E., Ukita N., Ratajczak M., Pigulski A., Kozłowski S. K., 2019, MNRAS, 484, 451

Henden A. A., Levine S. E., Terrell D., Smith T. C., Welch D., 2012, Journal of the American Association of Variable Star Observers, 40, 430

Hensberge H., Pavlovski K., Verschueren W., 2000, A&A, 358, 553

Higl J., Weiss A., 2017, A&A, 608, A62

Hilditch R. W., 2001, An Introduction to Close Binary Stars. Cambridge astrophysics series, Cambridge University Press

Høg E., et al., 2000, A&A, 355, L27

Holtzman J. A., Burrows C. J., Casertano S., Hester J. J., Trauger J. T., Watson A. M., Worthey G., 1995, Publications of the Astronomical Society of the Pacific, 107, 1065

Hong K., Woo Lee J., Rittipruk P., Park J.-H., Kim H.-Y., Han C., 2022, AJ, 164, 121

Howell S. B., et al., 2014, PASP, 126, 398

Hoxie D. T., 1973, A&A, 26, 437

Hurley J. R., Tout C. A., Pols O. R., 2002, MNRAS, 329, 897

Ilijić S., 2003, Master's thesis, University of Zagreb

Ilijić S., 2017, fd3: Spectral disentangling of double-lined spectroscopic binary stars (ascl:1705.012)

Ilijic S., Hensberge H., Pavlovski K., Freyhammer L. M., 2004, in Hilditch R. W., Hensberge H., Pavlovski K., eds, Astronomical Society of the Pacific Conference Series Vol. 318, Spectroscopically and Spatially Resolving the Components of the Close Binary Stars. pp 111–113

Jayaraman R., Handler G., Rappaport S. A., Fuller J., Kurtz D. W., Charpinet S., Ricker G. R., 2022, ApJL, 928, L14

Jenkins J. M., 2017, Kepler Data Processing Handbook: Overview of the Science Operations Center, Kepler Science Document KSCI-19081-002, id. 2, Edited by Jon M. Jenkins.

Jenkins J. M., et al., 2016a, in Chiozzi G., Guzman J. C., eds, Society of Photo-Optical Instrumentation Engineers (SPIE) Conference Series Vol. 9913, Software and Cyberinfrastructure for Astronomy IV. p. 99133E, doi:10.1117/12.2233418

Jenkins J. M., et al., 2016b, in Proc. SPIE. p. 99133E

Jennings Z., Southworth J., Maxted P. F. L., Mancini L., 2023a, Monthly Notices of the Royal Astronomical Society

Jennings Z., Southworth J., Pavlovski K., Van Reeth T., 2023b, Monthly Notices of the Royal Astronomical Society, 527, 4052

Jerzykiewicz M., Pigulski A., Handler G., Moffat A. F. J., Popowicz A., Wade G. A., Zwintz K., Pablo H., 2020, Monthly Notices of the Royal Astronomical Society, 496, 2391

Jofré P., Heiter U., Blanco-Cuaresma S., Soubiran C., 2014, in Astronomical Society of India Conference Series. pp 159–166 (arXiv:1312.2943), doi:10.48550/arXiv.1312.2943

Johnson H. L., 1965, ApJ, 141, 923

Johnston C., Tkachenko A., Aerts C., Molenberghs G., Bowman D. M., Pedersen M. G., Buysschaert B., Pápics P. I., 2019a, MNRAS, 482, 1231

Johnston C., Pavlovski K., Tkachenko A., 2019b, A&A, 628, A25

Joyce M., Tayar J., 2023, Galaxies, 11, 75

Kahraman Aliçavuş F., Soydugan E., Smalley B., Kubát J., 2017, MNRAS, 470, 915

Kahraman Aliçavuş F., Gümüş D., Kırmızıtaş Ö., Ekinci Ö., Çavuş S., Kaya Y. T., Aliçavuş F., 2022, Research in Astronomy and Astrophysics, 22, 085003

Kahraman Aliçavuş F., Çoban Ç. G., Çelik E., Dogan D. S., Ekinci O., Aliçavuş F., 2023, MNRAS, 524, 619

Kaye A. B., Handler G., Krisciunas K., Poretti E., Zerbi F. M., 1999, PASP, 111, 840

Keen M. A., Bedding T. R., Murphy S. J., Schmid V. S., Aerts C., Tkachenko A., Ouazzani R. M., Kurtz D. W., 2015, MNRAS, 454, 1792

Kennelly E. J., et al., 1998, ApJ, 495, 440

Kervella P., Thévenin F., Di Folco E., Ségransan D., 2004, A&A, 426, 297

Khaliullin K. F., Khaliullina A. I., 2010, MNRAS, 401, 257

Kippenhahn R., 1977, A&A, 58, 267

Kippenhahn R., Weigert A., Weiss A., 2013, Stellar Structure and Evolution. Springer, doi:10.1007/978-3-642-30304-3

Kirby E. N., 2011, PASP, 123, 531

Kirk B., et al., 2016, AJ, 151, 68

Knutson H. A., Charbonneau D., Noyes R. W., Brown T. M., Gilliland R. L., 2007, ApJ, 655, 564

Koch D. G., et al., 2010, ApJL, 713, L79

Kolbas V., et al., 2015, MNRAS, 451, 4150

Koo J.-R., Lee J. W., Kim S.-L., Lee C.-U., Lee B.-C., 2012, PASP, 124, 559

Kopal Z., 1959, Close binary systems. New York: Wiley

Kopal Z., 1966, An introduction to the study of the Moon. D. Reidel

Kounkel M., et al., 2021, The Astronomical Journal, 162, 184

Krivova N. A., Solanki S. K., Floyd L., 2006, A&A, 452, 631

Kurtz D. W., 2006, in Aerts C., Sterken C., eds, Astronomical Society of the Pacific Conference Series Vol. 349, Astrophysics of Variable Stars. p. 101

Kurtz M. J., Mink D. J., 1998, PASP, 110, 934

Kurtz D. W., Saio H., Takata M., Shibahashi H., Murphy S. J., Sekii T., 2014, MNRAS, 444, 102

Kurtz D. W., et al., 2020, MNRAS, 494, 5118

Kurucz R. L., 2005, Memorie della Societa Astronomica Italiana Supplementi, 8, 14

Kwee K. K., van Woerden H., 1956, BAN, 12, 327

Lacy C. H., 1977, ApJS, 34, 479

Lallement R., et al., 2018, A&A, 616, A132

Lamers H. J. G. L. M., 2017, Understanding stellar evolution. [IOP release 4], IOP Publishing, Bristol [England] (Temple Circus, Temple Way, Bristol BS1 6HG, UK)

Lampens P., 2021, Galaxies, 9, 28

Landin N. R., Mendes L. T. S., Vaz L. P. R., 2010, A&A, 510, A46

Landstreet J. D., Kupka F., Ford H. A., Officer T., Sigut T. A. A., Silaj J., Strasser S., Townshend A., 2009, A&A, 503, 973

Lastennet E., Valls-Gabaud D., 2002, A&A, 396, 551

Latham D. W., Nordstroem B., Andersen J., Torres G., Stefanik R. P., Thaller M., Bester M. J., 1996, A&A, 314, 864

Latham D. W., et al., 2009, ApJ, 704, 1107

LeBlanc F., 2010, An Introduction to Stellar Astrophysics. Wiley

Ledoux P., 1951, ApJ, 114, 373

Lee M., 2001, in Murdin P., ed., , Encyclopedia of Astronomy and Astrophysics. p. 2317, doi:10.1888/0333750888/2317

Lee U., Saio H., 1987a, MNRAS, 224, 513

Lee U., Saio H., 1987b, MNRAS, 225, 643

Lee U., Saio H., 1989, MNRAS, 237, 875

Lee J. W., Youn J.-H., Kim C.-H., Lee C.-U., Kim H.-I., 2008, AJ, 135, 1523

Lee J. W., Hong K., Kim H.-Y., 2021, AJ, 161, 129

Lehmann H., et al., 2011, A&A, 526, A124

Lehmann H., Southworth J., Tkachenko A., Pavlovski K., 2013, A&A, 557, A79

Lenz P., Breger M., 2005, Communications in Asteroseismology, 146, 53

Lester K. V., Gies D. R., Schaefer G. H., Farrington C. D., Monnier J. D., ten Brummelaar T., Sturmann J., Vargas N., 2019, AJ, 157, 140

Lester K. V., et al., 2022, AJ, 164, 228

Li G., Bedding T. R., Murphy S. J., Van Reeth T., Antoci V., Ouazzani R.-M., 2019, MNRAS, 482, 1757

Li G., Van Reeth T., Bedding T. R., Murphy S. J., Antoci V., Ouazzani R.-M., Barbara N. H., 2020a, MNRAS, 491, 3586

Li G., Guo Z., Fuller J., Bedding T. R., Murphy S. J., Colman I. L., Hey D. R., 2020b, MNRAS, 497, 4363

Liakos A., 2020, Astronomy & Astrophysics, 642, A91

Liakos A., 2021, arXiv e-prints, p. arXiv:2102.05931

Liakos A., Niarchos P., 2017, MNRAS, 465, 1181

Lightkurve Collaboration et al., 2018, Lightkurve: Kepler and TESS time series analysis in Python, Astrophysics Source Code Library (ascl:1812.013)

López-Morales M., 2007, ApJ, 660, 732

López-Morales M., Ribas I., 2005, ApJ, 631, 1120

Loumos G. L., Deeming T. J., 1978, Ap&SS, 56, 285

Lourakis M., 2005, A Brief Description of the Levenberg-Marquardt Algorithm Implemented by Levmar, 4

Lovekin C. C., Guzik J. A., 2017, ApJ, 849, 38

Lucy L. B., 1967, ZA, 65, 89

Lucy L. B., Sweeney M. A., 1971, AJ, 76, 544

MacDonald J., 2015, Structure and evolution of single stars : an introduction. [IOP release 2], Morgan & Claypool Publishers, San Rafael [California] (40 Oak Drive, San Rafael, CA, 94903, USA)

Maceroni C., et al., 2009, A&A, 508, 1375

Maceroni C., Montalbán J., Gandolfi D., Pavlovski K., Rainer M., 2013, A&A, 552, A60

Mathis S., 2009, A&A, 506, 811

Matson R. A., Gies D. R., Guo Z., Orosz J. A., 2016, AJ, 151, 139

Matson R. A., Gies D. R., Guo Z., Williams S. J., 2017, AJ, 154, 216

Maxted P. F. L., 2018, Astronomy & Astrophysics, 616, A39

Mendez R. A., Claveria R. M., Orchard M. E., Silva J. F., 2017, The Astronomical Journal, 154, 187

Mészáros S., et al., 2012, AJ, 144, 120

Miglio A., Montalbán J., Noels A., Eggenberger P., 2008, MNRAS, 386, 1487

Miszuda A., Szewczuk W., Daszyńska-Daszkiewicz J., 2021, MNRAS, 505, 3206

Miszuda A., Kołaczek-Szymański P. A., Szewczuk W., Daszyńska-Daszkiewicz J., 2022, MNRAS, 514, 622

Moe M., Di Stefano R., 2017, ApJS, 230, 15

Molenda-Żakowicz J., Latham D. W., Catanzaro G., Frasca A., Quinn S. N., 2011, Monthly Notices of the Royal Astronomical Society, 412, 1210

Mombarg J. S. G., Van Reeth T., Pedersen M. G., Molenberghs G., Bowman D. M., Johnston C., Tkachenko A., Aerts C., 2019, MNRAS, 485, 3248

Mombarg J. S. G., Dotter A., Reeth T. V., Tkachenko A., Gebruers S., Aerts C., 2020, The Astrophysical Journal, 895, 51

Monteiro M. J. P. F. G., 2008, Ap&SS, 316, 121

Montgomery M. H., O'Donoghue D., 1999, Delta Scuti Star Newsletter, 13, 28

Morales J. C., Ribas I., Jordi C., 2008, A&A, 478, 507

Moravveji E., Aerts C., Pápics P. I., Triana S. A., Vandoren B., 2015, A&A, 580, A27

Morrell S., Naylor T., 2019, MNRAS, 489, 2615

Morton D. C., 1960, ApJ, 132, 146

Moulton F. R., 1895, Popular Astronomy, 3, 136

Moya A., Garrido R., 2008, Ap&SS, 316, 129

Mullan D. J., MacDonald J., 2001, ApJ, 559, 353

Munari U., Zwitter T., 1997, A&A, 318, 269

Murphy S. J., 2018, arXiv e-prints, p. arXiv:1811.12659

Murphy S. J., et al., 2013, MNRAS, 432, 2284

Murphy S. J., Hey D., Van Reeth T., Bedding T. R., 2019, MNRAS, 485, 2380

Murphy S. J., Saio H., Takada-Hidai M., Kurtz D. W., Shibahashi H., Takata M., Hey D. R., 2020, MNRAS, 498, 4272

Murphy S. J., et al., 2021, MNRAS, 505, 2336

Naur P., Osterbrock D. E., 1953, ApJ, 117, 306

Nelson B., Davis W. D., 1972, ApJ, 174, 617

Newville M., et al., 2019, lmfit/lmfit-py 1.0.0, Zenodo, doi:10.5281/zenodo.3588521

Nguyen C. T., et al., 2022, A&A, 665, A126

Niemczura E., et al., 2015, Monthly Notices of the Royal Astronomical Society, 450, 2764

North P., Zahn J. P., 2004, NewAR, 48, 741

Ochsenbein F., Bauer P., Marcout J., 2000, A&AS, 143, 23

Olver F. W. J., 1956, Philosophical Transactions of the Royal Society of London Series A, 249, 65

Ouazzani R.-M., Salmon S. J. A. J., Antoci V., Bedding T. R., Murphy S. J., Roxburgh I. W., 2017, MNRAS, 465, 2294

Ouazzani R. M., Marques J. P., Goupil M. J., Christophe S., Antoci V., Salmon S. J. A. J., Ballot J., 2019, A&A, 626, A121

Ouazzani R. M., Lignières F., Dupret M. A., Salmon S. J. A. J., Ballot J., Christophe S., Takata M., 2020, A&A, 640, A49

Paczyński B., 1971, ARA&A, 9, 183

Pamyatnykh A. A., 1999, AcA, 49, 119

Pamyatnykh A. A., 2000, in Breger M., Montgomery M., eds, Astronomical Society of the Pacific Conference Series Vol. 210, Delta Scuti and Related Stars. p. 215 (`arXiv:astro-ph/0005276`)

Pamyatnykh A. A., 2003, Ap&SS, 284, 97

Papaloizou J. C. B., Savonije G. J., 1997, Monthly Notices of the Royal Astronomical Society, 291, 651

Pápics P. I., et al., 2017, A&A, 598, A74

Parsons S. G., et al., 2018, MNRAS, 481, 1083

Pasternacki T., et al., 2011, AJ, 142, 114

Pavlovski K., Hensberge H., 2005, A&A, 439, 309

Pavlovski K., Hensberge H., 2010, in Prša A., Zejda M., eds, Astronomical Society of the Pacific Conference Series Vol. 435, Binaries - Key to Comprehension of the Universe. p. 207 (arXiv:0909.3246), doi:10.48550/arXiv.0909.3246

Pavlovski K., Southworth J., Tamajo E., 2018, MNRAS, 481, 3129

Pavlovski K., et al., 2022, A&A, 658, A92

Pavlovski K., Southworth J., Tkachenko A., Van Reeth T., Tamajo E., 2023, A&A, 671, A139

Paxton B., Bildsten L., Dotter A., Herwig F., Lesaffre P., Timmes F., 2011, ApJS, 192, 3

Paxton B., et al., 2013, ApJS, 208, 4

Paxton B., et al., 2015, ApJS, 220, 15

Paxton B., et al., 2019, ApJS, 243, 10

Penoyre Z., Stone N. C., 2019, AJ, 157, 60

Perryman M. A. C., et al., 1997, A&A, 323, L49

Petersen J. O., Christensen-Dalsgaard J., 1996, A&A, 312, 463

Pickering E. C., 1890, The Observatory, 13, 80

Pietrinferni A., Cassisi S., Salaris M., Castelli F., 2004, ApJ, 612, 168

Piskunov N., Valenti J. A., 2017, A&A, 597, A16

Plez B., 2012, Turbospectrum: Code for spectral synthesis, Astrophysics Source Code Library, record ascl:1205.004 (ascl:1205.004)

Polfliet R., Smeyers P., 1990, A&A, 237, 110

Pols O. R., Tout C. A., Schroder K.-P., Eggleton P. P., Manners J., 1997, MNRAS, 289, 869

Pont F., et al., 2006, A&A, 447, 1035

Popper D. M., 1967, ARA&A, 5, 85

Popper D. M., 1980, ARA&A, 18, 115

Popper D. M., Etzel P. B., 1981, AJ, 86, 102

Pourbaix D., 2000, A&AS, 145, 215

Prša A., et al., 2016, AJ, 152, 41

Prša A., 2018, Modeling and Analysis of Eclipsing Binary Stars; The theory and design principles of PHOEBE, doi:10.1088/978-0-7503-1287-5.

Prša A., Zwitter T., 2005, ApJ, 628, 426

Prša A., et al., 2011, AJ, 141, 83

Prša A., et al., 2016, ApJS, 227, 29

Prša A., et al., 2022, ApJS, 258, 16

Rappaport S., Deck K., Levine A., Borkovits T., Carter J., El Mellah I., Sanchis-Ojeda R., Kalomeni B., 2013, ApJ, 768, 33

Rappaport S. A., et al., 2021, MNRAS, 503, 254

Rappaport S. A., et al., 2022, Monthly Notices of the Royal Astronomical Society, 513, 4341

Raskin G., et al., 2011, A&A, 526, A69

Rauer H., et al., 2022, in European Planetary Science Congress. pp EPSC2022–453, doi:10.5194/epsc2022-453

Reed M., Kawaler S. D., Kleinman S. J., 2001, in Provencal J. L., Shipman H. L., MacDonald J., Goodchild S., eds, Astronomical Society of the Pacific Conference Series Vol. 226, 12th European Workshop on White Dwarfs. p. 181

Reed M. D., Brondel B. J., Kawaler S. D., 2005, ApJ, 634, 602

Reif K., et al., 1999. pp 109–120

Remus F., Mathis S., Zahn J. P., 2012, A&A, 544, A132

Reyniers K., Smeyers P., 2003a, A&A, 404, 1051

Reyniers K., Smeyers P., 2003b, A&A, 409, 677

Ribas I., Jordi C., Giménez Á., 2000, MNRAS, 318, L55

Ricker G. R., et al., 2015, Journal of Astronomical Telescopes, Instruments, and Systems, 1, 014003

Rodríguez E., López-González M. J., López de Coca P., 2000, A&AS, 144, 469

Rodríguez E., García J. M., Gamarova A. Y., Costa V., Daszyńska-Daszkiewicz J., López-González M. J., Mkrtichian D. E., Rolland A., 2004, MNRAS, 353, 310

Saio H., Kurtz D. W., Takata M., Shibahashi H., Murphy S. J., Sekii T., Bedding T. R., 2015, MNRAS, 447, 3264

Saio H., Takata M., Lee U., Li G., Van Reeth T., 2021, MNRAS, 502, 5856

Salmon S. J. A. J., Ouazzani R. M., Antoci V., Bedding T. R., Murphy S. J., 2017, in European Physical Journal Web of Conferences. p. 05002 (arXiv:1709.03791), doi:10.1051/epjconf/201715205002

Samadi Ghadim A., Lampens P., Jassur D. M., 2018, AcA, 68, 425

Savonije G. J., Papaloizou J. C. B., 1997, Monthly Notices of the Royal Astronomical Society, 291, 633

Savonije G. J., Papaloizou J. C. B., Alberts F., 1995, Monthly Notices of the Royal Astronomical Society, 277, 471

Scargle J. D., 1982, ApJ, 263, 835

Schlafly E. F., Finkbeiner D. P., 2011, ApJ, 737, 103

Schmid V. S., Aerts C., 2016, A&A, 592, A116

Schmid V. S., et al., 2015, A&A, 584, A35

Scuflaire R., Montalbán J., Théado S., Bourge P. O., Miglio A., Godart M., Thoul A., Noels A., 2008, Ap&SS, 316, 149

Sekaran S., et al., 2020, A&A, 643, A162

Sekaran S., Tkachenko A., Johnston C., Aerts C., 2021, A&A, 648, A91

Shahaf S., Mazeh T., 2019, MNRAS, 487, 3356

Shi X.-d., Qian S.-b., Li L.-J., 2022, ApJS, 259, 50

Shin Y., Yoon S., Seo Y., Jin H., Seon J., 2015, Advances in Space Research, 55, 1792

Short C. I., Bayer J. H. T., Burns L. M., 2018, ApJ, 854, 82

Silvotti R., et al., 2020, Monthly Notices of the Royal Astronomical Society, 500, 2461

Simon K. P., Sturm E., 1994, A&A, 281, 286

Skrutskie M. F., et al., 2006, AJ, 131, 1163

Smalley B., 2005, Memorie della Societa Astronomica Italiana Supplementi, 8, 130

Smalley B., Smith K. C., M D. M., 2001, UCLSYN: User Guide (University College London)

Smart W. M., Green E. b. R. M., 1977, Textbook on Spherical Astronomy

Smeyers P., 2005, in Claret A., Giménez A., Zahn J. P., eds, Astronomical Society of the Pacific Conference Series Vol. 333, Tidal Evolution and Oscillations in Binary Stars. p. 39

Smeyers P., Moya A., 2007, A&A, 465, 509

Sneden C., Bean J., Ivans I., Lucatello S., Sobeck J., 2012, MOOG: LTE line analysis and spectrum synthesis, Astrophysics Source Code Library, record ascl:1202.009 (ascl:1202.009)

Southworth J., 2008, MNRAS, 386, 1644

Southworth J., 2009, Monthly Notices of the Royal Astronomical Society, 394, 272

Southworth J., 2010, MNRAS, 408, 1689

Southworth J., 2012, JKTEBOP: Analyzing light curves of detached eclipsing binaries, Astrophysics Source Code Library, record ascl:1207.013 (ascl:1207.013)

Southworth J., 2013, A&A, 557, A119

Southworth J., 2015, in Rucinski S. M., Torres G., Zejda M., eds, Astronomical Society of the Pacific Conference Series Vol. 496, Living Together: Planets, Host Stars and Binaries. p. 164 (`arXiv:1411.1219`)

Southworth J., 2020, The Observatory, 140, 247

Southworth J., 2021, Universe, 7, 369

Southworth J., 2022, arXiv e-prints, p. arXiv:2209.10384

Southworth J., Clausen J. V., 2007, A&A, 461, 1077

Southworth J., Maxted P. F. L., Smalley B., 2004a, MNRAS, 351, 1277

Southworth J., Zucker S., Maxted P. F. L., Smalley B., 2004b, MNRAS, 355, 986

Southworth J., Smalley B., Maxted P. F. L., Claret A., Etzel P. B., 2005a, MNRAS, 363, 529

Southworth J., Maxted P. F. L., Smalley B., 2005b, A&A, 429, 645

Southworth J., Wheatley P. J., Sams G., 2007, MNRAS, 379, L11

Southworth J., et al., 2009, MNRAS, 396, 1023

Southworth J., et al., 2011, MNRAS, 414, 2413

Southworth J., et al., 2014, MNRAS, 444, 776

Southworth J., Bohn A. J., Kenworthy M. A., Ginski C., Mancini L., 2020, A&A, 635, A74

Soydugan E., İbanoğlu C., Soydugan F., Akan M. C., Demircan O., 2006, MNRAS, 366, 1289

Springer O. M., Shaviv N. J., 2013, Monthly Notices of the Royal Astronomical Society, 434, 1869

Stancliffe R. J., Fossati L., Passy J. C., Schneider F. R. N., 2015, A&A, 575, A117

Steindl T., Zwintz K., Bowman D. M., 2021, A&A, 645, A119

Sterne T. E., 1941, Proceedings of the National Academy of Science, 27, 93

Stetson P. B., 1987, PASP, 99, 191

Storn R., Price K. V., 1997, Journal of Global Optimization, 11, 341

Strassmeier K. G., 2009, A&A Rv, 17, 251

Suárez J. C., Goupil M. J., 2008, Ap&SS, 316, 155

Suárez J. C., Bruntt H., Buzasi D., 2005, A&A, 438, 633

Suárez J. C., García Hernández A., Moya A., Rodrigo C., Solano E., Garrido R., Rodón J. R., 2014, A&A, 563, A7

Swayne M. I., et al., 2021, Monthly Notices of the Royal Astronomical Society

Takeda Y., Ohkubo M., Sadakane K., 2002, Publications of the Astronomical Society of Japan, 54, 451

Tamajo E., Pavlovski K., Southworth J., 2011, A&A, 526, A76

Tassoul M., 1980, ApJS, 43, 469

Taylor J. K., 2006, PhD thesis

Themeßl N., et al., 2018, Monthly Notices of the Royal Astronomical Society, 478, 4669

Tkachenko A., 2015, A&A, 581, A129

Tkachenko A., Van Reeth T., Tsymbal V., Aerts C., Kochukhov O., Debosscher J., 2013, A&A, 560, A37

Tkachenko A., et al., 2020, A&A, 637, A60

Tonry J., Davis M., 1979, AJ, 84, 1511

Torres G., 2007, ApJ, 671, L65

Torres G., 2013, Astronomische Nachrichten, 334, 4

Torres G., Ribas I., 2002, ApJ, 567, 1140

Torres G., Stefanik R. P., Andersen J., Nordstrom B., Latham D. W., Clausen J. V., 1997, AJ, 114, 2764

Torres G., Andersen J., Nordström B., Latham D. W., 2000, The Astronomical Journal, 119, 1942

Torres G., Lacy C. H., Marschall L. A., Sheets H. A., Mader J. A., 2006, The Astrophysical Journal, 640, 1018

Torres G., Winn J. N., Holman M. J., 2008, ApJ, 677, 1324

Torres G., Andersen J., Giménez A., 2010, A&A Rv, 18, 67

Torres G., Vanderburg A., Curtis J. L., Kraus A. L., Gaidos E., 2021, ApJ, 921, 133

Tout C. A., Pols O. R., Eggleton P. P., Han Z., 1996, MNRAS, 281, 257

Townsend R. H. D., Teitler S. A., 2013, MNRAS, 435, 3406

Triana S. A., Moravveji E., Pápics P. I., Aerts C., Kawaler S. D., Christensen-Dalsgaard J., 2015, ApJ, 810, 16

Triaud A. H. M. J., et al., 2017, A&A, 608, A129

Trypsteen M. F. M., Walker R., 2017, Electron Transitions and Formation of the Spectra. Cambridge University Press, p. 7–14, doi:10.1017/9781316694435.003

Ulrich R. K., 1986, ApJL, 306, L37

Uytterhoeven K., et al., 2011, A&A, 534, A125

Valenti J. A., Piskunov N., 1996, A&AS, 118, 595

Valle G., Dell'Omodarme M., Prada Moroni P. G., Degl'Innocenti S., 2017, A&A, 600, A41

Van Cleve J. E., Caldwell D. A., 2016, Kepler Instrument Handbook, Kepler Science Document KSCI-19033-002, id.1. Edited by Michael R. Haas and Steve B. Howell

Van Hamme W., 1993, AJ, 106, 2096

Van Reeth T., et al., 2015a, ApJS, 218, 27

Van Reeth T., et al., 2015b, A&A, 574, A17

Van Reeth T., Tkachenko A., Aerts C., 2016, A&A, 593, A120

Van Reeth T., et al., 2018, A&A, 618, A24

Van Reeth T., Southworth J., Van Beeck J., Bowman D. M., 2022, A&A, 659, A177

Van Reeth T., Johnston C., Southworth J., Fuller J., Bowman D. M., Poniatowski L., Van Beeck J., 2023, A&A, 671, A121

VandenBerg D. A., Bergbusch P. A., Dowler P. D., 2006, ApJS, 162, 375

Viani L. S., Basu S., M. J. O. J., Bonaca A., Chaplin W. J., 2018, The Astrophysical Journal, 858, 28

Virtanen P., et al., 2020, Nature Methods, 17, 261

Vogt S. S., 1987, PASP, 99, 1214

Wang S., et al., 2014, ApJS, 211, 26

Wang L., et al., 2020, AJ, 159, 4

Wang L., Gies D. R., Peters G. J., Han Z., 2023, AJ, 165, 203

Weiss W. W., et al., 2014, PASP, 126, 573

Wellstein S., Langer N., Braun H., 2001, A&A, 369, 939

Welsh W. F., et al., 2011, ApJS, 197, 4

Wikipedia contributors 2023, Helioseismology — Wikipedia, The Free Encyclopedia, https://en.wikipedia.org/wiki/Helioseismology#/media/File:ModelS_pmode_n14_l20_m16.png

Wilson R. E., 1979, ApJ, 234, 1054

Wilson R. E., 1990, ApJ, 356, 613

Wilson R. E., 2008, ApJ, 672, 575

Wilson R. E., Devinney E. J., 1971, ApJ, 166, 605

Wilson R. E., Van Hamme W., 2004, Computing Binary Star Observables (Wilson-Devinney program user guide), available at ftp://ftp.astro.ufl.edu/pub/wilson

Witte M. G., Savonije G. J., 1998, arXiv e-prints, pp astro–ph/9810493

Witte M. G., Savonije G. J., 1999, A&A, 350, 129

Witteborn F. C., Van Cleve J., Borucki W., Argabright V., Hascall P., 2011, in Shaklan S., ed., Society of Photo-Optical Instrumentation Engineers (SPIE) Conference Series Vol. 8151, Techniques and Instrumentation for Detection of Exoplanets V. p. 815117, doi:10.1117/12.892850

Wright J. T., Eastman J. D., 2014, PASP, 126, 838

Xiong D. R., Deng L., Zhang C., Wang K., 2016, MNRAS, 457, 3163

Xu X., Cisewski-Kehe J., Davis A. B., Fischer D. A., Brewer J. M., 2019, AJ, 157, 243

Yang T.-Z., Zuo Z.-Y., Li G., Bedding T. R., Murphy S. J., Joyce M., 2021, A&A, 655, A63

Zahn J. P., 1975, A&A, 41, 329

Zahn J. P., 1977, A&A, 57, 383

Zechmeister M., 2018, A&A, 619, A128

Zhang X. B., Luo C. Q., Fu J. N., 2013, ApJ, 777, 77

Zhang X., Chen X., Zhang H., Fu J., Li Y., 2020, ApJ, 895, 124

Zhou A. Y., 2010, arXiv e-prints, p. arXiv:1002.2729

Zhou G., et al., 2014, MNRAS, 437, 2831

Zhou G., et al., 2015, Monthly Notices of the Royal Astronomical Society, 451, 2263

Zucker S., Mazeh T., 1994, ApJ, 420, 806

Zucker S., Mazeh T., Alexander T., 2007, ApJ, 670, 1326

Zwintz K., et al., 2014, A&A, 567, A4

da Silva R., Maceroni C., Gandolfi D., Lehmann H., Hatzes A. P., 2014, A&A, 565, A55

de Mink S. E., Pols O. R., Hilditch R. W., 2007, A&A, 467, 1181

del Burgo C., Allende Prieto C., 2018, MNRAS, 479, 1953

von Boetticher A., et al., 2019, A&A, 625, A150

von Zeipel H., 1924, MNRAS, 84, 665